A PRECISION MEASUREMENT OF THE NEUTRON SPIN STRUCTURE FUNCTIONS USING A POLARIZED ^{3}He TARGET

by

Todd B. Smith

A dissertation submitted in partial fulfillment
of the requirements for the degree of
Doctor of Philosophy
(Physics)
in The University of Michigan
1998

Doctoral Committee:

Professor Timothy Chupp, Chairperson
Assistant Research Scientist Kevin P. Coulter
Professor Emeritus Robert Lewis
Assistant Professor Wolfgang Lorenzon
Professor Robert Sharp

For my wife, Elizabeth, with whom all things are possible.

ACKNOWLEDGEMENTS

First and foremost, I would like to begin by thanking my advisor, Timothy Chupp, who provided me with the support and encouragement necessary to complete a doctoral dissertation. I thank him for reminding me of what is important and for asking me the hard questions. I also thank him for his help and guidance, and for being an ideal role model throughout the graduate experience. I would like to thank the members of my committee for taking the time to read my thesis and correct the manuscript, and in Bob Lewis' case, for loaning me his office so that I might have a quiet place to work. I would also like to thank Kevin Coulter and Robert Welsh for all of their help in writing the thesis and in analyzing the data. It is possible Robert that you have convinced me that I do not hate Unix.

This experiment at SLAC was part of a rich program of spin physics which I have had the pleasure of being a part of since 1992. The collaborative effort of many physicists, all of whom cannot be mentioned here. I would like to thank our spokesman, Emlyn Hughes. My experience at SLAC would not have been the same without his enthusiasm and support. After all, if the target wasn't working, it was Emlyn who got to explain it to Burton Richter and David Leith. This experiment would not have been possible without all of the hard work and dedication of my fellow graduate students. Many thanks to Steve Churchwell, Sabastian Incerti, Yury Kolomensky, Greg Mitchell, Mike Olson, David Reyna, Mike Romalis, Franck Sabatie, Jason Wang, and Piotr Zyla. I would particularly like to thank David for all of the times he let me stay at his place, play bridge and drink beer, and Mike for all of the wonderful discussions we had about the target. I appreciated the discussions and help from Ray Arnold, Zein-Eddine Meziani, Makis Petratos, Richard Prepost, Steve Rock, Paul Souder, Alan Thompson, and Charlie Young. I would particularly like to thank Alan for teaching me so much when I first started in this field in 1992.

The polarized ^{3}He target was an exciting challenge, and its success is the result of a lot of hard work by many people. I would like to thank the members of the polarized ^{3}He target group. They are Tim Chupp, Kevin Coulter, Robert Welsh, Mike Romalis, Gordon Cates, Krishna Kumar, Paul Bogorad, Alan Thompson, Emlyn Hughes, and Jim Johnson. Mike Souza, the Princeton glass blower, belongs as an honorary member of this group for the miracles he performed in making the target cells. I would particularly like to thank Jim for his hard work and the enjoyment that I had working with him in the construction phase of the experiment.

Working in the Chupplab at The University of Michigan has always been an enjoyable experience, and I have my fellow students to thank for their help and friendship. I would like to thank Matt Rosen, Mark Rosenberry, Shenq-Rong Hwang, Jon Zerger, and Jeff Fixler. I would also like to thank my friend Brian Davis for being himself and for so many wonderful times. I also want to thank him for once getting me unstuck in a cave.

I would like to thank my parents who have always encouraged me to explore and challenge myself, ever since the day I learned how to take apart my toys. I would like to thank Chris Starkey and Greg Morrow, my friends from Notre Dame, whose companionship I enjoyed while turning my attention to the problems of physics. But most of all, I wish to thank my wife Elizabeth for her love, patience, help and understanding.

PREFACE

This thesis describes a precision measurement of the neutron spin dependent structure function, $g_1^n(x)$. The measurement was made by the E154 collaboration at SLAC using a longitudinally polarized, 48.3 GeV electron beam, and a ^{3}He target polarized by spin exchange with optically pumped rubidium. A target polarization as high as 50% was achieved. The elements of the experiment which pertain to the polarized ^{3}He target will be described in detail in this thesis. To achieve a precision measurement, it has been necessary to minimize the systematic error from the uncertainty in the target parameters. All of the parameters of the target have been carefully measured, and the most important parameters of the target have been measured using multiple techniques. The polarization of the target was measured using nuclear magnetic resonance techniques, and has been calibrated using both proton NMR and by measuring the shift of the Rb Zeeman resonance frequency due to the ^{3}He polarization. The fraction of events which originated in the ^{3}He, as measured by the spectrometers, has been determined using a physical model of the target and the spectrometers. It was also measured during the experiment using a variable pressure ^{3}He reference cell in place of the polarized ^{3}He target.

The spin dependent structure function $g_1^n(x)$ was measured in the Bjorken x range of $0.014 < x < 0.7$ with an average Q^2 of 5 $(\mathrm{GeV/c})^2$. One of the primary motivations for this experiment was to test the Bjorken sum rule. Because the experiment had smaller statistical errors and a broader kinematic coverage than previous experiments, the behavior of the spin structure function $g_1^n(x)$ could be studied in detail at low values of the Bjorken scaling variable x. It was found that $g_1^n(x)$ has a strongly divergent behavior at low values of x, calling into question the methods commonly used to extrapolate the value of $g_1^n(x)$ to low x. The precision of the measurement made by the E154 collaboration at SLAC puts a tighter constraint on the extrapolation of $g_1^n(x)$ to low x, which is necessary to evaluate the Bjorken sum rule.

TABLE OF CONTENTS

DEDICATION . . . . **ii**

ACKNOWLEDGEMENTS . . . . **iii**

PREFACE . . . . **v**

LIST OF FIGURES . . . . **ix**

LIST OF TABLES . . . . **xv**

CHAPTER

I. Introduction and Background 1

II. Spin Dependent Structure Functions 8

2.1 Definitions and List of Symbols 8
2.2 Structure Functions 9
2.3 The Virtual Photon - Nucleon Asymmetry 13
2.4 Experimental Asymmetries 15
2.4.1 Polarized ^{3}He as a Polarized Neutron 16
2.5 The Quark Parton Model 17
2.6 Sum Rules 18

III. SLAC Experiment E154 21

3.1 The Polarized Electron Beam 21

3.2 Møller Polarimeter 25
3.3 Polarized ^{3}He Target 29
3.4 Spectrometers 31
3.4.1 Magnets 31
3.4.2 Cherenkovs 32
3.4.3 Hodoscopes 34
3.4.4 Shower Counters 35
3.4.5 Electronics and DAQ 35

IV. Advances in ^{3}He Target Technology 37

4.1 Introduction 37
4.2 Theory of Operation 39
4.2.1 Optical Pumping 39
4.2.2 Spin Exchange 45
4.3 Target Cell Construction 50
4.3.1 Choice of Glass 51
4.3.2 Target Cell Dimensions 53
4.3.3 Target Cell Densities and Temperatures 56
4.4 Laser Pumping System 62
4.5 Measurement of Target Polarization 68
4.5.1 Adiabatic Fast Passage 68
4.5.2 Target NMR Polarimetry Apparatus 71
4.5.3 Calculation of AFP Signal 75
4.6 Calibration of Target Polarization 81
4.6.1 Water AFP Calibration 82
4.6.2 Water Signal Analysis 83
4.6.3 Results for Water Calibration 87
4.6.4 EPR Calibration 88
4.6.5 Comparison of Methods and Final Result 94
4.7 Target Model 96
4.7.1 Calculation of Rates 99

4.7.2 Radiative Corrections 102
4.7.3 Results 109

V. Data Analysis 114

5.1 Overview 114
5.2 Cherenkovs 115
5.3 Shower Counters 115
5.4 Hodoscopes and Tracking 117
5.5 Run Selection and Beam Cuts 118
5.6 Electron Identification 120
5.7 Reference Cell Analysis 120
5.7.1 Rate Dependence 123
5.7.2 Background Subtraction 125
5.7.3 Results and Comparison to Target Model 127

VI. Physics Analysis and Results 135

6.1 Asymmetry Analysis 135
6.1.1 Backgrounds 137
6.1.2 Rate Dependence 139
6.1.3 Electroweak Correction 142
6.1.4 Radiative Corrections 142
6.1.5 Results 144
6.2 The Spin Structure Function g_1^n 144
6.3 Integrals and Sum Rules 151
6.3.1 Low x 156
6.4 Conclusion 161

APPENDIX **165**

BIBLIOGRAPHY **172**

LIST OF FIGURES

Figure

1.1 Schematic view of electron scattering. 1

1.2 World spin structure function data before SLAC experiment E154. . 7

2.1 Deep inelastic electron nucleon scattering. 9

3.1 Layout of the E154 Spectrometers. 22

3.2 Layout of the E154 Møller Polarimeter. The center of mass scattering angles are indicated on each ray. 26

3.3 Electron beam polarization for SLAC experiment E154. 29

3.4 Kinematic coverage in x and Q^2 of SLAC experiment E154. 32

4.1 Rubidium energy levels and transitions. 40

4.2 Pumping cell fluorescence. 45

4.3 Dimensions of the target cell Picard. 54

4.4 Target cell showing RTD placement. 60

4.5 Temperature distribution of the target cell with linear fit. 60

4.6 Spin up comparison for Minnehaha. 63

4.7 Absorption curve for rubidium broadened by 10 amagats of ^{3}He and emission profiles of Ti:sapphire lasers and laser diode arrays. 65

4.8 Layout of the E154 laser hut. 66

4.9 Optics used with the laser diode arrays. 67

4.10 Experimental apparatus used for target polarization measurements. 71

4.11 Lower chamber of the target and NMR pickup coils. 73

4.12 ^{3}He AFP signal, Lorentzian fit and residuals. 74

4.13 Coordinate system for target cell and pickup coils. 76

4.14 Water AFP signal, Lorentzian fit and model prediction. 84

4.15 Results of numerical integration of the modified Bloch equations. . . 85

4.16 Ratio of the up and down water signals and results of the numerical simulation. 85

4.17 Correction to the water signal peak height. 87

4.18 Typical EPR data set taken after the experimental run. 93

4.19 Results for water and EPR and final E154 target polarization calibration constant for Picard. 96

4.20 Model dilution factor for Picard with and without radiative corrections. 99

4.21 GEANT picture of the SLAC experiment E154 target, magnets and collimators in the 2.75° spectrometer. 105

4.22 Tracks in the 5.50° spectrometer as simulated by GEANT. 105

4.23 Dilution factor for the target cell Picard in the 2.75° spectrometer. . 110

4.24 Dilution factor for the target cell Picard in the 5.50° spectrometer. . 110

5.1 Histogram of target polarization. 118

5.2 Series of cuts used for electron identification. 121

5.3 Dilution factor for the target cell Dave. 130

5.4 Dilution factor for the target cell Riker. 130

5.5 Dilution factor for the target cell Bob. 131

5.6 Dilution factor for the target cell SMC. 131

5.7 Dilution factor for the target cell Generals. 132

5.8 Dilution factor for the target cell Hermes. 132

5.9 Dilution factor for the target cell Prelims. 133

5.10 Dilution factor for the target cell Chance. 133

5.11 Dilution factor for the target cell Picard. 134

5.12 Dilution factor for the average target cell. 134

6.1 E/p spectrum for the $x = 0.017$ x-bin 138

6.2 Pion fraction 140

6.3 Pion asymmetry 140

6.4 Positron fraction 141

6.5 Positron asymmetry 141

6.6 Parallel experimental asymmetry for ^{3}He and polarized radiative corrections in the 2.75° spectrometer. Error bars are explained in the text. 145

6.7 Parallel experimental asymmetry for ^{3}He and polarized radiative corrections in the 5.50° spectrometer. Error bars are explained in the text. 145

6.8 Perpendicular experimental asymmetry for ^{3}He and polarized radiative corrections in the 2.75° spectrometer. Error bars are explained in the text. 146

6.9 Perpendicular experimental asymmetry for ^{3}He and polarized radiative corrections in the 5.50° spectrometer. Error bars are explained in the text. 146

6.10 The spin dependent structure function g_1^n plotted as xg_1^n. The error bars are statistical only and the shaded area has a height equal to 2 standard deviation systematic errors. The data for the 5.50° spectrometer has been offset slightly for clarity. (Note that the two spectrometers are at different Q^2s.) These are the results of this dissertation and not the 'official' SLAC experiment E154 results [90,91]. 150

6.11 The spin dependent structure function g_1^n at 5 (GeV/c)^2 plotted as g_1^n in the top graph and as xg_1^n in the bottom graph. The error bars are statistical only and the shaded area has a height equal to 2 standard deviation systematic errors. These are the results of this dissertation and not the 'official' SLAC experiment E154 results [90,91] 153

6.12 The spin dependent structure function g_1^n at 5 (GeV/c)^2 plotted as xg_1^n. The top graph is a comparison of SLAC experiment E154 with previous SLAC experiments and the bottom graph is a comparison with the results of the SMC collaboration at CERN. The error bars for SLAC experiment E154 are statistical only and the shaded area has a height equal to 2 standard deviation systematic errors. For the other experiments, the statistical and systematic errors have been added in quadrature. 154

6.13 The spin dependent structure function g_1^n of the neutron integrated from x_{min} to 1 and plotted versus x_{min}. The statistical and systematic error have been added in quadrature. The errors on the plot are strongly correlated from point to point. 156

6.14 The difference between the spin dependent structure functions g_1^p of the proton and g_1^n of the neutron integrated from x_{min} to 1 and plotted versus x_{min}. SLAC E154 data was used to evaluate g_1^n and a fit to the SLAC E143 and CERN SMC data was used for g_1^p. The statistical and systematic error have been added in quadrature. The errors on the plot are strongly correlated from point to point. 157

6.15 Low x fits to the neutron spin structure function $g_1^n(x)$. The filled circles are the SLAC E154 data and the open circles are the CERN SMC data. The dotted line is a fit to $g_1^n(x) = C$ for the SLAC E154 and the CERN SMC data below $x = 0.03$. The solid line is a fit to $g_1^n(x) = Cx^{-\alpha}$ for the last five SLAC E154 data points. 158

6.16 Power law fit to the difference in the the spin structure function for the proton, $g_1^p(x)$, and the neutron, $g_1^n(x)$. 161

A.1 Schematic of optical pumping in a double cell. 167

A.2 Spin up of the SLAC experiment E154 target cell SMC and fit to the model of equation A.14. 170

A.3 Model prediction for the time evolution of the polarization of the SLAC experiment E154 target cell Picard. 171

LIST OF TABLES

Table

2.1 Deep inelastic electron nucleon scattering variables. 10

3.1 Statistical and systematic errors for the electron beam polarization. 28

3.2 Parameters of the SLAC experiment E154 Cherenkov tanks. 34

4.1 Helium permeation velocity and iron impurity level of selected glasses. 52

4.2 Cell dimensions in millimeters. 55

4.3 Target cell and reference cell window thicknesses. 57

4.4 Cell densities at temperature equilibrium and fractional cell volumes. 58

4.5 Cell temperatures and densities under data taking conditions. . . . 62

4.6 AFP parameters. 73

4.7 Calculated coil flux (arbitrary units). 81

4.8 Cell independent water calibration error table. 89

4.9 Cell dependent water calibration error table. 89

4.10 Water calibration constants, C_w (%/mV). 89

4.11 Cell independent EPR calibration error table. 95

4.12 Cell dependent EPR calibration error table. 95

4.13 EPR calibration constants, C_{epr} (%/mV). 95

4.14 E154 target polarization calibration constants (%/mV). 96

4.15 Isotopic composition of Corning 1720 glass. 101

4.16 x independent errors on the model dilution factor. 101

4.17 x dependent errors on the model dilution factor in the 2.75° spectrometer. 103

4.18 x dependent errors on the model dilution factor in the 5.50° spectrometer. 103

4.19 Error on the dilution factor from external radiative corrections after scattering. 107

4.20 Error on the dilution factor from internal radiative corrections. . . . 108

4.21 Dilution factor for the target cells Dave, Riker, Bob, SMC, and Generals in the 2.75° spectrometer. 112

4.22 Dilution factor for the target cells Dave, Riker, Bob, SMC, and Generals in the 5.50° spectrometer. 112

4.23 Dilution factor for the target cells Hermes, Prelims, Chance, Picard, and g2 in the 2.75° spectrometer. 113

4.24 Dilution factor for the target cells Hermes, Prelims, Chance, Picard, and g2 in the 5.50° spectrometer. 113

5.1 Reference cell analysis errors that are independent of target and x-bin. 123

5.2 Target dependent error for the reference cell analysis. 125

5.3 Error on the slope due to background subtraction. 127

5.4 Error on the slope m of the target cell Picard due to counting statistics. 128

6.1 Parallel experimental asymmetry for ^{3}He in the 2.75° spectrometer . 147

6.2 Parallel experimental asymmetry for ^{3}He in the 5.50° spectrometer . 147

6.3 Perpendicular experimental asymmetry for ^{3}He in the 2.75° spectrometer 148

6.4 Perpendicular experimental asymmetry for ^{3}He in the 5.50° spectrometer 148

6.5 Results of this dissertation for the neutron spin structure function g_1^n and the photon-nucleon asymmetry A_1^n in the 2.75° spectrometer 149

6.6 Results of this dissertation for the neutron spin structure function g_1^n and the photon-nucleon asymmetry A_1^n in the 5.50° spectrometer 149

6.7 Results for the neutron spin structure function g_1^n at a Q^2 of 5 $(\mathrm{GeV/c})^2$. These are the results of this dissertation and not the 'official' SLAC experiment E154 results [90,91]. 152

CHAPTER I

Introduction and Background

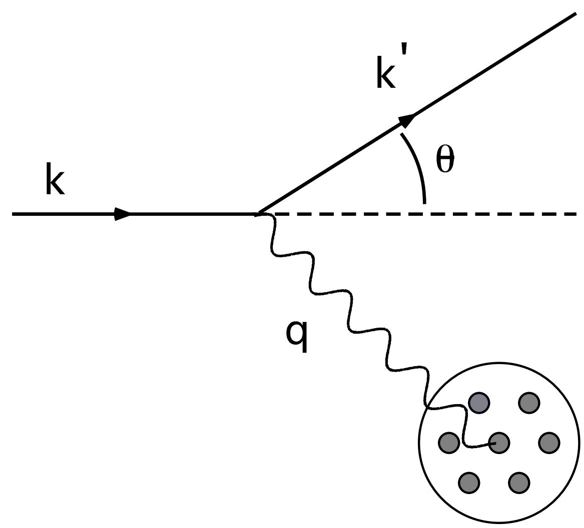

Figure 1.1: Schematic view of electron scattering.

One of the most fascinating problems of modern physics is the structure of protons and neutrons, the two most abundant baryons which together compose the atomic nucleus of ordinary matter. The nucleus itself was proposed and discovered only at the beginning of the 20th century by Rutherford, Geiger and Mardsen [1, 2]. Using α-particle scattering to probe the interior of the atom, Rutherford was surprised to find that many α-particles were scattered at large angles. The explanation for this was that the atom had its charge concentrated at its center, in the nucleus. If the positive charge were a continuous distribution over the atom, with electrons embedded in it like "raisins in plum pudding", then very few α-particles would have been scattered into large angles. Only by having a concentrated positive charge that an incoming α-particle could come very close to, would there be so many α-particles scattered into the large angles.

In a similar manner, the structure of the nucleon is probed using a beam of highly relativistic electrons. Electron scattering is shown schematically in figure 1.1, with the scattered electron making an angle θ with the incoming electron direction. However, in order to investigate the inside of a nucleon, the probe must have a resolving power small enough to see inside the nucleon and interact with whatever is there. This can only be accomplished if the incoming electron has enough momentum so that it does not scatter from the nucleon as a whole. The size of a nucleon is on the order of 10^{-15} m, and any attempt to probe inside a nucleon must be done with a probe capable of resolving structure on a scale smaller than this. Electrons can be used as a probe, so long as the resolving power of the virtual photon transferred between the electron and the nucleon is less than 10^{-15} m, which is to say that the electron has enough momentum to get inside the nucleon without scattering off it as a whole. Using the DeBroglie wavelength, $\lambda = h/p$, this requires that the virtual photon exchanged between the electron and the nucleon carry a momentum greater than about 1.0 GeV/c. At momenta less than this, the photon has a high probability of scattering off the nucleus as a whole, or coherently off one of the nucleons in the nucleus of the target. It can also excite the nucleus or one of the nucleons into an excited state, rather than probe the structure inside the nucleon. Above about 700 MeV/c, the probability of scattering coherently off a nucleus, or a nucleon, or of exciting either into a resonance decreases rapidly and the structure of the nucleon is probed. This is the region of deep inelastic scattering (DIS).

In the 1960's, under the leadership of W. K. H. Panofsky, the Stanford Linear Accelerator Center (SLAC) was built [3]. This two-mile-long machine was capable of producing electrons with an energy of 20 GeV. At this high energy, electrons could be used as probe of the structure of the nucleon through electron scattering in the deep inelastic region. In 1969, the first deep inelastic scattering experiments were performed at SLAC [4, 5]. Scattering electrons with an energy of 7–17 GeV from proton and deuteron targets, Kendall, Friedman and Taylor found that the cross sections did not decrease with increasing four-momentum transfer squared, q^2, as would be expected if the charge distribution of the proton was extended. If the proton were an extended object, then high momentum electrons would push their way through the proton without being deflected very much, and the cross section for scattering at some angle θ would be small. Conversely, if the proton were composed of pointlike scattering centers, then a high momentum electron would be able to get very close to a scattering center and scatter into a large angle. This would result in more electrons being scattered into large angles than would be for an extended proton, in analogy to Rutherford scattering. Furthermore, besides finding evidence that the proton had an internal structure of pointlike constituents, it was found that the measured cross section depended on a single parameter, x, called the Bjorken scaling parameter [6].

$$x = -\frac{q^2}{2M\nu}, \tag{1.1}$$

where M is the mass of the proton, q^2 is the four-momentum transfer squared and ν is the energy lost by the scattered electron. This was a very interesting result, for it meant that the cross section did not depend on the two independent variables of final electron energy and scattered angle, but only on a single variable, x. The cross sections were said to scale with x. Bjorken had predicted scaling by examining deep inelastic scattering under the assumption that the nucleon was composed of pointlike quarks. Starting from current algebra, Bjorken showed that there would be scaling of the structure functions $W_1(\nu, q^2)$ and $\nu W_2(\nu, q^2)$, which measure the deviation of the cross section for lepton–nucleon scattering from the Mott cross section. In the limit of ν, $|\mathrm{q}^2| \to \infty$, with q^2/ν fixed,

$$\begin{aligned} MW_1(\nu, q^2) &\rightarrow F_1(x), \\ \nu W_2(\nu, q^2) &\rightarrow F_2(x). \end{aligned} \tag{1.2}$$

Along with scaling, and the assumption that the currents coupling to the photon consist of spin 1/2 particles (current quarks), it has been shown that the structure functions F_1 and F_2 are not independent, but are related by the Callan-Gross relationship, $\mathrm{F}_2 = 2x\mathrm{F}_1$ [7].

Independently, Feynman had concluded from his analysis of hadronic collisions that the nucleon should be composed of pointlike constituents, which he called partons [8, 9]. This model helped to provide an intuitive picture of deep inelastic scattering. In this picture, known as the quark parton model, deep inelastic scattering was the incoherent sum of elastic scattering from the partons (quarks). In the high momentum limit, the quarks could be seen as non-interacting particles, and the Bjorken x variable became the fraction of the nucleon's linear momentum carried by the struck quark. However, this is only the zeroth approximation, since the interactions between quarks do not disappear at small distances; they only become small. Regardless of q^2, the struck quark can still emit a gluon. As a result, scaling is only approximately satisfied and perturbative QCD is necessary to extract a more complete solution, with the quark parton model being the lowest order approximation [10].

Also to be considered in deep inelastic scattering are the differences that arise from the long range quark-quark interactions. Known as the 'EMC effect', these differences in the quark distributions seen in scattering from free versus bound nucleons are another hint of the more complete solution [11, 12]. The early DIS data, along with additional experiments, showed that in the infinite momentum frame ($|q^2| \to \infty$) and within the framework of the quark parton model, the constituent quarks only carry about half of the total momentum of the struck nucleon. As $|q^2| \to \infty$, the quarks behave as free particles, but as has been discovered, the valence quarks are not the only thing in the nucleon, there are also sea quarks and gluons, which can carry some of the momentum of the nucleon.

Along with trying to determine the unpolarized structure functions, which determine the linear momentum distribution of the quarks, the polarized structure functions were also sought in an attempt to complete the picture of the quarks within the nucleon. These spin structure functions are the difference of the linear momentum distributions between spin up and spin down quarks and contain information about the spin of the quarks inside the nucleon. More than just a curiosity though, these could be used to test some of the fundamental predictions of QCD, such as the Bjorken sum rule, relating the spin dependent structure functions to the weak coupling constants found in neutron beta decay [13].

$$\int_0^1 g_1^p(x)dx - \int_0^1 g_1^n(x)dx = \frac{1}{6}\left(\frac{g_A}{g_V}\right), \tag{1.3}$$

where $g_1^p(x)$ is the spin structure function of the proton, $g_1^n(x)$ is the spin structure function of the neutron, and g_A/g_V is the ratio of the axial vector to vector coupling constant in neutron beta decay. Based only on QCD and isospin symmetry, the Bjorken sum rule is considered an inviolable prediction of QCD. An experimental measurement of the Bjorken sum rule then provides a strong argument either for or against the validity of QCD.

A measurement of $g_1^n(x)$ requires a polarized neutron target which is only possible in a polarized nucleon target such as ^{3}He or D. This was not at first feasible, and an attempt was made to separate the proton and neutron spin structure functions so that the proton spin structure function could be used as a QCD test. With the assumption of an unpolarized strange sea, the first moments of the proton and neutron spin structure functions could be related to the baryon octet beta decays using SU(3) symmetry. It was possible to separate the proton and neutron spin structure functions found in the Bjorken sum rule. This QCD test for the proton is the Ellis-Jaffe sum rule [14]. The theoretical value of the integral of the proton's spin structure function with first order QCD corrections is

$$\int_0^1 g_1^p(x)dx = 0.189 \pm 0.005. \tag{1.4}$$

The early experiments performed to extract the spin structure functions of the proton were E80 at SLAC in 1976 [15, 16], E130 at SLAC in 1982 [17], and EMC at CERN in 1988 [18, 19, 20]. These early experiments gave an experimental result for the integral of the proton's spin structure function g_1^p of

$$\int_0^1 g_1^p(x)dx = 0.126 \pm 0.010(stat) \pm 0.015(sys). \tag{1.5}$$

The early experimental data disagreed with the theory by three standard deviations, and there was much speculation about the probable cause for this discrepancy. Perhaps the most interesting bit of speculation was for the fraction of spin carried by the constituent quarks inside the proton. The quark parton model predicted that the fraction would be about 0.6 [21], but the experimental data led to a different result. Using the data to calculate the fraction of the spin carried by the constituent quarks inside the proton, a result of 0.12 with an error of 0.17 was obtained. This result was often quoted as being consistent with zero, which meant that none of the proton's spin was carried by the constituent quarks. Where was the spin of the nucleon if not in the constituent quarks? The situation was referred to as the 'spin crisis'. In the end it amounted to a non-crisis, because the assumptions that led to the Ellis-Jaffe sum rule proved to be incorrect [22], but at the time it served as a great impetus for conducting experiments that would more precisely measure the spin structure functions of both the proton and the neutron. It was clear that a polarized neutron target was needed.

Since a free neutron target is not practical, other possible polarized neutron targets have been built. Two different avenues have been pursued, with the SMC Collaboration at CERN choosing to extract the neutron spin structure functions from measurements on the deuteron and the proton, while the E142 Collaboration at SLAC chose to build a polarized ^{3}He target that would take advantage of the large neutron polarization in polarized ^{3}He [23]. Each target has its advantages and disadvantages, but what was most important is that two different targets were built. Since each target had its own inherent difficulties, agreement between the two experiments would help bolster confidence in the results. The SMC experiment at CERN extracted the spin structure functions of both the proton and the neutron by measuring the asymmetry in the scattering rates for polarized lepton–nucleon deep inelastic scattering of polarized muons from both polarized protons and polarized deuterons. At SLAC, the E142 Collaboration extracted the neutron spin structure functions by measuring the asymmetry in polarized deep inelastic electron scattering from polarized ^{3}He, while the proton and neutron spin structure functions were extracted by the E143 collaboration from measurements of the deep inelastic scattering asymmetry of polarized electrons from polarized protons and polarized deuterons. SMC was run at CERN in 1993 [24, 25, 26], E142 was run at SLAC in 1993 [27, 28], and E143 was run at SLAC in 1994 [29, 30]. The experiments at CERN were at a higher energy and able to reach a lower x, while the experiments at SLAC collected significantly more data and have much smaller statistical errors.

The data on the spin structure functions g_1^n and g_1^p for the neutron and proton are shown in figure 1.2 as they existed before SLAC experiment E154. As can be seen from the figure, there is a substantial amount of data from a number of experiments, and the results from the different experiments are in good agreement with each other. However, the error on the neutron spin structure function is still relatively

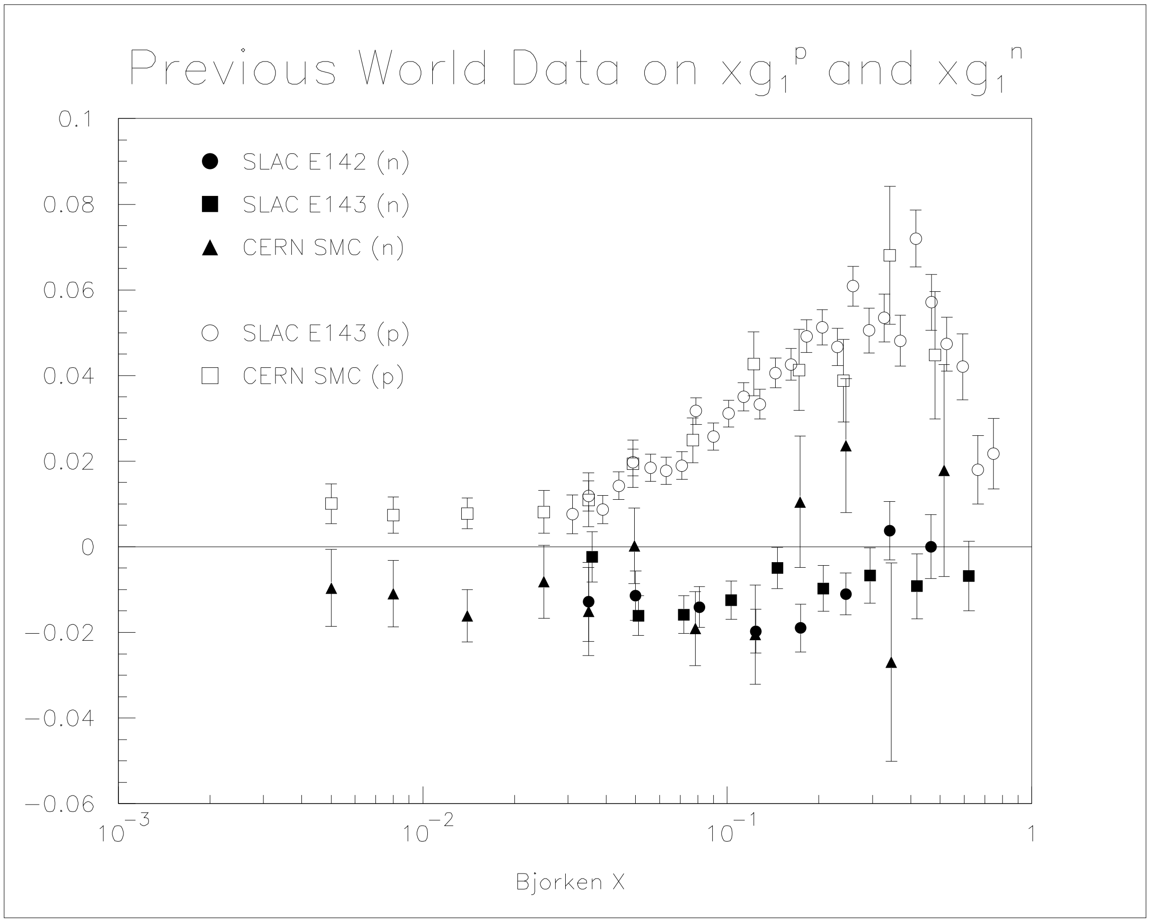

Figure 1.2: World spin structure function data before SLAC experiment E154.

large. There is also only one experiment that has provided data below x=0.03. The goal of experiment E154 at SLAC was to measure the spin structure functions of the neutron with greater precision than any previous measurement, and to a lower Bjorken x value than had been achieved by experiment E142. The ability to reach lower x was provided by an accelerator upgrade to SLAC's A-line. For experiment E142, the maximum beam energy was 30 GeV, for experiment E154, it was 50 GeV. The improved data would provide a strong test of the Bjorken sum rule, as well as constraining the low x behavior of the neutron spin structure function g_1^n. Precision data from two fixed angle spectrometers also provide input for a next-to-leading order (NLO) perturbative QCD analysis of the structure functions. The experiment was performed at SLAC in October and November of 1995, by a collaboration of 80 physicists from 25 institutions.

CHAPTER II

Spin Dependent Structure Functions

The goal of SLAC experiment E154 was to make a precise measurement of the spin-dependent structure functions, using the technique of deep inelastic scattering. As was outlined in the introduction, deep inelastic scattering has been used to study hadronic properties, and for good reason. In deep inelastic scattering, a leptonic probe whose properties are well understood because of its pointlike nature is used to study the dynamics of the quarks and gluons inside of nucleons. By controlling the polarization of the incident lepton and the nucleon target, information on the spin structure of the quarks and gluons can be obtained. For SLAC experiment E154, a beam of polarized electrons was scattered off of a polarized ^{3}He target to study the spin structure functions of the neutron.

2.1 Definitions and List of Symbols

In the region of deep inelastic scattering, the dominant mechanism is the lowest order electromagnetic interaction of one photon exchange as depicted in figure 2.1. At very high energies, other neutral current amplitudes such as Z^0 exchange must be considered. The 50 GeV energy of the SLAC electron beam is a factor of 2 smaller than the mass of the Z^0, however, it is not small enough that corrections due to the Z^0 can be ignored, and a non-negligible correction is applied to the data. The incident electron has a definite four momentum and spin given by $k^\mu = \left(E, \vec{k}\right)$ and $\vec{s}$. Working in the lab frame, the target nucleon has a four momentum and spin given by $P^\mu = \left(M, \vec{0}\right)$ and $\vec{S}$, where M is the mass of the nucleon. The scattered electron, whose spin is not measured, has a four momentum which is given by $k'^{\mu} = \left(E', \vec{k'}\right)$. The scattered electron makes an angle θ with the incident electron direction given by $\theta = \arccos\left(\vec{k} \cdot \vec{k'}/|\vec{k}||\vec{k'}|\right)$. The four momentum of the virtual photon is given by $q^{\mu} = (k^{\mu} - k'^{\mu})$. The outgoing electron is detected in two independent fixed angle spectrometers while the hadronic products that result from the breakup of the nucleon target are not detected. In this way, an inclusive hadronic cross section is measured. There are two invariants that characterize the scattering process, $Q^2 = -q^2$ and $\nu = (P \cdot q)/M = (E - E')$ in the lab frame. The two invariants can also be characterized by Q^2 and $x = Q^2/(2M\nu)$, where x is the Bjorken x variable. Since an inclusive cross section in the deep inelastic region is being measured, all of the final possible states X have the same invariant mass squared, $W^2 = (P^{\mu} + q^{\mu})^2$, (in the deep inelastic region, $W^2 >> M^2$). Table 2.1 gives a list of the variables used in deep inelastic electron nucleon scattering.

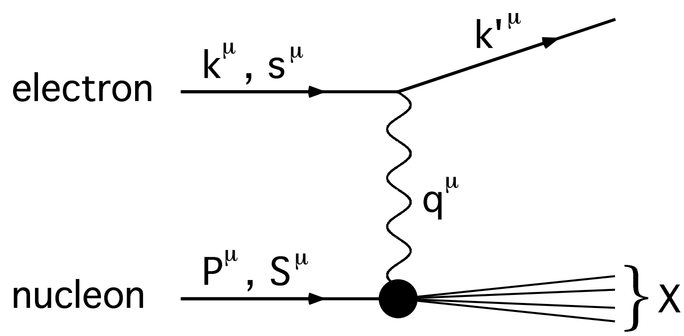

Figure 2.1: Deep inelastic electron nucleon scattering.

2.2 Structure Functions

The differential cross section for one photon exchange is [10, 31, 32]

$$\frac{d^2\sigma}{d\Omega dE'} = \frac{\alpha^2}{Q^4}\frac{E'}{E}L_{\mu\nu}W^{\mu\nu}, \tag{2.1}$$

where α is the fine structure constant, $L_{\mu\nu}$ is the leptonic tensor describing the leptonic vertex for the electron, and $W_{\mu\nu}$ is the hadronic tensor describing the hadronic vertex of the nucleon. Since the electron is a fundamental particle, the leptonic

Variable	Expression	Definition
m		Electron mass
E		Incident electron energy
$\vec{k}$		Incident electron three momentum
k^μ	$(E,\vec{k})$	Incident electron four momentum
$\vec{s}$		Incident electron three vector spin
E'		Scattered electron energy
$\vec{k'}$		Scattered electron three momentum
θ		Scattered electron angle
k'^μ	$(E',\vec{k'})$	Scattered electron four momentum
M		Nucleon target mass
P^μ	$(M,\vec{0})$	Nucleon target four momentum
$\vec{S}$		Nucleon target three vector spin
q^μ		Virtual photon four momentum
Q^2	$-q^2 = 4EE'\sin^2\frac{\theta}{2}$	Squared four momentum transfer
ν	$\frac{P\cdot q}{2M} = (E-E')$	Energy transfer (loss)
x	$\frac{Q^2}{2M\nu} = \frac{2EE'\sin^2\frac{\theta}{2}}{M\,(E-E')}$	Bjorken x

Table 2.1: Deep inelastic electron nucleon scattering variables.

tensor can be written according to the Feynman rules.

$$L_{\mu\nu} = 2\left(k_\mu k'_\nu + k'_\mu k_\nu - \frac{1}{2}Q^2 g_{\mu\nu} + im\epsilon_{\mu\nu\alpha\beta}q^\alpha s^\beta\right), \tag{2.2}$$

where the leptonic tensor has both symmetric and antisymmetric components. The spin of the electron appears only in the last term of the leptonic tensor, which is also the only antisymmetric term.

The hadronic tensor $W_{\mu\nu}$ contains all of the information on the structure of the hadron. Lorentz invariance requires that it be constructed in its most general form from all of the second rank tensors that can be created using P, q and S. In the limit of massless leptons, $q_\mu L^{\mu\nu} = 0$ and a number of the terms in the hadronic tensor are not independent. Also eliminated is a term that is parity odd and enters only in weak interactions. The remaining terms are

$$\begin{aligned} W_{\mu\nu} &= -W_1\left(g_{\mu\nu}+\frac{q_\mu q_\nu}{Q^2}\right)+\frac{1}{M^2}W_2\left(P_\mu+q_\mu\frac{P\cdot q}{Q^2}\right)\left(P_\nu+q_\nu\frac{P\cdot q}{Q^2}\right) \\ &\quad +i\epsilon_{\mu\nu\alpha\beta}q^\alpha S^\beta MG_1+i\epsilon_{\mu\nu\alpha\beta}q^\alpha\left(S^\beta q\cdot P-P^\beta q\cdot S\right)\frac{1}{M}G_2, \end{aligned} \tag{2.3}$$

where $W_{1,2}$ and $G_{1,2}$ are real scalar functions of Q^2 and x, and the current for the electromagnetic interaction has been conserved, $q_\mu W^{\mu\nu}=0$. The hadronic tensor has both symmetric and antisymmetric components, and the spin of the nucleon appears only in the last two terms of the hadronic tensor, which are also the only antisymmetric terms.

The structure functions $W_{1,2}$ and $G_{1,2}$ are nearly independent of Q^2 for large energy transfer, as occurs in deep inelastic scattering. This is generally known as Bjorken scaling, and the structure functions $W_{1,2}$ and $G_{1,2}$ are written as functions of Bjorken x only:

$$\begin{aligned} MW_1(x,Q^2) &\rightarrow F_1(x) \\ \nu W_2(x,Q^2) &\rightarrow F_2(x) \\ (P\cdot q)\,MG_1(x,Q^2) &\rightarrow g_1(x) \\ \frac{1}{M}(P\cdot q)^2\,G_2(x,Q^2) &\rightarrow g_2(x). \end{aligned} \tag{2.4}$$

However, Bjorken scaling is only exact in first order. The phenomenon of scaling reveals a local interaction between the hard photons and the pointlike charged constituents inside the nucleon. These are the quarks (partons) of current theory. The degree to which scaling is violated is the degree to which the sudden approximation does not hold because of radiation from the initial state. Quantum chromodynamics can be used to describe this radiation, and shows that at large Q^2, the violation is a smooth, slowly varying logarithmic function of Q^2.

Contracting $L_{\mu\nu}W^{\mu\nu}$ gives

$$\begin{aligned} L_{\mu\nu}W^{\mu\nu} &= 4\left(\frac{1}{M}\right)F_1\left(k\cdot k'\right)+4\left(\frac{1}{Q^2}\right)F_2\left(2\left(P\cdot k\right)\left(P\cdot k'\right)-M^2\left(k\cdot k'\right)\right) \\ &\quad -2m\left(\frac{1}{P\cdot q}\right)\left(g_{\mu\alpha}g_{\nu\beta}-g_{\mu\beta}g_{\nu\alpha}\right)q^\mu S^\nu q^\alpha s^\beta g_1 \\ &\quad -m\left(\frac{1}{P\cdot q}\right)^2\left(g_{\mu\alpha}g_{\nu\beta}-g_{\mu\beta}g_{\nu\alpha}\right)q^\mu\left(q\cdot PS^\nu-q\cdot SP^\nu\right)q^\alpha s^\beta g_2, \end{aligned} \tag{2.5}$$

from which it can be seen that in order to measure the spin structure functions of a nucleon, a polarized beam and a polarized target are necessary, since spin averaging over either would eliminate the terms proportional to g_1 and g_2.

The goal of SLAC experiment E154 was to measure the spin dependent structure functions g_1 and g_2 under the assumption that the spin independent structure functions are known. Indeed, a recent measurement by the NMC collaboration provides precision data for F_1 and F_2 over a large range of x and Q^2 [33]. By measuring sums and differences of the cross sections, it is possible to isolate the spin structure functions g_1 and g_2. Let $\uparrow$,$\downarrow$ indicate the longitudinal electron polarization, let $\Uparrow$,$\Downarrow$ indicate the longitudinal target nucleon polarization, and let $\Leftarrow$,$\Rightarrow$ indicate the transverse target nucleon polarization. This gives

$$\frac{d^2\sigma}{d\Omega dE'}^{\downarrow\Uparrow(\Leftarrow)} + \frac{d^2\sigma}{d\Omega dE'}^{\uparrow\Uparrow(\Leftarrow)} = \frac{8\alpha^2(E')^2}{MQ^4}\left[2\sin^2\frac{\theta}{2}F_1\left(x,Q^2\right) + \frac{M}{\nu}\cos^2\frac{\theta}{2}F_2\left(x,Q^2\right)\right] \tag{2.6}$$

for the sum over both electron polarizations, with the target nucleon polarization either longitudinal or transverse. The differential cross sections are

$$\frac{d^2\sigma}{d\Omega dE'}^{\downarrow\Uparrow} - \frac{d^2\sigma}{d\Omega dE'}^{\uparrow\Uparrow} = \frac{4\alpha^2 E'}{MQ^2E\nu}\left[(E+E'\cos\theta)\,g_1\left(x,Q^2\right) - 2xMg_2\left(x,Q^2\right)\right] \tag{2.7}$$

for longitudinally polarized electrons and longitudinally polarized target nucleons, while

$$\frac{d^2\sigma}{d\Omega dE'}^{\downarrow\Leftarrow} - \frac{d^2\sigma}{d\Omega dE'}^{\uparrow\Leftarrow} = \frac{4\alpha^2(E')^2}{MQ^2E\nu}\sin\theta\left[g_1\left(x,Q^2\right) + \frac{4xME}{Q^2}g_2\left(x,Q^2\right)\right] \tag{2.8}$$

for longitudinally polarized electrons and transversely polarized target nucleons. When a longitudinally polarized target is used, the result is primarily a measurement of g_1, since g_2 is suppressed by a factor of $(2xM)/(E+E'\cos\theta) \approx 0.01$ for SLAC experiment E154. When a transversely polarized target is used, the result is more sensitive to g_2.

Rather than measure differential cross sections that require a careful monitoring and calibration of the electron beam parameters and spectrometer acceptance and efficiency, asymmetries are measured. By reversing the electron and/or the target polarizations frequently, the slowly varying parameters of the experiment cancel between the different polarization states. The longitudinal and transverse asymmetries are

$$A_{\|} = \frac{\dfrac{d^2\sigma}{d\Omega dE'}^{\downarrow\Uparrow} - \dfrac{d^2\sigma}{d\Omega dE'}^{\uparrow\Uparrow}}{\dfrac{d^2\sigma}{d\Omega dE'}^{\downarrow\Uparrow} + \dfrac{d^2\sigma}{d\Omega dE'}^{\uparrow\Uparrow}} \tag{2.9}$$

and

$$A_{\perp} = \frac{\dfrac{d^2\sigma}{d\Omega dE'}^{\downarrow\Leftarrow} - \dfrac{d^2\sigma}{d\Omega dE'}^{\uparrow\Leftarrow}}{\dfrac{d^2\sigma}{d\Omega dE'}^{\downarrow\Leftarrow} + \dfrac{d^2\sigma}{d\Omega dE'}^{\uparrow\Leftarrow}}, \tag{2.10}$$

where the target and the beam are fully polarized and the target is composed entirely of ^{3}He.

2.3 The Virtual Photon - Nucleon Asymmetry

Polarized deep inelastic scattering is used to study the spin structure of the target nucleon and the asymmetries calculated above can be used to extract the structure functions. Also instructive are the cross sections for forward virtual Compton scattering, $\gamma^* + N \to \gamma^* + N$, which can be related to the total photoabsorption cross section through the optical theorem. In this way, the hadronic vertex in figure 2.1 can be studied. The leptonic vertex, representing the emission of a virtual photon by the incident lepton, is completely calculable in QED. There are only four independent helicity amplitudes for a virtual photon with spin projection $\pm 1, 0$ and a nucleon with spin projection $\pm 1/2$ [32]. They can be found by using the virtual photon polarization vector ε_λ^μ in the leptonic tensor $L_{\mu\nu}$,

$$\mathcal{M}_{i(i'),j(j')} = \varepsilon_\lambda^{\mu\dagger} \varepsilon_\lambda^\nu W_{\mu\nu} \tag{2.11}$$

where $i(i')$ are the initial spin projections of the photon and nucleon and $j(j')$ are the final states. The four independent helicity amplitudes are

$$\mathcal{M}_{1(1/2),1(1/2)}, \quad \mathcal{M}_{1(-1/2),1(-1/2)}, \quad \mathcal{M}_{1(-1/2),0(1/2)}, \quad \mathcal{M}_{0(1/2),0(1/2)}. \tag{2.12}$$

Using equations 2.1 and 2.3, the relationship between the virtual photoabsorption cross sections and the helicity amplitudes can be calculated, as well as the relationship between the virtual photoabsorption cross sections and the structure functions:

$$\begin{aligned}
\sigma_{1/2} &= \frac{4\pi^2\alpha}{\left(\nu - \frac{Q^2}{2M}\right)}\mathcal{M}_{1(-1/2),1(-1/2)} \\
&= \frac{8\pi^2\alpha}{\left(2M\nu - Q^2\right)}\left[F_1\left(x,Q^2\right) + g_1\left(x,Q^2\right) - \frac{2Mx}{\nu}g_2\left(x,Q^2\right)\right] \\
\sigma_{3/2} &= \frac{4\pi^2\alpha}{\left(\nu - \frac{Q^2}{2M}\right)}\mathcal{M}_{1(1/2),1(1/2)} \\
&= \frac{8\pi^2\alpha}{\left(2M\nu - Q^2\right)}\left[F_1\left(x,Q^2\right) - g_1\left(x,Q^2\right) + \frac{2Mx}{\nu}g_2\left(x,Q^2\right)\right] \\
\sigma_L &= \frac{4\pi^2\alpha}{\left(\nu - \frac{Q^2}{2M}\right)}\mathcal{M}_{0(1/2),0(1/2)} \\
&= \frac{8\pi^2\alpha}{\left(2M\nu - Q^2\right)}\left[-F_1\left(x,Q^2\right) + \frac{F_2\left(x,Q^2\right)}{2x}\left(1 + \frac{Q^2}{\nu^2}\right)\right] \\
\sigma_{TL} &= \frac{4\pi^2\alpha}{\left(\nu - \frac{Q^2}{2M}\right)}\mathcal{M}_{0(1/2),1(-1/2)} \\
&= \frac{8\pi^2\alpha}{\left(2M\nu - Q^2\right)}\frac{\sqrt{Q^2}}{\nu}\left[g_1\left(x,Q^2\right) + g_2\left(x,Q^2\right)\right],
\end{aligned} \tag{2.13}$$

where the total transverse photoabsorption cross section, σ_T, is the average of the cross sections for total photon-nucleon spin projection equal to 1/2 and 3/2,

$$\sigma_T = \left(\tfrac{1}{2}\right)\left(\sigma_{1/2} + \sigma_{3/2}\right) = \frac{8\pi^2\alpha}{\left(2M\nu - Q^2\right)}F_1\left(x,Q^2\right). \tag{2.14}$$

The cross section for longitudinally polarized photons is σ_L, and σ_{TL} is the interference term between the transverse and longitudinal amplitudes.

The virtual photon-nucleon asymmetries are defined as

$$\begin{aligned}
A_1\left(x,Q^2\right) &= \frac{\sigma_{1/2} - \sigma_{3/2}}{\sigma_{1/2} + \sigma_{3/2}} = \frac{g_1\left(x,Q^2\right) - \gamma^2 g_2\left(x,Q^2\right)}{F_1\left(x,Q^2\right)} \\
A_2\left(x,Q^2\right) &= \frac{\sigma_{TL}}{\sigma_T} = \frac{\gamma\left(g_1\left(x,Q^2\right) + g_2\left(x,Q^2\right)\right)}{F_1\left(x,Q^2\right)},
\end{aligned} \tag{2.15}$$

where $\gamma = \sqrt{Q^2/\nu^2}$. The ratio of the longitudinal to transverse cross sections is

$$R\left(x,Q^2\right) = \frac{\sigma_L}{\sigma_T} = \frac{\left(1+\gamma^2\right)}{2xF_1\left(x,Q^2\right)}F_2\left(x,Q^2\right) - 1, \tag{2.16}$$

and can be used to connect the two unpolarized structure functions,

$$F_1\left(x,Q^2\right) = \frac{F_2\left(x,Q^2\right)}{2x}\frac{\left(1+\gamma^2\right)}{\left(1+R\left(x,Q^2\right)\right)}. \tag{2.17}$$

In the limit of infinite momentum, $Q^2 \to \infty$, with x fixed, $\gamma \to 0$, $R\left(x,Q^2\right) \to 0$, and equation 2.17 becomes the Callan-Gross relationship, $2xF_1(x,Q^2) = F_2(x,Q^2)$.

2.4 Experimental Asymmetries

Combining equations 2.6 – 2.10 and equation 2.15, the experimental asymmetries can be written in terms of the virtual photon asymmetries.

$$\begin{aligned} A_{\|} &= D\left(A_1 + \eta A_2\right) \\ A_{\perp} &= d\left(A_1 - \zeta A_2\right), \end{aligned} \tag{2.18}$$

where

$$\begin{aligned} D &= \frac{1-\varepsilon\left(\frac{E'}{E}\right)}{1+\varepsilon R\left(x,Q^2\right)} \\ \eta &= \frac{\varepsilon\sqrt{Q^2}}{E-\varepsilon E'} \\ d &= D\sqrt{\frac{2\varepsilon}{1+\varepsilon}} \\ \zeta &= \eta\frac{(1+\varepsilon)}{2\varepsilon} \\ \varepsilon &= \frac{1}{1+2\left(1+\nu^2/Q^2\right)\tan^2\left(\theta/2\right)} \end{aligned} \tag{2.19}$$

and D is the virtual photon depolarization factor that arises because the emitted virtual photon is not parallel to the nucleon's initial spin.

The spin structure functions can also be written in terms of the experimental asymmetries:

$$g_1 = \frac{F_1\left(x,Q^2\right)}{D'}\left(A_{\|}\left(x,Q^2\right) + \tan\left(\theta/2\right)A_{\perp}\left(x,Q^2\right)\right) \tag{2.20}$$

$$g_2 = \frac{\nu F_1\left(x,Q^2\right)}{D'2E\sin\left(\theta\right)}\left(\frac{E+E'\cos\left(\theta\right)}{E'}A_{\perp}\left(x,Q^2\right) - \sin\left(\theta\right)A_{\|}\left(x,Q^2\right)\right), \tag{2.21}$$

where

$$D' = \frac{(1-\varepsilon)(2-\nu/E)}{(\nu/E)\left(1+\varepsilon R\left(x,Q^2\right)\right)}. \tag{2.22}$$

In order to extract the spin structure functions g_1 and g_2 from the measured asymmetries, the values of F_1 and R are needed. These are however known to sufficient accuracy from unpolarized deep inelastic scattering experiments [33, 34].

2.4.1 Polarized ^{3}He as a Polarized Neutron

For SLAC experiment E154, a polarized ^{3}He target was used to study the spin structure functions of the neutron. Polarized ^{3}He was chosen because to a good approximation, the ^{3}He nucleons are in a spatial symmetric S state. Because of the Pauli principle, the two protons are in an antisymmetric spin state and a symmetric isospin state. In this approximation then, the total spin of the ^{3}He is carried by the neutron and a measurement of the ^{3}He asymmetry is a measurement of the neutron asymmetry. A more complete model of ^{3}He must include the ^{3}He wave functions other than the spatially symmetric S state. The contributions from the S' and D wavefunctions have been calculated by both Friar *et al.* [23] and Ciofi degli Atti *et al.* [35], and show that the effects of the non-S wave components for values of $x < 0.9$ can be taken into account by using the effective proton and neutron polarizations generated by the S' and D wavefunctions, while nuclear binding and Fermi motion can be accounted for by the EMC effect [12]. The spin structure function of the ^{3}He (g_1^3) and its asymmetry (A_3) can then be written as the incoherent sum of the neutron and proton spin structure functions

$$\begin{aligned} g_1^3(x,Q^2) &= 2P_p g_1^p(x,Q^2) + P_n g_1^n(x,Q^2) \\ A_3(x,Q^2) &= 2P_p f_p(x,Q^2) A_p(x,Q^2) + P_n f_n(x,Q^2) A_n(x,Q^2), \end{aligned} \tag{2.23}$$

where $f_{p(n)}(x,Q^2)$ is the fraction of events from the proton (neutron), and given by

$$f_{p(n)}(x,Q^2) = \frac{F_2^{p(n)}(x,Q^2)}{\left(2F_2^p(x,Q^2) + F_2^n(x,Q^2)\right) f_{EMC}^3(x,Q^2)} \tag{2.24}$$

and $f_{EMC}^3(x,Q^2)$ is the EMC factor for a nucleus with $A = 3$.

The effective polarization of the neutron is 0.87 ± 0.02, while that of the proton is -0.027 ± 0.004 [23]. Thus, a measurement of the ^{3}He asymmetry is primarily a measurement of the neutron asymmetry because of the small effective proton polarization. However, in order to extract the spin structure function of the neutron from the data, it will be necessary to use a measured value of the spin structure function of the proton from the previous CERN and SLAC experiments [25, 29].

2.5 The Quark Parton Model

The Quark Parton Model (QPM) was formulated by Bjorken, Feynman and Paschos. The two main assumptions of the model being that a nucleon is composed of spin 1/2 quarks and that in the infinite momentum frame the scattering of a virtual photon from a nucleon can be described as incoherent elastic scattering from the quarks. The assumption of the impulse approximation is not strictly valid, and when it is assumed to be true, the model is typically called the naive Quark Parton Model. For the naive Quark Parton Model, the relationship between the structure functions and the quark momentum distributions is straightforward, with

$$F_1(x) = \frac{1}{2x} F_2(x) \tag{2.25}$$

$$F_2(x) = x \sum_i e_i^2 \left[(q+\overline{q})^{\uparrow}(x) + (q+\overline{q})^{\downarrow}(x) \right] \tag{2.26}$$

$$g_1(x) = \frac{1}{2} \sum_i e_i^2 \left[(q+\overline{q})^{\uparrow}(x) - (q+\overline{q})^{\downarrow}(x) \right], \tag{2.27}$$

where e_i is the charge of the i^{th} flavor quark carrying a fraction x of the nucleon's total momentum and having a helicity in the same (opposite) direction as the parent nucleon.

Because the impulse approximation is not strictly valid, the quark momentum distributions are not functions of the Bjorken scaling variable x only, but evolve with Q^2 due to quark-gluon interactions inside the nucleon. These interactions are in the form of gluon emission and gluon induced quark-anti-quark pair creation. The quarks cannot be considered 'free', regardless of Q^2. Additional higher order terms are present in the construction of the spin structure function $g_1(x, Q^2)$ from the quark momentum distributions

$$g_1(x,Q^2) = \frac{1}{2}\sum_i e_i^2 \left[(q+\overline{q})^{\uparrow}(x,Q^2) - (q+\overline{q})^{\downarrow}(x,Q^2) + \ldots\right]. \tag{2.28}$$

The first few terms after the plus sign can be calculated using next-to-leading order perturbative QCD and since they have their origin in the gluon content of the nucleon, a precision measurement of the nucleon spin structure function $g_1(x,Q^2)$ can be used to gain insight into the role that the gluons play in nucleon helicity. The precision of SLAC experiment E154 is sufficient to provide a first hint at the corrections beyond the naive quark parton model; however, these will not be discussed in detail in this thesis.

In the naive quark parton model, the quarks are 'free' and the spin of a nucleon can be considered as arising from the spin of its quarks,

$$g_1(x) = \frac{1}{2}\left[\frac{4}{9}\Delta u(x) + \frac{1}{9}\Delta d(x) + \frac{1}{9}\Delta s(x)\right], \tag{2.29}$$

where only the three lightest quarks have been considered . It is helpful to examine the SU(3) flavor combinations:

$$\begin{aligned}
\Delta q_0(x) &= \Delta u(x) + \Delta d(x) + \Delta s(x) \\
\Delta q_3(x) &= \Delta u(x) - \Delta d(x) \\
\Delta q_8(x) &= \Delta u(x) + \Delta d(x) - 2\Delta s(x).
\end{aligned} \tag{2.30}$$

The combination $\Delta q_0(x)$, or more commonly, $\Delta\Sigma(x)$ is a singlet combination and can be interpreted as the nucleon helicity of the quarks. The other two combinations, $\Delta q_3(x)$ and $\Delta q_8(x)$, are non-singlet. *Ab initio*, calculation of the x dependence of the polarized quark distributions are not meaningful. However, the moments (*i.e.* the integrals over x) of the structure functions can be calculated and provide predictions for the structure of the nucleon in QCD.

2.6 Sum Rules

There are two sum rules that can be addressed by measurements of $g_1(x)$ in spin dependent deep inelastic scattering: the Bjorken sum rule and the Ellis-Jaffe sum rule. Previous experiments [26, 28, 30] have shown a violation of the Ellis-Jaffe sum rule for the neutron at the two standard deviations level, and have called into question the assumptions upon which it is based. As it is not a rigorous prediction of QCD, the violation of the Ellis-Jaffe sum rule is not surprising and as much has been said by one of the authors [22]. The Bjorken sum rule, however, has only a few fundamental assumptions and these assumptions are known to be valid in the framework of QCD.

The Bjorken sum rule was originally proposed in 1966 [13], before the advent of QCD, using current algebra and the assumptions of isospin invariance and the naive quark parton model using the standard assignments for the quark charges. The Bjorken sum rule relates the difference in the integral of the spin structure function of the proton and the neutron to the ratio of the axial vector to vector coupling constants, g_A/g_V, observed in beta decay. In the Bjorken limit ($Q^2 \to \infty$), the Bjorken sum rule has the value [36]

$$\int_0^1 \left(g_1^p(x) - g_1^n(x)\right) dx = \frac{1}{6}\left|\frac{g_A}{g_V}\right| = 1.2601 \pm 0.0025. \tag{2.31}$$

The combination of quark helicities that forms the Bjorken sum rule, namely $\Delta q_3(x) = \Delta u(x) - \Delta d(x)$, is a singlet distribution. At finite Q^2, the only QCD modification to the Bjorken sum rule comes from the radiative corrections for the photon-quark interaction. These corrections can be calculated using the method of operator product expansion and have been calculated to third order in α_s [37],

$$\begin{aligned}\int_0^1 \left(g_1^p(x) - g_1^n(x)\right) dx &= \frac{1}{6}\left|\frac{g_A}{g_V}\right| \left[1 - \frac{\alpha_s(Q^2)}{\pi} - 3.5833\left(\frac{\alpha_s(Q^2)}{\pi}\right)^2\right. \\ &\left. -20.2153\left(\frac{\alpha_s(Q^2)}{\pi}\right)^3 - O(130)\left(\frac{\alpha_s(Q^2)}{\pi}\right)^4\right]. \end{aligned}\tag{2.32}$$

The Ellis-Jaffe sum rule is an extension of the Bjorken sum rule under the additional assumptions of an unpolarized strange sea and SU(3) symmetry [14]. Its original value came from its ability to make separate predictions for the integral of the spin structure function of the proton and that of the neutron. Without QCD corrections, the Ellis-Jaffe sum rules for the proton and neutron are

$$\int_0^1 g_1^p(x)dx = \frac{1}{18}\left[5\left|G_A^{n\Sigma}\right| + 4\left|\frac{g_A}{g_V}\right|\right] \tag{2.33}$$

$$\int_0^1 g_1^n(x)dx = \frac{1}{18}\left[5\left|G_A^{n\Sigma}\right| + \left|\frac{g_A}{g_V}\right|\right], \tag{2.34}$$

where $G_A^{n\Sigma}$ is the ratio of the axial vector to vector coupling constants observed in hyperon decay ($\Sigma^- \to ne^-\overline{\nu_e}$). SLAC experiment E154 provides data which also confirm the violation of the Ellis-Jaffe sum rule for the neutron and test the Bjorken sum rule to the level of 8%. Testing the fundamental prediction of the Bjorken sum rule was one of the primary goals of SLAC experiment E154.

CHAPTER III

SLAC Experiment E154

Using longitudinally polarized electrons accelerated to 48.3 GeV by the Stanford Linear Accelerator, SLAC experiment E154 collected deep inelastic scattering data in End Station A in the fall of 1995. An overview of the polarized ^{3}He target and the spectrometer elements can be seen in the schematic of figure 3.1. The polarized electrons were scattered from a polarized ^{3}He target into two independent magnetic spectrometers. The large acceptance spectrometers were centered about the angles of 2.75° and 5.5° relative to the electron beam line, which allowed a measurement of the spin dependent structure functions $g_1^n(x, Q^2)$ and $g_2^n(x, Q^2)$ in the kinematic range of $0.014 \leq x \leq 0.7$ and $1\ (\mathrm{GeV/c})^2 \leq Q^2 \leq 17\ (\mathrm{GeV/c})^2$. The electron beam had an average polarization of 82.4%, as measured by a Møller polarimeter in End Station A [39]. The ^{3}He target was polarized using spin exchange with optically pumped rubidium inside a glass cell and had an average polarization of 38% using the statistical error on the measured asymmetry to weight the target polarization of each run. Approximately half of the events measured in the spectrometers originated in the polarized ^{3}He, with the remaining events originating in the glass walls of the spin exchange cell and the nitrogen gas that was placed inside the cell for the purpose of optical pumping efficiency.

3.1 The Polarized Electron Beam

The polarized electrons were produced at the source using photoemission from a strained GaAs photocathode [38]. They were delivered at a rate of 120 Hz in bunches

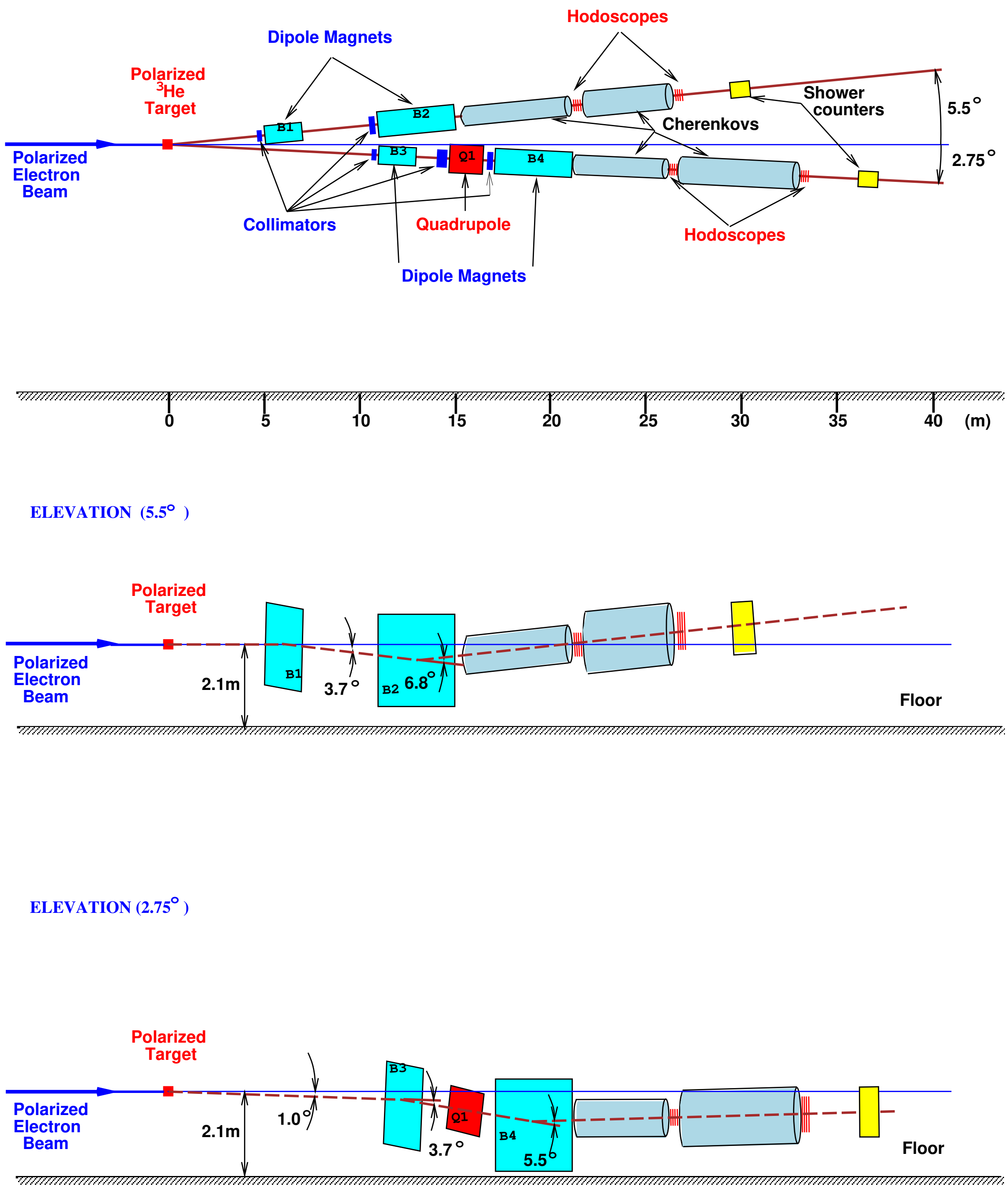

Figure 3.1: Layout of the E154 Spectrometers.

200–250 ns in length with 0.5–2.0 $\times$ 10^{11} electrons per bunch. Of the 120 bunches per second, 119 were used for the experiment, and the remaining bunch was used for accelerator diagnostics and tuning. This 'witness' pulse was dumped before entering End Station A and not used for the experimental measurement.

A Pockels cell was included in the optics for the electron source's Ti:sapphire laser, and was able to reverse the polarization of the laser light used for photoemission on a pulse by pulse basis. The polarization of the laser light was determined by the sign of the high voltage supply connected to the Pockels cell, which was connected to a pseudo-random number generator. This generated a polarized electron beam whose helicity changed in a pseudo-random manner. The helicity was determined by a pseudo-random bit generator that controlled the high voltage supply to the Pockels cell. Although the pseudo-random nature of the electron beam helicity reversals was not necessary for this experiment, the fast electron beam helicity reversals were important for reducing systematic errors, as possible false asymmetries due to slow changes in the spectrometer would be averaged out by the fast electron beam helicity reversals. The sign of the beam helicity was sent to the data acquisition system using four separate paths: the PMON line, the MACH line, the Pockels Cell High Voltage Line, and the Veto Bits. Also, since the bit generator for the Pockels cell was only pseudo-random, a prediction for the electron beam helicity could be made once 33 consecutive polarization bits had been read. This prediction could then be compared to the value from the other beam helicity monitors to test for consistency.

The energy of the beam was continuously monitored and recorded approximately every 10 minutes during data taking. The momentum of the electrons passing through the A-line between the linac and End Station A was determined by measuring the magnetic field strength of the dipole magnets in the A-line that steer the beam into End Station A. Using the value for the strength of the magnetic field of the dipole magnets, the momentum of the incident electrons could be determined to approximately 0.1%. Three adjustable slits were used in the A-line to control the energy spread of the beam, $\delta E/E$, and restrict it to 1% full width. An absolute calibration of the energy of the electron beam in End Station A was made by the Møller Polarimeter in End Station A.

The charge of the electron beam was measured on a pulse by pulse basis using the current pulse induced in two independent ferromagnetic toroids that were located 38 meters and 3 meters upstream from the target. Each toroid consisted of a ferrite core with a number of loops of wire wrapped around the core. These loops were connected to a resonant LC circuit and an induced signal was generated in the circuit when the electron beam passed through the toroid. The size of the induced signal was proportional to the amount of charge in the electron beam pulse. The circuit was calibrated by discharging a known amount of charge from a precision capacitor through the toroid and measuring the induced signal. The toroids were calibrated every few hours and measured the total charge of each beam pulse to a precision of approximately 0.5%.

The position and steering of the electron beam were controlled by MCC (the Main Control Center) using a number of monitors and feedbacks. The position and width of the electron beam were measured and written to tape on a pulse by pulse basis using a wire array located 10.5 meters downstream of the target. The spacing of the wire array was 1.1 mm in both the x and y directions and provided a measurement of the electron beam position to better than 1 mm. Also monitoring the electron beam position and quality were a pair of scintillator paddles. The first one, called the 'bad spill monitor', was located at the end of the A-line and was sensitive to beam scraping. The second one, called the 'good spill monitor', was located just downstream from the target and a few meters from the beam pipe. It was primarily sensitive to particles created in or scattered from the target. The signals from these scintillators were integrated and written to tape to use in the data analysis. Also monitoring the position of the beam were a pair of traveling wave beam position monitors located upstream of the target. These monitors measured the deviation of the beam from the beamline, with one measuring the deviation in x and one measuring the deviation in y.

Tuning of the electron beam generally consisted of centering the beam on the wire array while minimizing the signal from both the 'good spill monitor' and the 'bad spill monitor'. The signal from the 'good spill monitor' was minimized because the target was thinnest in the center; the glass side walls of the target cell being thicker by a factor of 1000. Once the beam was tuned and stable, automatic adjustments were made to the beam steering using feedback from the traveling wave beam position monitors. To prevent the electron beam from wandering too far from center, an aluminum foil with a small hole was placed immediately before the target as a secondary emission monitor. The electron beam never actually wandered far enough from center during the course of the experiment to raise the signal from the secondary emission monitor above threshold and crash the electron beam. However, the secondary emission monitor did crash the electron beam a number of times during the experiment.

3.2 Møller Polarimeter

The polarization of the electron beam was measured every few days in End Station A using a single arm Møller polarimeter [39, 40]. The Møller polarimeter consisted of a polarized thin ferromagnetic target foil, a target mask to define the acceptance, an analyzing magnet to measure the momentum of the scattered electrons, and a segmented detector to measure the rate of scattered electrons. The Møller target foils, analyzing magnet and detector were all located upstream of the target. The electron beam pipe passed through the center of the analyzing magnet, and was shielded by an iron septum to greatly reduce the size of the magnetic field inside the electron beam pipe. This allowed the unscattered electrons to reach the beam dump. The layout of the Møller polarimeter is shown in figure 3.2. The analyzing magnet is labeled B203.

Møller scattering is elastic electron-electron scattering and the cross section is fully calculable in QED. The cross section has a large spin dependence due to helicity conservation [41]:

$$\frac{d\sigma}{d\Omega} = \frac{\alpha^2}{s}\frac{(3+\cos^2\theta)^2}{\sin^4\theta}\left[1 - P_z^B P_z^T A_z(\theta)\right], \tag{3.1}$$

where s is the square of the center of mass energy, θ is the center of mass scattering angle, P_z^B is the longitudinal beam polarization, and P_z^T is the longitudinal target foil electron polarization. The angular scattering asymmetry is

$$A_z(\theta) = \frac{(7+\cos^2\theta)\sin^2\theta}{(3+\cos^2\theta)^2}, \tag{3.2}$$

which is a maximum at 90° in the center of mass frame. Consequently, the Møller detectors were centered near 90°. The center of mass scattering angles are shown in

Figure 3.2: Layout of the E154 Møller Polarimeter. The center of mass scattering angles are indicated on each ray.

figure 3.2. A measurement of the Møller scattering asymmetry can then be used to calculate the beam polarization

$$A = \frac{N^{\uparrow\uparrow} - N^{\uparrow\downarrow}}{N^{\uparrow\uparrow} + N^{\uparrow\downarrow}} = P_z^B P_z^T A_z(\theta), \tag{3.3}$$

where $N^{\uparrow\uparrow}$ is the number of counts per incident electron for Møller scattering with the beam and target polarizations parallel, and $N^{\uparrow\downarrow}$ is the number of counts per incident electron for Møller scattering with the beam and target polarizations anti-parallel.

There were six Møller target foils used for SLAC experiment E154. The foils were made of Permendur, (49% Fe, 49% Co and 2% Va), and had thicknesses of 20 μm, 20 μm, 30 μm, 40 μm, 40 μm, and 154 μm. Most of the data for SLAC experiment E154 were taken using a 40 μm foil. Since magnetizing a thin film normal to the surface requires impractically large fields, the foils were mounted at an angle of 20.7° relative to the beam line and magnetized along the beam direction by a magnetic field of approximately 100 G generated by a set of Helmholtz coils.

The polarization of the Møller target foils was determined both before and after the run by measuring the magnetization of the target foils, $\vec{M}$. A pickup coil was wrapped around the target foil and the external field, $\vec{H}$, was ramped up and down. The changing flux through the pickup coil induces a current through the pickup coil windings according to Lenz' Law. The presence of the target foil inside the pickup coil modifies the magnetic field according to $\vec{B}_{foil} = \vec{H} + 4\pi\vec{M}$. By measuring the induced current in the pickup coils with the foil in and then out, the magnetization of the foil can be calculated from the induced emf, $\mathcal{E}_{ind}$,

$$4\pi\left|\vec{M}\right| = \frac{1}{N\left|\vec{A}_{foil}\right|}\left(\int_{foilin}\mathcal{E}_{ind}\mathrm{dt} - \int_{foilout}\mathcal{E}_{ind}\mathrm{dt}\right), \tag{3.4}$$

where N is the number of turns in the pickup coil and A is the area of the foil. The magnetization of the target foils is related to the foil polarization by

$$P_z^T = \left(\frac{g}{g-1}\frac{g'-1}{g'}\right)\frac{\left|\vec{M}\right|}{n\mu_B}, \tag{3.5}$$

where g is the gyromagnetic ratio of the electron, $g'= 1.916 \pm 0.02$ is the gyromagnetic ratio of Permendur [42], n is the number density of electrons, and μ_B is the Bohr magneton. The magnetizations of the foils were measured both before and after the run with the two measurements agreeing to better than 1%.

There were two Møller detectors, each consisting of a linear array of silicon detectors. They were arranged in two stripes, one above the other. The top Møller detector was finely segmented and contained 48 channels, while the bottom detector consisted of 5 separate silicon detectors. The detectors were mounted on a plate whose position could be remotely controlled, and were centered on the Møller peak. In the top detector, the Møller peak was approximately 6 channels wide, while in the bottom detector it was usually contained in a single detector.

Electron beam polarization measurements were made using the Møller polarimeter throughout the course of the SLAC experiment E154 data taking period. There were a total of approximately 140 Møller runs each of approximately one half hour in length. The signals from the silicon detectors were pre-amplified and read out by ADCs. The electron beam helicity state was used to construct the Møller asymmetry as given in equation 3.3. Since only approximately 2 of the outer shell electrons in Fe and Va are polarized, the typical foil polarization is only approximately 8% and there is a large background from the unpolarized electrons in the foils. Subtraction of the background was accomplished by fitting the unpolarized signal $\left(N^{\uparrow\uparrow} + N^{\uparrow\downarrow}\right)$ and taking into account the difference in atomic motion of the inner shell electrons which are typically unpolarized and the outer shell electrons which are polarized [43].

The results for the statistical and systematic errors can be found in table 3.1. The systematic error of the electron beam polarization is dominated by the error in the foil polarization and the background subtraction. The polarization of the electron beam as a function of run number can be seen in figure 3.3, with the error bars being statistical only. The rise in beam polarization from 76% to 82.4% is a result of tuning the source laser wavelength, as discussed in the next paragraph.

Statistical Error	
Run Range	Polarization
1329–1411	0.759 ± 0.004
1456–1684	0.775 ± 0.005
1691–2311	0.814 ± 0.002
2316–3371	0.824 ± 0.001
3377–3788	0.826 ± 0.002

Systematic Error	
Source	Error
Background Subtraction	2.0%
Foil Magnetization	1.9%
Kinematic Acceptance	0.3%
Fit Range	0.3%
Total Error	2.8%

Table 3.1: Statistical and systematic errors for the electron beam polarization.

Before the run, the Møller detector was used to optimize the polarization of the electrons at the source by providing a measurement of the electron beam polarization as a function of source laser wavelength. The Møller detector was also used to calibrate the energy of the electron beam in End Station A. Electrons from the linac are deflected by 24.5° into End Station A. Because of the anomalous magnetic moment of the electron, $(g \neq 2)$, the spin of the electron precesses. The amount of precession, θ_{pre}, is related to the angle through which the electron has been deflected, θ_{def},

$$\theta_{pre} = \left(\frac{\gamma}{2}\right)(g-2)\,\theta_{def}. \tag{3.6}$$

At certain energies (i.e. certain gammas) the precession of the longitudinally polarized electrons is a multiple of π; and the electrons entering End Station A are

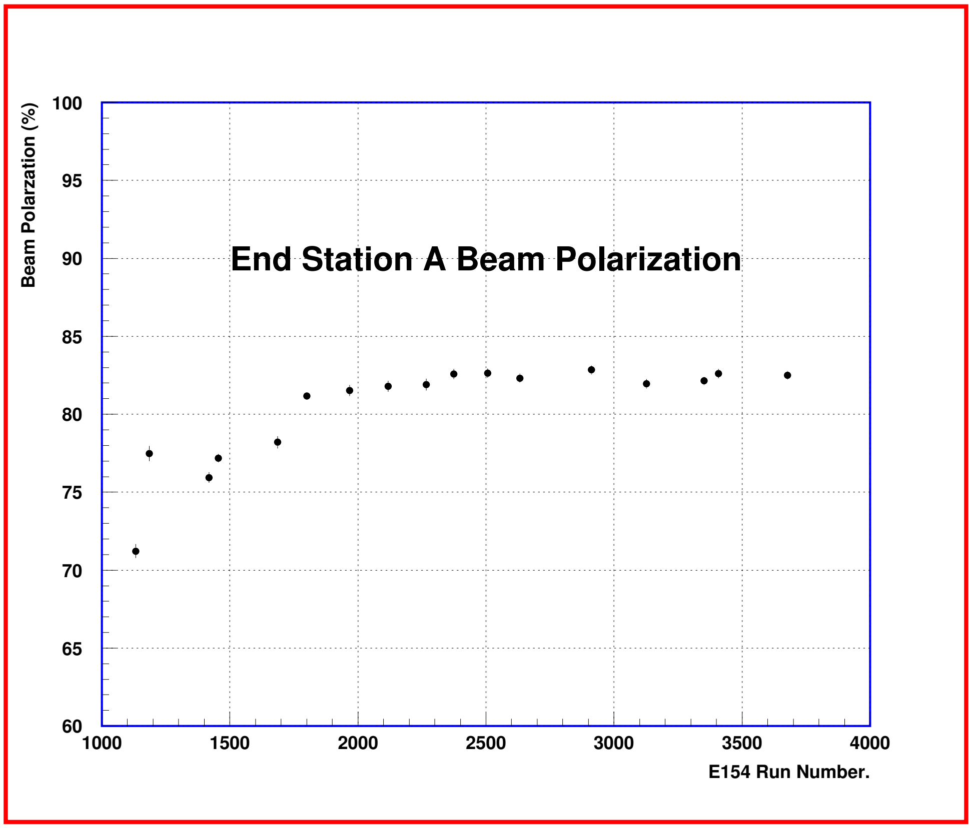

Figure 3.3: Electron beam polarization for SLAC experiment E154.

longitudinally polarized. A precession of 15π corresponds to an energy of 48.35 GeV in End Station A, which is the energy at which SLAC experiment E154 was conducted. There is a loss of approximately 0.3 GeV due to synchrotron radiation while bending the electron beam in the A-line [44]. This synchrotron radiation must be taken into account when calculating the electron beam energy. By measuring the polarization of the electron beam as a function of energy, the energy of the electron beam was calibrated, and set to provide maximum longitudinal electron polarization in End Station A.

3.3 Polarized ^{3}He Target

Only an outline of the polarized ^{3}He target will be given here; a detailed discussion of the polarized ^{3}He target can be found in chapter 4. The polarized ^{3}He target was of a double cell design with only the lower cell in the electron beam [45].

Nine different target cells were used during SLAC experiment E154, with the target cell named Picard, the last cell used of the nine, providing the most statistically significant data. The target cells were identical in design, and very similar in dimensions, with the lower cell of Picard being 299 mm in length and containing 2.65×10^{20} ^{3}He atoms/cm^3 under normal data taking conditions. Also in the target cell Picard, under normal data taking conditions, were 2.3×10^{18} N_2 molecules/cm^3 and 4×10^{11} Rb atoms/cm^3. The N_2 and the Rb were necessary to polarize the ^{3}He using the technique of spin exchange with optically pumped Rb. The thickness of the end windows of the glass target cells, through which the electron beam passed, were between 42 μm and 83 μm with the end windows on the target cell Picard being 69 μm and 62 μm. Windows this thin were one of the most important features of the SLAC experiment E154 target cells, since roughly half of the events in the spectrometers came from the polarized ^{3}He. However, since the ^{3}He density in the target cell corresponds to a pressure of 11 atmospheres, windows this thin had a finite lifetime in the electron beam before catastrophic failure. The minimum end window thickness which would survive in the SLAC experiment E154 electron beam was not known before SLAC experiment E154. However, the minimum thickness was estimated to be slightly smaller than the thickness of the end windows which were created for the SLAC experiment E154 target cells. Given that it took approximately 24 hours to replace and polarize a target cell that had exploded, it was advantageous to the experiment to use target cells with windows this thin so long as the target cells survived a minimum of 3–4 days in the electron beam. All of the target cells used in SLAC experiment E154 survived for at least this long.

The SLAC experiment E154 target cells were mounted in a plastic hanger assembly that was driven up and down by a stepping motor. Also mounted in the same assembly 1.5 inches below the polarized ^{3}He target cell was a glass reference cell identical in design to the target cell. This reference cell was connected to a gas manifold and could be filled with ^{3}He up to a pressure of approximately 175 psi. The reference cell was used to determine the number of observed events that originated in the ^{3}He by measuring the count rate as a function of the reference cell pressure.

3.4 Spectrometers

The layout of the E154 spectrometers can be seen in figure 3.1. The uppermost schematic is the layout of the spectrometers as seen from above, while the lower two schematics are the side views of the two spectrometers. The two spectrometers were centered at 2.75° and 5.50° with respect to the incident electron direction and operated independently. Each spectrometer contained a set of magnets, used for momentum determination and elimination of neutral backgrounds, as well as a detector package capable of particle identification, tracking and calorimetry. The spectrometers were designed to accept a high instantaneous counting rate while unambiguously identifying electrons scattered from the target amidst a large background of charged hadrons and low energy neutral particles. With a beam energy of 48.3 GeV and a fixed angle, the 2.75° spectrometer was capable of measuring electrons with momentums between 10 and 44 GeV/c, while the 5.50° spectrometer was capable of measuring electrons with momentums between 10 and 39 GeV/c. The low momentum limit coming from a desire to keep the charged hadron background at a tolerable level and to keep the radiative corrections small. The high momentum limit is set by the requirement that the electron come from the deep inelastic region, $W^2 > 4$ GeV^2. Together, the two spectrometers cover the kinematic range $0.014 \leq x \leq 0.8$ and $1\ (\mathrm{GeV/c})^2 \leq Q^2 \leq 17\ (\mathrm{GeV/c})^2$ as can be seen in figure 3.4. The detector package in each spectrometer consisted of two gas Cherenkov tanks, four planes of highly segmented plastic scintillators, and a lead glass calorimeter in a fly's eye configuration. The four hodoscope planes were divide into two pairs with each pair having two hodoscope planes whose 'fingers' were mounted at 90 degrees with respect to each other. The position of these elements can be seen in figure 3.1.

3.4.1 Magnets

Each of the spectrometers used two dipoles whose magnetic fields were aligned antiparallel. This 'double bounce' design was chosen to reduce the neutral background since neutral particles would have to scatter twice from the magnets and/or the collimators in order to reach the detectors. A quadrapole magnet was placed in the 2.75° spectrometer to defocus the electrons and spread them more evenly across

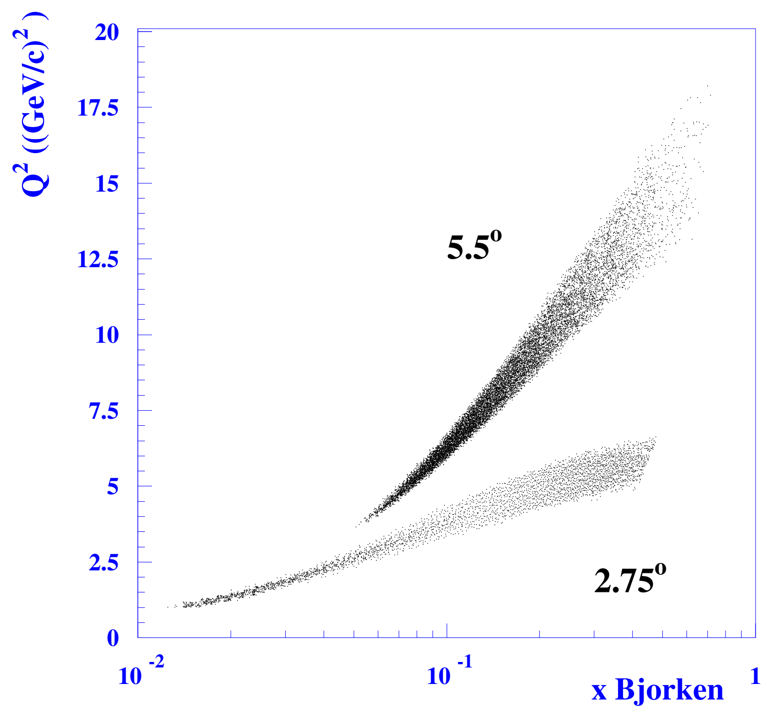

Figure 3.4: Kinematic coverage in x and Q^2 of SLAC experiment E154.

the detector elements, thus reducing the instantaneous rate in the detector elements that would have been most hit. Adjustable collimators were used to define the acceptance of the spectrometers and the collimators in the 2.75° spectrometer were adjusted over the course of SLAC experiment E154 to maintain a constant event rate with different target thicknesses and beam charge. The magnetic field of the magnets was mapped out prior to the data taking and the field inside the magnets was monitored during the data taking with NMR probes. Using the geometry of the spectrometers and the field maps, an optics model of the spectrometers was created and provided the necessary matrix elements for converting a measured electron position and momentum in the spectrometer into a position and momentum at the target. The optics model of the spectrometers was checked before the data taking run using a special 8 GeV run in which the elastic peak of the proton was measured.

3.4.2 Cherenkovs

The gas Cherenkov detectors were used in threshold mode to distinguish between electrons and heavier charged particles, typically pions. When a charged particle enters a medium in which it's velocity is greater than the velocity of light in that medium, Cherenkov radiation is emitted. By filling the Cherenkov tanks with nitrogen to an absolute pressure of 1–2 psi, the index of refraction inside the Cherenkov tanks could be raised so that nearly all of the scattered electrons would be above the Cherenkov threshold and emit Cherenkov radiation. The nitrogen gas pressure was kept low enough so that most of the heavier pions that passed through the Cherenkov tanks would be below the Cherenkov threshold. The threshold for Cherenkov radiation is

$$\beta = \frac{p}{\sqrt{p^2 + m^2c^2}} > \frac{1}{n}, \tag{3.7}$$

where n is the index of refraction inside the Cherenkov tanks and a function of the nitrogen pressure. The 2.75° (5.50°) Cherenkov tank was filled to an absolute pressure of 1.4 psi (2.0 psi), giving it an index of refraction of 1.000027 (1.000038) and a pion threshold of 19 GeV/c (16 GeV/c).

The Cherenkov tanks were constructed of aluminum with thin aluminum entrance and exit windows 1.0–1.5 mm thick. Cherenkov radiation is emitted in a forward cone with an angle given by

$$\cos\theta_{cher} = \frac{1}{\beta n}. \tag{3.8}$$

To detect these photons, spherical mirrors were mounted inside the Cherenkov tanks near the exit window and focused upon a photomultiplier tube. The photomultiplier tubes were connected to Flash ADCs that were capable of recording the output of the photomultiplier tubes in 1 ns intervals for the entire 250 ns duration of a beam pulse. Also connected to the last dynode of the photomultiplier tube was a TDC. This TDC recorded the time of the photomultiplier signals that exceeded a preset threshold. The number of Cherenkov photons emitted by a charged particle above threshold is proportional to $\mathrm{L}_{rad}\sin^2\theta_{cher}$, so the length of the Cherenkov tanks was chosen to be sufficiently long to reduce the probability that an electron passing through the Cherenkov tanks would emit 0 photons to less than 1%. The parameters of the SLAC experiment E154 Cherenkov tanks can be found in table 3.2. For pions above threshold, the number of Cherenkov photons rises slowly with momentum, reaching 75% of the number for electrons at approximately twice the threshold value, 32–38 GeV/c. This is not a problem, however, as the pion production rate at these high momenta is effectively zero.

Tank	Nitrogen Pressure (psia)	Pion Threshold (GeV)	Effective Length (m)	Mirror Curvature (m)	Observed N_{pe}
2C1	1.4	19	5.3	1.2	5.7
2C2	1.4	19	6.1	1.6	5.1
5C1	2.0	16	5.6	1.2	6.2
5C2	2.0	16	4.0	1.6	5.0

Table 3.2: Parameters of the SLAC experiment E154 Cherenkov tanks.

3.4.3 Hodoscopes

The momentum of a charged particle as it passed through the spectrometer was measured by reconstructing the track that the electron made in the hodoscopes after passing through the bending magnets. The hodoscopes consisted of paired planes of finely segmented plastic scintillators that had a 90° rotation of the fingers between planes within each pair. The hodoscopes were placed in groups after each Cherenkov tank, with 6 (4) planes after the first tank and 4 (4) planes after the second tank in the 2.75° (5.50°) spectrometer. The fingers in each plane were composed of a plastic scintillator that would emit approximately 10-15 photons in the UV region for each charged particle that passed through it [46]. The fingers were wrapped in aluminum foil and black electrical tape to provide shielding from external sources of light and to provide a reflective surface for the photons. The fingers overlapped by approximately 1/3 of their width to provide better resolution. A small quantity of organic wavelength shifter was added to the plastic fingers to convert the UV photons into the visible. The photons traveled down the fingers through total internal reflectance and by reflecting from the aluminum to the end of the fingers where a photomultiplier tube was mounted. The photomultiplier tubes were connected to discriminators and multi-hit TDCs to record the time at which a charged particle passed through a hodoscope finger.

3.4.4 Shower Counters

At the end of each spectrometer was an electromagnetic calorimeter in a fly's eye configuration. The total length of the shower counter for electrons was 24 interaction lengths, allowing the entire electromagnetic shower to be contained within the calorimeter. Each of the two shower counters consisted of 200 lead glass blocks arranged in 20 rows of 10 blocks each. Each of the blocks was 6.2 cm by 6.2 cm and 75 cm long, and was wrapped in aluminum foil and black tape. A photomultiplier tube was attached to the downstream end of each block. The integrated signal from the photomultiplier tubes was read by an ADC. A discriminator was also used with a multi-hit TDC to determine the beginning and ending time of each shower. This timing information was used to reconstruct events whose showers overlapped in time.

The electromagnetic shower spreads out transversely due to Coulomb scattering, and the transverse size can be found from the Moliére radius, $R_m \approx 5$ cm. This means that the electromagnetic shower caused by an electron is typically contained in 9 adjacent lead glass blocks with most of the energy deposited in the central block.

For a charged hadron, the nuclear interaction length is much longer, being 34 cm for a pion. This means that the shower counter is approximately 2 interaction lengths long for the pions and only a fraction of the energy of the pion is deposited within the shower counter. Because of this, the shower counter can be used for electron identification by requiring that the energy of the event measured in the shower counter be nearly equal to the momentum measured by the hodoscopes.

3.4.5 Electronics and DAQ

The data acquisition system used VME processors to read out the CAMAC modules that were connected to most of the detector electronics as well as to read out those detectors that could interface directly to the VME crates. A VME based data acquisition system (DAQ) was chosen to handle the high data transfer rates necessitated by the short electron beam pulse length, with the throughput of the DAQ being approximately 0.7–0.8 Mbytes/s. The actual data rates were sufficiently smaller than the maximum throughput so that a negligible amount of data was lost due to truncations. The front end of the DAQ used three VME crates of which one was located in End Station A and was shielded from the beam by being placed inside the concrete spectrometer hut of the 2.75° spectrometer. The electronics for both spectrometers were also located inside the 2.75° spectrometer hut, which included the electronics for the Cherenkov tanks, the hodoscopes, and the shower counters that have already been described. One of the VME crates in the counting house was used to interface with a CAMAC branch that gathered the beam data and read a number of scalars that contained various operating parameters for the experiment, such as the target operating parameters. The third VME crate was used as a local data server and connected to the data logging systems.

The data were sent to an automated tape silo in the SLAC computing center to be recorded, and a total of 1.4 Tbytes of data were written to tape during SLAC experiment E154.[1] The local data server was also capable of serving the data over the network to various workstations that were used for on-line analysis of the experiment. Two dedicated workstations were used to monitor the two spectrometers during the experiment, with one workstation per spectrometer running the on-line analysis.

[1]A backup system for writing the data to 8 mm tape in End Station A existed but was never needed during SLAC experiment E154.

CHAPTER IV

Advances in ^{3}He Target Technology

4.1 Introduction

Polarization of the ^{3}He nuclei for SLAC experiment E154 was accomplished using spin exchange with optically pumped rubidium. Spin exchange with optically pumped rubidium is a two step process in which a sample of rubidium vapor is electronically polarized by optical pumping with laser light on or near resonance, and then, the electronic polarization of the rubidium is transferred to the ^{3}He nuclei through hyperfine interactions that occur during binary collisions.[1] Polarized ^{3}He was first produced with this technique by Bouchiat, Carver and Varnum in 1960 [48]. Using a Rb lamp to optically pump a 30 cm^3 Pyrex cell containing a rubidium vapor and 5.6×10^{19} atoms of ^{3}He (2.1 amagats[2]), a polarization of 0.01% was achieved in the ^{3}He. A second method of producing polarized ^{3}He was later developed using metastability exchange [49]. In metastability exchange, metastable ^{3}He atoms are produced using an RF discharge, and then direct optical pumping is done on the $^3S_1$ metastable state of ^{3}He. Polarization is then transferred to the ground state ^{3}He atoms via metastability exchanging collisions. These early efforts to produce polarized ^{3}He were limited primarily by two things, the low intensity of the light source for optical pumping and the large depolarization rate for ^{3}He–glass collisions which occurred at and in the glass walls of the cell. At present, both of these limitations

[1] While rubidium was used for SLAC experiment E154, it should be noted that the spin exchange process also works for other alkali metal vapors [47].

[2] The density of an ideal gas at STP is 1 amagat = 2.6868×10^{19} cm^{-3}.

have been reduced to the point that a ^{3}He polarization greater than fifty percent can be produced in large, high density cells.

While the method of metastability exchange is limited to low ^{3}He densities, it allowed the creation of ^{3}He polarizations large enough to investigate wall relaxation times for polarized ^{3}He cells. The work of Fitzsimmons and Walters successfully identified aluminosilicate glass as a substance with a small ^{3}He–wall depolarization rate [50]. Later work by Timsit, Daniels and May investigating the depolarization of ^{3}He on various solid surfaces gave further insight into the various depolarization mechanisms [51]. This work allowed a number of glasses to be identified as suitable for long lifetime, polarized ^{3}He cells. At present, with proper glass cleaning procedures, high pressure spin-exchange cells can be made with ^{3}He–glass depolarization rates small enough to yield spin exchange cells with lifetimes in the hundreds of hours. This is more than sufficient to achieve high polarizations in spin exchange cells. For experiment E154 at SLAC, the aluminosilicate glass Corning 1720 was chosen for construction of the ^{3}He target cells, since the properties of Corning 1720 glass were suitable for the production of long lifetime polarized ^{3}He cells.

The first light source to reach a power of 1 watt with a bandwidth sufficiently narrow for optical pumping of the 795 nm D1 line of rubidium was the dye laser. This allowed a rubidium optical pumping rate sufficiently large to achieve a high polarization in a dense rubidium vapor [52]. The number of ^{3}He atoms that can be polarized in a spin exchange cell is limited by the amount of light that is available for optical pumping. A large cell requires more light to maintain a high rubidium polarization, and consequently, a larger and more elaborate laser pumping system. A large cell might require a system of ten dye lasers, or ten thousand Rb lamps, with the expense and difficulty of assembling such a system exceeding the capacity of the experimenters. While the advances created by the dye laser were significant, the dye laser was not the final advancement in laser technology. Ti:sapphire lasers followed and were able to produce more output power with greater reliability. The latest step forward in laser technology for optical pumping of rubidium was the diode laser array. With a reasonably narrow bandwidth and an output power three times greater than the Argon ion pumped Ti:sapphire laser, a cost of only a tenth as much, and a greater ease of use, a laser pumping system for a large spin exchange cell based on laser diode arrays could be assembled and operated without being too expensive or time consuming. For SLAC experiment E154, three 20 watt laser diode arrays were added to the four Argon ion Ti:sapphire lasers used in SLAC experiment E142.

4.2 Theory of Operation

4.2.1 Optical Pumping

Polarization of the ^{3}He by spin exchange with optically pumped rubidium is a two step process in which the rubidium electrons are first polarized by optical pumping and then their electronic polarization is transferred to the ^{3}He nuclei through hyperfine interactions during collisions. To achieve a high polarization in the ^{3}He nuclei, it is necessary in each of the two steps to maximize the polarizing processes while minimizing the depolarizing processes. In the case of the ^{3}He, the velocity averaged cross section for spin exchange is $\langle\sigma_{SE}v\rangle = 1.2 \times 10^{-19}$ cm^3/s [53, 54], giving a characteristic time for spin exchange of approximately ten hours at practical rubidium densities. With the spin exchange rate so small, a great deal of care must be taken to minimize ^{3}He nuclear depolarization processes.

Optical pumping was first introduced in 1950 by Kastler [55], and can be viewed as the transfer of angular momentum from photons to atoms via resonant scattering. A more thorough treatment of optical pumping in a dense rubidium vapor can be found in Happer [47] or Wagshul and Chupp [56]. The valence electron of ground state rubidium is in the $5^2S_{\frac{1}{2}}$ state. The first excited state is the $5^2P_{\frac{1}{2}}$ state, which is separated by 795 nm. The transition between these two states is called the D1 transition. In a magnetic field, the two m_j sublevels of the rubidium are split and transitions can be made from one sublevel to the other through the absorption of circularly polarized light (See figure 4.1). An incoming photon with a projection of +1 unit of angular momentum (σ_+) can be absorbed by a rubidium electron in the $m_j = -\frac{1}{2}$ ground state, exciting it into the $m_j = +\frac{1}{2}$ excited state. In a rubidium vapor with low pressures of ^{3}He, the atoms in the excited state would remain there until they decayed, returning 2/3 of the time to the $m_j = -\frac{1}{2}$ ground state and 1/3 of the time to the $m_j = +\frac{1}{2}$ ground state, as indicated by the Clebsh-Gordon

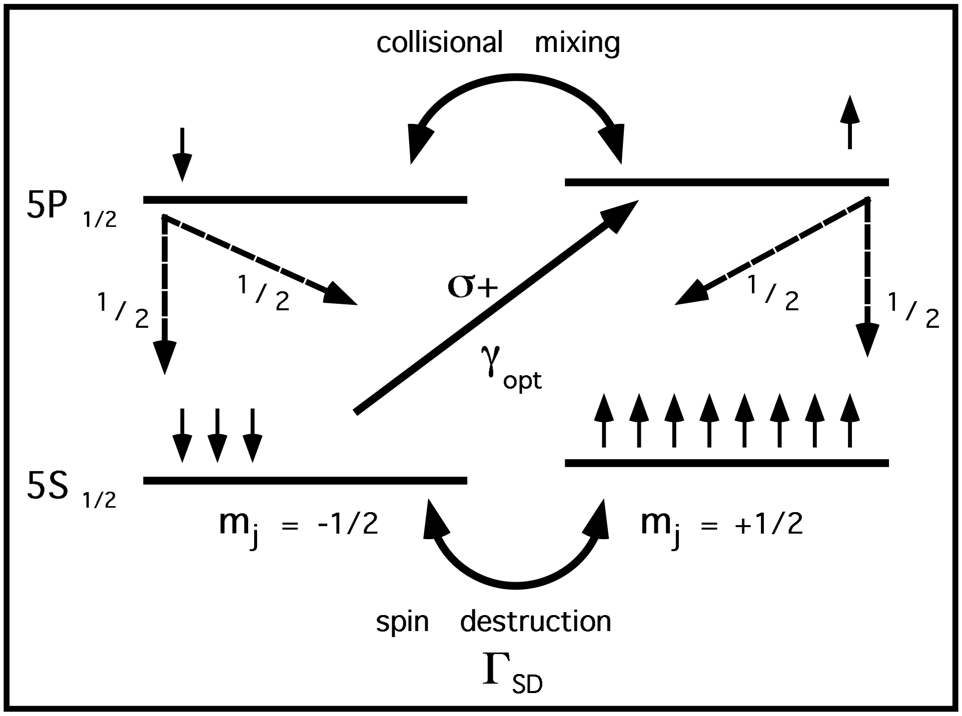

Figure 4.1: Rubidium energy levels and transitions.

coefficients.

There are a number of effects to consider that complicate this simple two level picture. In the SLAC experiment E154 target cells, there is a large buffer gas pressure of ^{3}He (10–13 atmospheres) which collisionally mixes the excited states. The mixing time at this pressure is much shorter than the excited state lifetime and a rubidium atom that has been excited has an almost equal probability of being in either excited state when it decays. This gives a probability of an excited rubidium atom decaying into the m$_j$ = $+\frac{1}{2}$ ground state of 1/2 instead.

The simple two level description maintained up to this point ignores the nuclear spin of the rubidium. There are two isotopes of rubidium, ^{85}Rb and ^{87}Rb with natural abundances of 28% and 72%, respectively, and with nuclear spins of $I = 5/2$ and $I = 3/2$, respectively. The ground and excited states of the D1 transition contain two hyperfine multiplets, $F = I + 1/2$ and $F = I - 1/2$. The ground state (for $I = 3/2$) consists of eight levels, as does the $5^2\mathrm{P}_{\frac{1}{2}}$ excited state, and a circularly polarized photon with +1 unit of angular momentum (σ_+) can excite any of 12 transitions satisfying $\Delta m_F = +1$. The only state with no allowed transitions is the $F = 2, m_F = 2$ state and optical pumping will drive the rubidium atoms into this state. Polarizing the rubidium electrons thus requires polarizing both the electrons and the nucleus through a number of optical pumping transitions. The effect on the optical pumping process of including the nuclear spin is only to lengthen the time it takes the rubidium electrons to reach their equilibrium polarization; the equilibrium value itself is unchanged. The effect is often characterized by a 'slowing down' factor, S, which has been calculated to be approximately 5 for highly polarized, naturally occurring rubidium [56].

Also to be considered is the high rubidium density at which the SLAC experiment E154 target was typically operated. The rubidium vapor at this density is optically thick, and a photon emitted by an atom in the excited state decaying back to the ground state has a significant chance of being reabsorbed. This would not be a problem if it were not for the fact that the excited states can emit a photon that can carry either +1 unit of angular momentum (σ_+) or -1 unit of angular momentum (σ_-). The σ_- photons that are emitted are detrimental to the optical pumping process as they remove electrons from the desired state when they are reabsorbed. This multiple scattering of photons in an optically thick vapor is known as 'radiation trapping' [57]. To prevent radiation trapping, a small quantity of nitrogen was added to the spin exchange cells. Collisions between an excited rubidium atom and a nitrogen molecule provided a non-radiative relaxation mechanism for the rubidium by transferring the energy to the vibrational and rotational modes of the nitrogen molecule. This process is known as 'quenching', and nitrogen was used in the SLAC experiment E154 target cells because it has a large quenching cross section [58].

The inherent lifetime of the excited state of rubidium is approximately 30 ns [58]. The excited state lifetime is shortened to approximately 1.0 ns by the presence of approximately 90 torr of nitrogen in the pumping chamber of the spin exchange cell under normal running conditions. The collisional mixing time for the excited rubidium states in the presence of 10–13 atmospheres of ^{3}He, as was typical during the optical pumping process, is approximately 10 ps. Under these conditions, the two m_j excited states are well mixed, and a σ_- photon is estimated to be emitted only 1% of the time. Because the atoms spend so little time in the excited state, the processes that determine the equilibrium rubidium polarization are the optical pumping rate and the ground state spin relaxation rate.

The optical pumping rate is determined by the overlap integral of the intensity of the circularly polarized light in the cell and the absorption cross section, according to the equation

$$\gamma_{opt}(\vec{r}) = \int \Phi(\nu, \vec{r})\sigma(\nu)d\nu, \tag{4.1}$$

where $\Phi(\nu, \vec{r})$ is the intensity of the light as a function of frequency and position and $\sigma(\nu)$ is the pressure broadened cross section for absorption as a function of frequency. The spatial dependence of γ_{opt} is determined by the spatial dependence of the light intensity, Φ, which depends on both the spatial dependence of the light source and the absorption of the light as it propagates through the cell. Light sources that are effective for optical pumping must have line widths that are not much broader than the absorption line width of the rubidium. In the SLAC E154 cells, the presence of 10–13 atmospheres of ^{3}He broadens the rubidium absorption line to approximately 0.4 nm and allows a number of light sources to work effectively. Laser light sources for SLAC experiment E154 will be discussed in section 4.4, and figure 4.7 shows a plot of the rubidium absorption line in the presence of 10 amagats of ^{3}He. Wagshul has estimated the amount of light that must be absorbed for efficient optical pumping in a cell similar to the SLAC experiment E154 cell to be on the order of 10–20 watts, giving an optical pumping rate on the order of γ_{opt} = 100,000 Hz [56]. Depending on the linewidth of the light and the efficiency with which the light can be transported to the cell and its spatial profile matched to the spatial profile of the spin exchange cell, the amount of light that must be produced is typically a factor of 2 or 3 greater than this.

The ground state spin relaxation of the rubidium has two primary sources: collisions between the rubidium and the other gases in the cell, and wall collisions. For the ^{3}He density at which the SLAC experiment E154 target cells were typically operated, the diffusion length of the rubidium is very short and wall collisions only effect a thin boundary layer near the walls. At the walls, the polarization of the rubidium drops to zero because the rubidium remains adsorbed on the walls long enough to become completely depolarized. For the SLAC experiment E154 target cells, this boundary layer is most important in the front of the pumping cell where the laser light enters since a significant amount of laser light is absorbed in this front boundary layer. Wagshul and Chupp estimate this to be on the order of 300 mW/cm^2, which for the SLAC E154 target cells is approximately 4 watts of power [56].

In the bulk, ground state spin relaxation is primarily due to rubidium-rubidium collisions and collisions between the rubidium and the other gases (^{3}He and N_2) which randomize the electronic polarization (often referred to as spin destruction). The rate constants for collisional relaxation of Rb polarization due to Rb–Rb collisions and Rb–N_2 collisions have been reported by Wagshul and Chupp [56]. Wagshul and Chupp also place an upper limit on the Rb–^{3}He collisonal rate for rubidium ground state spin relaxation. Using these constants, one can calculate the ground state spin relaxation rate

$$\begin{aligned} \Gamma_{SD} \quad &= (8 \times 10^{-13} cm^3/s)\,[Rb] \\ &+ (8 \times 10^{-18} cm^3/s)\,[N_2] \\ &+ (\leq 2 \times 10^{-18} cm^3/s)\,[^3He]\,. \end{aligned} \tag{4.2}$$

For the SLAC experiment E154 target cells, typical densities during data taking were $[Rb] = 4 \times 10^{14}$ cm^{-3}, $[N_2] = 2 \times 10^{18}$ cm^{-3}, and $[^3He] = 2 \times 10^{20}$ cm^{-3}, giving a maximum ground state spin relaxation rate of approximately 700 Hz in the bulk. The ground state spin relaxation rate due to Rb–Rb collisions is approximately equal to the Rb–^{3}He ground state spin relaxation rate. The nitrogen density is too low to play a significant role. In the bulk, there must be at least enough light to repump each rubidium atom that decays. Since it takes 2 photons on average per rubidium atom, this requires a laser power in the bulk of

$$P_{bulk} > 2\Gamma_{SD}\,[Rb]\,V h\nu, \tag{4.3}$$

where Γ_{SD} is the bulk ground state spin relaxation rate, $[Rb] = 4 \times 10^{14}$ cm^{-3} is the rubidium density at 180°C, V is the volume of the pumping cell, typically 80 cm^3, h is Planck's constant, and ν is the frequency of the radiation. This gives a minimum power for efficient optical pumping of approximately 12 watts in the bulk.

With the short lived excited state, a simple rate equation for the bulk polarization of the cell can be written $\left(P_{Rb} = \left(Rb(+\frac{1}{2}) - Rb(-\frac{1}{2})\right) / \left(Rb(+\frac{1}{2}) + Rb(-\frac{1}{2})\right)\right)$

$$\frac{dP_{Rb}}{dt} = \frac{\gamma_{opt}}{S}\,(1 - P_{Rb}) - \frac{\Gamma_{SD}}{S} P_{Rb} \tag{4.4}$$

which has the solution

$$P_{Rb} = \left(\frac{\gamma_{opt}}{\gamma_{opt} + \Gamma_{SD}}\right)\left(1 - e^{-\left(\frac{\gamma_{opt}+\Gamma_{SD}}{S}\right)t}\right), \tag{4.5}$$

with the initial condition $P_{Rb} = 0$. The equilibrium value for the rubidium polarization is $\gamma_{opt}/(\gamma_{opt} + \Gamma_{SD})$, and is achieved with a characteristic time constant of $S\,(\gamma_{opt} + \Gamma_{SD})^{-1}$. The characteristic time for polarizing the rubidium is a few milliseconds in a SLAC E154 target cell, which is essentially instantaneous when compared with the Rb–^{3}He spin exchange time of several hours. Of course the average rubidium polarization in the cell is lower than the polarization of the bulk. The portions of the cell near the walls have low polarization and the portions of the cell for which the optical pumping rate drops to zero have zero polarization. As the laser light propagates through the cell, a 'hole is burned' into the center of the spectral distribution. This occurs because the probability of absorption for a photon at resonance is much higher than for one in the wings of the spectral distribution. Once a significant 'hole' has been created in the center of the spectral distribution, the optical pumping rate drops below the ground state spin relaxation rate and the polarization of the rubidium falls to near zero. This description is best applied to broad sources such as laser diode arrays. In the case of narrow lasers such as Ti:sapphires, the 'hole' which would be burned is wider than the bandwidth of the light source, and the transition between light and dark areas of the cell is sharp, as the laser light is fully absorbed.

For light sources with linewidths less than the rubidium absorption linewidth, the fraction of the cell's volume that is fully illuminated by the laser light is referred to as the 'filling factor', and the average rubidium polarization has an upper limit of the filling factor. During experiment E154, the filling factor for the cell was maximized visually by observing the 780 nm fluorescence from the cell. The cell was viewed with a CCD camera fitted with a 780 nm filter. The fluorescence of the D2 line ($5^2\mathrm{P}_{\frac{3}{2}}$ - $5^2\mathrm{S}_{\frac{1}{2}}$ transition) was chosen in order to filter out the intense pumping light. A mirror was mounted above the cell to allow both the side view and the top view to be visible with a single CCD camera. An example of the fluorescence from the pumping cell as was seen during the experiment is shown in figure 4.2. The upper image is the top view from the mirror and the lower image is the side view. The transfer tube leading down to the target chamber can be seen in the side view at the bottom. From the image, an estimate of 0.7–0.8 can be made for the filling factor and the average rubidium polarization.

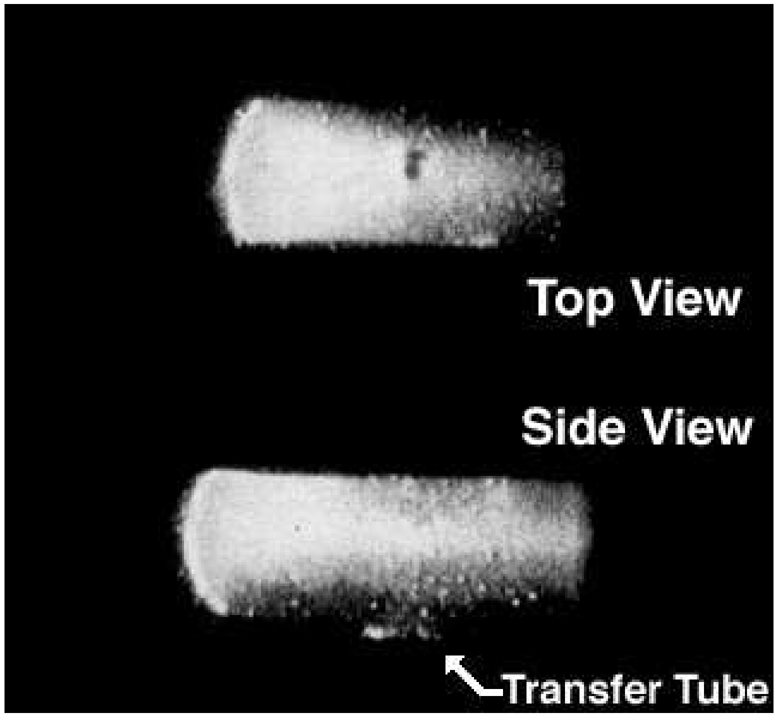

Figure 4.2: Pumping cell fluorescence.

4.2.2 Spin Exchange

During collisions between the rubidium and the ^{3}He, there is a small overlap of the electronic wavefunction of the rubidium and the nuclear wavefunction of the ^{3}He. The resulting hyperfine interaction is responsible for spin exchange between the rubidium and the ^{3}He [59, 60],

$$\mathcal{H}_{SE} = \alpha\,(K \cdot S)\,, \tag{4.6}$$

where $\mathcal{H}_{SE}$ is the spin exchange hamiltonian, α is the strength of the interaction, K is the nuclear spin of the ^{3}He and S is the electronic spin of the rubidium. This interaction mixes the eigenstates of the ^{3}He nucleus and the rubidium electron and causes the transfer of angular momentum between the two,

$$Rb\,(\uparrow) + {}^3He\,(\downarrow) \longrightarrow Rb\,(\downarrow) + {}^3He\,(\uparrow)\,, \tag{4.7}$$

It is also responsible for shifting the electronic energy levels of the rubidium resulting in a ^{3}He nuclear polarization dependent shift in the rubidium Zeeman frequency, a feature that can be exploited for polarimetry as will be discussed in section 4.6.4.

The cross section for this interaction is small, on the order of 10^{-24} cm^2 [61], and the electronic spin of the rubidium is quickly realigned by optical pumping after a spin exchanging interaction because the optical pumping process is approximately six orders of magnitude faster. The result is that the ^{3}He nuclear polarization is driven towards the average rubidium polarization because each ^{3}He atom diffuses through the cell, thus averaging the rubidium polarization. Competing with this polarizing mechanism are a number of ground state spin relaxation mechanisms that drive the ^{3}He nuclear polarization to zero. Achieving a large ^{3}He nuclear polarization is then a matter of maximizing the polarizing mechanisms while minimizing the ground state spin relaxation mechanisms. This is no easy task because the spin exchange rate is so small; however, the ground state spin relaxation mechanisms can be made even smaller and polarizations greater than 50% can be achieved.

The temporal evolution of the ^{3}He polarization due to spin exchange is similar to that of the rubidium polarization, namely

$$\frac{dP_{He}}{dt} = \gamma_{SE}\left(\langle P_{Rb}\rangle - P_{He}\right) - \Gamma P_{He} \tag{4.8}$$

which has the solution (with $P_{He} = 0$ at $t = 0$)

$$P_{He} = \langle P_{Rb}\rangle \left(\frac{\gamma_{SE}}{\gamma_{SE} + \Gamma}\right)\left(1 - e^{-(\gamma_{SE}+\Gamma)t}\right), \tag{4.9}$$

where $\langle P_{Rb}\rangle$ is the average rubidium polarization, γ_{SE} is the Rb–^{3}He spin exchange rate and Γ is the total ^{3}He ground state spin relaxation rate. In this equation, the spin-exchange rate and the total ground state spin relaxation rate are averages over the entire cell. The rates in each of the two chambers are, of course, different. Since there is a negligible rubidium density in the cold target cell, the spin exchange rate there is zero. The spin exchange rate for the entire cell is then smaller than the rate in the pumping cell by the ratio of the number of atoms in the pumping cell to the number of atoms in the entire cell, a factor of almost three. In the pumping cell, the spin exchange rate is $\gamma_{SE} = \langle v\sigma_{SE}\rangle\,[Rb]$, where $\langle v\sigma_{SE}\rangle$ is the velocity averaged spin exchange cross section and $[Rb]$ is the rubidium density. Using the value of

$\langle v\sigma_{SE}\rangle = (1.2 \pm 0.2)\times10^{-19}$ cm^3/s measured by Coulter [53], and a rubidium density of $[Rb] = 4\times10^{14}$ cm^{-3} for a pumping cell at 180°C, this gives a spin exchange time constant in the pumping cell of ${\gamma_{SE}}^{-1} = 5.8$ hours. Another complication of the double cell is caused by the finite transfer time of approximately 50 minutes for the polarization to travel between the pumping cell and the target cell. This leads to a small difference of approximately 3% between the average polarization in the pumping cell and the average polarization in the target cell. For target polarimetry, pickup coils were mounted around the target cell so that the polarization of the target cell could be measured directly. However, for one of the methods used to calibrate the polarization of the target cell, the polarization of the pumping cell must also be known, and for this purpose a more complete solution to the process of spin exchange in a double chambered target must be known. This more complete description of the spin exchange process in a double chambered target cell can be found in the appendix.

There are two classes of ground state spin relaxation mechanisms that significantly contribute to the depolarization of a SLAC E154 polarized ^{3}He target cell. There are internal mechanisms which are inherent to the cell, such as ^{3}He–^{3}He magnetic dipole interactions, ^{3}He–wall depolarizing collisions, and ^{3}He collisions with paramagnetic gas impurities in the cell. The sum of these rates is the inverse of the cell lifetime

$$ {\tau_{cell}}^{-1} = \Gamma_{He-He} + \Gamma_{wall} + \Gamma_{gas}. \tag{4.10} $$

With the appropriate choice of glass and proper glass cleaning procedures, as well as stringent gas purity requirements, the depolarization rate from sources other than ^{3}He–^{3}He magnetic dipole interactions could be made small, and one of the criteria that was used to choose a target for SLAC experiment E154 was the cell's lifetime. The rate for ^{3}He ground state spin relaxation in a high pressure cell from the ^{3}He–^{3}He magnetic dipole interaction has been calculated by Newbury *et al.* [62],

$$ {\Gamma_{He-He}}^{-1} = \frac{744}{[^3\mathrm{He}]} \text{ hours}, \tag{4.11} $$

where [^{3}He] is expressed in amagats (1 amagat = 2.6868×10^{19} cm^{-3}).

Once a cell had been made and kept at a high temperature for an extended period of time, the lifetime of the cell typically became constant. A period of a few days to a week is necessary to allow a monolayer of rubidium to coat the inner surfaces of the glass cell; this rubidium coating often improves the lifetime of the cell. After being at an elevated temperature for an extended period of time, the cell could typically withstand temperature cycling without any adverse effects. There are a few cells that have gone 'bad' after filling, but it is not clear what the cause was except in the case of those cells that developed leaks. For those cells that developed leaks, the cause was evident in the loss of gas from the cell and the discoloration of the rubidium caused by reacting with the high concentration of gas impurities. For those cells that did go bad, nearly all went bad within the first week of high temperature operation.

The second class of ground state spin relaxation mechanisms are those external to the cell, such as magnetic field gradients and electron beam induced depolarizations. For a high density ^{3}He cell, these have been worked out by Chupp *et al.* [63]. The ground state spin relaxation rate caused by magnetic field gradients is given by

$$\Gamma_{\nabla B} = D_{He}\left(\frac{\nabla {B_T}^2}{{B_z}^2}\right), \tag{4.12}$$

where D_{He} is the ^{3}He diffusion constant of 0.3 cm^2/s at 10 amagats, ∇B_T is the transverse field gradient and B_z is the magnetic holding field. To achieve a negligible rate for ground state spin relaxation from this source ($1/\Gamma_{\nabla B} > 1000$ hours) it is necessary to reduce the transverse field gradient such that $|\nabla B_T|\ /\ B_z < 0.001$ cm^{-1}. This was accomplished for SLAC experiment E154 with a pair of 150 cm diameter Helmholtz holding coils for the target and the removal of all ferromagnetic material from the vicinity of the target. The target was also placed far enough from the spectrometer magnets to avoid large fringe fields.

For SLAC experiment E154, the ground state spin relaxation from the beam has two forms: ionization and pulsed beam gradients [63, 64]. The production of $^3He^+$ ions and He_2^+ molecular ions can lead to the depolarization of the nuclear spin through coupling of the nuclear spin to the unpaired electron spin and the rotational angular momentum of the molecular ions. In a high density ^{3}He target with 50–100 torr of nitrogen, the formation of molecular ions is highly suppressed and the rate for ground state spin relaxation by beam ionization can be written as

$$\Gamma_{ion} = k_{ion} \left(\frac{l}{V_0} \right) i_b, \tag{4.13}$$

where k_{ion} is the cross section for beam induced ground state spin relaxation, i_b is the average beam current, l is the length of the cell traversed by the beam, and V_0 is the total cell volume. With $k_{ion} \approx 2.4$ cm^2/C for a high density target in a 50 GeV electron beam, $i_b = 0.6$–1.8 μA, $l = 30$ cm, and $V_0 = 190$ cm^3, this gives a relaxation time from ion induced ground state spin relaxation of 400–1200 hours.

The short pulse length of 200–250 ns for the electron beam used in SLAC experiment E154 causes a large instantaneous current of 25-75 mA and therefore the sudden appearance of large transverse field gradients with the onset of a pulse. The rate for pulsed beam ground state spin relaxation is given by [63]

$$\Gamma_{pulse} = \frac{Rl}{2\pi V_0} \left(\frac{\mu_0 I}{4 B_0} \right)^2, \tag{4.14}$$

where R = 120 Hz is the pulse rate, $l = 30$ cm is the length of the cell traversed by the beam, $V_0 = 190$ cm^3 is the total cell volume, I is the instantaneous beam current, and $B_0 = 8$–19 Gauss is the holding field magnitude. In the beginning of the experimental run, the instantaneous current was 75 mA and the holding field was 19 Gauss, while at the end of the experimental run the target holding field was as low as 8 Gauss and the instantaneous beam current had been reduced to 25 mA. This gives a relaxation time from pulsed beam ground state spin relaxation of 70–180 hours, depending on the beam current and the target holding field.

There are therefore two primary mechanisms for ground state spin relaxation that are unavoidable, ^{3}He–^{3}He magnetic dipole interactions and pulsed beam effects. It is also possible during cell filling to create a cell for which the ground state spin relaxation rates from wall collisions and gas impurities are not negligible. The degree to which a cell has been made which minimizes ground state spin relaxation from wall collisions and gas impurities is monitored by measuring the lifetime of the cell. During SLAC experiment E154, the cells used were those with the longest lifetimes. For the target Picard, the measured lifetime of the cell both before and after the experiment was 84 ± 5 hours, as compared to the ^{3}He–^{3}He magnetic dipole interaction limit of 84 hours. This indicates that additional ground state spin relaxation mechanisms must have had relaxation times in excess of 1000 hours. During the experimental run, the lifetime of the target Picard was measured with the beam on. This occurred during transverse running of the target polarization because it was not possible to optically pump the target while the polarization was transverse. Consequently, the target was cooled and allowed to depolarize with the beam on. The lifetime of the target Picard was measured to be 55 $\pm$ 3 hours with the beam on. This indicates that the beam provided an additional source of ground state spin relaxation with a relaxation time of 159 hours, in good agreement with a value of 140 hours as given by equation 4.14 using the experimental conditions for Picard transverse running. It is expected that the value from equation 4.14 should be less than that measured during Picard transverse running because the electron beam was not continuously on, and therefore the beam induced ground state spin relaxation was not present for all of the lifetime measurement.

An additional source of ground state spin relaxation was observed during the SLAC E154 experimental run, but a careful study of the ground state spin relaxation source has not been undertaken. This source was spin-coil coupling which coupled the bulk magnetization of the ^{3}He spins in the target cell to the pickup coils. For large enough polarizations, energy could be transferred to the pickup coils and then fed back into the cell, even though the target holding field was chosen so that the Larmor frequency of the ^{3}He spins was far from the resonance of the coils. This feedback created transverse magnetic fields that would depolarize the cell. The effect was seen in the target SMC and it is not understood why it was seen in SMC and not in other cells. However, in an attempt to reduce this possible ground state spin relaxation mechanism, the holding field was reduced near the end of the run. Whether or not reducing the holding field to 8 Gauss reduced the spin-coil coupling, the reduced target holding field did contribute to a higher beam pulse ground state spin relaxation rate as given by equation 4.14.

4.3 Target Cell Construction

The polarized ^{3}He spin exchange cells used as targets for SLAC experiment E154 were constructed at Princeton University. For the purpose of determining the fraction of observed events that originated in the ^{3}He, the cells can be viewed as thin-windowed glass cylinders filled with ^{3}He gas. There is also a small quantity of N_2 gas inside the cells for the purpose of optical pumping. The goal was to make a polarized ^{3}He target with a ^{3}He thickness of approximately 300 amagat-cm to provide a high counting rate in the spectrometers. With a practical limit of 30 cm on the length of the target, this meant filling the cells with ^{3}He to a density of approximately 10 amagats (2.6868×10^{20} cm^{-3}). To maximize the statistical significance of the data taken by the spectrometers, the windows on the cell would have to be as thin as possible, and the goal was to make the windows thin enough so that at least half of the events would originate from the ^{3}He. To accomplish this, the windows would have to be on the order of 40–70 μm thick, while the target cell would have to be pressurized with ^{3}He to a pressure of 10–13 atmospheres under normal running conditions.

4.3.1 Choice of Glass

When choosing a glass for a spin exchange cell, the two most important things to consider are the rate at which the helium moves through the glass (as given by the helium permeation velocity) and the paramagnetic impurity level (typically Fe^{+++}) in the glass. It is easy to see how these two glass characteristics work together to affect the ^{3}He depolarization rate. When the ^{3}He is in the glass or at the surface of the glass, its spin will follow the local magnetic field. If there are paramagnetic impurities present, then it is possible for the spin to rotate away from the holding field direction and become 'lost' in subsequent collisions. The longer the ^{3}He spends in the glass, the longer it is exposed to the fields of the paramagnetic impurities. Therefore, a porous glass (one with a large helium permeation velocity) must have a small paramagnetic impurity level. As helium permeation velocity decreases, the acceptable paramagnetic impurity level increases. An ideal glass would have a helium permeation velocity of zero and no paramagnetic impurities. A glass with a small helium permeation velocity could have a reasonable number of paramagnetic impurities, while a glass with a moderate helium permeation velocity would be required to have a small number of paramagnetic impurities. Also possible is a compromise of midrange helium permeation velocity and midrange paramagnetic impurity level.

	1720	7056	Pyrex	fused silica
Permeation velocity (0°C)	1×10^{4}	2×10^{8}	1×10^{10}	2×10^{11}
Permeation velocity (170°C)	2×10^{8}	1×10^{11}	1×10^{12}	4×10^{12}
Iron impurity level	150 ppm	76 ppm	62 ppm	1 ppm

Table 4.1: Helium permeation velocity and iron impurity level of selected glasses.

Three glasses for which long lifetime ^{3}He spin exchange cells can be made are Corning 1720, Corning 7056 and low iron fused silica. Table 4.1 lists the helium permeation velocity (in units of atoms per second times mm of thickness per cm^2 of area per atmosphere of pressure) and the iron impurity level of these three glasses as well as for Pyrex. The difference between a good glass for a spin-exchange cell and a bad glass is a fine one; although the primary characteristics of Pyrex are not that different from one of the other glasses (Corning 7056) they are enough to make Pyrex a glass for which long lifetime ^{3}He cells cannot be made.

The glass chosen for the SLAC experiment E154 target cells was Corning 1720, an aluminosilicate glass. It was chosen because spin exchange cells could be made from this glass that had extremely small ground state spin relaxation rates for the polarized ^{3}He. The primary reason for the small ground state spin relaxation rates of this glass is its small helium leak rate of approximately 50,000 atoms/second from a 1 cm^3 glass sphere with 1 mm thick walls at a temperature of 273K and a pressure of 1 atmosphere. While the glass does have a moderately high concentration of iron impurities, 150 ppm, the helium permeation velocity is so low that the ^{3}He simply does not spend enough time in the glass to suffer large ground state spin relaxation rates. The other benefit of using an aluminosilicate glass such as the Corning 1720 is that the low helium permeation velocity allows the ^{3}He to be contained in the cell for the duration of the three month long experiment. The amount of ^{3}He leaked from the cell is estimated to be less than 0.005%. This estimate has been calculated from the helium permeation velocity, the cell dimensions and the approximate amount of time at an elevated temperature, using the relationship

$$N(t) = N_0 \exp(-Rt), \tag{4.15}$$

where R is the helium leak rate time constant and given by the equation

$$R = \frac{K(T)AP}{lN}, \tag{4.16}$$

where $K(T)$ is the temperature dependent helium permeation velocity, A is the surface area in cm^2, P is the pressure in atmospheres, l is the wall thickness in mm, and N is the number of atoms in the cell. This relationship has been verified by measurements of the density of a cell that has been at an elevated temperature for an extended period of time.

While this is the best choice of glass in terms of its low ^{3}He–glass ground state spin relaxation rate, which is the most crucial factor in choosing a glass for constructing a polarized target, the disadvantage of using Corning 1720 is that it is a very difficult glass for the glass blower to work. This factor becomes critical when one of the design considerations are extremely thin windows as was necessitated by the small forward angles of the spectrometers. However, the skill of Mike Souza, the Princeton glass blower, allowed target cells to be constructed from Corning 1720 with inverted end windows as thin as 40 μm.

While Corning 1720 was the best choice of glass for this experiment, it should be emphasized that there are other glasses that are suitable for polarized ^{3}He spin exchange cells. Long lifetime ^{3}He spin exchange cells have been constructed from fused silica and Corning 7056 glass as well [65]. Both of these glasses meet the necessary criteria of a small wall depolarization rate for ^{3}He. However, they both have a higher permeation velocity constant for helium and would have, over the course of the experiment, leaked a larger fraction of the ^{3}He.

4.3.2 Target Cell Dimensions

Figure 4.3 shows the dimensions of the target cell Picard, which is statistically the most important of the nine target cells used, while table 4.2 lists the dimensions of all of the cells used for SLAC experiment E154. The target cell was of a double chamber design, consisting of an upper chamber and a lower chamber. The upper chamber was used for optical pumping and spin exchange, and as a result was maintained at an elevated temperature by being inserted into a hot air oven. The lower chamber was aligned with its long axis along the electron beam. The upper chamber shall

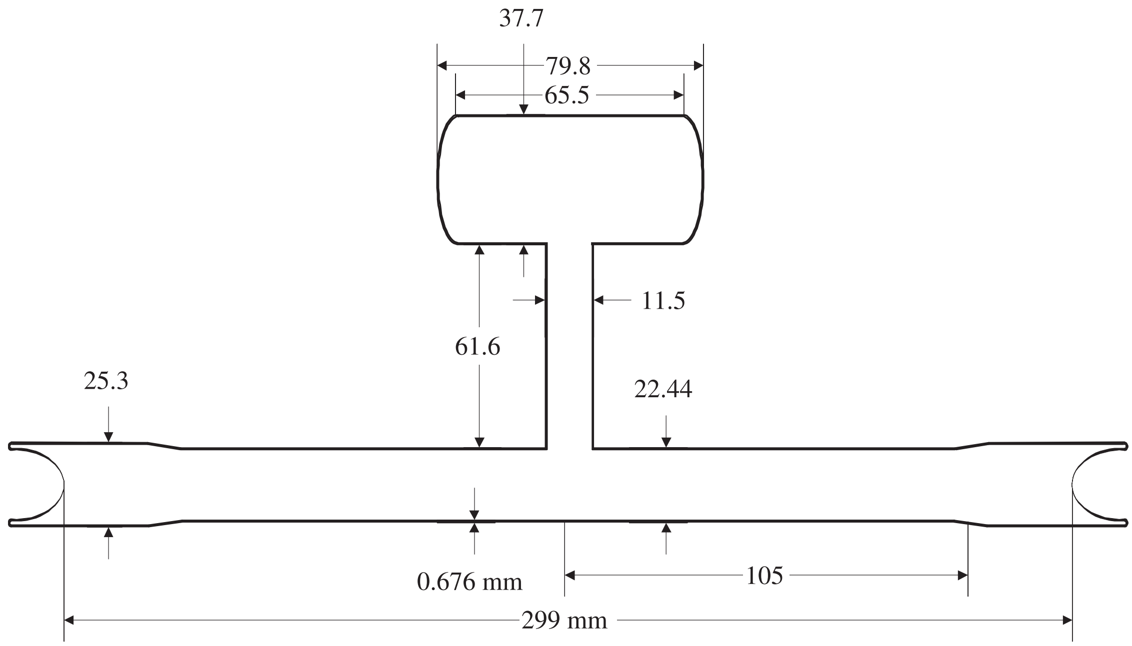

Figure 4.3: Dimensions of the target cell Picard.

be referred to as the pumping cell and the lower chamber shall be referred to as the target cell.

The most critical dimensions for the target are those of the target cell, particularly the thickness of the end windows. For the purpose of calculating the number of events that originated in the ^{3}He, the length of the cell and the thickness of the windows must be known. For the purpose of calculating the radiative corrections to a scattered electron, the shape and thickness of the target cell sidewalls must be known. For the purpose of polarimetry, the diameter of the target cell must be known accurately. The length of the target cell and the position of the flare were measured with a micrometer and are known to 0.7% (2 mm for the length of the target cell). The diameter of the target cell was also measured with a micrometer along the length of the target and both the error in the measurement and the variation of the thickness measurements were used to determine the error in the target cell diameter, which is 0.1 mm. The thickness of the target cell walls was calculated using the measurements of the target cell diameter, the measurements of the stock tubing diameter and wall thickness, and the assumption of volume conservation. It is assumed that when the stock tubing was reblown to create the target cell, the glass was not stretched, and the thickness of the wall is inversely proportional to the diameter of the target cell

Cell Name	Target Cell			Flare		Transfer Tube		Pumping Cell		
	OD	Wall	Len.	Start	OD	OD	Len.	OD	L. 1	L. 2
Dave	20.75	0.730	291	110	26.7	12.4	61.5	36.3	84.0	95.1
Riker	21.72	0.697	300	105	25.7	11.8	60.0	37.2	70.6	82.3
Bob	20.80	0.728	299	115	26.6	12.3	61.2	36.1	79.0	94.6
SMC	20.66	0.733	302	110	26.3	12.2	63.5	37.8	77.7	90.7
Generals	21.62	0.700	297	110	25.9	12.9	59.2	36.0	66.8	80.0
Hermes	20.53	0.737	295	110	26.7	11.9	62.9	37.7	74.8	89.4
Prelims	21.24	0.713	300	110	26.0	12.9	59.4	36.1	68.3	80.5
Chance	21.33	0.710	299	120	25.4	13.5	67.0	35.8	79.0	93.0
Picard	22.44	0.676	299	105	25.3	11.5	61.6	37.7	65.5	79.8
Water I	20.55	0.737	302	102	24.8	14.0	59.7	36.8	74.9	88.9
Water II	22.62	0.669	297	112	25.4	13.2	72.6	36.8	73.7	94.5
Ref Cell 1	21.20	0.712	303.5	110	25.0					
Ref Cell 2	21.70	0.689	297.4	110	25.2					
Ref Cell 3	22.10	0.685	304.3	115	24.9					
Ref Cell 4	21.30	0.711	302.3	110	25.1					

Table 4.2: Cell dimensions in millimeters.

according to volume conservation. A number of test cells were broken and their side wall thicknesses measured with a micrometer to verify this relationship. Using this assumption, the error in the wall thickness is 0.02 mm. Measurements of the dimensions of the transfer tube and the pumping cell were done using a calipers and are accurate to 0.5 mm.

The thickness of the windows was measured by three different techniques: mechanical measurements, x-ray absorption, and optically using laser interferometry. The mechanical measurements were initially performed on the cells, but were only accurate to 5%. To improve the accuracy with which the window thicknesses were known, x-ray absorption was used next. It was performed on all of the cells before the run except two, Picard and Riker. Measuring the attenuation of x-rays as they passed through the windows of the target was accurate to 3%. After the experimental run was finished, the optical method of laser interferometry which measured the interference of the light reflected from the front and back surfaces of the window as a function of laser wavelength was used. The equation for the time averaged reflected power is

$$P = A + B\sin^2\left(2\pi n\frac{t}{\lambda}\right), \tag{4.17}$$

where P is the time averaged reflected power, A and B are constants, $n = 1.52 \pm 0.01$ is the index of refraction of the glass, λ is the wavelength of the laser light, and t is the thickness of the window. An accuracy of 1% was obtained by scanning the laser wavelength over more than two periods of the sine function. Regrettably, because the method of laser interferometry was not employed until after the experimental run was over, it could not be used on those windows that were destroyed during the experimental run. This is particularly unfortunate for the target Riker, which was therefore only measured mechanically, and installed without knowledge of which window was upstream and which was downstream. For targets that were installed without knowledge of which window was upstream and which window was downstream (Riker and SMC) the window thickness quoted is the average of the two individual window thickness measurements and the error contains the difference between the two measurements as well as the error in the measurement technique that was employed. Table 4.3 gives the thickness of the target windows for the target cells and reference cells used during SLAC experiment E154 as well as the method used to measure them, with the following abbreviations: m: mechanical, x: x-ray, o: optical, b: broke in beam, and *: which window was upstream and which window was downstream is unknown.

4.3.3 Target Cell Densities and Temperatures

The density of the cells was measured carefully at the time of filling using two techniques: measurements of number and density, and pressure broadening. In the first method, the amount of ^{3}He and N_2 introduced into the cell was measured at the time of filling by determining the number of atoms that passed through a calibrated volume. Using a measurement of the pressure before and after a valve between

	Upstream Window			Downstream Window		
Cell Name	Thickness (μm)	Error (μm)	Method	Thickness (μm)	Error (μm)	Method
Dave	45.00	1.35	x,b	52.50	0.53	x,o
Riker	63.25	4.43	m,b,*	63.25	4.43	m,b,*
Bob	70.10	2.10	x,b	69.50	0.70	x,o
SMC	66.50	2.39	m,x,o,*	66.50	2.39	x,o,*
Generals	51.90	1.56	m,x,b	59.90	0.60	m,x,o
Hermes	46.90	1.41	x,b	59.00	0.59	x,o
Prelims	45.80	0.46	m,x,o	42.00	1.26	m,x,b
Chance	83.00	0.83	x,o	83.00	0.83	x,o
Picard	69.30	0.69	m,o	61.60	0.62	m,o
Ref Cell 1	58.40	1.75	x,b	46.50	1.40	x,b
Ref Cell 2	74.20	0.74	x,o	45.90	0.46	x,o
Ref Cell 3	57.30	0.57	x,o	48.10	0.48	x,o
Ref Cell 4	72.10	0.71	x,o	61.90	0.62	x,o

Table 4.3: Target cell and reference cell window thicknesses.

the calibrated volume and the target cell was opened, the number of atoms that entered the cell could be calculated using the ideal gas law and a measurement of the room temperature. Knowing the number of atoms, the volume of the cells must also be known to calculate the density. The volume of the cell was calculated using a measurement of the buoyant force on the cells when submerged in water and the density of corning 1720 glass (2.52 ± 0.02 g/cm^3). The second method measured the pressure broadening of the rubidium D1 and D2 absorption lines after the cells were filled. In the presence of ^{3}He, the width of the rubidium absorption line is broadened by 18.7 ± 0.3 GHz/amagat for the D1 line, and 20.8 ± 0.3 GHz/amagat for the D2 line [66]. For N_2, the line is broadened by 17.8 ± 0.3 GHz/amagat for the D1 line, and 18.1 ± 0.3 GHz/amagat for the D2 line [66]. The two methods are in excellent agreement and give an error in the fill density of 1%.

Of greater importance is the density of the pumping and target cells under data taking conditions in which the pumping cell was sealed inside of a hot air oven, typically at a temperature of 180°C, while the target cell was typically at an average temperature of 65°C. This temperature difference caused a nonuniform density in the cell, and better knowledge of the individual volumes was necessary to calculate the average density in the pumping cell as well as the density distribution in the target cell. To accomplish this, the volume of each part of the cell was calculated using its measured dimensions. While this method gave a result for the overall volume that was different by a few percent from the results of the buoyancy measurements, only the fraction of the overall volume contained in each part of the cell is necessary, and this quantity has a smaller error, estimated to be 1%. However, a conservative error of 3% has been assigned. Table 4.4 gives the fill densities and the fractional volumes of the target cells used.

Cell Name	^{3}He Density (amagats)	N_2 Density (amagats)	Cell Volume (cm^3)	Fractional Target Cell Volume	Fractional Pumping Cell Volume	Fractional Transfer Tube Volume
Dave	8.78	0.075	186.8	0.536	0.440	0.024
Riker	8.87	0.047	187.8	0.591	0.389	0.020
Bob	8.83	0.075	189.0	0.553	0.425	0.022
SMC	8.84	0.079	190.0	0.548	0.429	0.023
Generals	8.77	0.079	180.1	0.605	0.369	0.026
Hermes	8.74	0.079	183.9	0.547	0.431	0.022
Prelims	8.90	0.078	178.6	0.590	0.383	0.027
Chance	8.91	0.078	180.5	0.576	0.392	0.032
Picard	8.87	0.078	191.5	0.600	0.381	0.019

Table 4.4: Cell densities at temperature equilibrium and fractional cell volumes.

Calculating the density distribution then becomes a matter of measuring the temperature distribution of the cell, since the pressure in the cell is a constant. For this purpose a number of resistance temperature detectors (RTDs) were attached to the cell. One was attached to the pumping cell with heat sink compound in the hot air oven while five were attached to the target cell as shown in figure 4.4. The target cell was heated by conduction from the hot pumping cell above and cooled at the ends by a 7 liters/minute flow of ^{4}He gas. The cooling flow was necessary to remove the heat deposited in the windows by the electron beam. This lead to a temperature gradient across the target cell. Once the RTDs were calibrated, a test was made to verify that the temperature inside the cell was the same as the temperature measured by an RTD on the outside of the cell. It was found that an RTD on the outside of the cell gave a good measurement of the temperature on the inside of the cell, as measured by an RTD inserted into a cell, except in the case of the pumping cell when the pumping lasers were on. The pumping lasers deposited a significant amount of heat directly into the rubidium vapor and raised the gas temperature inside the pumping cell above the temperature of the cell walls. This effect was measured by comparing the ^{3}He NMR signal amplitudes with the lasers on and off. The NMR signal amplitude is proportional to the density, and measurements of the change in the ^{3}He NMR signal amplitude could be used to calculate the temperature difference in the pumping cell between the conditions of the lasers being on or off. Measurements of the NMR signal amplitude were taken after a period of time long enough for the two chambers to come into polarization equilibrium, but short enough that the helium polarization had not changed significantly. It was found that the lasers caused a $10 \pm 3°$C temperature offset from the measured RTD value.

The temperature distribution in the target cell can be seen in figure 4.5, along with a linear fit to the temperature distribution. Diffusion models assuming a point source of heat at the center of the cell and localized cooling at the ends lead to an exponential temperature distribution, but do not fit the data as well, most probably because the heating and cooling sources were not delta functions at the center and ends of the target cell, respectively. The density function, $n(\vec{r})$, can be found from the following equations for the pressure and the number of atoms inside the cell

$$\begin{aligned} P &= Rn\left(\vec{r}\right)T\left(\vec{r}\right) \\ N &= \int n\left(\vec{r}\right)dV. \end{aligned} \tag{4.18}$$

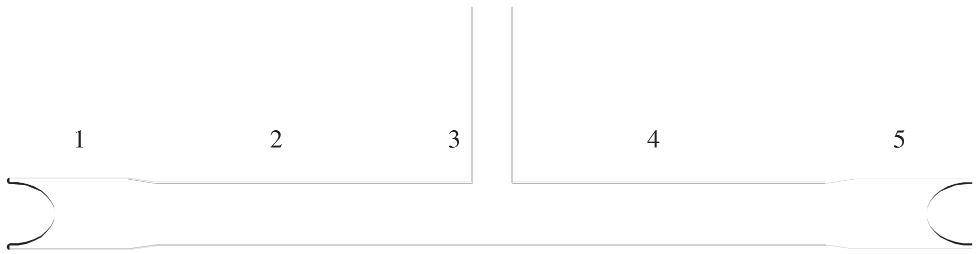

Figure 4.4: Target cell showing RTD placement.

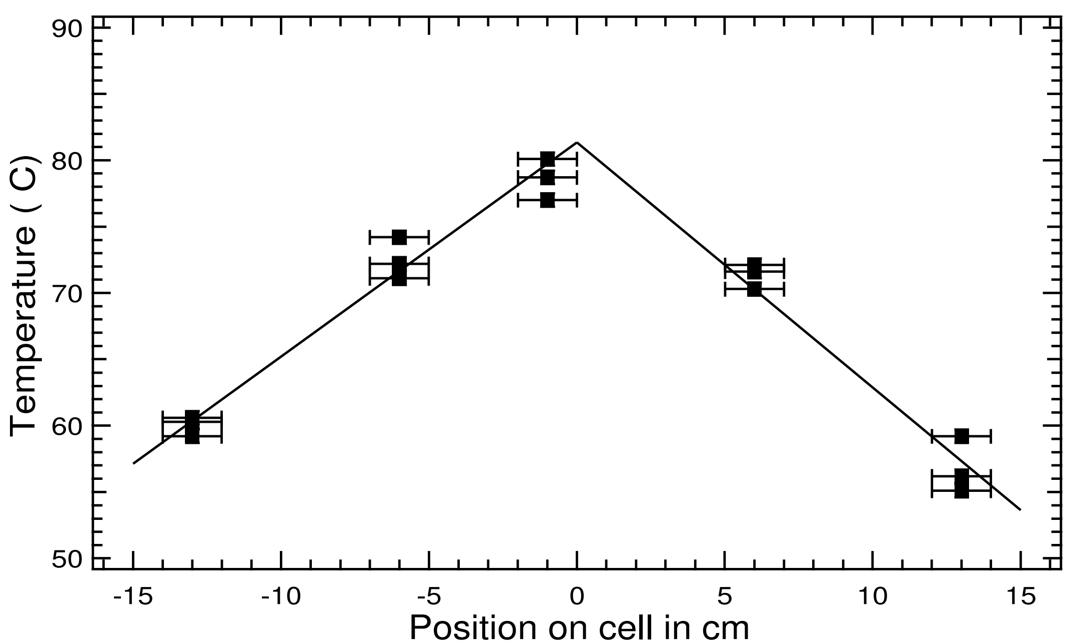

Figure 4.5: Temperature distribution of the target cell with linear fit.

In the case of a double cell in which both the target cell and the pumping cell are at a constant, uniform temperature, the solution to the above equations is

$$n_t = n_0 \left(1 + \frac{V_p}{V_0}\left(\frac{T_t}{T_p} - 1\right)\right)^{-1}$$
$$n_p = n_0 \left(1 + \frac{V_t}{V_0}\left(\frac{T_p}{T_t} - 1\right)\right)^{-1}. \tag{4.19}$$

In the case of the SLAC E154 target, the linear fit to the temperature distribution is used in the target cell to calculate the density. Results for the average density of the target and pumping cells are expressed in terms of the temperature that would be necessary to produce the average density according to equation 4.19. Also included in table 4.5 are the ratios of the densities of the individual cells to the fill density. For the target Picard, the average temperature of the target cell is 65°C (338K) using the linear fit, compared to a simple average of the 5 RTDs of 68°C (341K).

While this average density is the necessary quantity for calculating the number of events that originated in the ^{3}He, there is another weighted density that must be calculated to determine the polarization of the target. For polarimetry, the density function must be weighted by the amount of flux through the pickup coils that a dipole at that position would produce. Since the pickup coils were only 100 mm long and centrally located, more flux is produced through the pickup coils from the ^{3}He atoms located in the center of the cell than is produced from the atoms at the ends of the cell. The density in the center of the cell is lower than at the ends and the ends have more volume because of the flare. The result is that the density of the target cell as seen by the pickup coils is less than the average density of the target cell. A calculation of the flux through the pickup coils will be discussed in further detail in section 4.5.3, but the results for the calculation will be included in table 4.5. The difference in the flux through the pickup coils between using a constant density or the linear fit is approximately 2%, depending on the cell, which corresponds to a difference in the temperature of approximately 7°C. The error on the target cell temperature, T_t and the coil weighted target cell temperature, T_c are 5°C, while the error in the pumping cell temperature, T_p is 10°C.

Cell	T_t	T_c	T_p	n_t/n_0	n_c/n_0	n_p/n_0
Dave	65	71	200	1.14	1.12	0.82
Riker	68	76	200	1.12	1.10	0.81
Bob	69	77	190	1.13	1.10	0.84
SMC	63	70	185	1.13	1.11	0.83
Generals	65	73	190	1.11	1.09	0.82
Hermes	67	74	185	1.13	1.10	0.84
Prelims	67	75	200	1.12	1.10	0.81
Chance	66	74	195	1.12	1.10	0.82
Picard	65	73	180	1.11	1.08	0.83

Table 4.5: Cell temperatures and densities under data taking conditions.

4.4 Laser Pumping System

For the E142 experiment in 1992, the best available laser technology for optically pumping the 795 nm Rubidium D1 line was Argon ion laser pumped Ti:sapphire lasers. These lasers provided a significant improvement over dye lasers which had been used previously to optically pump rubidium. The Ti:sapphire laser has to be pumped with an Argon ion laser which requires a 3 phase, 480 volt electrical supply running at 60 amps per phase for maximum output, and a cooling water supply of 5 gal/min. Running at an optical output of 20 watts in the green requires an electrical input of 56 kilowatts, and the ability to remove a quantity of heat of nearly the same amount. The Ti:sapphire laser could convert this 20 watts in the green into 4–5 watts in the near infrared. Both of these lasers require a certain amount of expertise to set up and periodic tuning and cleaning. SLAC experiment E142 used 5 Argon ion and 5 Ti:sapphire lasers and required many hours of maintenance every few days by skilled operators. At the time of the experiment, the amount of total laser power necessary to pump a cell with 5×10^{22} molecules of ^{3}He was not precisely known. It was estimated to be somewhere on the order of 10-20 watts based upon experiments with smaller cells, the uncertainty arising from the extrapolation to much larger cells and higher densities [56]. A cell this large (165 cm^3 at a relative density of 7.8 amagats) had never before been attempted.

What was learned from SLAC experiment E142 was that the laser power of 20 watts provided by the 5 Ti:sapphire lasers was insufficient for a large high density spin exchange cell. Each time that a laser lost a significant amount of power, the polarization of the cell dropped. It was necessary to secure additional laser power for SLAC experiment E154. In May of 1995, a 15 watt fiber coupled laser diode array from Optopower Corporation was tested in the full target setup at SLAC. For the test, Minnehaha, the primary target cell from SLAC experiment E142 was used. Minnehaha is a 7.8 amagat cell with a volume of 165 cm^3, similar in design to the E154 target cells. Results for the spin up of the target cell Minnehaha using a single 15 W fiber coupled laser diode array can be seen in figure 4.6 along with the actual performance for the target cell during SLAC experiment E142 in 1992. Minnehaha was an exceptional cell, with a lifetime of 95 $\pm$ 5 hours. The results were outstanding and a decision to purchase a number of laser diode arrays for SLAC experiment E154 was made.

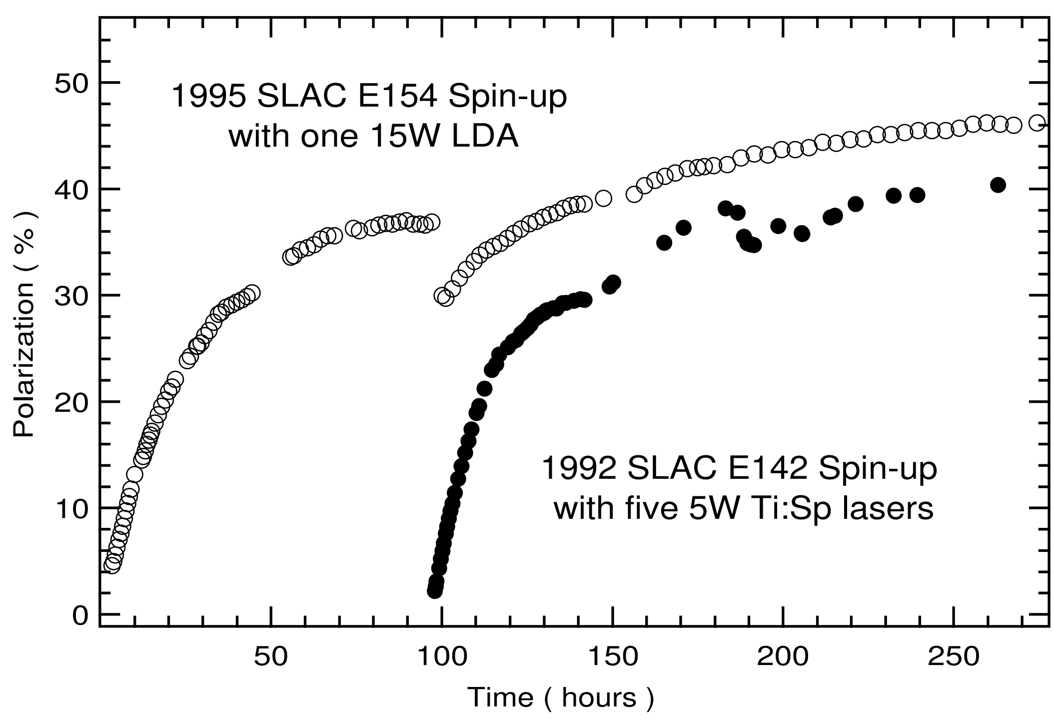

Figure 4.6: Spin up comparison for Minnehaha.

A few comments on figure 4.6 are necessary. For the laser diode array spin up, the magnetic holding field was accidently turned off at approximately 100 hours, which caused a loss of polarization. At about 150 hours, the temperature of the pumping cell, and consequently the rubidium density of the pumping cell, was optimized during the laser diode array test. The spin up using Ti:sapphire lasers began with only four Ti:sapphire lasers, the fifth was added at approximately 145 hours. The electron beam was passed through the target cell beginning at approximately 190 hours during SLAC experiment E142, and a program of optimizing the temperature (and rubidium density) was begun at that time. The electron beam was intermittent during the spin up as the experiment was getting underway.

The ability of a light source to polarize the rubidium in a high density spin exchange cell was discussed in section 4.2.1, and the optical pumping rate is given by equation 4.1. The ability of a laser diode array to produce a large γ_{opt} can be seen in figure 4.7. While the laser diode array is much broader than the Ti:sapphire laser, it is not too broad compared with the pressure broadened rubidium absorption line. A single fiber coupled diode laser array typically has 3 times the total power of a Ti:sapphire laser, so while the off-resonance light is less effective for optical pumping, it still contributes to γ_{opt}, and helps polarize the rubidium.

For SLAC experiment E154, 3 Optopower fiber coupled laser diode arrays, models OPC-A015-795-FCPS and OPC-B015-795-FCPS, were used in conjunction with 4 Spectra-Physics Argon ion and Ti:sapphire lasers, models 2040E and 3900S respectively. The laser diode arrays were set to the correct wavelength using an ILX Lightwave wavemeter, model 3900B. After being set to the correct wavelength for optical pumping, each of the laser diode arrays maintained a constant power of 15–17 watts and a constant wavelength setting. The Argon ion Ti:sapphire lasers could be tuned up to a power of 20 watts per Argon ion laser and 5 watts per Ti:sapphire laser with a sufficient amount of cleaning and mirror tuning, but were unable to maintain an output of 5 watts in the dusty environment of the laser hut. As a result, the power from the Ti:sapphire lasers was typically less than 20 watts, and on average 12 watts. The laser diode arrays were the real workhorses of the experiment.

There are a few technical difficulties that had to be addressed to implement the use of the fiber coupled laser diode arrays. The first was the large divergence of the beam at the output of the fiber. A simple method of overcoming this difficulty

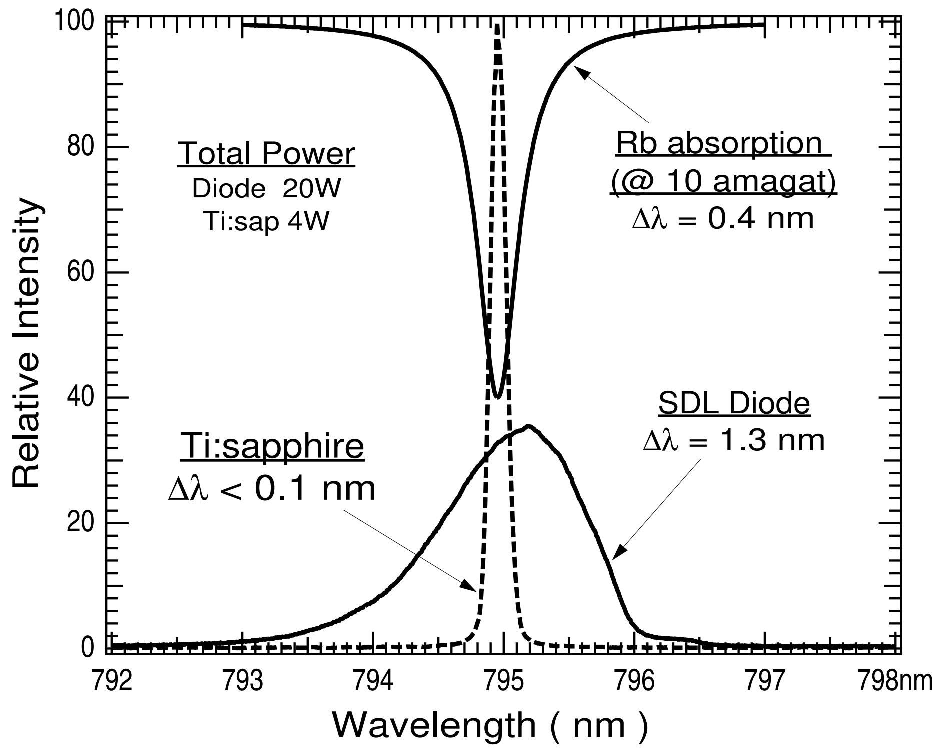

Figure 4.7: Absorption curve for rubidium broadened by 10 amagats of ^{3}He and emission profiles of Ti:sapphire lasers and laser diode arrays.

would have been to put the output end of the fiber near the pumping cell. However, this was not possible for SLAC experiment E154 due to laser safety regulations that restricted the location of the diode laser arrays to the laser hut, along with the Argon ion and Ti:sapphire lasers. The laser hut was built in 1992 to house the laser system for SLAC experiment E142, which consisted of 5 Argon ion and 5 Ti:sapphire lasers. Four of the five Argon ion lasers and four of the five Ti:sapphire lasers from SLAC experiment E142 were used for SLAC experiment E154. The laser hut was built with 3 foot thick concrete walls and served the dual purpose of protecting the lasers from the radiation in the Endstation when the electron beam was present, and of protecting personnel in the Endstation when the lasers were on. The layout of the laser hut can be seen in figure 4.8. All of the lasers sat on two 5 foot by 10 foot optical tables, and all of the laser beams were delivered from the laser hut to the scattering chamber through a 10 inch, light-tight PVC pipe. The acceptance of the PVC pipe and the mirror system in the scattering chamber necessitated a fly's eye type mirror array for delivery of the 10 laser beams to the pumping cell. There is one laser beam per Ti:sapphire laser and 2 laser beams per laser diode array, as will be described shortly.

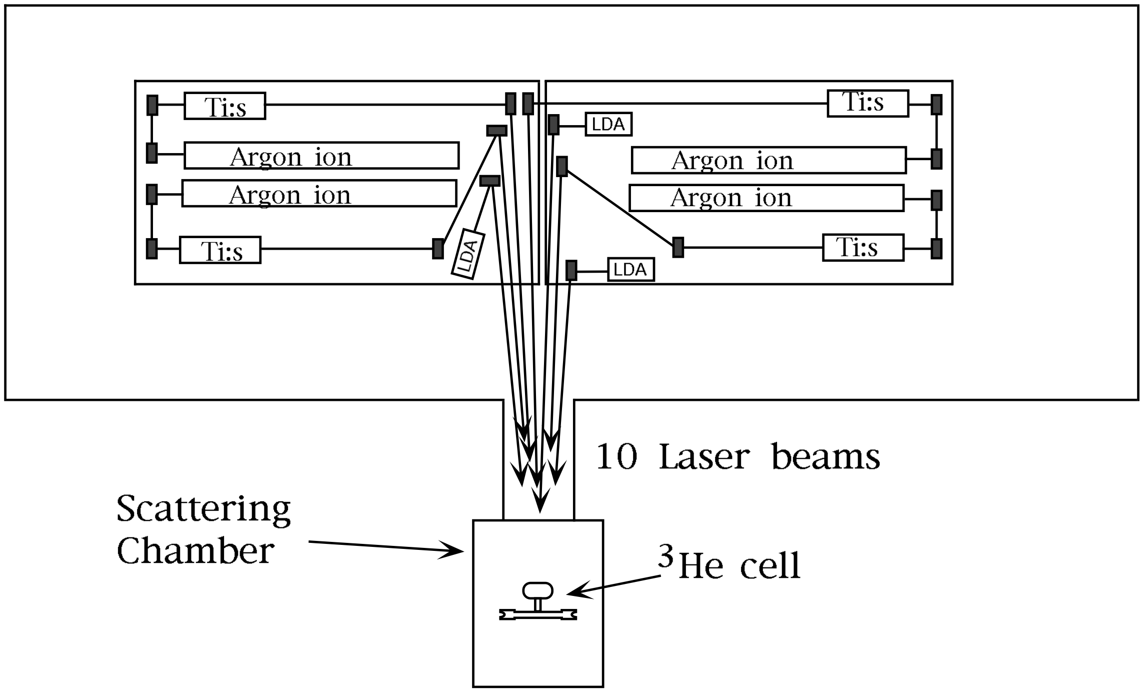

Figure 4.8: Layout of the E154 laser hut.

The full cone divergence of the fiber from the laser diode arrays was 12 degrees, as depicted in figure 4.9, and the laser safety requirement of containing the laser system in the laser hut caused the distance from the last lens to the pumping cell to be on the order of 5 meters. Simple imaging techniques were used to select the appropriate lens for collimating the output of the fiber coupled laser diode array. The size of the laser diode array fiber bundle was 1.5 mm, and the size of the pumping cell was approximately 36 mm, this required a magnification of 24, and therefore a ratio of image distance (s_i) to object distance (s_o) of 24. Using the simple lens equation, $f^{-1} = {s_i}^{-1} + {s_o}^{-1}$, gives a focal length approximately equal to the object distance. The lens chosen had a focal length of 175 mm, and was placed a distance of 182 mm from the end of the fiber bundle, as depicted in figure 4.9. Because the size of the beam spot had grown to 38 mm by the time the beam reached the lens at 182 mm, a 2 inch diameter lens was used for SLAC experiment E154.

The reason a lens with a focal length of 175 mm was chosen was because of the polarization of the light at the output of the fiber bundle. Each of the approximately

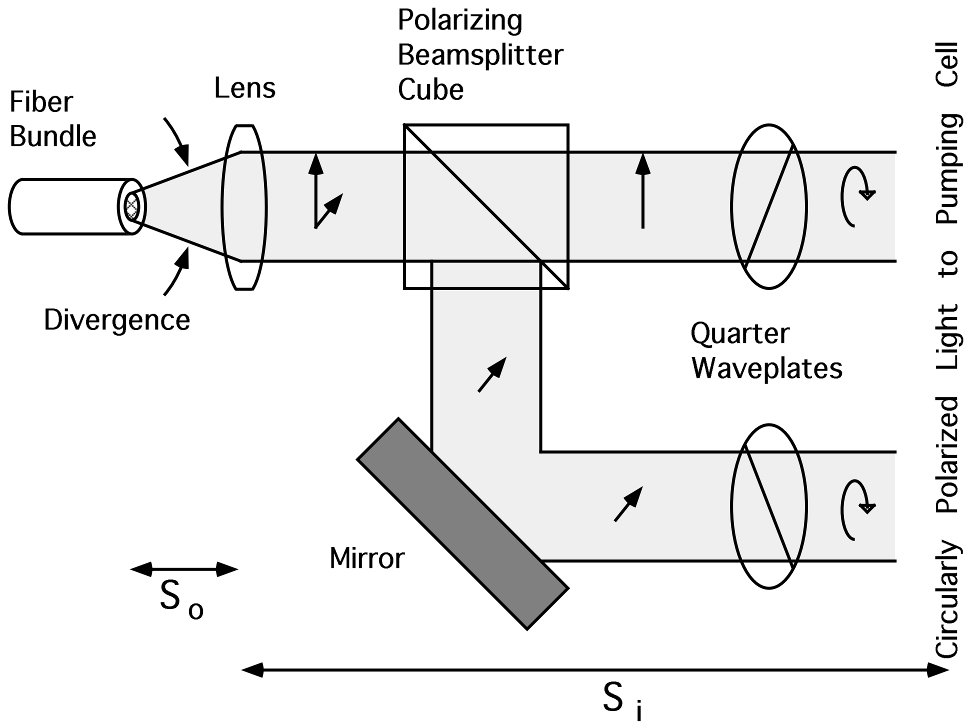

Figure 4.9: Optics used with the laser diode arrays.

20 individual diode lasers stripes in the diode laser array is coupled into a single optical fiber and then the optical fibers are bundled together. The optical fiber used is not polarization preserving, nor are the fibers bundled in a manner that prevents them from twisting with respect to each other. The result is that the output of the optical fiber bundle is not 100% linearly polarized, and closer to 85%. This posed a problem since a quarter waveplate could not then be used to produce 100% circularly polarized light. The solution was to separate the two linear polarizations in the output of the fiber bundle and then convert each into circularly polarized light through the use of a quarter waveplate. To accomplish this, a linearly polarizing beam splitting cube was inserted into the output of the fiber bundle after the collimating lens. The linearly polarizing beam splitting cube was only efficient at separating the two linear polarization states for light at normal incident, and insertion of the linearly polarizing cube before the lens where the laser light was highly divergent proved to be inefficient. The linearly polarizing beam splitting cube worked most efficiently on the output of the fiber bundle after the beam was allowed to expand to the size of the pumping cell and then collimated, as was the case with a 175 mm focal length lens.

4.5 Measurement of Target Polarization

The polarization of the ^{3}He target was measured during the run using the technique of adiabatic fast passage nuclear magnetic resonance, to be abbreviated AFP–NMR or simply AFP. This technique uses two magnetic fields, one large and nearly static to give the spins a quantization axis, and one perpendicular to the first, oscillating near the Larmor frequency of the ^{3}He nuclei to produce a rotating effective field that can be used to flip the nuclear spins. The holding field is swept from a value just below resonance to a value just above resonance, slowly enough so that the ^{3}He spins remain aligned with the effective field, thus *adiabatic*, but also fast enough so that the nuclei do not dephase during *passage* through resonance, thus *fast*. During the passage through resonance, the precessing magnetization of the ^{3}He nuclei produce an oscillating magnetic flux through a pair of pickup coils mutually orthogonal to the holding field coils and the RF coils. The measured voltage induced in the pickup coils is proportional to the ^{3}He polarization and used to monitor the target polarization. In principle, this proportionality constant may be calculated. In practice, the ^{3}He AFP signal is calibrated with an AFP measurement of a sample of water and with a measurement of the electron paramagnetic resonance (EPR) shift of the rubidium Zeeman transition due to the ^{3}He polarization. These calibrations will be discussed in section 4.6.

4.5.1 Adiabatic Fast Passage

This section will describe the technique of AFP using a classical description. It can be shown that the quantum mechanical treatment for the coupling of the nuclear spins with an applied magnetic field produces an equation of the same form as the classical description for the z component. A more detailed description of the theory of nuclear magnetism and the techniques of nuclear magnetic resonance can be found in Abragam [67].

Classically, a magnetic moment $\vec{M}$ in a magnetic field $\vec{H}$ experiences a torque equal to the time derivative of the angular momentum,

$$\frac{d\vec{M}}{dt} = \gamma \vec{M} \times \vec{H}, \tag{4.20}$$

where γ is the gyromagnetic ratio, $\vec{M}$ is the bulk magnetization, and $\vec{H}$ is the applied field. However, one must also include the rate of decay of the magnetization back to the thermal equilibrium value. This is done using the time constants for longitudinal relaxation and transverse relaxation, T_1 and T_2, respectively. The magnetization in the rotating frame then evolves according to the modified Bloch equations

$$\begin{aligned} \frac{dM_x}{dt} &= \gamma M_y (H - H_0) - \frac{(M_x - \chi H_1)}{T_2} \\ \frac{dM_y}{dt} &= -\gamma M_x (H - H_0) + \gamma M_z H_1 - \frac{M_y}{T_2} \\ \frac{dM_z}{dt} &= -\gamma M_y H_1 - \frac{(M_z - \chi H)}{T_1}, \end{aligned} \tag{4.21}$$

where $H_0 = \gamma\omega_0$ and ω_0 is the frequency of the oscillating field. The magnetic holding field H is in the z direction, the oscillating field H_1 is in the x direction, and when the RF field is off and the DC field is constant, the magnetization has a thermal equilibrium value of $M = \chi H$.

For a SLAC experiment E154 target cell with a lifetime of greater than 40 hours, $(\gamma H_1 T_{1,2})^{-1} < 10^{-4}$ and the terms containing T_1 and T_2 can be ignored. In this case an analytical solution is possible for the flux through the pickup coils. In the case of a cell filled with water, as was used in one of the methods to calibrate the target polarization, the proton relaxation times are less than $(\gamma H_1)^{-1}$ and a correction must be applied. This will be discussed in section 4.6.2.

The form of the magnetic fields is

$$\begin{aligned} \vec{H} &= (H_0 + \alpha t)\hat{z} \\ \vec{H}_1 &= 2H_1 \cos(\omega_0 t)\hat{x}, \end{aligned} \tag{4.22}$$

where ω_0 is the frequency of the oscillating field and H_0 is the resonance field given by $H_0 = \gamma\omega_0$. A sweep of the magnetic holding field $H(t)$ begins at a time $t_i < 0$ and ends at a time $t_f > 0$, passing through resonance at $t = 0$. A solution can be found by transforming into a coordinate system that is rotating with the applied RF field around the z axis. In this frame, the RF field has the form

$$\left(\vec{H}_1\right)_\pm = H_1 \hat{x}'_\pm \quad , \quad \hat{x}'_\pm = \cos(\omega_0 t)\hat{x} \pm \sin(\omega_0 t)\hat{y} \tag{4.23}$$

In the rotating frame, the effective field sensed by the ^{3}He nuclei is

$$\vec{H}_{eff} = (H - H_0)\,\hat{z} + H_1 \hat{x}' \tag{4.24}$$

provided that the RF field strength is small enough to avoid the Bloch-Siegert frequency shift associated with the counter rotating component of H_1 [68]. For SLAC experiment E154, the shift is on the order of ${H_1}^2/4{H_0}^2 \approx 10^{-6}$.

The magnetic holding field $H(t)$ begins at a value below resonance such that $|H(t) - H_0| >> H_1$ and the effective field is almost parallel to the $\hat{z}$ axis. The field is then swept to a value above resonance slowly enough for the spins to follow the effective field adiabatically. At the end of the sweep, the value of $(H(t) - H_0)$ has switched sign and the spins are now aligned nearly parallel to the $\hat{z}$ direction but in the opposite direction. The measured AFP signal in the pickup coils is proportional to the transverse component of the magnetization

$$S(t) \propto \left(\vec{M}\right)_\perp = M\frac{\left(\vec{H}_{eff}\right)_\perp}{\left|\vec{H}_{eff}\right|} = M\frac{H_1}{\sqrt{\left(H(t) - H_0\right)^2 + {H_1}^2}}. \tag{4.25}$$

To minimize losses during AFP sweeps, the speed with which the magnetic holding field was swept was optimized between the two AFP constraints. To satisfy the adiabatic condition, the rate of change in the effective magnetic field must be much less than the Larmor frequency of the spins. The maximum rate of change of H_{eff} occurs at resonance and has a value of $\dot{H}/H_1$. The Larmor frequency in an effective field of strength H_1 is $\omega_1 = \gamma H_1$. The relaxation of the spins is also greatest near the resonance where the effective field is smallest, and satisfying fast passage means that the sweep must be fast compared to the relaxation time of the spins in a rotating field at resonance, T_{1r}. For a dense gas, Abragam gives the relaxation rate as $1/T_{1r} = D\left|\vec{\nabla}H_z\right|^2/{H_1}^2$, where D is the diffusion constant and $\left|\vec{\nabla}H_z\right|$ is the magnitude of the magnetic field gradient [67]. This gives the following inequalities for AFP in general and in particular, estimates for the SLAC experiment E154 ^{3}He target

$$\begin{array}{ccccc} D_{He}\dfrac{\left|\vec{\nabla}H_z\right|^2}{{H_1}^2} & << & \dfrac{\dot{H}}{H_1} & << & \gamma H_1 \\ 0.00075\ \mathrm{s}^{-1} & << & 16.6\ \mathrm{s}^{-1} & << & 233.5\ \mathrm{s}^{-1}. \end{array} \tag{4.26}$$

The sweep rate was optimized and AFP losses were measured to be approximately 0.1% per AFP measurement, which consisted of two sweeps, one from low field to high field and then one from high field to low field. The second sweep was used to return the spins to the original energy state after the polarization measurement.

4.5.2 Target NMR Polarimetry Apparatus

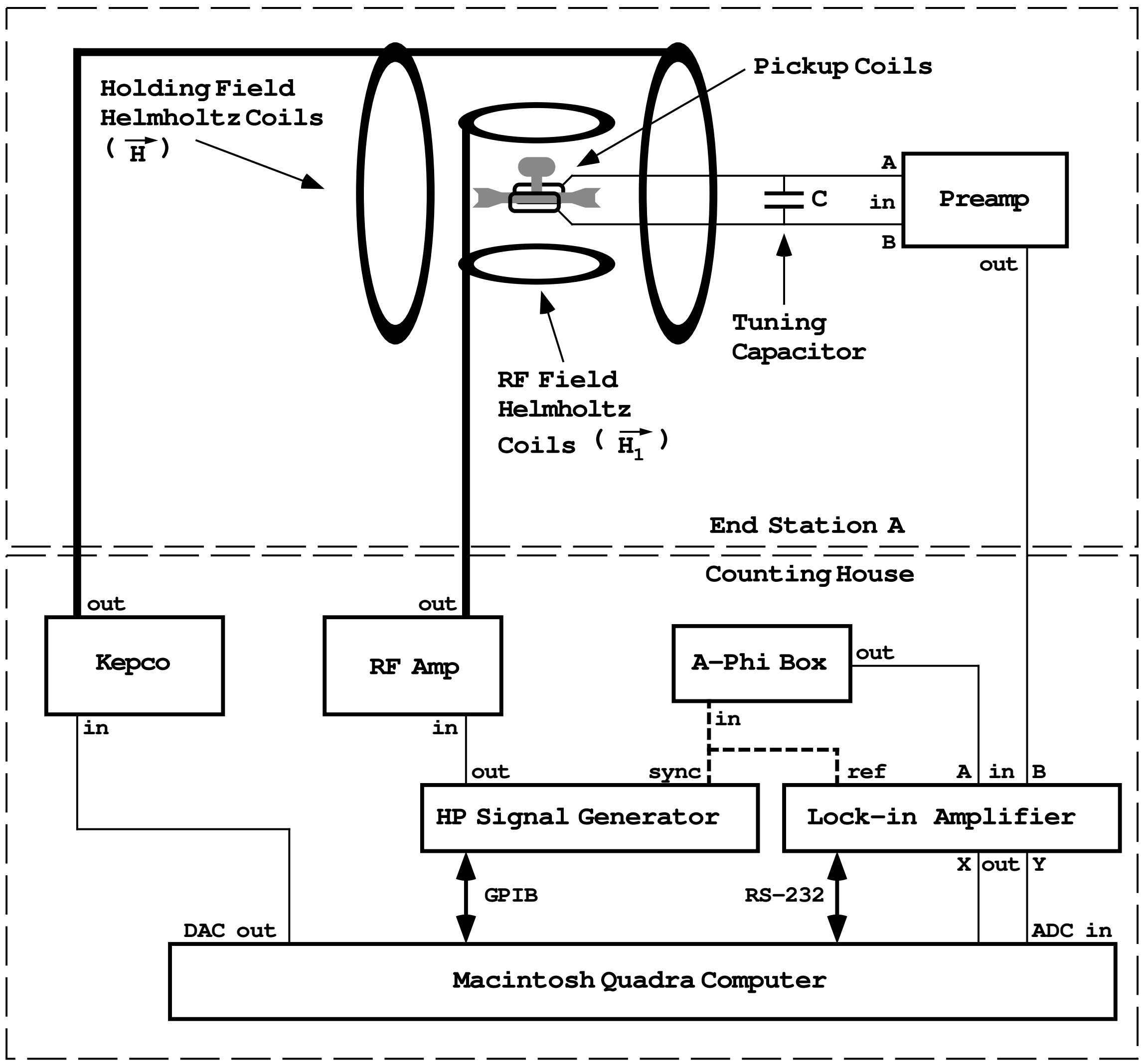

Figure 4.10: Experimental apparatus used for target polarization measurements.

The experimental setup for SLAC experiment E154 target polarimetry is shown in figure 4.10. It is similar to the experimental apparatus used for SLAC experiment E142 [28, 45], with the two primary upgrades being a faster computer and a better pickup coil design. The target polarization data acquisition system was controlled by an Apple Macintosh Quadra personal computer running IGOR Pro software from WaveMetrics, INC. Installed in the Macintosh were a National Instruments GPIB interface board and a GW Instruments MacAdios II ADC/DAC board. The magnetic holding field was swept up and down through resonance by sending a linear ramp from the DAC out to the Kepco power supply, model BOP 36-12M. The Kepco power supply drove the current through the holding field Helmholtz coils which had a diameter of 1.45 m and were mounted such that the magnetic field produced was co-linear with the electron beam direction. The RF field coils had a diameter of 44 cm and were mounted orthogonally to the holding field coils, with the magnetic field in the vertical direction. A 92 kHz sine wave was produced with an HP3325B function generator controlled by the target computer through a GPIB interface. This RF wave was then amplified by an ENI RF power amplifier, model 2100L, and sent to the RF field coils. For stabilization, the RF was typically turned on a few seconds before the holding field was swept and then turned off after the sweep. The sync output of the HP signal generator was used as a reference for both the lockin amplifier and the Aϕ box, which produced a sine wave with an adjustable amplitude and phase. The Kepco power supply and the RF power amplifier were situated with the target computer in the Counting House, and separated from the target in the Endstation by approximately 100 m of cable. The details of the polarized ^{3}He target for SLAC experiment E154 can also be found in the E154 target polarization technical note [69].

For SLAC experiment E142, the error on the target polarization was limited by the signal to noise ratio of the water signals used for calibration. To improve the signal to noise ratio, the pickup coils were redesigned to bring them closer to the target cell so that they would capture more of the flux, resulting in an improvement of the signal to noise ratio by a factor of 4. The pickup coils for E142 were also problematic in that they were in the acceptance of one of the spectrometers for the upstream portion of the target, including the upstream window from which approximately 1/3 of the counts originated in E142. For E154, the downstream ends of the pickup coils were bent outwards to remove them from the acceptance of the spectrometers, as is shown in figure 4.11.

The pickup coils contained 150 turns and were center tapped and tuned with a capacitor to a resonance value of 101.5 kHz. An SRS preamplifier, model SR560, was placed next to the target in the Endstation, and used to drive the 100 m cable from the Endstation to the Counting House. In the Counting House, the signal was sent into one of the differential inputs of the SRS lockin amplifier, model SR530. The pickup coils were mounted on an adjustable table and centered about the target

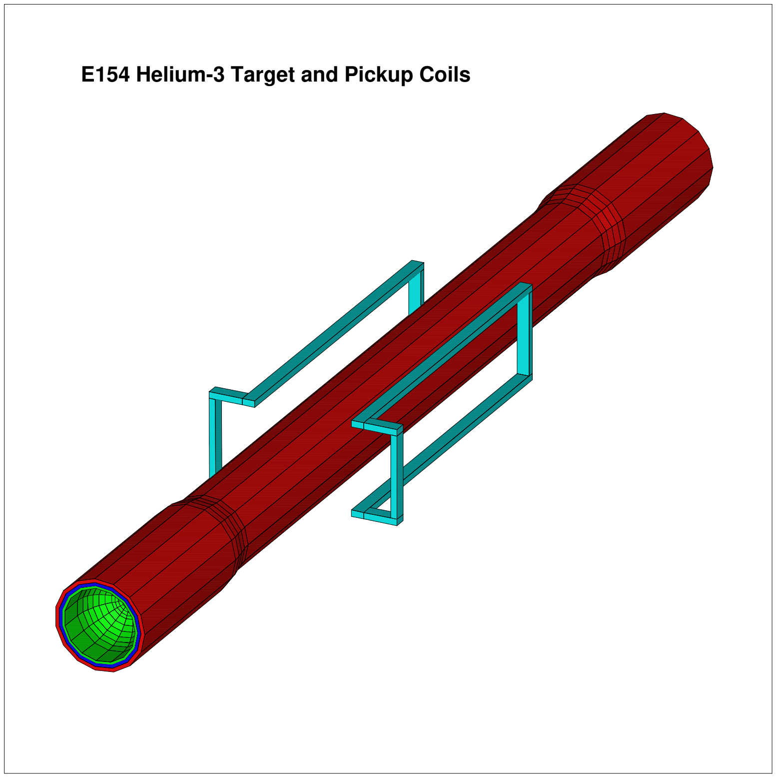

Figure 4.11: Lower chamber of the target and NMR pickup coils.

Parameter	^{3}He value	Water value
Resonance frequency	92.0 kHz	92.0 kHz
Resonance field	28.37 G	21.61 G
Sweep starting field	18.32, 8.80 G	17.59 G
Sweep ending field	35.92 G	24.92 G
Sweep rate	1.19 G/s	1.19 G/s
Delay between sweeps	0 s	15 s
RF field strength	72 ± 2 mG	86 ± 3 mG
Lockin amplifier time constant	10 ms	10 ms
Digitizing Rate	15 ms	15 ms

Table 4.6: AFP parameters.

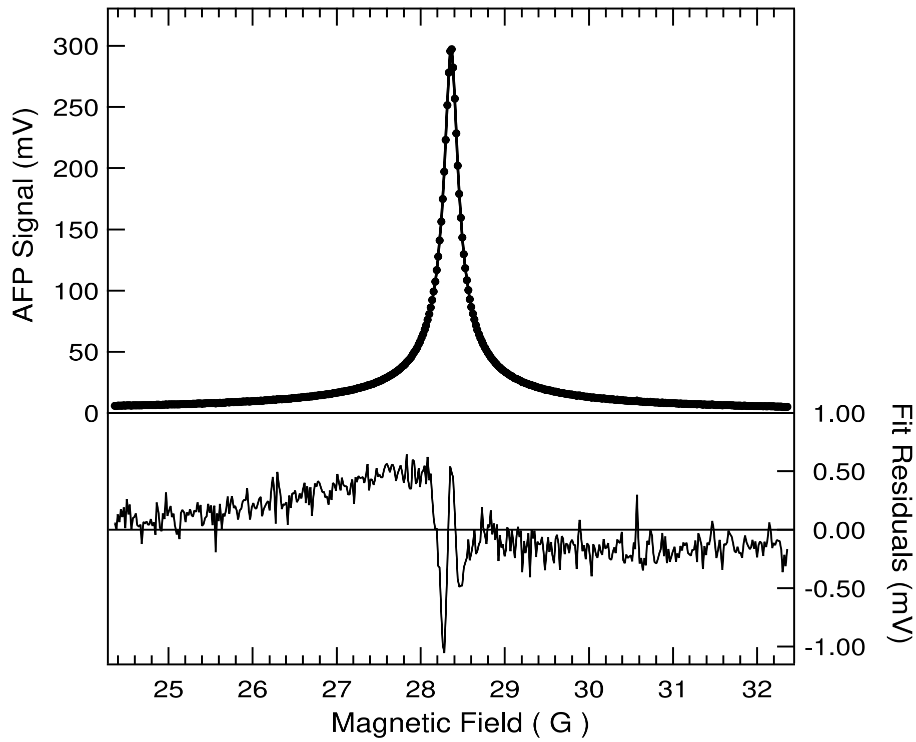

Figure 4.12: ^{3}He AFP signal, Lorentzian fit and residuals.

such that the direct pickup was minimized. The remaining direct pickup from the RF drive field was canceled by adding a sine wave of adjustable amplitude and phase, produced by an Aϕ box, to the other differential input of the lockin amplifier. Both of the output channels of the lockin amplifier were digitized and recorded, even though the phase of the lockin amplifier was adjusted to put all of the signal into one channel. Communication with the lockin amplifier was performed using an RS-232 connection driven by an IGOR Pro software module. Table 4.6 lists a number of the parameters for AFP of both ^{3}He and water (see section 4.6). The 15 second delay between sweeps for water allows the proton spins to return to thermal equilibrium, and the lower starting field value of 8.80 G was used towards the end of the run. Figure 4.12 shows a typical ^{3}He AFP signal, a fit to the shape (4.25), and the residuals of the fit. Five parameters were used in the fit: the height, width and center of the peak as well as constant and linear background components. The residuals of the fit are quite small, and the height of the signal can be extracted with a fractional error of less than 0.2%. The structure of the residuals is partly due to the shaping of the signal by the lockin amplifier time constant and to the magnetic field inhomogeneities, as will be described shortly.

4.5.3 Calculation of AFP Signal

The conversion from an AFP signal height to a target polarization can be more easily understood by breaking the problem up into two parts. The first step is to understand how the AFP signal height relates to the flux that is passing through the pick-up coils. The second step is to understand how the flux that is passing through the pick-up coils is related to the polarization of the target. For a given flux passing through the pick-up coils, a signal is generated in the pick-up coil circuit with a gain determined by the Q of the circuit. This signal is then amplified by the preamplifier, which sits in the Endstation next to the target and sent up to the Counting House. In the Counting House the signal is filtered and amplified by the lockin amplifier and then sent to the ADC board in the MacIntosh. The ^{3}He AFP signal is then given by:

$$S_3 = G_{lockin3} G_{preamp3} G_{coil3} \Phi_3, \tag{4.27}$$

where Φ is the flux through the pickup coils and G stands for the gain and the subscript 3 refers to ^{3}He. In the case of water, the 3 will be replaced with a W (see section 4.6.1).

The total flux that passes through the pick-up coils can be found by integrating the flux from a dipole of size $\mu P n \mathrm{d}V$ in a volume element $\mathrm{d}V$ over the volume of the double cell, where μ is the magnetic moment, P is the polarization, and n is the density of dipoles (see figure 4.13).

$$\Phi_3 = \int_{V_3} \int_{A_{coil}} \mu_3 B(\vec{r}, \vec{r}\,') P_3(\vec{r}) n_3(\vec{r}) d^3\vec{r} dA'. \tag{4.28}$$

The coupling constant $B(\vec{r}, \vec{r}\,')$ is the flux from a dipole of unit magnitude at position $\vec{r}$, through a surface area dA' of the pick-up coils at position $\vec{r}\,'$. This integral can of course be calculated, but it has an uncertainty of approximately 5% based on our knowledge of all of the appropriate dimensions. This error was avoided by calibrating the AFP setup with either a water cell or with an EPR technique. For the water calibration, the integral is calculated for both ^{3}He and water; the calibration is then sensitive only to the relative error.

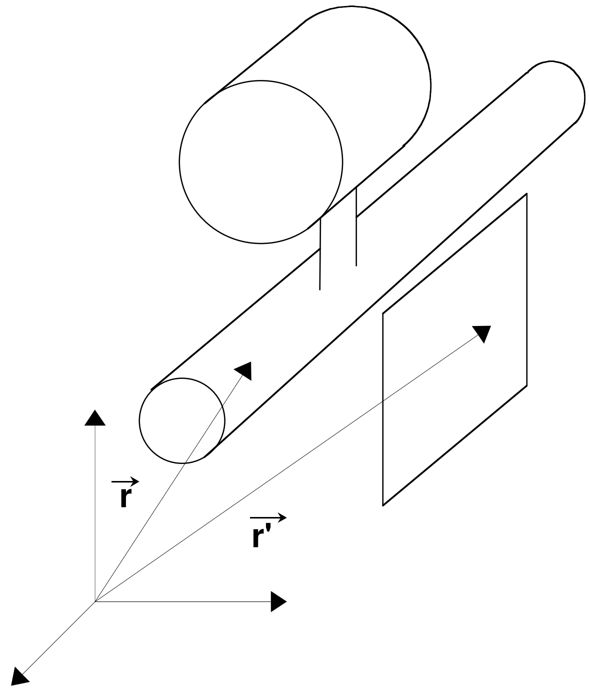

Figure 4.13: Coordinate system for target cell and pickup coils.

Given a model for the polarization and density in the target and pumping cells, the equation for Φ_3 can be rewritten as the sum of integrals over the separate cell volumes. In this case, the integral over the volume of the target, V, will be divided into two integrals, one over V_P, the volume of the pumping cell, and one over V_T, the volume of the target cell. It will be assumed that the polarization is uniform in each chamber of the cell: $P_3(\vec{r}_p) = P_{3p}$ in the pumping cell and $P_3(\vec{r}_t) = P_{3t} = P_{3p}D_{tt}$ in the target cell. The depolarization coefficient D_{tt} is primarily due to the finite transfer time for the polarization from the pumping cell to the target cell. This produces a slightly lower polarization in the target cell and will be discussed in more detail later. This is a reasonable assumption since the mixing time due to gas collisions in either the pumping cell or the target cell is much shorter than the spin exchange time. The density in the pumping cell will be assumed uniform: $n_3(\vec{r}_p) = n_{3p}$, which is reasonable since the pumping cell is far from the pickup coils. However, the target cell has a density gradient that cannot be neglected and the density in the target cell is: $n_3(\vec{r}_t) = n_{3t} + \delta n_{3t}(\vec{r})$, where n_{3t} is the average target density. The term $(1 + \delta n_{3t}(\vec{r})/n_{3t})$ equals the ratio of the actual density in the target cell to the average density. It is a necessary correction since the integral for Φ_3 weights the central third of the target cell, between the pick-up coils, much more heavily than the ends of the target cell. However, the magnitude of $\delta n_{3t}(\vec{r})/n_{3t}$ is much smaller than 1 at all points and $\int_{V_{3t}} \delta n_{3t}(\vec{r}) = 0$.

Putting all of this together gives

$$\begin{aligned}
\Phi_3 &= \mu_3 P_{3t} n_{3t} \int_{V_{3t}} \int_{A_{coil}} B(\vec{r}, \vec{r}\,') d^3\vec{r} dA' \\
&+ \mu_3 P_{3t} \int_{V_{3t}} \int_{A_{coil}} \delta n_{3t}(\vec{r}) B(\vec{r}, \vec{r}\,') d^3\vec{r} dA' \\
&+ \mu_3 P_{3p} n_{3p} \int_{V_{3p}} \int_{A_{coil}} B(\vec{r}, \vec{r}\,') d^3\vec{r} dA'.
\end{aligned} \tag{4.29}$$

The double integral of $B(\vec{r}, \vec{r}\,')$ is known as the filling factor for the cell,

$$\begin{aligned}
\eta_3 &= \int_{V_3} \int_{A_{coil}} B(\vec{r}, \vec{r}\,') d^3\vec{r} dA' \\
&= \int_{V_{3t}} \int_{A_{coil}} B(\vec{r}, \vec{r}\,') d^3\vec{r} dA' + \int_{V_{3p}} \int_{A_{coil}} B(\vec{r}, \vec{r}\,') d^3\vec{r} dA'.
\end{aligned} \tag{4.30}$$

Making some substitutions and completing volume integrals gives

$$\begin{aligned}
\Phi_3 &= \mu_3 P_{3t} n_{3t} \eta_3 + \mu_3 P_{3t} \int_{V_{3t}} \int_{A_{coil}} \delta n_{3t}(\vec{r}) B(\vec{r}, \vec{r}\,') d^3\vec{r} dA' \\
&+ \mu_3 \left(P_{3t} {D_{tt}}^{-1} n_{3p} - P_{3t} n_{3t} \right) \int_{V_{3p}} \int_{A_{coil}} B(\vec{r}, \vec{r}\,') d^3\vec{r} dA'.
\end{aligned} \tag{4.31}$$

Defining Δ_T and Δ_P as the corrections to the ^{3}He flux gives

$$\Delta_T = \left(\frac{1}{\eta_3}\right) \int_{V_{3t}} \int_{A_{coil}} \frac{\delta n_{3t}(\vec{r})}{n_{3t}} B(\vec{r}, \vec{r}\,') d^3\vec{r} dA' \tag{4.32}$$

$$\Delta_P = \left(\frac{n_{3p}}{D_{tt} n_{3t}} - 1\right) \left(\frac{1}{\eta_3}\right) \int_{V_{3p}} \int_{A_{coil}} B(\vec{r}, \vec{r}\,') d^3\vec{r} dA'. \tag{4.33}$$

The relation between the flux through the pick-up coils for ^{3}He and the polarization inside the target cell is then

$$\Phi_3 = \mu_3 P_{3t} n_{3t} \eta_3 \left(1 + \Delta_T + \Delta_P\right). \tag{4.34}$$

The correction terms Δ_T and Δ_P are small compared to one, with a magnitude of 0.010–0.025. The correction term Δ_T is negative and Δ_P is positive. It should be noted however, that they are slightly cell dependent, due to the slightly different geometries of the SLAC experiment E154 target cells.

Combining equations 4.27 and 4.34 gives the relationship between the AFP signal and the target polarization,

$$S_3 = G_{lockin3} G_{preamp3} G_{coil3} \mu_3 P_{3t} n_{3t} \eta_3 \left(1 + \Delta_T + \Delta_P\right). \tag{4.35}$$

Using the dimensions, densities and positions of the SLAC experiment E154 target cells, as well as the dimensions, position and number of turns of the pickup coils, the value of the filling factor, η, and the correction terms Δ_T and Δ_P can be calculated by numerical integration. While this method is accurate to approximately 5%, its true value lies in its usefulness at calculating the dependence of the flux on the various target parameters. The absolute scale is then set by a measurement of the flux from a water cell whose thermal polarization is known, and whose correction terms Δ_T and Δ_P are equal to zero. The most important quantity is the diameter of the target cell, because the flux through the pickup coils increases as the square of the target cell diameter.

Before giving the results of the numerical integration of η, Δ_T, and Δ_P, the remaining quantities necessary for the integration, D_{tt} and the relative position of the cells with respect to the pickup coils will be discussed. The value of the depolarization coefficient D_{tt} is approximately 0.97 and is discussed in greater detail in the appendix. It is not an important quantity for the flux calculation since the size of the correction term Δ_P is only 0.01–0.02. However, it is an important quantity for the EPR calibration and will discussed in section 4.6.4.

All of the cells (^{3}He and water) were placed within 1 mm of the center of the pickup coils when installed in the scattering chamber. The water cells remained where they were installed, but the ^{3}He cells moved in a reproducible fashion under two conditions: the heating of the scattering chamber caused by the flow of hot air to the pumping cell oven and the pumping down of the scattering chamber to rough vacuum. Both of these conditions lowered the target cell by lowering the hanger in which the target cell was mounted. The hanger included a large diameter plastic rod that passed through a teflon bushing to a motor mounted above the scattering chamber. The teflon bushing included a viton o-ring seal. In the case of the heating of the scattering chamber, the weight of the target pulled the hanger down, while in the case of the vacuum, the evacuation of the scattering chamber sucked the rod down further into the scattering chamber. Both of these effects were highly reproducible and were measured after the run with all three of the surviving cells, Picard, SMC and Chance. By using a polarized target, the flux from the cell could be measured as a function of position by moving the target up and down via the motor and the target hanger. The data near the maximum are well described by a parabola. In this way it was found that the targets were typically 2.7 ± 0.3 mm below the center. This resulted in a reduction of the AFP signal by approximately 3% of it's value. Using a micrometer, no motion of the cells was detected in the horizontal direction, and any such motion would cancel to first order due to the symmetry of the two pickup coils.

Two measurements were made with the water cells to check the accuracy of the flux calculation. The first was a measurement of the ratio of the flux from a water cell with the entire water cell full of water and then with the target cell full of water and the pumping cell empty. The calculated ratio agrees with the measured ratio to 1.2%, and the measured ratio has an uncertainty of 1.4%. The second measurement was the ratio of the flux from the two different water cells. The two water cells had very different target cell diameters and the calculated ratio for the flux is 1.25, while the measured ratio is 1.26 ± 0.02. For both of these measurements, the calculation predicts the change in flux as a function of target dimensions, particularly with target cell diameter.

The overall scale of the calculation was checked by comparing the value of the measured signal with the calculated value. However, in order to make this comparison, a number of additional effects will have to be considered. These are: the gains of the pickup coils, the preamplifier and the lockin amplifier, the loading of the output of the preamplifier by the 100 m cable, and the shaping of the signal by the magnetic field inhomogeneities. The Q curve of the pick-up coils was periodically measured during the run using an excitation loop. The voltage induced in the pick-up coils as a function of frequency can be described by

$$V(\nu) = \frac{A\nu}{\sqrt{\left(\left(\frac{\nu}{\nu_0}\right)^2 - 1\right)^2 + \frac{1}{Q^2}}}, \tag{4.36}$$

where A is an arbitrary constant and the additional factor of ν in the numerator comes from the inductive coupling between the pick-up coils and the excitation loop. The absolute size of the circuit gain at 92 kHz was measured to be 5.533± 0.05 while the coils were cold, as was the case for a measurement of the polarization of a water cell. When the coils were hot, as was the case for a polarized ^{3}He target cell, the gain of the circuit was measured to be 5.583± 0.05. The variation of the gain of the LC circuit during the run was 0.5%.

The gain of the preamplifier was set to 1 for ^{3}He and to 20 for water, with a linearity of 0.5%. The BNC cable running from the preamplifier in the Endstation to the lockin amplifier in the Counting House loaded the output of the preamplifier which has an output impedance of 50Ω. At 92 kHz, the cable can be treated as a capacitor with a capacitance of 30 pF/ft. The cable was connected to the 600Ω output of the preamplifier, and the signal was reduced by 3±1% due to the loading by the cable.

The gain of the lockin amplifier was set to 10 for ^{3}He and to 200 for water, with a linearity of 0.5%. However, the 10 ms time constant on the output of the lockin amplifier modified the shape of the signal and reduced the measured value of the peak height. The effect of the lockin amplifier time constant can be accurately modeled using

$$S\left(t\right) = \int_{-\infty}^{t} \frac{dV(t')}{dt'} e^{-(t-t')/\tau} dt', \tag{4.37}$$

This integral was evaluated on Mathematica for $\tau = 10$ ms. The height of the signal is reduced by 0.5% for water and by 0.7% for ^{3}He. The residuals of the fit are 0.2%. This effect will be included in the gain of the lockin amplifier for ^{3}He and water.

The field inhomogeneity causes the spins in different parts of the cell to come into resonance at different times during the sweep, which broadens the signal and reduces its height. The dB_z/dz component of the gradient causes the biggest effect, because the cell is elongated along z. The modified signal is

$$S\left(t\right) = \int \frac{H_1}{\sqrt{H_1^2 + (\alpha t - b)^2}} g\left(b\right) db, \tag{4.38}$$

where $g(b)$ gives the relative number of the spins experiencing a gradient field b. For a linear gradient in the z direction, a square pulse distribution extending from $-b_0$ to b_0 can be used. b_0 can be determined by studying the height of the AFP signals as a function of H_1. This was done for Picard and Chance over a range of

H_1 from 55 to 88 mG. The data first have to be corrected for the shaping due to the lockin amplifier time constant by evaluating the integral (equation 4.37). The analysis of the data gives $b_0 = 18 \pm 5$ mG or roughly $dB_z/dz = 3.6$ mG/cm. When the signals are fit to a function of the form (equation 4.25) plus a constant and linear background, the height is reduced by 0.9% for ^{3}He, but only by 0.7% for water because of the smaller H_1 field. The residuals of the fit are approximately 0.4%, consistent with Figure 4.12. This effect will be taken into account by reducing the water signal height by 0.2%, so that it is consistent with the conditions of ^{3}He AFP.

Combining all of these effects, a value of 0.592 V was calculated for the water signal. This is only 3% different from the size of the measured signal. This comparison is an extremely powerful check of the model calculations. Since they are able to reproduce the absolute size of the water signal, it is assumed that they can be used to reproduce the scaling between different cells. The flux numbers generated by the numerical integration are given in table 4.7.

Dave	Riker	Bob	SMC	Generals	Hermes
32.62	36.50	32.89	32.35	36.25	31.84
Prelims	Chance	Picard		Water I	Water II
34.77	35.26	39.01		32.01	40.84

Table 4.7: Calculated coil flux (arbitrary units).

The errors are dominated by the diameter of the target cell, contributing 1% to the flux error, and the uncertainty in the vertical position of the cell, contributing 1% to the flux error, except for the water cell.

4.6 Calibration of Target Polarization

To extract the absolute polarization of the ^{3}He, the signal has to be calibrated. This is typically done by measuring the NMR signal from protons in water, where the absolute polarization is known from the Boltzman distribution. The water calibration procedure is complicated by several factors. First of all, the AFP signal from water is 10^5 times smaller than the ^{3}He signal because the thermal polarization of water is only 7.5 $\times 10^{-9}$ at the magnetic field used during SLAC experiment E154. It is quite difficult to detect, and one usually has to resort to averaging many signals to get an acceptable signal to noise ratio. In our case, each set of water data consisted of approximately 50 sweeps. Second, the cell used for the water calibration had slightly different dimensions and position between the pick-up coils, and these differences require a correction to the signal height. Third, the relaxation processes in water are different than in ^{3}He and so the signal (equation 4.25) is significantly modified. Fourth, the water calibration was a time consuming procedure and consequently was done only before and after the run. So, one has to worry about changes in various other quantities that might affect the signal height between the two water signal measurements. Each of these problems will be addressed in the next section. An EPR calibration of the ^{3}He AFP signal was also performed after the run as will be discussed in section 4.6.4.

4.6.1 Water AFP Calibration

The usefulness of a water cell for calibration comes from the fact that the water cell has a uniform density and polarization. This allows a measurement of the filling factor, (η_w), to be made for the water cell between the pick-up coils, with

$$\Phi_w = \mu_w P_w n_w \int_{V_w} \int_{A_{coil}} B(\vec{r}, \vec{r}\,') d^3\vec{r} dA' \tag{4.39}$$

$$\eta_w = \int_{V_w} \int_{A_{coil}} B(\vec{r}, \vec{r}\,') d^3\vec{r} dA' \tag{4.40}$$

$$\eta_w = \frac{S_w}{G_{lockinW} G_{preampW} G_{coilW} \mu_w P_w n_w}. \tag{4.41}$$

A calculation of the ^{3}He filling factor, η_3, is made by expanding around the measured flux of the water cell, η_w, with

$$\eta_3 = \eta_w + \frac{\partial \eta_w}{\partial x_i} \Delta x_i, \tag{4.42}$$

where x_i refers to the position and dimensions of the target, with the most important dimension being the target cell diameter. The results for this expansion were given in the previous section. Defining F_{3w} as the ratio of the ^{3}He target cell filling factor to the water cell filling factor gives

$$\eta_3 = F_{3w}\eta_w. \tag{4.43}$$

Then for the water calibration

$$S_3 = S_w \left(\frac{G_{lockin3} G_{preamp3} G_{coil3}}{G_{lockinW} G_{preampW} G_{coilW}} \right) \left(\frac{\mu_3 P_{3t} n_{3t}}{\mu_w P_w n_w} \right) F_{3w} \left(1 + \Delta_T + \Delta_P\right). \tag{4.44}$$

During water calibration measurements, the temperature of the cell was measured to be 22° ± 3°C. The density of protons in water at 22°C is 6.670 $\times 10^{22}$ cm^{-3}. The thermal polarization of the protons in the water cell is equal to

$$S_w = \tanh \frac{\mu_W H}{kT} = \tanh \frac{h\nu_0}{2kT} = 7.481 \times 10^{-9}. \tag{4.45}$$

The fractional error in the thermal polarization is 1%. The magnetic moment of ^{1}H is $2.79285\mu_N$ and the magnetic moment of ^{3}He is $-2.1274\mu_N$.

4.6.2 Water Signal Analysis

The ^{3}He cell was replaced with a water cell to calibrate the AFP setup both before and after the run. To achieve a good signal to noise ratio, 50 measurements were taken and averaged together. Figure 4.14 shows one of the AFP water signals. Also shown in the figure are a Lorentzian fit to the data (equation 4.25) and a prediction for the signal shape based on a model for the time evolution of the proton magnetization using numerical integration of the modified Bloch equations (equation 4.21) as will be described shortly.

The analysis of the water signals is complicated because the thermal relaxation time for protons in water is comparable to the sweep time, so the shape of the water signals is not exactly a Lorentzian as given by equation 4.25. The shape of the water signals can be calculated from the evolution of the proton magnetization during the sweep as given by the modified Bloch equations (equation 4.21). However, in order to perform such a calculation, the longitudinal and transverse relaxation times, T$_1$ and T$_2$, of the water used for the water calibration must be known. The approach taken in this analysis was to fit the water signals to the same analytic function as

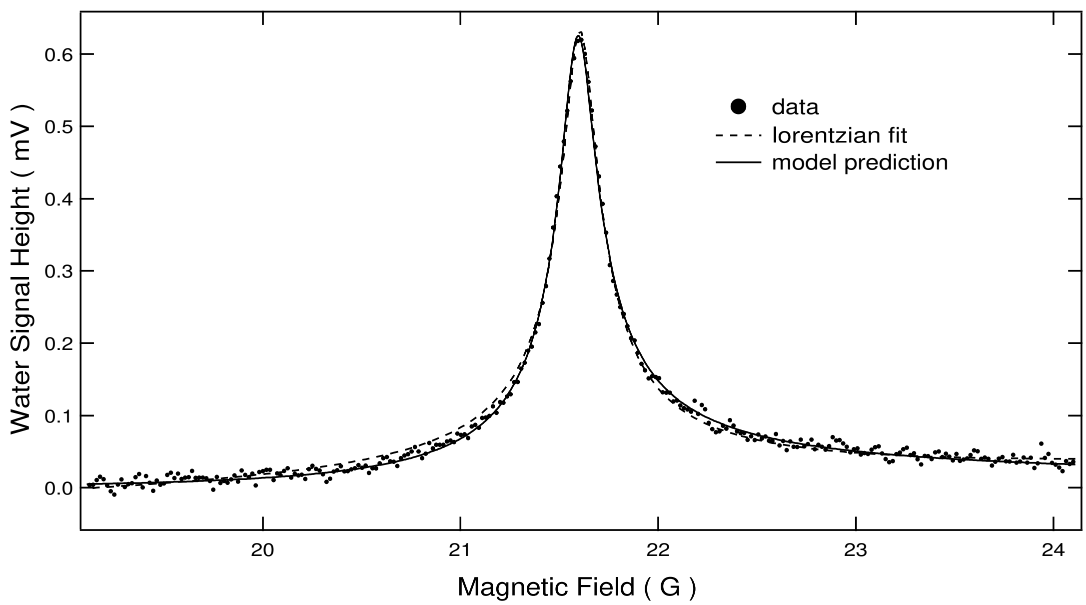

Figure 4.14: Water AFP signal, Lorentzian fit and model prediction.

the ^{3}He signals and then calculate the correction that is necessary to account for the small T_1 and T_2 of water.

To study the effect of T_1 and T_2 on the shape of the AFP signals, a number of AFP curves were generated by numerical integration of the modified Bloch equations (equation 4.21). These curves were then fit to the same analytic function as the ^{3}He signals given by equation 4.25. As can be seen in figure 4.15, the ratio of the peak heights for the up and down sweeps has a strong dependence on the longitudinal relaxation time T_1, but very little dependence on the difference between the longitudinal relaxation time T_1 and the transverse relaxation time T_2. This can be understood as follows: if T_1 and T_2 are long compared to the sweep time, then the value of the magnetization at resonance would be the value of the field at which the sweep started and the protons thermalized. However, because T_1 and T_2 are not long compared to the sweep time, the magnetization decays towards the current value of the magnetic field, which causes the ratio of the peak heights to approach 1 as T_1 goes to zero. If T_2 is less than T_1, the peak height of both the up and down sweeps is reduced by nearly the same amount and there is little effect on the ratio of the peak heights.

Using the measured ratio of the peak heights of 0.8130 ± 0.0120 before the run

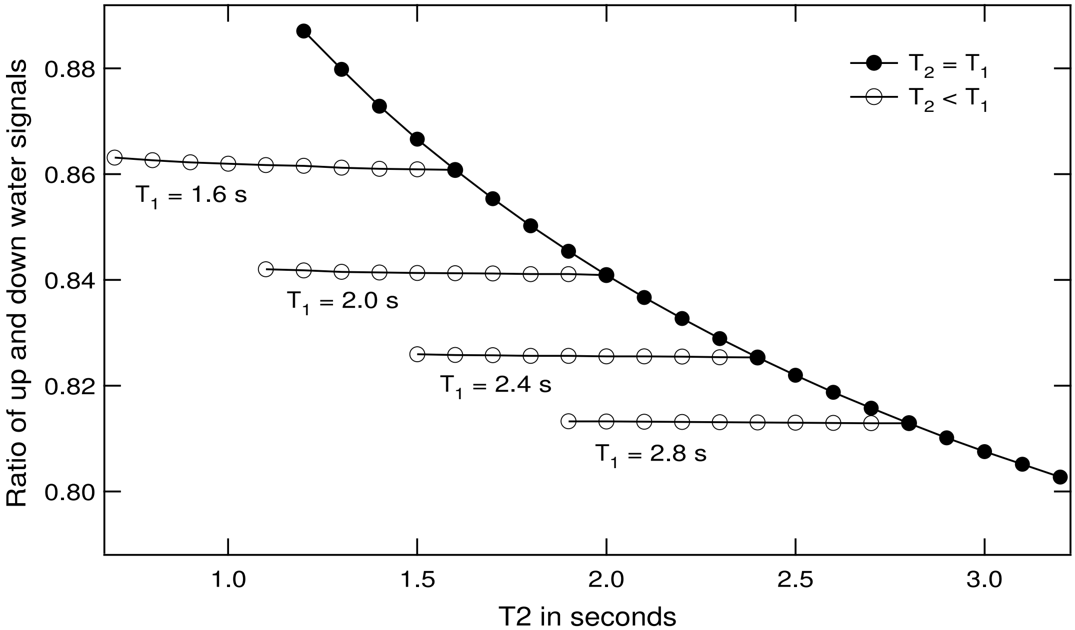

Figure 4.15: Results of numerical integration of the modified Bloch equations.

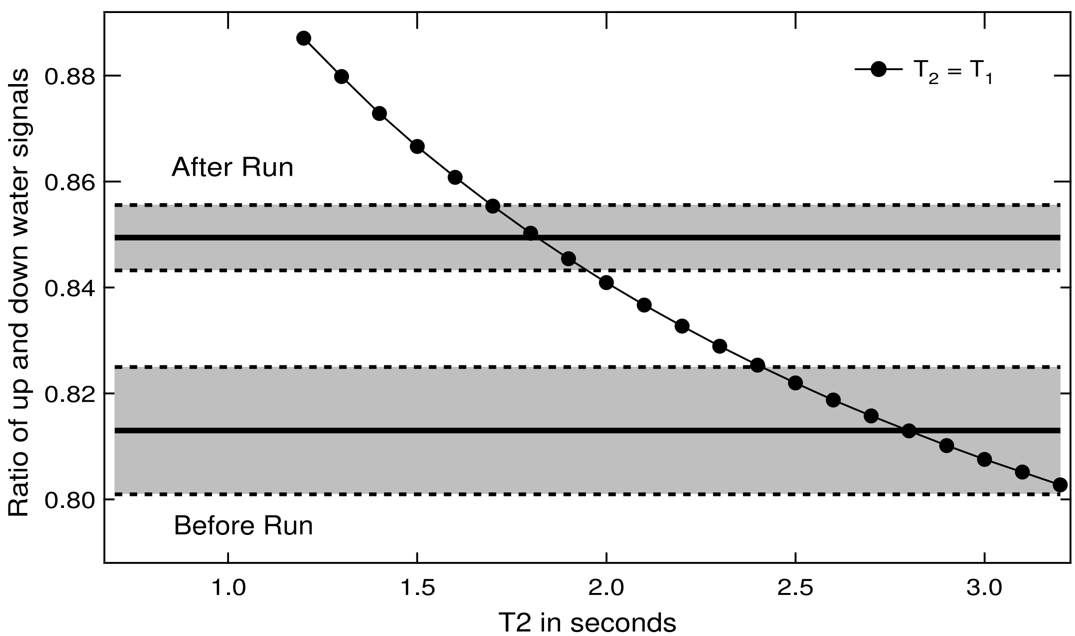

Figure 4.16: Ratio of the up and down water signals and results of the numerical simulation.

and 0.8494 ± 0.0062 after the run, a value of 2.80 ± 0.41 s is calculated for T_1 before the run and 1.82 ± 0.13 s is calculated for T_1 after the run. The shaded area in figure 4.16 is the error band for the measured value of the water signal ratio. The filled circles are the calculated value for the ratio based on numerical integration of the modified Bloch equations and the condition $T_2 = T_1$. It is not surprising to find that T_1 is different for the water before and after the run since T_1 for water depends on the amount of O_2 dissolved in the water, with the value of T_1 for deoxygenated water being 2.95 seconds at 20°C [70].

Naively, it is expected that $T_2 = T_1$ for water since the correlation time, τ_c, associated with the translation and rotation of the molecules is much shorter than the Larmor frequency. However, several high field measurements [71, 72, 73] show that: $1/T_2 = 1/T_1 + 0.125\,\text{sec}^{-1}$ for neutral (i.e. pH=7.0) water. The reason for this turns out to be the presence of 0.037% of ^{17}O isotope in natural water [72]. ^{17}O has a spin of 5/2 and a scalar coupling to the proton spins. The correlation time for ^{17}O–^{1}H coupling is approximately 10^{-3} s leading to a difference between T_1 and T_2. Meiboom [72] has also studied the effect of the size of the RF field on the correlation time, and using his treatment for an RF field of 86 mG, it is found that

$$\frac{1}{T_2} = \frac{1}{T_1} + 0.033\ \text{s}^{-1}. \tag{4.46}$$

Using this treatment, a value of $T_2 = 2.56$ s is obtained for the transverse relaxation time before the run and 1.70 s after the run. A conservative estimate of the error on the difference between T_1 and T_2 is assumed to be the size of the difference, thus allowing the amount of ^{17}O to range from zero to twice the natural abundance.

The prediction of the model which uses numerical integration of the modified Bloch equations is show in figure 4.17. The filled circles are calculated values for the ratio based on numerical integration of the modified Bloch equations and the condition $T_2 = T_1$. The open circles are the results of the model for $T_2 < T_1$ and values of T_1 equal to 1.8 s and 2.8 s. The filled squares are the calculated values of the correction before the run, (1.014 ± 0.004 with $T_1 = 2.80$ s and $T_2 = 2.56$ s), and after the run, (1.016 ± 0.004 with $T_1 = 1.82$ s and $T_2 = 1.70$ s). The box around the calculated correction is the one sigma error region for T_1 and T_2.

The results for fitting the water signals to equation 4.25 are 0.601 ± 0.009 mV before the run and 0.610±0.006 mV after the run. Applying the correction calculated by the model gives: $S_w = 0.609 \pm 0.009$ before the run and $S_w = 0.620 \pm 0.007$ after the run. Remembering that the RF field was larger for water than it was for ^{3}He, a 0.2% correction from the magnetic field inhomogeneities is applied to the water signal to make it consistent with the conditions of ^{3}He AFP. This gives a final answer for the water signal of 0.615 ± 0.007 mV.

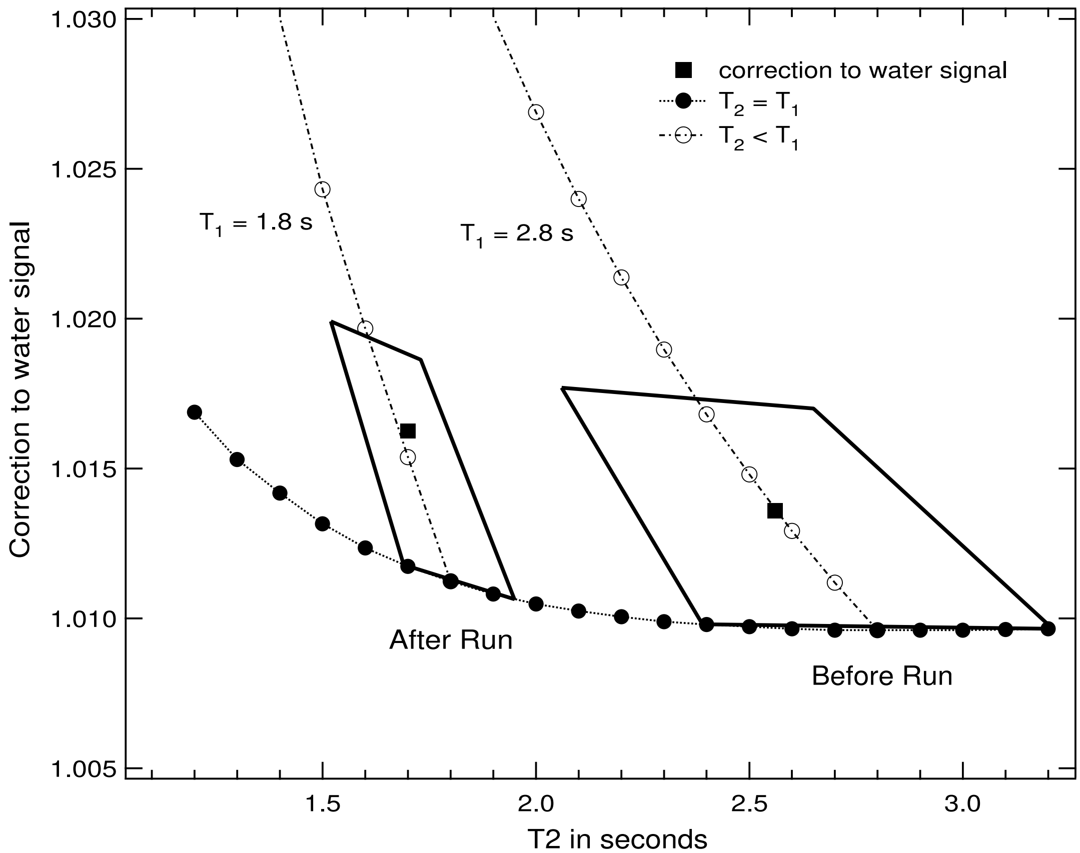

Figure 4.17: Correction to the water signal peak height.

4.6.3 Results for Water Calibration

Equation 4.44 gives the ^{3}He signal as a function of target cell polarization. Defining a water calibration constant C_w, such that $P_{3t} = C_w S_3$. Then for C_w:

$$C_w = \left(\frac{P_w}{S_w}\right)\left(\frac{\mu_w n_w}{\mu_3 n_{3t}}\right)\left(\frac{G_{lockinW} G_{preampW} G_{coilW}}{G_{lockin3} G_{preamp3} G_{coil3}}\right)\left(\frac{1}{F_{3w}(1+\Delta_T+\Delta_P)}\right). \quad (4.47)$$

Each of the parameters and their errors are shown in tables 4.8 and 4.9. The results for the water calibration constants for the cells are given in Table 4.10. The total error on a water calibration constant is 3.1%.

4.6.4 EPR Calibration

The electron paramagnetic resonance (EPR) method of calibration uses the ^{3}He polarization dependent shift in the frequency of one of the rubidium Zeeman transitions to determine the polarization of the ^{3}He in the target and calibrate the AFP measurements. This method was first reported by Grover [74], and studied by Schaefer [75]. The electronic energy levels of the rubidium are split in the presence of the magnetic holding field, and there is an additional splitting caused by the presence of the polarized ^{3}He. Transitions between two Zeeman levels can be used to determine the strength of the magnetic field plus the polarization of the ^{3}He in which the rubidium is present. In the case of EPR frequency shift polarimetry, the difference in the frequency of a Zeeman transition is measured between the polarization states in which the ^{3}He polarization is parallel and antiparallel to the magnetic holding field. The measured shift caused by the polarized ^{3}He has two sources: a classical bulk magnetic field and a contact term that is due to the spin exchange interaction. The frequency shift is large, being approximately 20 kHz out of the Zeeman transition of 8.6 MHz. The EPR calibration was performed after the experimental run on the target cell Picard.

The effect of the polarized ^{3}He on the energy eigenstates of the rubidium in the presence of a magnetic holding field can be seen from the Hamiltonian [59, 75, 76]

$$\mathcal{H} = A\vec{I} \cdot \vec{S} + \alpha\vec{K} \cdot \vec{S} + g_e\mu_B\vec{B} \cdot \vec{S} + g_I\mu_N\vec{B} \cdot \vec{I}, \tag{4.48}$$

where I and S are the nuclear and electronic spins of the rubidium atom, K is the nuclear spin of the ^{3}He, and B is the sum of the holding field and the bulk magnetization of the polarized ^{3}He. The constant A is the rubidium hyperfine splitting, and the constant α is the frequency shift parameter. The strongest interaction is the $\vec{I} \cdot \vec{S}$ interaction, with $A = 1012$ MHz $>> g_e\mu_B B/h = 8.6$ MHz at 18.3 G. Therefore,

Parameter	Value	Error	%Error
P_w	7.481×10^{-9}	0.075×10^{-9}	1.0
S_w	0.615 mV	0.007 mV	1.1
μ_w/μ_3	1.313	-	-
n_w	2482 amg.	2 amg.	0.1
G_{coilW}/G_{coil3}	0.991	0.005	0.5
$G_{preampW}/G_{preamp3}$	20.00	0.14	0.7
$G_{lockinW}/G_{lockin3}$	20.04	0.15	0.8

Table 4.8: Cell independent water calibration error table.

	n_{3t}	δn_{3t}	F_{3w}	δF_{3w}	Δ_T	$\delta\Delta_T$	Δ_P	$\delta\Delta_P$
Dave	10.04 amg	0.19 amg	1.002	0.013	-0.018	0.005	0.017	0.004
Riker	9.94 amg	0.19 amg	1.126	0.014	-0.024	0.006	0.013	0.003
Bob	9.93 amg	0.19 amg	1.013	0.013	-0.024	0.006	0.014	0.004
SMC	9.98 amg	0.19 amg	0.996	0.013	-0.021	0.005	0.015	0.003
Generals	9.74 amg	0.18 amg	1.119	0.014	-0.024	0.006	0.012	0.003
Hermes	9.83 amg	0.19 amg	0.981	0.013	-0.021	0.005	0.014	0.003
Prelims	9.98 amg	0.19 amg	1.071	0.013	-0.024	0.006	0.014	0.003
Chance	9.99 amg	0.19 amg	1.089	0.014	-0.024	0.006	0.011	0.003
Picard	9.82 amg	0.19 amg	1.206	0.013	-0.024	0.006	0.011	0.003

Table 4.9: Cell dependent water calibration error table.

Dave	Riker	Bob	SMC	Generals	Hermes	Prelims	Chance	Picard
0.1567	0.1422	0.1581	0.1594	0.1462	0.1644	0.1488	0.1466	0.1347

Table 4.10: Water calibration constants, C_w (%/mV).

the eigenstates of the hyperfine hamiltonian ($\vec{I} \cdot \vec{S}$) will be used. These are also the eigenstates of the total angular momentum $\vec{F} = \vec{I} + \vec{S}$, and their energy is given by the Breit-Rabi formula

$$E_{F=I\pm 1/2,\mathrm{m_q}} = -\frac{h\nu_{HF}}{2\,(2I+1)} - g_I\mu_N B\mathrm{m_q} \pm \frac{h\nu_{HF}}{2}\left(1+\frac{4\mathrm{m_q}}{2I+1}x+x^2\right)^{1/2}, \quad (4.49)$$

where $\nu_{HF} = A\,(I+1/2)$ and $x = \left(g_e\mu_B B + g_I\mu_N B + (h\alpha)\left\langle\vec{K}\right\rangle\right)/h\nu_{HF}$.

By holding the magnetic field constant, radio frequency Zeeman transitions can be induced between neighboring $\mathrm{m_q}$ sublevels and the resonant frequency can be measured with both orientations of the target polarization, $\left\langle\vec{K}\right\rangle > 0$ ($\uparrow$) and $\left\langle\vec{K}\right\rangle < 0$ ($\downarrow$). The difference in the two frequencies is the EPR frequency shift, which has two terms: one from the bulk magnetization of the ^{3}He and one from the spin exchange interaction. At low magnetic fields, $x << 1$, and only the first two terms in the approximation of the square root need to be kept. In this case, the EPR frequency shift is

$$\begin{aligned}\Delta\nu_{EPR} &= \frac{\Delta E_\uparrow - \Delta E_\downarrow}{2h} \\ &= \frac{1}{(2I+1)h}\left(g_e\mu_B - 2Ig_I\mu_N\right)B_3 + \frac{1}{(2I+1)h}\left(\alpha\left\langle\vec{K}\right\rangle\right), \quad (4.50)\end{aligned}$$

where B_3 is the bulk magnetic field created by the ^{3}He polarization and is given by the formula

$$B_3 = \frac{\mu_0}{4\pi}P_{3p}n_{3p}\mu_3 G, \quad (4.51)$$

where P_{3p} is the polarization in the pumping cell, n_{3p} is the ^{3}He density in the pumping cell, μ_3 is the magnetic moment of ^{3}He, and G is a geometrical factor that takes into account the shape of the SLAC experiment E154 target cell. Note that for a sphere, $G = 8\pi/3$.

It is customary to write the formula for the EPR frequency shift not in terms of the bulk magnetic field B_3 and the frequency shift parameter α, but instead, in terms of κ_0, the frequency shift caused by the contact term plus the bulk field due to a sphere, and K_G, the difference between the geometrical factor for a spherical cell and that of the actual target cell. (The first experiments were done with spherical cells.) Also, since $\mu_B = 1836\mu_N$, the terms containing g_I will be dropped. Then for the EPR frequency shift at low fields

$$\Delta\nu_{EPR} = \frac{\mu_0}{4\pi}\frac{g_e\mu_B\mu_3}{(2I+1)h}\left(\frac{8\pi}{3}\kappa_0 + K_G\right) n_{3p}P_{3p}. \qquad (4.52)$$

In the case of SLAC experiment E154, the magnetic field used during the EPR calibration was large enough that it is necessary to keep an additional term in the expansion of the Breit-Rabi equation (equation 4.49). This gives the following for the EPR frequency shift under the conditions of SLAC experiment E154

$$\Delta\nu_{EPR} = \frac{\mu_0}{4\pi}\frac{g_e\mu_B\mu_3}{(2I+1)h}\left(1 - \frac{2\,(2\mathrm{m_q}-1)}{2I+1}\frac{g_e\mu_B B}{h\nu_{HF}}\right)\left(\frac{8\pi}{3}\kappa_0 + K_G\right) n_{3p}P_{3p}, \qquad (4.53)$$

where the high field correction is dependent on the particular Zeeman transition, $\mathrm{m_q}$, that is measured.

There were two requirements for the success of the EPR calibration at SLAC: that the magnetic holding field be held constant to a part in 10^5, and that a precision measurement of κ_0 be made since the value of κ_0 is not known with sufficient accuracy from calculations based on interatomic potentials. An attempt to lock the magnetic holding field for the purpose of performing an EPR calibration was made after SLAC experiment E142, but failed. For SLAC experiment E154 the magnetic holding field was successfully locked to 18.324 G using a Flux–Gate magnetometer to measure the strength of the magnetic field and a feedback loop to drive the magnetic holding field's Kepco power supply.

The value of κ_0 was measured at Princeton using the technique of Barton *et al.* [77], in which κ_0 is extracted from two measurements of the EPR frequency shift in a cylindrical cell differing in orientation by 90 degrees. The measurement at Princeton was performed to a higher precision than previous measurements, and under the conditions of the target cells of SLAC experiment E154. The temperature dependent value obtained was $\kappa_0 = 4.52 + 0.00934T$ near 180°C, where T is the temperature of the cell in degrees Celsius. This measurement has an error of 1% and further details describing it can be found in the target polarization technical note [69]. For calibrating the SLAC experiment E154 target polarization, the error in the pumping cell temperature is 10°C, which gives a total error of 1.8% to the value of κ_0.

Having locked the magnetic field, the EPR resonance was detected by monitoring the fluorescence of a portion of the pumping cell while applying an RF field of approximately 8.6 MHz. The ^{85}Rb in the pumping cell is highly polarized when the pumping lasers are on, and most of the rubidium atoms are in the $m_q = 3$ state, ($m_q = -3$ for the opposite polarization). Once a rubidium atom makes a transition to the $m_q = 2$ state, it can be optically pumped to the 5P state. From the 5P state, it decays back to the 5S state emitting a photon (795 nm or 780 nm) approximately 2% of the time. The typical decay mode is nonradiative quenching caused by the nitrogen. By mounting a small RF coil on the side of the pumping oven, a RF field could be generated in the pumping cell. When the frequency of the RF field is tuned to the transition for $m_q = 3 \rightarrow 2$, the rate of absorption increases as does the rate of fluorescence.

The fluorescence of the pumping cell was detected using a photodiode. To avoid stray light from the pumping lasers, which are tuned to the D1 = 795 nm line, a D2 = 780 nm filter was placed in front of the photodiode. The output of the photodiode was differentiated and used to drive a feedback circuit to hold the RF frequency at the resonant value. The RF frequency was then measured by a counter and transfered to the Macintosh via GPIB. An EPR frequency shift calibration consisted of measuring the EPR frequency for approximately one minute, flipping the ^{3}He polarization and then measuring the EPR frequency again. The reversal of the ^{3}He spins was accomplished using AFP, but by sweeping the RF frequency instead of the magnetic field. In this way, the magnetic field could be held constant at all times. The same RF coils and ENI RF power amplifier were used for the EPR calibration as were used for the target polarization AFP measurements. A typical EPR data set is shown in figure 4.18.

There are two isotopes of rubidium, ^{85}Rb and ^{87}Rb. ^{85}Rb has a nuclear spin of $I = 5/2$ and ^{87}Rb has a nuclear spin of $I = 3/2$. The natural abundance of ^{85}Rb is 28% and ^{87}Rb is 72%. The lines are well separated and for SLAC experiment E154, the EPR calibration was performed on the Zeeman transitions of ^{85}Rb, as was assumed in the previous paragraph. At 18.324 G, the different m_q transitions are separated by 45 kHz. The full width of the EPR signal is 13 kHz, allowing a particular m_q state to be probed. The strongest signal comes from the $m_q = 3$ state and this was the one chosen for the EPR calibration. Knowing the magnetic field, the nuclear spin and the state m_q, the high field correction term can be calculated,

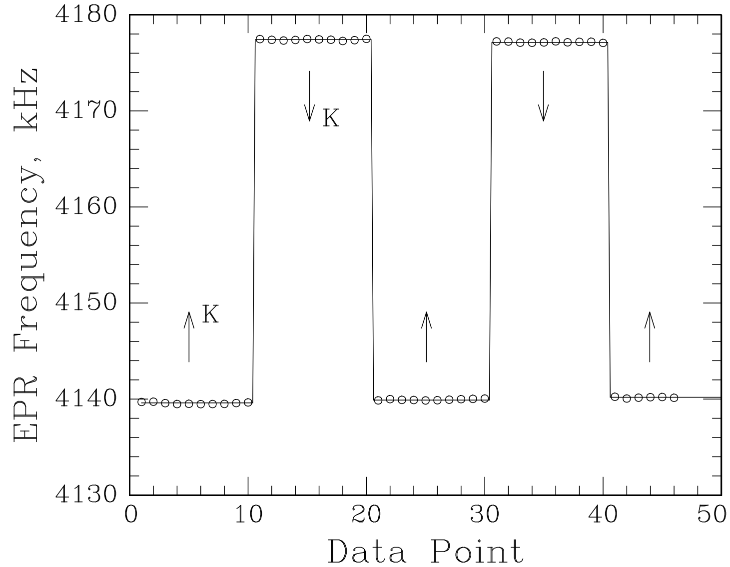

Figure 4.18: Typical EPR data set taken after the experimental run.

and is equal to 0.028. The collection of fundamental constants can also be evaluated to give

$$\begin{aligned} C_{fund} &= \frac{\mu_0}{4\pi}\frac{g_e\mu_B\mu_3}{(2I+1)h}\left(1-\frac{2\,(2\mathrm{m_q}-1)}{2I+1}\frac{g_e\mu_B B}{h\nu_{HF}}\right) \\ &= 4.8784\times10^{-18}\ \frac{\mathrm{cm}^3}{\mathrm{s}} = 131.1\ \frac{\mathrm{Hz}}{\mathrm{amagat}}. \end{aligned} \tag{4.54}$$

In order to calibrate the target AFP setup, measurements of the target polarization using the AFP setup were made immediately before and after an EPR calibration. There was some loss in the target polarization caused by the EPR calibration measurement, but not enough to significantly change the target polarization. However, there is a complication because the AFP measurement is a measurement of the ^{3}He polarization in the target cell while an EPR calibration is a measurement of the polarization in the pumping cell. With a transfer time of approximately 50 minutes for the polarization between the two cells, there is a small error introduced by making the measurement in the pumping cell. Using the depolarization coefficient, D_{tt} from the appendix and $P_{3t} = P_{3p}D_{tt}$, a calibration constant for the EPR calibration can be written such that $P_{3t} = C_{epr}S_3$

$$C_{epr} = \left(\frac{\Delta\nu_{EPR}}{S_{3,EPR}}\right)\frac{D_{tt}}{C_{fund}n_{3p}F_{3EPR}}\left(\frac{8\pi}{3}\kappa_0 + K_G\right)^{-1}, \tag{4.55}$$

where $\Delta\nu_{EPR}/S_{3,EPR}$ is the ratio of the EPR frequency shift to the AFP signal height from the target cell Picard during the EPR calibration, and F_{3EPR} is the ratio of the flux from a given target cell to that of the target cell used for the EPR calibration.

The measurement of $\Delta\nu_{EPR}/S_{3,EPR}$ was performed under a variety of conditions to test the stability of the result. The amount of laser pumping power, the temperature of the cell, the strength of the magnetic holding field and the target polarization were varied. The average of the measured values was 68.9 $\pm$ 1.0 Hz/mV, with the 1.4% fractional error being the spread in the measured values which exceeded the 0.5% error on a single measurement and is therefore attributed to some unknown systematic effect.

The value of the bulk magnetic field and K_G were calculated using Mathematica. However, there was some uncertainty as to where in the cell the light that entered the photodiode originated. The photodiode was approximately 30 cm from the pumping cell and light from the cell was collimated using a lens. The origin of the light in the cell is conservatively estimated to be uncertain to 2 cm, which gives a result for K_G of 2.4 $\pm$ 0.7.

Each of the parameters used for the EPR calibration and their errors are shown in tables 4.11 and 4.12. The results for the EPR calibration constants for the SLAC experiment E154 target cells are given in table 4.13. An additional systematic error of 0.5% was added to the water calibration to allow for drift in the AFP system during the run, as evidenced by the difference in the water signals before and after the run. Likewise for EPR, an additional 0.5% error accounts for drift in the AFP system over the course of the run. The total error on the EPR calibration constant is 3.0% for the target cell Picard, 3.3% for the other target cells and 3.2% for the entire experimental data set. The error is less than the addition of the individual errors in quadrature because of a pumping cell temperature correlation between the values of κ_0 and the density in the pumping cell, n_{3p}.

4.6.5 Comparison of Methods and Final Result

The results of the two methods are shown for the SLAC experiment E154 target cell Picard in figure 4.19 along with the final answer for the target polarization calibration constant. The two results differ by 5.5%, and the final error of 4.5% was

Parameter	Value	Error	%Error
C_{fund}	131.1 Hz/amagat	0.1 Hz/amagat	0.1
κ_0	6.20 @ 180°C	0.11	1.8
K_G	2.4	0.7	30.0
D_{tt}	0.970	0.015	1.5
$\Delta\nu_{EPR}/S_{3,EPR}$	68.9 Hz/mV	1.0 Hz/mV	1.4

Table 4.11: Cell independent EPR calibration error table.

	n_{3p}	δn_{3p}	F_{3EPR}	δF_{3EPR}
Dave	7.20 amg	0.14 amg	0.836	0.011
Riker	7.18 amg	0.14 amg	0.936	0.012
Bob	7.42 amg	0.14 amg	0.843	0.011
SMC	7.34 amg	0.14 amg	0.829	0.011
Generals	7.19 amg	0.14 amg	0.929	0.012
Hermes	7.34 amg	0.14 amg	0.816	0.011
Prelims	7.21 amg	0.14 amg	0.891	0.012
Chance	7.31 amg	0.14 amg	0.904	0.012
Picard	7.36 amg	0.14 amg	1.000	0.000

Table 4.12: Cell dependent EPR calibration error table.

Dave	Riker	Bob	SMC	Generals	Hermes	Prelims	Chance	Picard
0.1559	0.1396	0.1500	0.1542	0.1405	0.1566	0.1460	0.1420	0.1275

Table 4.13: EPR calibration constants, C_{epr} (%/mV).

calculated such that if half of a large number of measurements were made with the water technique and half were made with the EPR technique, then 68.2% of the measurements would fall within one sigma of the average value. The final values for the target polarization calibration constant are give in table 4.14.

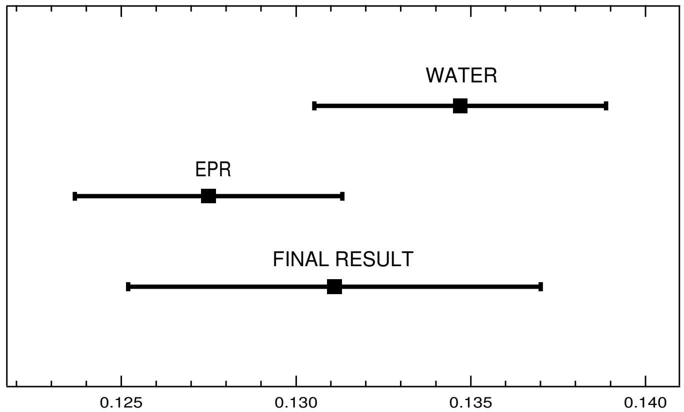

Figure 4.19: Results for water and EPR and final E154 target polarization calibration constant for Picard.

Dave	Riker	Bob	SMC	Generals	Hermes	Prelims	Chance	Picard
0.1563	0.1409	0.1541	0.1568	0.1434	0.1605	0.1474	0.1443	0.1311

Table 4.14: E154 target polarization calibration constants (%/mV).

4.7 Target Model

In order to calculate the asymmetry of the ^{3}He (A_3) from the measured raw asymmetry (A^{raw}) for the electrons from deep inelastic scattering, the fraction of observed events that originated in the ^{3}He must be known. This ratio is traditionally called the dilution factor and labeled f_3, the 3 indicating that it is the dilution of the ^{3}He in the target

$$A_3(x, Q^2) = \frac{A^{raw}(x, Q^2)}{P_{3t} P_B f_3(x, Q^2)}, \tag{4.56}$$

where P_{3t} is the polarization of the ^{3}He in the target cell and P_B is the polarization of the electron beam. The dilution factor f_3 is the ratio of events originating from the ^{3}He to the total number of events

$$f_3(x, Q^2) = \frac{N_3(x, Q^2)}{N_{\text{total}}(x, Q^2)}. \tag{4.57}$$

Calculation of the absolute number of events that are expected in the spectrometers requires a precise knowledge of the electron beam parameters, the cross sections for the target materials, and the spectrometer acceptances and efficiencies. The dilution factor is a ratio of the number of events and therefore does not require such precise knowledge. What is necessary is a precise knowledge of the target parameters, such as the density of the ^{3}He and the thickness of the glass windows. Using our knowledge of the target parameters, as given in tables 4.2, 4.3, 4.4, and 4.5, the ratio of the number of events from ^{3}He that are generated in the target to the total number of events that are generated in the target can be calculated using the measured values of F_2 for the proton and the deuteron. The structure functions may be used instead of the cross sections since the kinematic factors and spectrometer acceptances cancel in the ratio for each bin in x and Q^2.

To construct a physical model of the SLAC experiment E154 targets, the target will be divided into four components. Along the electron beam line, the target is composed of a glass upstream window, a column of ^{3}He, an intermixed column of N_2, and a glass downstream window. For the purpose of calculating the dilution factor, the target will be considered to be composed of these four components. The equation for the dilution factor is then

$$f_3(x, Q^2) = \frac{N_3(x, Q^2)}{N_3(x, Q^2) + N_{N2}(x, Q^2) + N_{gu}(x, Q^2) + N_{gd}(x, Q^2)}, \tag{4.58}$$

where $N_3(x, Q^2)$ is the number of events from ^{3}He, $N_{N2}(x, Q^2)$ is the number of events from the diatomic nitrogen molecules, $N_{gu}(x, Q^2)$ is the number of events from the glass upstream window, and $N_{gd}(x, Q^2)$ is the number of events from the glass downstream window, for a given counting time.

The largest complication to calculating the model dilution factor comes from the radiative corrections. The number of events as a function of x and Q^2 measured in the spectrometers is different than the number of events as a function of x and Q^2 generated in the target using only the cross section for DIS single photon exchange. Depending on the location of the scattering center, an incoming electron passes through different thicknesses of material before scattering and exits the target through different thicknesses after scattering. Also, the probability of scattering depends not only on single DIS photon exchange as given by F_2, but also on other processes such as elastic scattering, quasi-elastic scattering, inelastic scattering and those processes that involve additional photon exchange or photon emission. The events measured in the spectrometer, as a function of x and Q^2, will be different than those generated in the target because of these radiative corrections which shall be labeled as external before, internal, and external after. These radiative corrections are responsible for a large percentage of the error in the model dilution factor, especially in the lowest x-bins. Using $C_i(x, Q^2)$ to represent the total radiative correction to the i^{th} component of the target, the model dilution factor becomes

$$f_3 = \frac{N_3 C_3}{N_3 C_3 + N_{N2} C_{N2} + N_{gu} C_{gu} + N_{gd} C_{gd}}, \tag{4.59}$$

where all quantities are functions of x and Q^2.

The single photon exchange (Born) scattering cross sections for the four individual components of the target will be constructed using the structure functions for the proton (F_2^p) and the deuteron (F_2^d) which have been measured most recently by NMC [33]. For an element with atomic number A and Z protons, the cross section will be calculated by summing the cross sections for $(A - Z)$ deuterons and $(2Z - A)$ protons and then multiplying by the correction for the nuclear binding effects as determined by EMC [12] in an element of atomic number A , with

$$\sigma(x, Q^2) = K(x, Q^2) \left((A - Z) 2 F_2^d(x, Q^2) + (2Z - A) F_2^p(x, Q^2) \right) F_{EMC}^A(x), \tag{4.60}$$

where $K(x, Q^2)$ contains the kinematic factors, $F_2^d(x, Q^2)$ is the unpolarized structure function of the deuteron, $F_2^p(x, Q^2)$ is the unpolarized structure function of the proton, and $F_{EMC}^A(x)$ is the EMC factor for a nucleus of atomic number A. The additional factor of 2 before $F_2^d(x, Q^2)$ is necessary because the unpolarized structure function of the deuteron is defined as the unpolarized structure function per nucleon.

The formula for the model dilution factor is then

$$f_3 = \frac{R_3 C_3}{R_3 C_3 + R_{N2} C_{N2} + R_{gu} C_{gu} + R_{gd} C_{gd}}, \tag{4.61}$$

where all quantities are functions of x and Q^2, and

$$R(x, Q^2) = \left((A - Z) 2 F_2^d(x, Q^2) + (2Z - A) F_2^p(x, Q^2) \right) F_{EMC}^A(x, Q^2) Ln \tag{4.62}$$

is the rate at which first order Born events are generated in the i^{th} component of the target with length L_i and density n_i.

4.7.1 Calculation of Rates

Using the values for the target parameters as given in tables 4.2, 4.3, 4.4, and 4.5, the model dilution factor in the absence of radiative corrections can be calculated. A plot of the model dilution factor in the two spectrometers without radiative corrections is given in figure 4.20 for the SLAC E154 target Picard. Also plotted for comparison is the model dilution factor with full radiative corrections so that the size of the radiative corrections may be seen. The large radiative correction in the lowest x-bins of the 2.75° spectrometer has its source in the internal corrections. At the low Q^2 of these bins, the elastic, quasi-elastic, and inelastic processes become important. Differences in the form factors for ^{3}He and glass cause different corrections to the individual rates. In the 5.50° spectrometer, the large difference in the highest and lowest x-bins arises from the external radiative corrections for these x-bins where the spectrometer acceptance is changing rapidly.

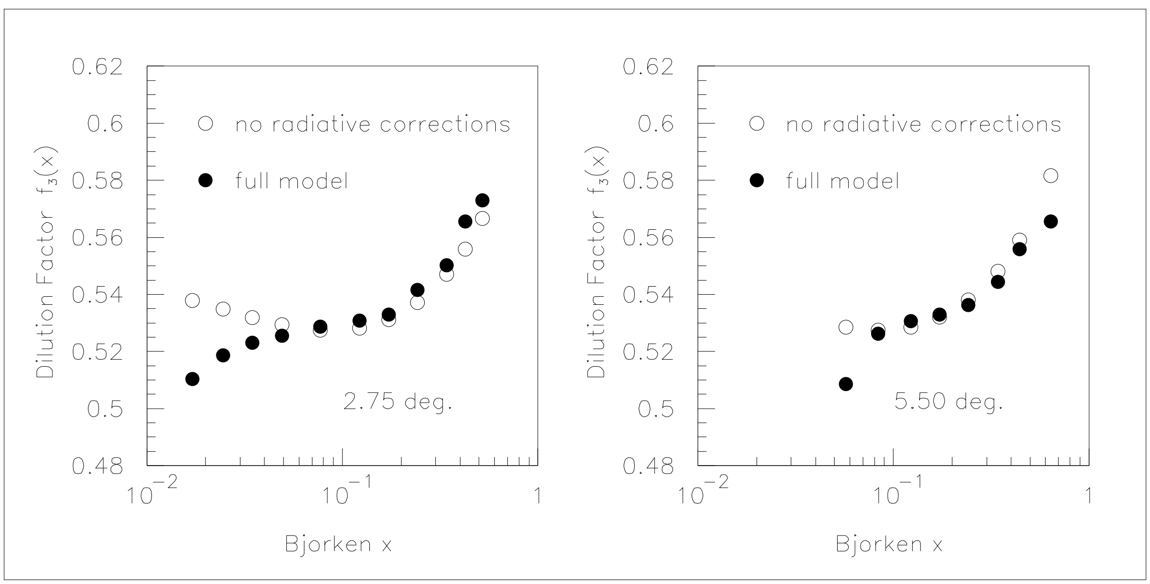

Figure 4.20: Model dilution factor for Picard with and without radiative corrections.

For ^{3}He, $Z = 2$ and $A = 3$, so that the ^{3}He component of the target will be modeled using 1 deuteron and 1 proton. The nitrogen component of the target is diatomic, with each atom having $Z = 7$ and $A = 14$, so that the N_2 component of the target will be modeled using two atoms each with 7 deuterons. Actually, the natural abundance of ^{14}N is 99.64%, with the remaining 0.36% being ^{15}N. However, since the amount of nitrogen in the target is small, the natural abundance of ^{15}N is small, and the difference in the EMC effect between ^{14}N and ^{15}N is small, the effect of including the ^{15}N is negligible.

For the components of the target that were composed of glass, namely the upstream and the downstream windows, the rate can be found by summing the individual rates from each of the isotopes of each the elements of the glass. Corning 1720 glass is composed of 59.9% SiO_2, 18.2% Al_2O_3, 8.8% MgO, 7.4% CaO, 4.7% B_2O_3, and 1.0% Na_2O by weight [78]. Using the natural abundances for the individual elements, the fraction of the glass composed of each element and isotope is given in table 4.15.

The values of F_2^p and F_2^d were taken from the 1995 NMC data [33]. The value of $F_{EMC}^A(x, Q^2)$ was calculated using the Smirnov parameterization [79] for $x < 0.7$ and a fit to the SLAC experiment E139 data by Javier Gomez for $x > 0.7$. [80].

The error in the model dilution factor that does not come from the radiative corrections has pieces that are x independent and pieces that are x dependent. The x independent pieces include errors from the uncertainty in the window thicknesses and the helium density, as well as other target parameters, while the x dependent pieces have errors from the structure functions F_2^d and F_2^p and from the EMC effect. The contributions to the error in the model dilution factor from each of the parameters are summarized in tables 4.16, 4.17, and 4.18. Since it is the most statistically significant target, the SLAC E154 target cell Picard is used to illustrate the fractional error in the dilution factor due to each parameter. For the x independent errors, the error in the window thicknesses is 3.0% for both the upstream and the downstream window of Picard, which gives a total x independent error of 1.7% for Picard.

The interaction length of the glass side walls of the target is 10,000 larger than the interaction length of the target along its center line. A small beam halo can generate a large number of events from the unpolarized glass side walls. To study the number of events created by beam halo, a halo target was constructed that was identical in design to the lower chamber of the polarized ^{3}He target cells, with the exception of

Atom	Fraction	Isotope	Natural Abundance
O	0.621	^{16}O	0.9976
		^{17}O	0.0004
		^{18}O	0.0020
Si	0.200	^{28}Si	0.9223
		^{29}Si	0.0467
		^{30}Si	0.0310
Al	0.073	^{27}Al	1.0000
Mg	0.044	^{24}Mg	0.7899
		^{25}Mg	0.1000
		^{26}Mg	0.1101
Ca	0.037	^{40}Ca	0.9694
		^{42}Ca	0.0065
		^{43}Ca	0.0013
		^{44}Ca	0.0209
		^{48}Ca	0.0019
B	0.019	^{10}B	0.8000
		^{11}B	0.2000
Na	0.006	^{23}Na	1.0000

Table 4.15: Isotopic composition of Corning 1720 glass.

Quantity	Fractional Error	df_3/f_3
$L_3 = L_{N2}$	0.7%	0.3%
n_3	1.9%	0.9%
n_{N2}	1.9%	0.1%
L_{gu}	3.0%, 5.0%, 7.0%	0.7%, 1.1%, 1.6%
L_{gd}	3.0%, 5.0%, 7.0%	0.7%, 1.1%, 1.6%
n_g	0.8%	0.3%
beam halo		1.0%
Total		1.7% – 2.7%

Table 4.16: x independent errors on the model dilution factor.

having its end windows removed. The end windows were attached to the halo target in the same manner as they are attached to a polarized ^{3}He target cell, and then the end windows were removed, leaving the glass weld intact. The halo target was used before the data taking run in conjunction with the reference cell. Data run 1093 contains electron scattering data for the halo target and data run 1094 taken immediately afterwards contains electron scattering data for the reference cell filled with ^{3}He to a pressure equal to the nominal running pressure of the polarized ^{3}He target cells. The ratio of the number of events in the spectrometers is approximately 5×10^{-4}, indicating that a negligible number of events originated in the unpolarized glass side walls of the target.

However, over the course of the data taking run, the beam conditions were changed, including the spot size of the electron beam at the target. In at least one of these cases, a full reference cell was used to measure the counting rate in the spectrometers immediately before and after a beam tune that included a beam spot size change. The ratio of the number of events in this case was consistent with 1.0 with an error of approximately 0.5%. Because measurements of the number of counts from the beam halo made at isolated times may not be indicative of the true beam halo during data taking conditions, a conservative error will be assigned to the dilution factor from the beam halo. A value of zero will be used for the number of counts from the unpolarized glass side walls, as was measured, but with an error on the dilution factor equal to the size of the fluctuations in the number of events per incident electron. This assumes that all fluctuations in the number of counts can be attributed to changing beam halo. The size of the fluctuations is approximately 1%.

4.7.2 Radiative Corrections

There are three classes of radiative corrections to calculate: external before, internal, and external after. The strategy used to calculate them was to generate a large number of electron tracks in the target, evenly distributed in x, Q^2, z, and ϕ for each component of the target, and then calculate the position and momentum of these electrons as they enter the spectrometer. The dilution factor for the target is formed by weighting each track by the probability that an electron scatter took place at the x and Q^2 of that track. The probability that an electron scatter occurred is

x	Q^2 (GeV/c)^2	$(\mathrm{d}f_3/f_3)_{EMC}$	$(\mathrm{d}f_3/f_3)_{F_2}$	$(\mathrm{d}f_3/f_3)_{EMC+F_2}$
0.017	1.2	0.94%	1.03%	1.40%
0.025	1.6	0.86%	0.98%	1.31%
0.035	2.1	0.80%	0.95%	1.24%
0.049	2.6	0.74%	0.92%	1.18%
0.077	3.3	0.68%	0.84%	1.08%
0.122	4.1	0.64%	0.80%	1.02%
0.172	4.7	0.63%	0.82%	1.04%
0.242	5.1	0.66%	0.87%	1.09%
0.341	5.5	0.75%	0.92%	1.19%
0.425	5.9	0.87%	0.89%	1.24%
0.519	6.1	1.05%	0.82%	1.33%

Table 4.17: x dependent errors on the model dilution factor in the 2.75° spectrometer.

x	Q^2 (GeV/c)^2	$(\mathrm{d}f_3/f_3)_{EMC}$	$(\mathrm{d}f_3/f_3)_{F_2}$	$(\mathrm{d}f_3/f_3)_{EMC+F_2}$
0.057	4.0	0.74%	0.97%	1.22%
0.084	5.5	0.67%	0.87%	1.10%
0.123	7.2	0.64%	0.85%	1.07%
0.173	8.9	0.64%	0.83%	1.04%
0.242	10.7	0.67%	0.83%	1.06%
0.342	12.5	0.77%	0.86%	1.16%
0.442	13.8	0.93%	0.84%	1.25%
0.638	15.6	1.39%	0.84%	1.63%

Table 4.18: x dependent errors on the model dilution factor in the 5.50° spectrometer.

proportional to the unpolarized structure function multiplied by the internal radiative correction. However, loss of energy by the incoming electron before the electron scatter transforms the probability for the electron scatter into an integral over the possible initial beam energies of the initial beam energy probability multiplied by the unpolarized structure function and internal radiative correction for an electron at that initial energy with a final momentum equal to that of the electron track.

The external radiative corrections for SLAC experiment E154 were calculated using a model of the SLAC experiment E154 spectrometers created using the GEANT Detector Description and Simulation Tool from CERN [81]. The spectrometer model was created by Dr. Robert C. Welsh from The University of Michigan and served the dual purpose of providing a tool for calculating the external radiative corrections after, as well as providing a single event display which functioned online during the experimental run as a monitoring and debugging tool. Figures 4.21 and 4.22 give examples of the spectrometers as seen by GEANT. In figure 4.21 some of the elements of the 2.75° spectrometer can be seen as they exist in GEANT. On this scale, the target appears as a small smudge within the scattering chamber on the left, with the magnets and collimators clearly visible on the right. A more detailed picture of the target cell as seen by GEANT can be seen in figure 4.11. Figure 4.22 shows a collection of monte carlo electron tracks as they pass through the magnets and collimators in the 5.50° spectrometers.

Using GEANT, the energy lost and the change in scattered angle by the scattered electrons due primarily to bremsstrahlung can be calculated for each electron track as its passes from the vertex to the spectrometers. Most of the electron's energy is lost as it passes through the dense side walls of the target. While the side walls are only approximately 0.075 cm thick, the small scattering angle creates a long interaction region, particularly for electron tracks in the 2.75° spectrometer. It is the difference in the length of side wall that electrons pass through from the different components of the target which gives rise to the external radiative corrections after. Electrons from the upstream glass window must pass through the side wall to get to the spectrometers, while only some of the electrons from the ^{3}He must pass through the side wall, and none of the electrons from the downstream glass window must pass through the side wall. The GEANT package uses the screened Bethe-Heitler

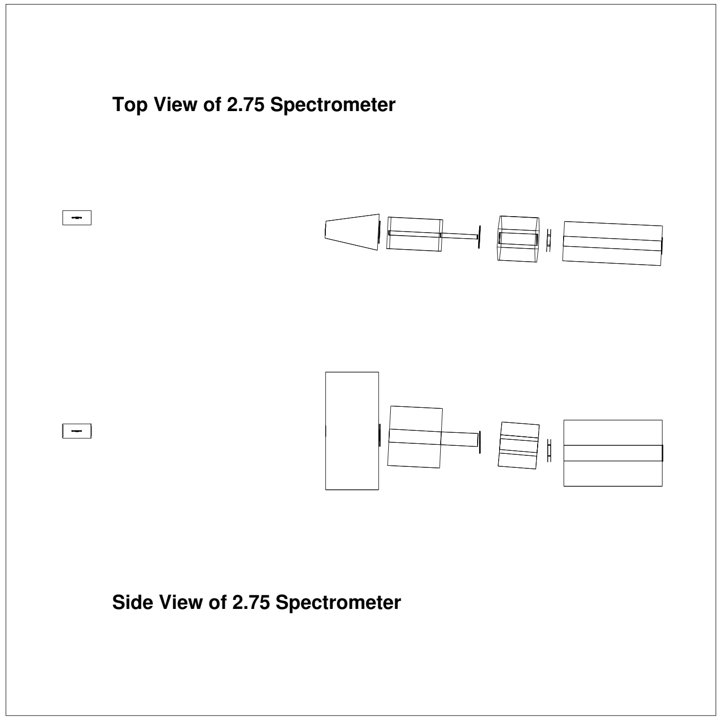

Figure 4.21: GEANT picture of the SLAC experiment E154 target, magnets and collimators in the 2.75° spectrometer.

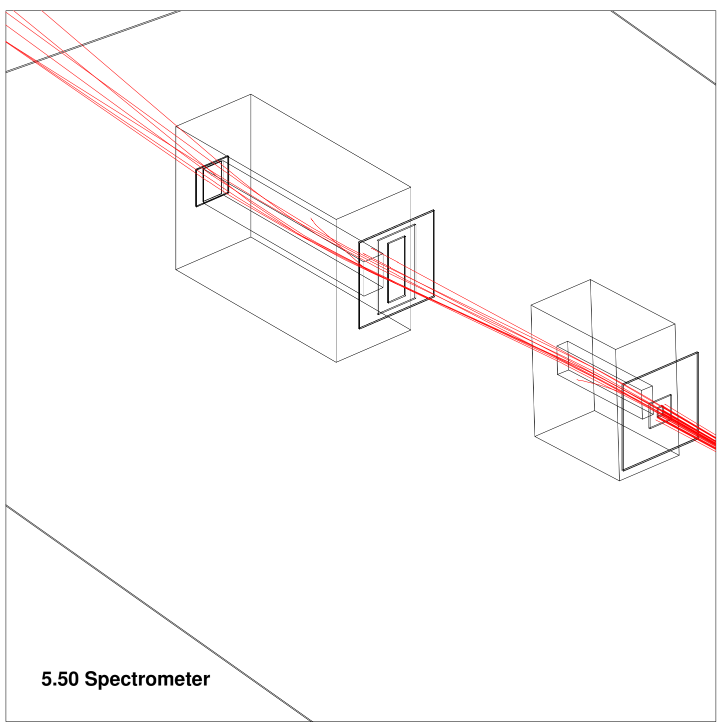

Figure 4.22: Tracks in the 5.50° spectrometer as simulated by GEANT.

cross section with Midgal corrections for the bremsstrahlung interaction. This cross section is accurate to 5%–6%, and since it treats electrons from all components of the target equally, the error in the dilution factor due to the bremsstrahlung cross section is negligible.

The limit on our knowledge of the external corrections after is statistical, depending on the number of tracks that were used in the GEANT monte carlo. A total of approximately 500 million tracks were used for the monte carlo, not only to generate the dilution factor, but also to study the dependence of the dilution factor on the target parameters, such as the thickness of the side wall and the position of the flare (see section 4.3.2 for a description of the target). A large number of tracks was also needed to ensure that the acceptance of the spectrometers was properly taken into account. Electron tracks were generated over a solid angle greater than the acceptance of the spectrometer to allow bremsstrahlung interactions to 'kick' electrons into or out of the spectrometer acceptance. Enough electron tracks were used in the monte carlo to reduce the statistical error to approximately the 0.5% level in most of the x-bins.

There is an additional error on the external radiative corrections after from the target parameters, and this error is limited by the statistics with which the monte carlo was run while varying the various target parameters. The target parameters that were studied were the thickness of the side walls, the position of the flare, the thickness of the wall within the flare, and the size of the glass weld that held the end windows onto the cell (see section 4.3.2 for a description of the target). While varying these parameters, the change in the dilution factor was consistent with zero for all of them except the thickness of the side wall. The statistical error for those target parameters that did not change the dilution factor will be taken as the standard deviation of the distribution around zero. This gives an error of 0.2%–0.3% for most of the x-bins. Particular attention was paid to the position of the flare, since there is the unfortunate possibility that the flare might fall into the center of the acceptance of the 2.75° spectrometer. No significant change in the dilution factor was found for any position of the flare from 103.75 cm to 116.25 cm within the statistical error of the monte carlo. For the thickness of the side wall, the error on the dilution factor will be taken to be the sum of the magnitude of the change in the dilution factor with respect to the side wall thickness plus the statistical error, multiplied by the error in the thickness of the side wall. Since the error in the thickness of the side wall is only 0.01 cm, the contribution to the error in the dilution factor is negligible. The error in the external radiative correction after is given in table 4.19, with the percentage error given referenced to the SLAC E154 target Picard.

2.75° spectrometer		
x	Q^2 (GeV/c)^2	$(\mathrm{d}f_3/f_3)$
0.017	1.2	0.8%
0.025	1.6	0.7%
0.035	2.1	0.7%
0.049	2.6	0.6%
0.077	3.3	0.6%
0.122	4.1	0.7%
0.172	4.7	0.8%
0.242	5.1	0.9%
0.341	5.5	1.0%
0.425	5.9	1.3%
0.519	6.1	1.3%

5.50° spectrometer		
x	Q^2 (GeV/c)^2	$(\mathrm{d}f_3/f_3)$
0.057	4.0	1.8%
0.084	5.5	0.6%
0.123	7.2	0.5%
0.173	8.9	0.6%
0.242	10.7	0.5%
0.342	12.5	0.6%
0.442	13.8	0.6%
0.638	15.6	0.6%

Table 4.19: Error on the dilution factor from external radiative corrections after scattering.

The internal radiative corrections were calculated using best fits to the world's data for unpolarized elastic, quasi-elastic, and inelastic scattering as well as the calculated ratios for the higher order deep inelastic scattering cross sections to the Born cross section. Above approximately 3 (GeV/c)^2, the cross section for the elastic, quasi-elastic, and inelastic scattering processes has fallen significantly and the internal radiative corrections are dominated by the higher order deep inelastic scattering interactions. These have been calculated using up to fourth order corrections in α. For the interactions above approximately 3 (GeV/c)^2, the difference between a quark in ^{3}He and in glass is insignificant, and the dilution factor is unchanged by the inclusion of the internal radiative correction. At low Q^2, however, the soft processes of elastic, quasi-elastic, and inelastic scattering become important and the differences between the form factors for ^{3}He and glass cause a substantial correction to the dilution factor. Estimating the error in the internal radiative corrections is difficult at these low values of Q^2, and to be conservative, the size of the internal radiative correction has been taken as the error. The error on the internal radiative correction is given in table 4.20, with the percentage error given referenced to the SLAC E154 target Picard.

2.75° spectrometer		
x	Q^2 (GeV/c)^2	$(\mathrm{d}f_3/f_3)$
0.017	1.2	5.8%
0.025	1.6	3.1%
0.035	2.1	1.6%
0.049	2.6	0.7%
0.077	3.3	0.2%
0.122	4.1	0.2%
0.172	4.7	0.2%
0.242	5.1	0.2%
0.341	5.5	0.1%
0.425	5.9	0.1%
0.519	6.1	0.1%

5.50° spectrometer		
x	Q^2 (GeV/c)^2	$(\mathrm{d}f_3/f_3)$
0.057	4.0	0.2%
0.084	5.5	0.2%
0.123	7.2	0.2%
0.173	8.9	0.2%
0.242	10.7	0.2%
0.342	12.5	0.1%
0.442	13.8	0.1%
0.638	15.6	0.1%

Table 4.20: Error on the dilution factor from internal radiative corrections.

When calculating the rate at which an electron event was generated for a given electron track, it is necessary to evaluate the structure function and the internal radiative correction for the E' and θ of the track. This is complicated by the loss of energy by the electrons before scattering due primarily to bremsstrahlung in the target material traversed before scattering. The initial beam energy is no longer a delta function at 48.3 GeV, but is instead a distribution highly peaked at 48.3 GeV, with a long tail trailing down to lower energies. The rate for an electron track at a particular E' and θ is then proportional to the probability for the electron to be at an initial energy multiplied by the structure function for that E, E' and θ, with

$$R(E',\theta) \propto \int_0^{E_0} P(E_0, E, X_{rad}) F_2(E, E', \theta) dE, \tag{4.63}$$

where $P(E_0, E, X_{rad})$ is the probability for an electron with an initial energy of E_0 to have an energy of E after passing through a thickness of material with a radiation length of X_{rad}.

The total radiation length of the SLAC experiment E154 targets was between 0.0015 and 0.0021. Being this thin, the difference between the value for the rate given by the integral in equation 4.63 and $F_2(E_0, E', \theta)$ is less than 0.2% for the upstream glass window, 0.7% for the ^{3}He, and 1.2% for the downstream glass window over the entire kinematic acceptance of the spectrometers. The average difference is approximately 1/3 of these values with these extremum occurring in the highest x-bins. The effect on the dilution factor for these modified rates is even smaller because of the symmetry of the SLAC experiment E154 target cells, namely a column of ^{3}He between two glass end windows. In this configuration, the average radiation length of the glass components of the target and the ^{3}He component are nearly equal. For the target cell with the greatest difference between the average radiation lengths for glass and ^{3}He, namely the SLAC E154 target cell Hermes with a downstream end window 26% thicker than its upstream end window, the average radiation length of the glass is 0.00081 and the average radiation length of the ^{3}He is 0.00072. Using this small difference in the average radiation lengths, the correction to the dilution factor for the target cell Hermes is estimated to be less than 0.1% when external radiation before scattering is included. The external radiative correction before scattering for the other target cells will be even smaller. Because of the small size of the effect, the correction was not made, and an additional error of 0.1% was included in the error in the dilution factor from the external radiative corrections before scattering.

4.7.3 Results

The results for the SLAC experiment E154 target Picard are plotted in figures 4.23 and 4.24. The error bars represent the total error which is the statistical error and systematic error added in quadrature. The shape of the dilution factor for the other targets is similar, and can be found plotted along with the results for the reference cell method of determining the dilution factor at the end of Chapter 5. The target cell Picard was chosen as an example to show the shape of the dilution factor because it is the most statistically significant of the SLAC experiment E154 target

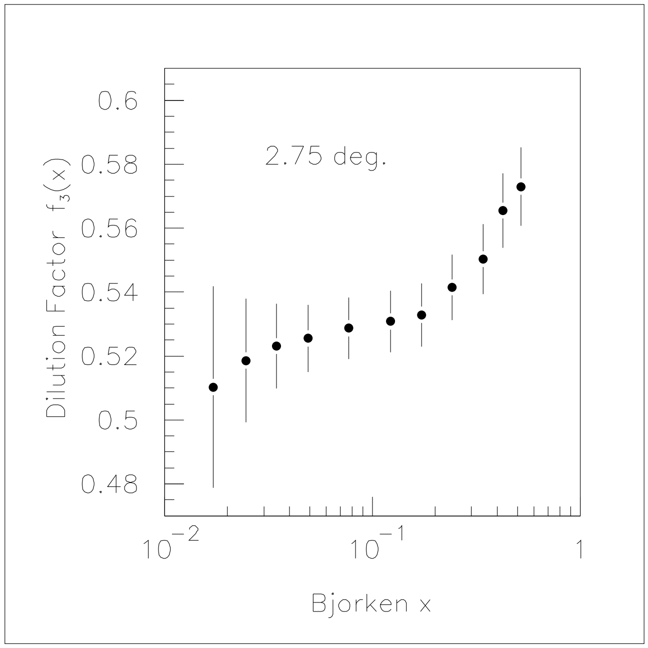

Figure 4.23: Dilution factor for the target cell Picard in the 2.75° spectrometer.

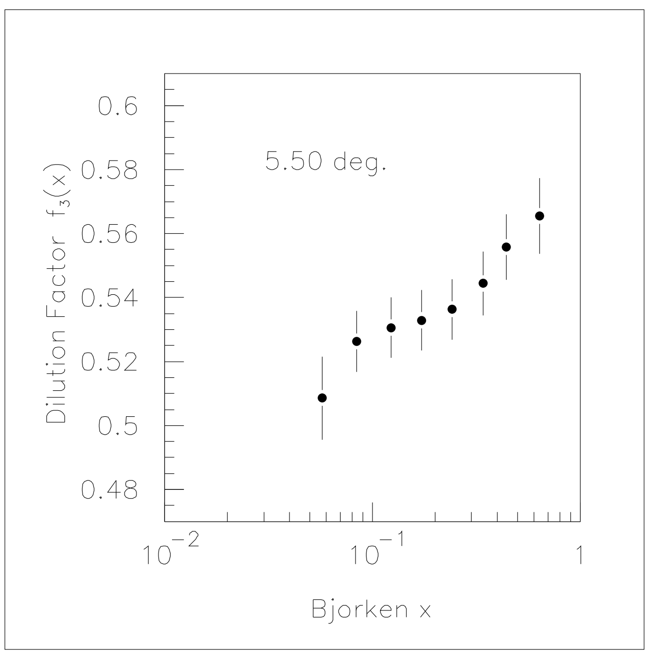

Figure 4.24: Dilution factor for the target cell Picard in the 5.50° spectrometer.

cells. The results for all of the SLAC experiment E154 targets in both spectrometers are given in tables 4.21–4.24. The target labeled g2 is the target cell Picard under the data taking conditions for perpendicular asymmetry running. Since the systematic error is highly correlated between targets, very little reduction occurs when the data from all nine targets are combined.

x	Q^2	Dave f_3	Dave $\mathrm{d}f_3$	Riker f_3	Riker $\mathrm{d}f_3$	Bob f_3	Bob $\mathrm{d}f_3$	SMC f_3	SMC $\mathrm{d}f_3$	Generals f_3	Generals $\mathrm{d}f_3$
0.017	1.2	0.576	0.030	0.531	0.034	0.499	0.032	0.512	0.032	0.543	0.031
0.025	1.6	0.585	0.019	0.540	0.023	0.509	0.020	0.522	0.020	0.552	0.019
0.035	2.1	0.589	0.013	0.545	0.018	0.513	0.014	0.527	0.014	0.556	0.013
0.049	2.6	0.591	0.011	0.547	0.016	0.515	0.011	0.528	0.012	0.558	0.011
0.077	3.3	0.594	0.010	0.550	0.015	0.518	0.010	0.531	0.011	0.561	0.010
0.122	4.1	0.594	0.010	0.551	0.015	0.519	0.010	0.532	0.011	0.561	0.010
0.172	4.7	0.596	0.010	0.553	0.015	0.522	0.011	0.535	0.012	0.563	0.010
0.242	5.1	0.604	0.010	0.562	0.016	0.531	0.011	0.544	0.012	0.571	0.011
0.341	5.5	0.612	0.011	0.570	0.016	0.540	0.012	0.553	0.012	0.579	0.011
0.425	5.9	0.626	0.012	0.585	0.016	0.556	0.012	0.569	0.013	0.593	0.012
0.519	6.1	0.633	0.012	0.592	0.017	0.563	0.013	0.576	0.014	0.600	0.012

Table 4.21: Dilution factor for the target cells Dave, Riker, Bob, SMC, and Generals in the 2.75° spectrometer.

x	Q^2	Dave f_3	Dave $\mathrm{d}f_3$	Riker f_3	Riker $\mathrm{d}f_3$	Bob f_3	Bob $\mathrm{d}f_3$	SMC f_3	SMC $\mathrm{d}f_3$	Generals f_3	Generals $\mathrm{d}f_3$
0.057	4.0	0.592	0.013	0.537	0.018	0.507	0.014	0.521	0.014	0.557	0.013
0.084	5.5	0.596	0.010	0.550	0.015	0.518	0.010	0.531	0.011	0.564	0.010
0.123	7.2	0.596	0.010	0.552	0.015	0.520	0.010	0.533	0.011	0.564	0.010
0.173	8.9	0.597	0.010	0.553	0.015	0.521	0.010	0.534	0.011	0.564	0.010
0.242	10.7	0.599	0.010	0.557	0.015	0.525	0.010	0.538	0.011	0.567	0.010
0.342	12.5	0.606	0.010	0.564	0.015	0.532	0.011	0.545	0.011	0.574	0.010
0.442	13.8	0.616	0.010	0.575	0.015	0.543	0.011	0.555	0.012	0.585	0.011
0.638	15.6	0.624	0.011	0.584	0.016	0.552	0.012	0.564	0.013	0.593	0.012

Table 4.22: Dilution factor for the target cells Dave, Riker, Bob, SMC, and Generals in the 5.50° spectrometer.

		Hermes		Prelims		Chance		Picard		g2	
x	Q^2	f_3	df_3	f_3	df_3	f_3	df_3	f_3	df_3	f_3	df_3
0.017	1.2	0.555	0.031	0.603	0.029	0.459	0.032	0.510	0.032	0.483	0.032
0.025	1.6	0.564	0.019	0.612	0.018	0.469	0.020	0.519	0.019	0.491	0.019
0.035	2.1	0.568	0.013	0.616	0.013	0.473	0.013	0.523	0.013	0.496	0.013
0.049	2.6	0.570	0.011	0.618	0.010	0.475	0.011	0.526	0.011	0.498	0.010
0.077	3.3	0.572	0.010	0.621	0.010	0.478	0.010	0.529	0.010	0.501	0.009
0.122	4.1	0.572	0.010	0.622	0.010	0.479	0.010	0.531	0.010	0.504	0.009
0.172	4.7	0.574	0.010	0.624	0.010	0.481	0.010	0.533	0.010	0.506	0.009
0.242	5.1	0.583	0.011	0.633	0.010	0.490	0.011	0.542	0.010	0.514	0.009
0.341	5.5	0.591	0.011	0.642	0.011	0.499	0.011	0.550	0.011	0.523	0.010
0.425	5.9	0.605	0.012	0.656	0.011	0.515	0.012	0.566	0.012	0.539	0.011
0.519	6.1	0.611	0.012	0.662	0.012	0.522	0.013	0.573	0.012	0.546	0.012

Table 4.23: Dilution factor for the target cells Hermes, Prelims, Chance, Picard, and g2 in the 2.75° spectrometer.

		Hermes		Prelims		Chance		Picard		g2	
x	Q^2	f_3	df_3	f_3	df_3	f_3	df_3	f_3	df_3	f_3	df_3
0.057	4.0	0.576	0.013	0.605	0.013	0.466	0.013	0.509	0.013	0.481	0.012
0.084	5.5	0.576	0.010	0.619	0.009	0.478	0.010	0.526	0.010	0.499	0.009
0.123	7.2	0.575	0.010	0.622	0.009	0.480	0.010	0.531	0.010	0.503	0.009
0.173	8.9	0.575	0.010	0.624	0.009	0.481	0.010	0.533	0.010	0.506	0.009
0.242	10.7	0.578	0.010	0.627	0.009	0.485	0.010	0.536	0.010	0.509	0.009
0.342	12.5	0.584	0.010	0.635	0.010	0.492	0.010	0.544	0.010	0.517	0.009
0.442	13.8	0.594	0.010	0.645	0.010	0.503	0.011	0.556	0.010	0.529	0.010
0.638	15.6	0.602	0.012	0.654	0.011	0.512	0.012	0.566	0.012	0.538	0.011

Table 4.24: Dilution factor for the target cells Hermes, Prelims, Chance, Picard, and g2 in the 5.50° spectrometer.

CHAPTER V

Data Analysis

5.1 Overview

The data analysis for SLAC experiment E154 was performed in parallel by two separate groups which were at SLAC and at Caltech. Both groups used the same data and analyzed the data using the same general procedure, but differed in some of their analysis techniques. The analysis presented in this thesis was done at SLAC using the SLAC data.

The data taken for SLAC experiment E154 during October and November of 1995 were written to magnetic tape in the SLAC computing center's tape silo. A total of 1.4 TBytes of data in the form of 1800 runs were written to tape with each run typically being 200,000 spills. or approximately thirty minutes long. The 1800 data runs were composed of electron asymmetry data in both parallel and perpendicular configurations, reference cell data for determining the ^{3}He dilution in the target, asymmetry data with the magnets reversed for determining charge symmetric backgrounds, and data taken during calibrations and testing.

The data analysis was performed in three steps. In the first step the raw data tapes were searched for Cherenkov hits, shower clusters, and tracks in each spectrometer. These data were written to the Data Summary Tapes (DSTs) along with the beam information. This first step reduced the amount of data by a factor of approximately six. In the second step, the information on the DSTs was used to select electron events and bin them in x and Q^2 for each beam helicity. The data from the second step were written to a set of summary files. In the third step, the data in the summary files were analyzed to produce the physics asymmetries and spin structure functions.

5.2 Cherenkovs

The output of the photomultiplier tube on each of the Cherenkov tanks was digitized and recorded by the flash ADCs (flash analog to digital converter) for the entire electron spill. Analysis of the Cherenkov data consisted of searching the data for pulses by looking for discontinuities in the derivative of the photomultiplier tube signal. Once a pulse was found, it's height, area, and time were determined. Before proceeding to look for the next pulse in time, an average Cherenkov pulse shape, scaled by the height of the pulse, was subtracted from the Cherenkov data. The time of the pulse was determined using the timing data from both the flash ADCs and the TDC (time to digital converter), and the time resolution was 0.8 ns. The effective deadtime of the Cherenkov detector was 5 ns.

5.3 Shower Counters

Each of the lead glass blocks in the shower counter was equipped with an ADC that recorded the integrated charge from the photomultiplier tube for the entire spill. Each lead glass block also had at least one multi-hit TDC to record the leading edge time and the trailing edge time of the photomultiplier tube pulses. In this way, the total energy deposited in each block and the time at which the energy was deposited were recorded. Analysis of the shower counter data consisted of searching the array of lead glass blocks for clusters that overlapped in time and space. This was made difficult, especially in the 2.75° spectrometer, because of the high instantaneous rate that often resulted in more than one electromagnetic shower per spill. To increase the efficiency of the spectrometer, those portions of the spectrometer that had the highest rate were instrumented with 3 TDCs set to different discriminator thresholds rather than the usual 1 TDC.

Clusters were located in the shower counter data using a 'cellular automaton' program that searched the blocks first for cells in time [82]. A cell is found in any lead glass block that has both a leading edge and a trailing edge time, and more than one cell might be found in the same lead glass block so long as it is separated by at least 17 ns. If more than one cell is found in a block, then the total energy measured by the ADC is 'shared' between the cells by using the length of the pulse in time as measured by the leading edge and trailing edge times. The relationship between the pulse lengths and the total energy deposited in a lead glass block was determined using a clean sample of electrons. Once all of the cells have been found, and if necessary, the energy has been 'shared' between them, they are searched in 2D space and time to find those blocks that belong to the same cluster. Each cluster will have a central block and eight nearest neighbors. Once the cluster has been constructed, the centroid is found using an energy weighted average of the nine blocks in the cluster, and the time is found by averaging the leading edge TDC time of the central block and the neighboring blocks that have an energy of at least 10% of the central block. The resolution of the shower counter for tracking was 1.0 cm in space and 0.9 ns in time.

To aid in the identification of electrons, the shape of the electromagnetic shower in the shower counters was studied. The profile for an electron that develops into an electromagnetic shower is significantly different from a pion, which undergoes strong interactions and creates hadronic showers. To analyze the shower profile, a multi-layered 'neural network' program was created that could analyze the shower counter data in a non-linear fashion to maximize the sensitivity to electron identifying characteristics and pion identifying characteristics [82]. Rather than using a set of predetermined coefficients for the relative weights of the input parameters, the 'neural network' was 'trained' on a sample of pions so that the coefficients that provided the maximum sensitivity could be found. The 'neural network' code returned a value for each cluster that was between -1 for a pion and +1 for an electron.

5.4 Hodoscopes and Tracking

Since there are no magnets after the first Cherenkov tank, the track of a particle from the first Cherenkov tank to the shower counter is a straight line. Because the magnets before the Cherenkov tanks create a one-to-one mapping of the particle track position to particle momentum, tracks in the spectrometer can be used to measure the momentum of a particle that passes through the spectrometer. We identify particle tracks using a combination of the Cherenkov counters, the hodoscope planes, and the shower counters. The tracking algorithm begins by using the Cherenkov data and the shower counter data to create an initial track position and time for a candidate track. Then the hodoscope elements that have hits that correspond in time are identified and used to create tracks. The timing information of the hodoscope elements is one of the most important inputs for the tracking algorithm and for this reason, it was necessary to correct the hodoscope TDC time for the time delay caused by the propagation of light from the particle track location to the photomultiplier tube. Once the hodoscope elements that correspond in time are identified, they are required to pass a broad kinematic cut. A fitting routine then adjusts the location of the track in time and space to minimize the χ^2 for the track in the remaining hodoscope hits and in the shower counter and Cherenkov tanks. The overall electron reconstruction efficiency is estimated to be 70–80 %.

5.5 Run Selection and Beam Cuts

Not every run written to tape was used for the asymmetry analysis. A number of runs were rejected for one or more reasons such as low target polarization, beam problems, data acquisition problems, and short run length. In all, a total of approximately 1000 runs were used for the asymmetry analysis. Polarized target runs for which the ^{3}He polarization was less than 25% were not used in the data analysis. These runs typically occurred early in the 'spin-up' of a cell or during target tests when the target polarization was changing. A histogram of the polarization of the target for SLAC experiment E154 can be seen in figure 5.1. The cut removed a total 190 runs and had a negligible impact on the overall statistics of SLAC experiment E154.

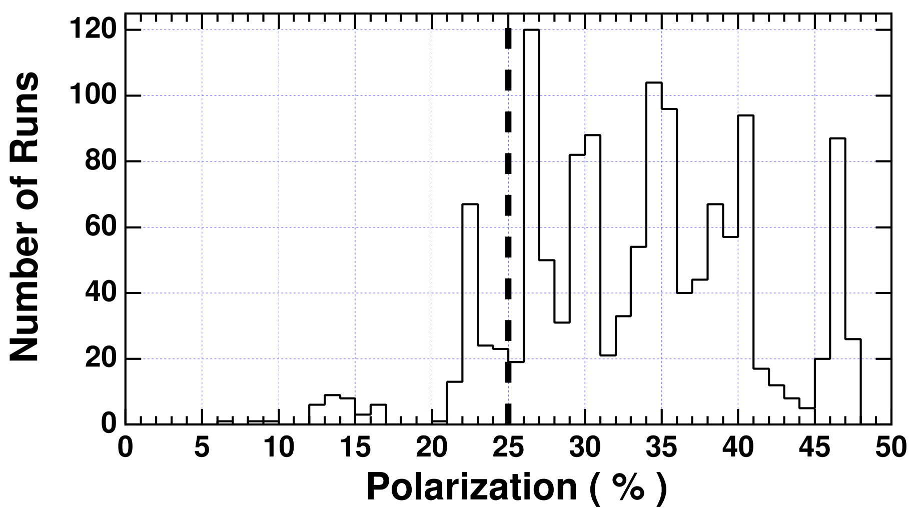

Figure 5.1: Histogram of target polarization.

A number of runs were identified as bad and removed from the data sample due to observations of unsatisfactory beam or data acquisition conditions by the experimenter. These included periods of noticeable unstable beam, data acquisition hardware failures and tests, and data acquisition control program software problems. Runs shorter than 30,000 spills, (as compared to a typical run size of 200,000 spills), were also removed. This eliminated 270 runs from the data sample.

The charge and the beam position asymmetry were also used to remove runs from the data sample. Because the raw asymmetry is only on the order of 10^{-3}, it is important to maintain the beam asymmetries below a level that would allow them to create a systematic effect on the asymmetry data. This meant keeping the beam charge asymmetry below 10^{-3} for every run. A total of 34 runs were eliminated because they had a beam charge asymmetry greater than 5×10^{-3}. The thickness of the cell changes slowly with beam position and achieving a position dependent asymmetry of less than 5×10^{-5} would require the position of the beam for the two polarization states to be within 0.1 mm. A conservative cut of 0.004 mm in the average x position of the two helicities and 0.005 mm in the average y position of the two helicities was used since it meant only cutting 33 data runs from the asymmetry analysis.

The polarization of the electron beam was monitored using four separate signals, the PMON line, the Mach line, the Pockels Cell High Voltage line, and the Veto bits. The polarization of the electron beam could also be predicted because the algorithm used by the pseudo-random number generator to determine the electron polarization was known. Careful attention was paid to the polarization of the electron beam because of problems in the analysis of SLAC experiment E142 that were related to the electron beam polarization. All five methods of determining the electron beam polarization were required to agree to better than 10^{-3} in each run of approximately 200,000 spills. For 18 runs, the five methods disagreed above this limit and were not used in the asymmetry analysis.

A number of beam cuts were used while analyzing the data to discard those spills that were more than 4σ beyond the average value. These cuts were placed on the beam monitoring devices: the beam position on the traveling wave beam position monitors, the beam position on the wire arrays, the beam width on the wire arrays, the ‘good spill’ ADC, the ‘bad spill’ ADC, and the amount of charge in a spill.

5.6 Electron Identification

Electrons were identified in the spectrometers using a combination of requirements from each of the individual detectors. The identification process can be seen for the 2.75° spectrometer in figure 5.2 as the candidate events are passed through the cuts. The upper left plot shows the number of events as a function of E/p for each event that had a pulse in at least one Cherenkov tank, a shower in the shower counter, and a track in the spectrometer. The value of E is determined by the cluster in the shower counter and the value of p is determined by the track in the hodoscopes. The upper right plot shows the events that remain after requiring that the energy of the cluster in the shower counter be greater than 7.5 GeV. This eliminates a great number of pions which do not deposit their full energy in the shower counter, but no electrons from the target since the minimum energy for an electron shower is approximately 10 GeV. The lower left plot shows the events that remain after requiring that both Cherenkov tanks have a pulse greater than 1.5 photoelectrons. This Cherenkov cut is a compromise between pion rejection and electron efficiency, and significantly reduces the number of pions remaining in the sample. The lower right plot shows the events that remain after requiring that the neural net identify them as an electron with a high degree of probability. Additional cuts placed on the data include an E/p cut of $0.8 < E/p < 1.2$, an acceptance cut, and the kinematic cuts of $1\ (\mathrm{GeV/c})^2 < Q^2 < 25\ (\mathrm{GeV/c})^2$ and $W^2 > 8\ \mathrm{GeV}^2$.

5.7 Reference Cell Analysis

At the end of Chapter 4, a model of the SLAC experiment E154 target cells was constructed for the purpose of determining the dilution factor of the target. In this section, a second method of determining the number of events that originated in the ^{3}He is presented. Combining equations 4.56 and 4.57 for the ^{3}He asymmetry and the

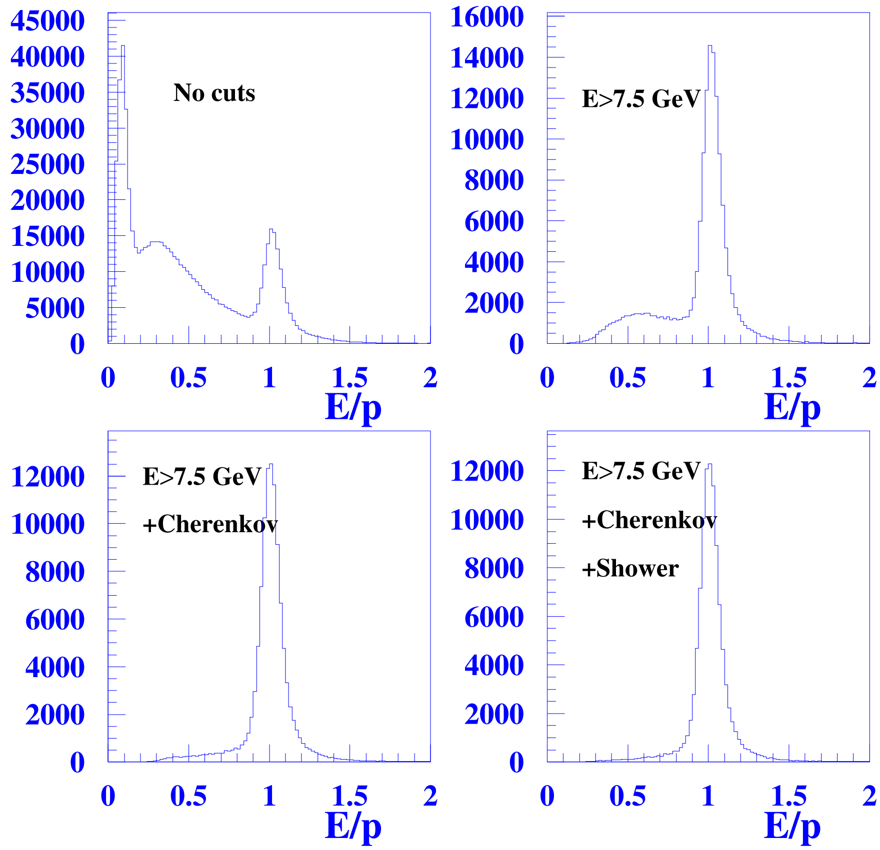

Figure 5.2: Series of cuts used for electron identification.

dilution factor gives

$$A_3(x,Q^2) = \frac{A_{raw}(x,Q^2)N_{\text{total}}(x,Q^2)}{P_{3t}P_B N_3(x,Q^2)}, \tag{5.1}$$

where $A_{raw}(x,Q^2)$ is the measured raw asymmetry, $N_{\text{total}}(x,Q^2)$ is total number of events from the target, P_{3t} is the polarization of the ^{3}He in the target cell, P_B is the polarization of the electron beam, and $N_3(x,Q^2)$ is the number of events from the ^{3}He. The measured raw asymmetry is the ratio of the difference in the number of events for the two spin states to the sum of the number of events for the two spin states. This gives an immediate cancellation between the denominator of $A_{raw}(x,Q^2)$ and $N_{\text{total}}(x,Q^2)$ on a run by run basis. All that is required to measure the ^{3}He dilution factor is to determine the number of events from the ^{3}He.

To determine the number of events from the ^{3}He, a variable pressure reference cell was filled with ^{3}He and substituted for the polarized ^{3}He target. The reference cell was identical in design to the polarized ^{3}He target cells. By measuring the number of events from the reference cell as a function of ^{3}He thickness (Ln), the density and length of the polarized ^{3}He target cells could be used to determine the number of events from the ^{3}He. This method requires no radiative corrections as the number of events from ^{3}He are being measured directly by the spectrometers. The disadvantage of using the reference cell to measure the dilution factor is that the efficiency of the spectrometers increases with decreasing rate. What must be known is the number of events that originated in the ^{3}He under normal running conditions. This means that a rate dependent correction must be applied to the number of events measured in the spectrometers whenever the thickness of the reference cell is not the same as the thickness of the polarized ^{3}He target, such as when the reference cell is evacuated.

Without the rate dependent correction, the number of events per incident electron from the ^{3}He is

$$N_3(x, Q^2) = m(x, Q^2) n_3 L_3, \tag{5.2}$$

where n_3 is the density of the polarized ^{3}He target cell, L_3 is the length of the polarized ^{3}He target cell, and the slope $m(x, Q^2)$ is the number of events per target thickness given by

$$m(x, Q^2) = \frac{N_B(x, Q^2) - N_A(x, Q^2)}{(n_B - n_A) L_{ref}}, \tag{5.3}$$

where $N_A(x, Q^2)$ and $N_B(x, Q^2)$ are the measured number of events from the reference cell filled with ^{3}He to a density of n_A and n_B, respectively, and L_{ref} is the length of the reference cell. The density of the reference cell was calculated by measuring its pressure and temperature and using the ideal gas law.

The error on the number of events from the ^{3}He depends in part on a number of parameters that are both independent of x and the target. These parameters are the length of the polarized ^{3}He target cell, the length of the reference cell, the density of the polarized ^{3}He target cell, the temperature of the reference cell, and the pressure of ^{3}He in the reference cell. The error due to these parameters is given in table 5.1.

Equation 5.3 for the slope assumes that the number of events per amagat of ^{3}He

quantity	L_3	L_{ref}	n_3	T_t	P_{ref}
$\frac{dq}{q} = \frac{dN_3(x,Q^2)}{N_3(x,Q^2)}$	0.7%	0.7%	1.9%	0.9%	0.5%

Table 5.1: Reference cell analysis errors that are independent of target and x-bin.

will be measured using only two data runs. In actuality, there were a number of reference cell data runs, typically in groups of two or three, with typical densities of approximately 10 and 0 amagats or 10, 5 and 0 amagats. These reference cell data runs are usually referred to as full, half-full, and empty. A group of reference cell runs was referred to as a reference cell scan, and a reference cell scan was done typically once every few days. In analyzing the reference cell data runs, two methods were used to find the slope. In the first, all of the reference cell data runs taken during the experimental running period of a polarized ^{3}He target cell were used to find the slope. In the second, each pair of reference cell runs that occurred back-to-back were used to find the slope at that moment, and then all of the slopes for a particular polarized ^{3}He target were averaged together. The difference in the results for the two methods is much smaller than the error, indicating that there were no significant fluctuations in spectrometer efficiency during the data taking lifetime of an individual polarized ^{3}He target cell. For the analysis of the reference cell data runs to be detailed subsequently, the second method using back-to-back runs was employed.

5.7.1 Rate Dependence

The efficiency of the spectrometers was studied as a function of rate, which is linearly dependent on target thickness. The number of events from ^{3}He measured in the spectrometers is proportional to the rate multiplied by the efficiency of the spectrometers, where the efficiency decreases with increasing rate due to increasing event overlap. The equation for the slope $m(x, Q^2)$ is then

$$m(x,Q^2) = \frac{N_B(x,Q^2)\left(1+\alpha\left(\frac{t_3-t_B}{t_3}\right)\right) - N_A(x,Q^2)\left(1+\alpha\left(\frac{t_3-t_A}{t_3}\right)\right)}{(n_B-n_A)L_{ref}} \tag{5.4}$$

where the spectrometer efficiency has been normalized to 1 at a rate equal to that of the polarized ^{3}He target, with thickness $t_3 = (n_3 + n_{N2})L_3 + n_{gl}(L^3_{gu} + L^3_{gd})$. The thickness of the reference cell is $t_B = n_B L_{ref} + n_{gl}(L^{ref}_{gu} + L^{ref}_{gd})$ when the ^{3}He density in the reference cell is n_B and $t_A = n_A L_{ref} + n_{gl}(L^{ref}_{gu} + L^{ref}_{gd})$ when the ^{3}He density in the reference cell is n_A. The linear change in spectrometer efficiency with target thickness is given by the coefficient α.

The coefficient α for each target was found using a method termed 'pulse fiction' [83]. In this method, the raw data forms for a spill in each of the individual detectors from two different runs were combined to create single data forms with twice the number of events. The raw data forms were then analyzed to determine the number of events at twice the rate, and the loss of events was used to determine the change in spectrometer efficiency. The coefficient α is then

$$\alpha = \frac{N_{12}(x,Q^2) - (N_1(x,Q^2) + N_2(x,Q^2))}{(N_1(x,Q^2) + N_2(x,Q^2))}, \tag{5.5}$$

where $N_1(x, Q^2)$ is the number of events found from data run 1, $N_2(x, Q^2)$ is the number of events found from data run 2, and $N_{12}(x, Q^2)$ is the number of events found from the data set created by combining the individual raw wave forms from data sets 1 and 2.

The determination of the rate dependent α coefficient for each polarized ^{3}He target is statistically limited, but can be found to better than 0.5% using the 100 or so data runs for each polarized ^{3}He target. The sign of α is negative and the magnitude of α varies from 6%–13% in the 2.75° spectrometer, and from 2%–5.5% in the 5.50° spectrometer, and it has a mild x dependence. The magnitude of α decreased with time as the instantaneous rate decreased with decreasing beam current. The instantaneous rate for Chance was higher than Prelims and Picard due to its thick end windows.

The value of α is calculated using the efficiency of the spectrometers at a rate equal to that of the polarized ^{3}He target and twice that of the polarized ^{3}He target. This value is extrapolated to the rates for the reference cell, from approximately half the rate of the polarized ^{3}He target to the rate of the polarized ^{3}He target. To be conservative, it is assumed that the error on this rate dependent correction to the number of events from ^{3}He is as large as the correction. Since the correction and its error are significantly larger than the mild x dependence in α, the mild x dependence in α is ignored and the average value of α is used for each target. The value of α and its contribution to the error in the slope m is given in table 5.2.

	2.75° spectrometer		5.50° spectrometer	
Target	α	dm/m	α	dm/m
Dave	-0.128	6.4%	-0.056	2.8%
Riker	-0.110	5.5%	-0.046	2.3%
Bob	-0.090	4.5%	-0.048	2.4%
SMC	-0.076	3.8%	-0.044	2.2%
Generals	-0.060	3.0%	-0.034	1.7%
Hermes	-0.080	4.0%	-0.032	1.6%
Prelims	-0.070	3.5%	-0.028	1.4%
Chance	-0.086	4.3%	-0.040	2.0%
Picard	-0.078	3.9%	-0.018	0.9%

Table 5.2: Target dependent error for the reference cell analysis.

5.7.2 Background Subtraction

The number of events from ^{3}He contains not only the scattered electrons from the deep inelastic scattering processes, but also electrons from charge symmetric processes (pair production), as well as a small number of misidentified pions. For most of the x-bins, the fraction of measured events that are electrons is nearly one, but in the lowest x-bins, the fraction of events that are electrons that are from deep inelastic scattering processes falls to as low as 0.88. If the fraction of the number of events from the ^{3}He that were from charge symmetric processes and misidentified pions were to remain constant for all pressures of the reference cell, then no correction would need to be applied to the slope $m(x, Q^2)$. However, the number of electrons from charge symmetric processes was measured to be 16% larger for an empty reference cell than for a full reference cell. Assuming the correction to be linear with target thickness, the formula for the slope $m(x, Q^2)$ is then

$$\begin{aligned} m(x,Q^2) &= \left(N_B(x,Q^2)\left(1+\alpha\left(\tfrac{t_3-t_B}{t_3}\right)\right)\left(1+\beta\left(\tfrac{t_3-t_B}{t_3}\right)\right)\right. \\ &\left. -N_A(x,Q^2)\left(1+\alpha\left(\tfrac{t_3-t_A}{t_3}\right)\right)\left(1+\beta\left(\tfrac{t_3-t_A}{t_3}\right)\right)\right)(n_B-n_A)^{-1}L_{ref}^{-1}, \end{aligned} \tag{5.6}$$

where β is the dimensionless correction for differences in the amount of background events. Most likely, the difference in the number of charge symmetric events is caused by the difference in the average interaction length of the target after scattering. The average interaction length of the target after scattering decreases linearly with ^{3}He density as the average interaction length of the target after scattering for a particle originating in the ^{3}He is less than that for the glass of the empty reference cell. This reduction in the amount of moderator should lead to a reduction in pair production. To be conservative, the size of the change in the slope will be used as the error on the slope due to the background subtraction correction, even though this error is larger than the propagation of the measured errors for the number of charge symmetric events from the empty and full reference cell. The size of the effect and the error on the slope can be seen in table 5.3.

2.75° spectrometer		
x	Q^2 (GeV/c)^2	(dm/m)
0.017	1.2	1.7%
0.025	1.6	0.7%
0.035	2.1	0.3%
0.049	2.6	0.3%
0.077	3.3	0.1%
0.122	4.1	0.0%
0.172	4.7	0.0%
0.242	5.1	0.0%
0.341	5.5	0.0%
0.425	5.9	0.0%
0.519	6.1	0.0%

5.50° spectrometer		
x	Q^2 (GeV/c)^2	(dm/m)
0.057	4.0	0.8%
0.084	5.5	0.2%
0.123	7.2	0.1%
0.173	8.9	0.0%
0.242	10.7	0.0%
0.342	12.5	0.0%
0.442	13.8	0.0%
0.638	15.6	0.0%

Table 5.3: Error on the slope due to background subtraction.

5.7.3 Results and Comparison to Target Model

Eliminating the terms second order in target thickness, the equation for the slope becomes

$$m(x,Q^2) = \frac{N_B(x,Q^2)\left(1+(\alpha+\beta)\left(\frac{t_3-t_B}{t_3}\right)\right) - N_A(x,Q^2)\left(1+(\alpha+\beta)\left(\frac{t_3-t_A}{t_3}\right)\right)}{(n_B-n_A)L_{ref}}. \tag{5.7}$$

In order to compare the results of the reference cell analysis for the slope and the number of events from the ^{3}He with the dilution factor from the target model it is necessary to use the total number of events for each target as given by equation 4.57. The total number of events for each target has been calculated using the same selection of runs that have been used for the asymmetry analysis, and the same analysis code as that used for the asymmetry analysis. This is also the same analysis code that was used to extract the number of events from the ^{3}He for the reference cell runs used in the reference cell analysis. The comparison between the two methods of calculating the dilution factor is shown in figures 5.3–5.11. For most of the targets, the error is limited by the rate correction in the low x-bins of the 2.75° spectrometer, and by statistics in the high x-bins of the 2.75° spectrometer and in the 5.50° spectrometer. For a few of the targets, only one reference cell scan was performed, and for these targets, the statistical error in the 2.75° spectrometer is comparable to the rate correction error in the low x-bins. For a few of the targets, many reference cell scans were performed, and for these targets, the statistical error in the 2.75° spectrometer and the 5.50° spectrometer is comparable to the rate correction error. As an example of the statistical error on the slope $m(x, Q^2)$, the error due to statistics on the slope $m(x, Q^2)$ for the target cell Picard is given in table 5.4. There were 4 reference cell scans of 2 runs each for the target cell Picard.

2.75° spectrometer		
x	Q^2 (GeV/c)^2	(dm/m)
0.017	1.2	2.0%
0.025	1.6	1.6%
0.035	2.1	1.9%
0.049	2.6	1.7%
0.077	3.3	1.7%
0.122	4.1	2.3%
0.172	4.7	3.0%
0.242	5.1	3.2%
0.341	5.5	5.3%
0.425	5.9	8.5%
0.519	6.1	17.3%

5.50° spectrometer		
x	Q^2 (GeV/c)^2	(dm/m)
0.057	4.0	25.8%
0.084	5.5	3.6%
0.123	7.2	3.1%
0.173	8.9	4.2%
0.242	10.7	4.1%
0.342	12.5	6.9%
0.442	13.8	10.1%
0.638	15.6	15.2%

Table 5.4: Error on the slope m of the target cell Picard due to counting statistics.

The statistical error on the dilution factor from the reference cell method will be reduced when more than one target is used to calculate the asymmetry. The error on the target model, however, remains nearly the same. In order to compare the effect that the two methods for determining the dilution factor have on the final answer for the asymmetry, the average dilution factor has been calculated for the two methods. To calculate the average dilution factor, the dilution factor for each target was weighted using the same weighting for each run as was used for the asymmetry analysis. The result for the average dilution factor for each target can be seen in figure 5.12. The results for the reference cell analysis are lower than those for the target model in the first three x-bins of the 2.75° spectrometer, and higher in the other x-bins of the 2.75° spectrometer, while being typically lower than the target model in the 5.50° spectrometer. When the two spectrometers are combined, the results for the dilution factor are in good agreement between the two methods in all but the lowest two x-bins. The error on the reference cell method is significantly larger than the error on the target model in all but the lowest two x-bins. Regrettably, these are also the two most important x-bins for extrapolating the g_1 results to low x. In the lowest two x-bins, the value for the target model is 0.536 ± 0.031 and 0.546 ± 0.019; the results for the reference cell analysis are 0.527 ± 0.029 and 0.535 ± 0.026. For the asymmetry analysis, the results of the target model were used since the error on the target model is smaller and the χ^2 between the two models is much less than one.

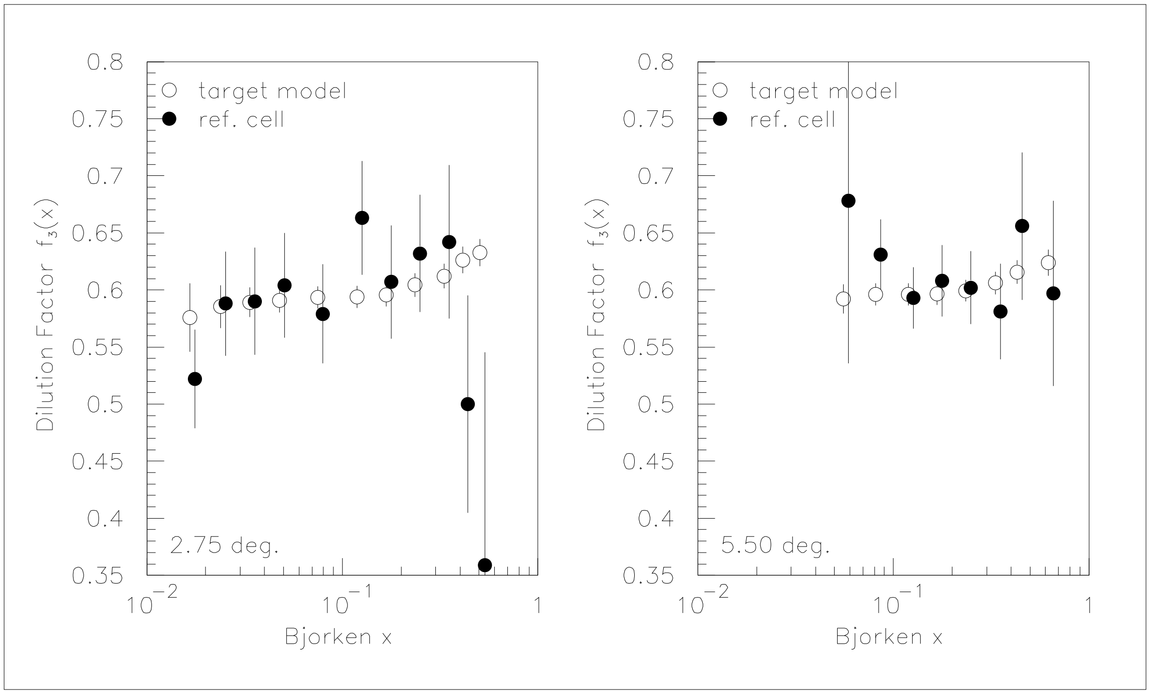

Figure 5.3: Dilution factor for the target cell Dave.

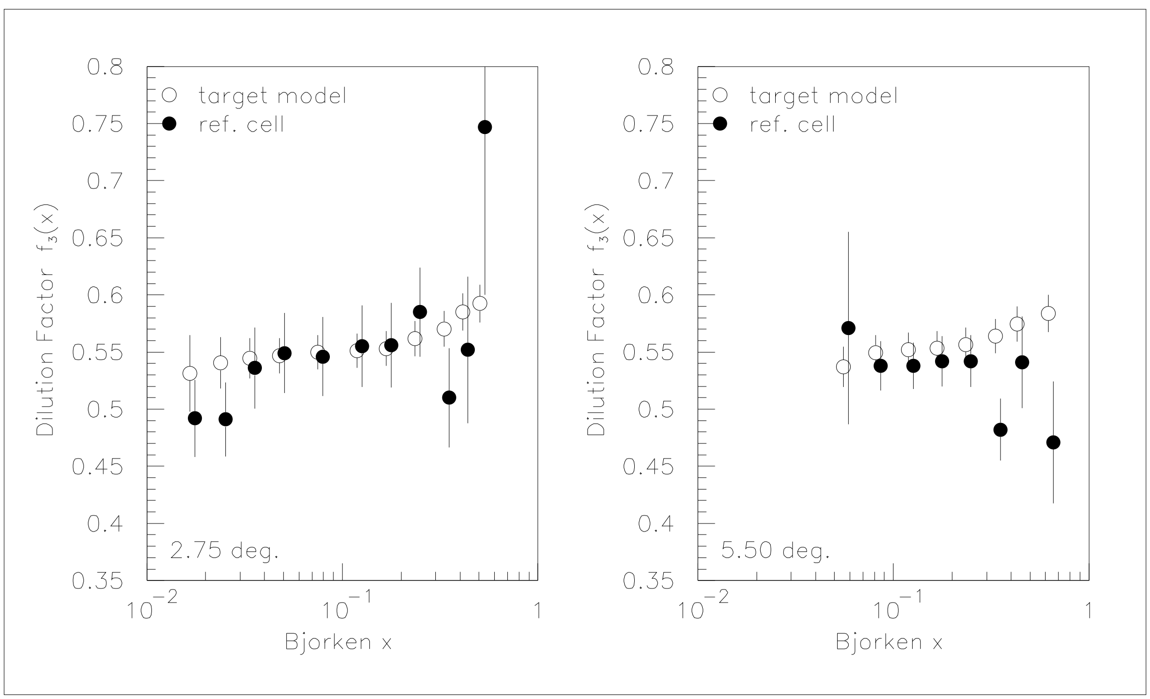

Figure 5.4: Dilution factor for the target cell Riker.

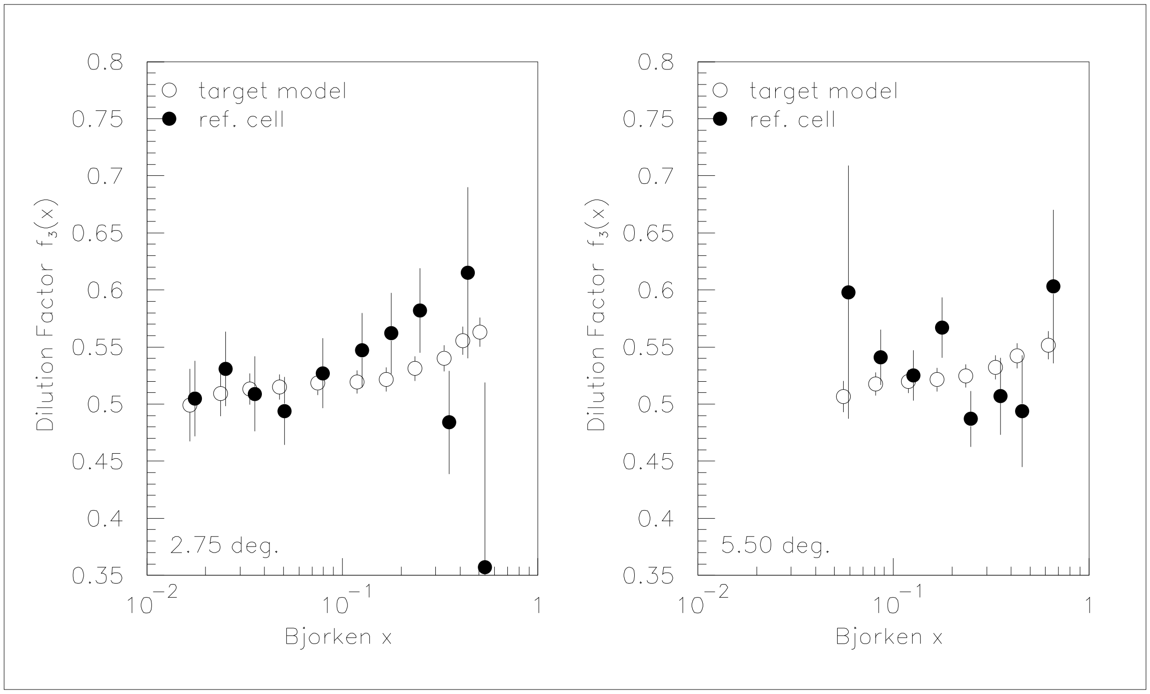

Figure 5.5: Dilution factor for the target cell Bob.

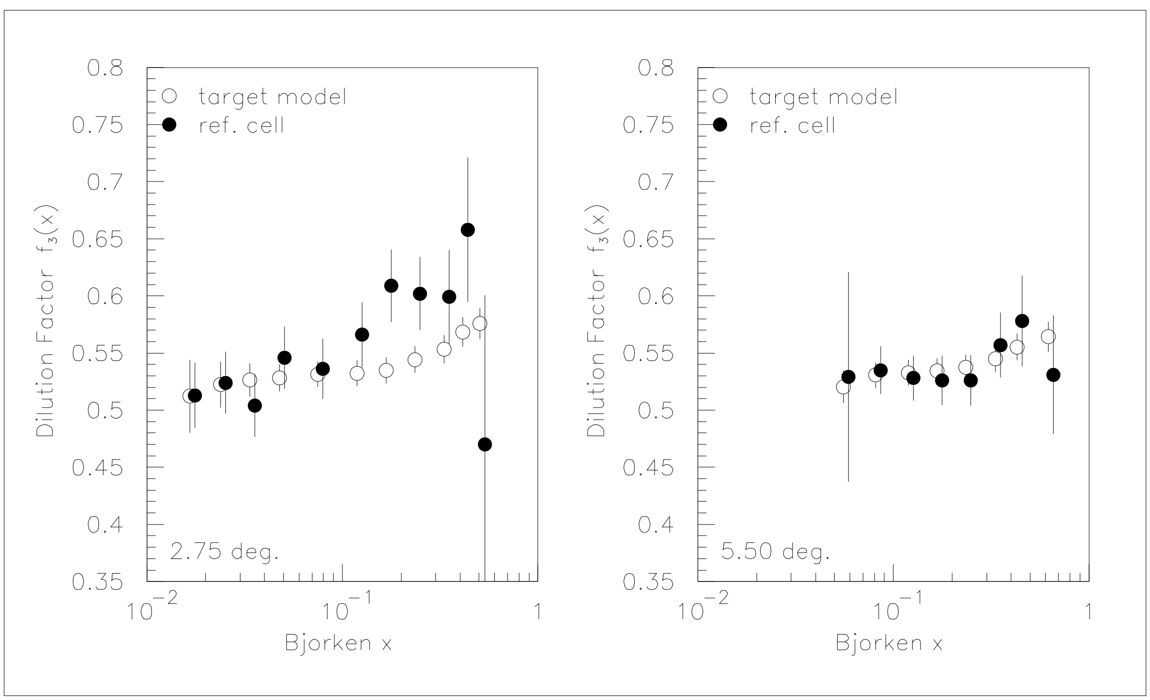

Figure 5.6: Dilution factor for the target cell SMC.

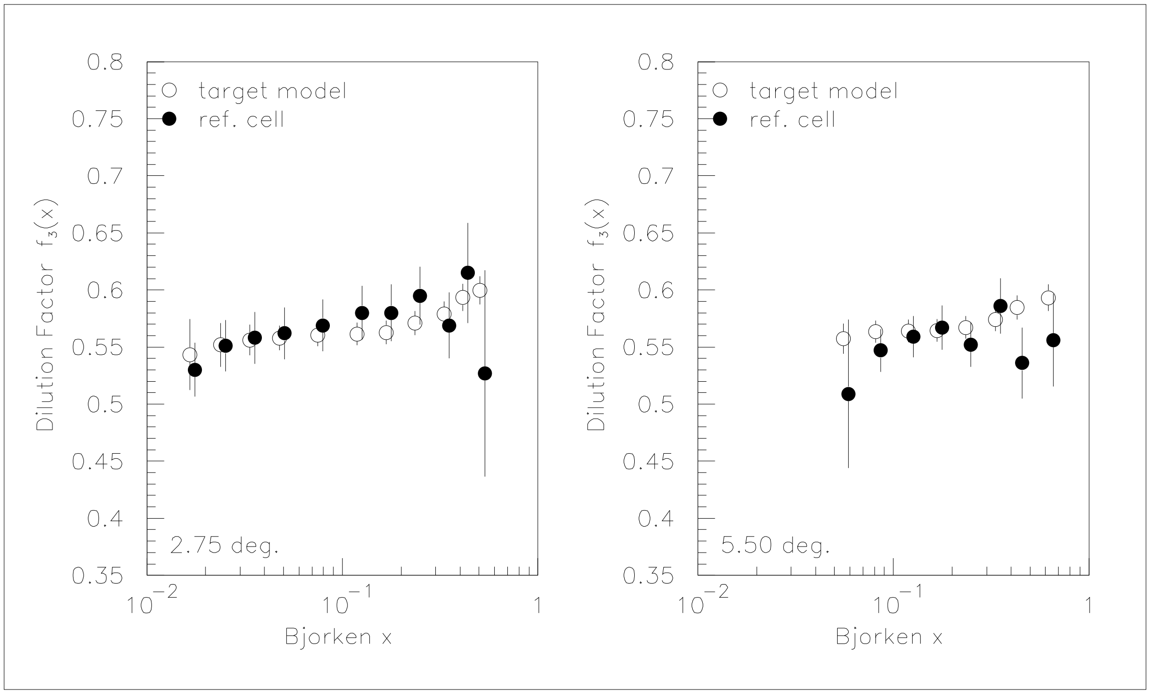

Figure 5.7: Dilution factor for the target cell Generals.

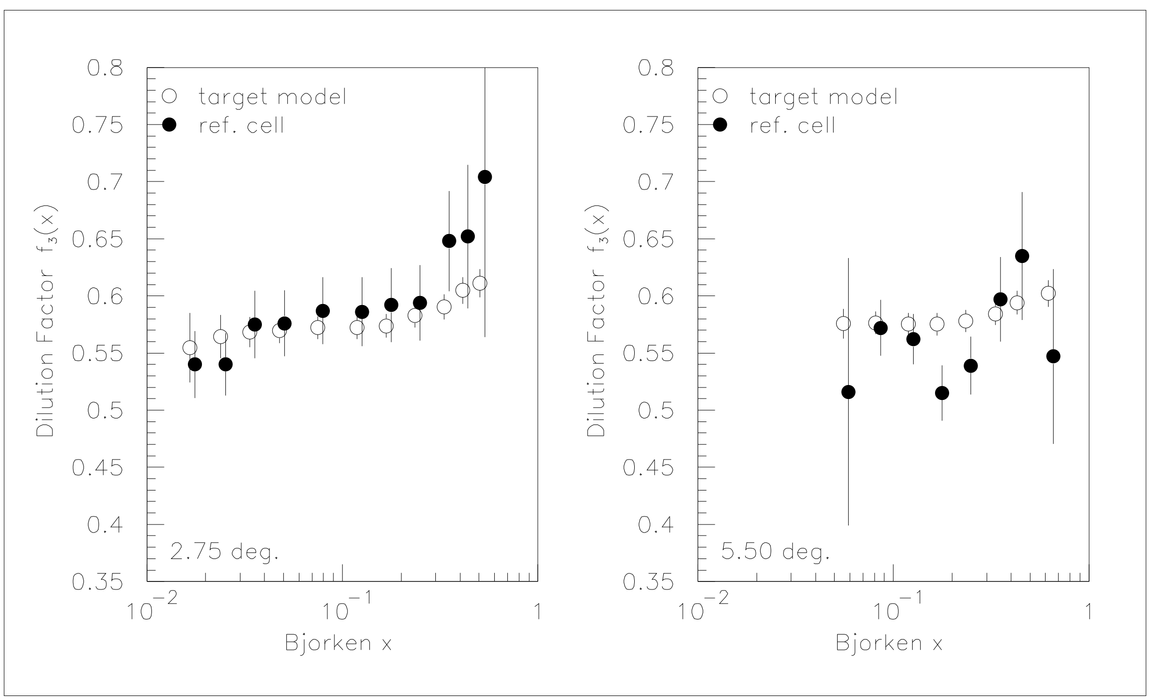

Figure 5.8: Dilution factor for the target cell Hermes.

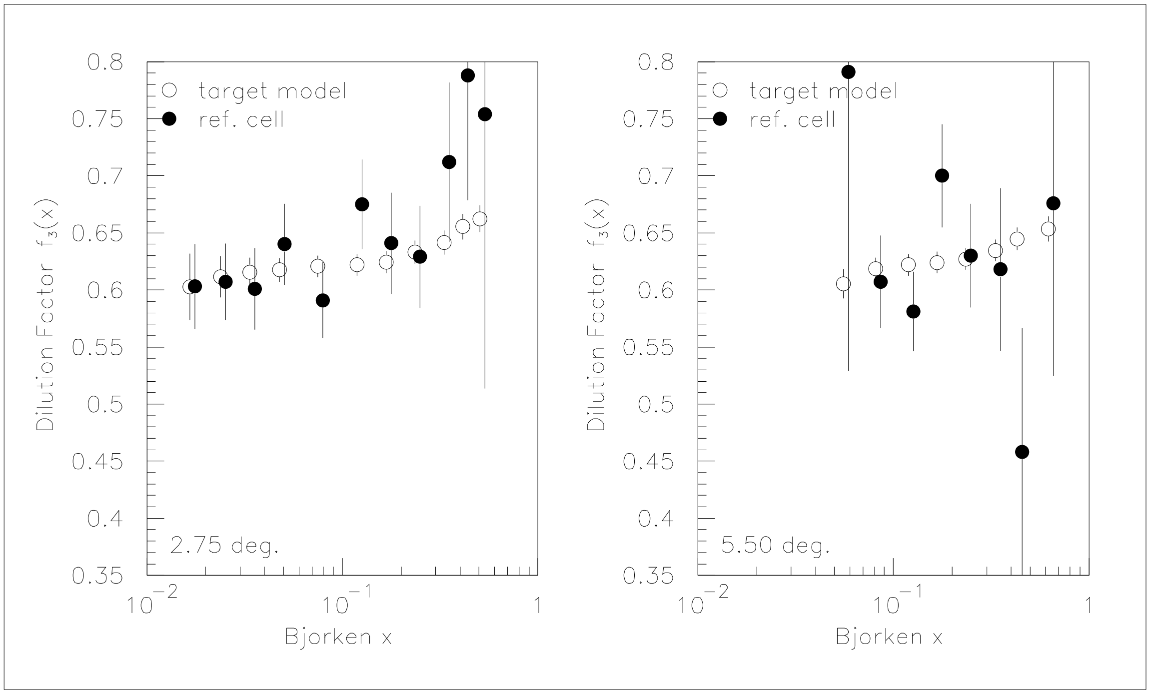

Figure 5.9: Dilution factor for the target cell Prelims.

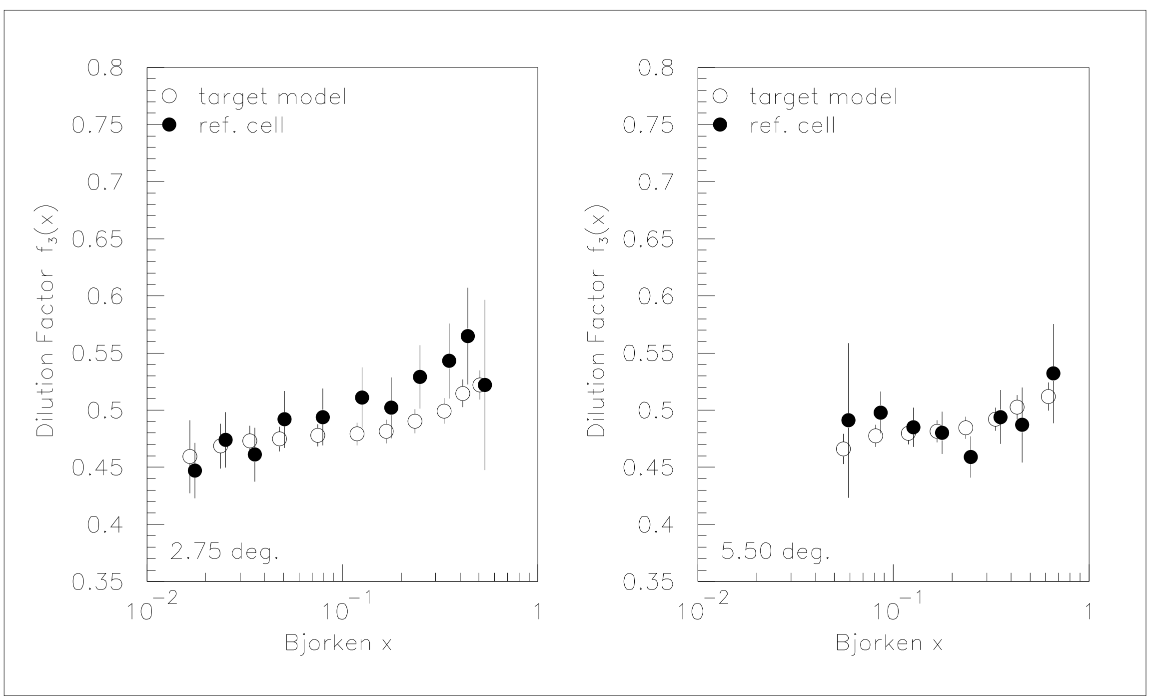

Figure 5.10: Dilution factor for the target cell Chance.

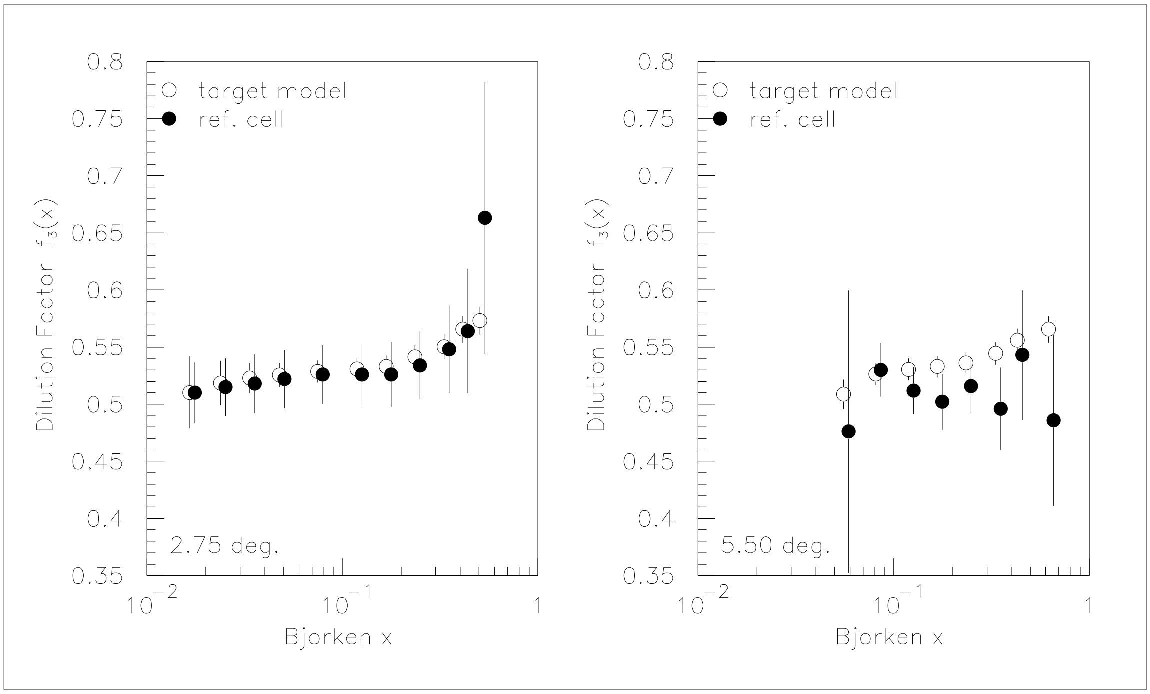

Figure 5.11: Dilution factor for the target cell Picard.

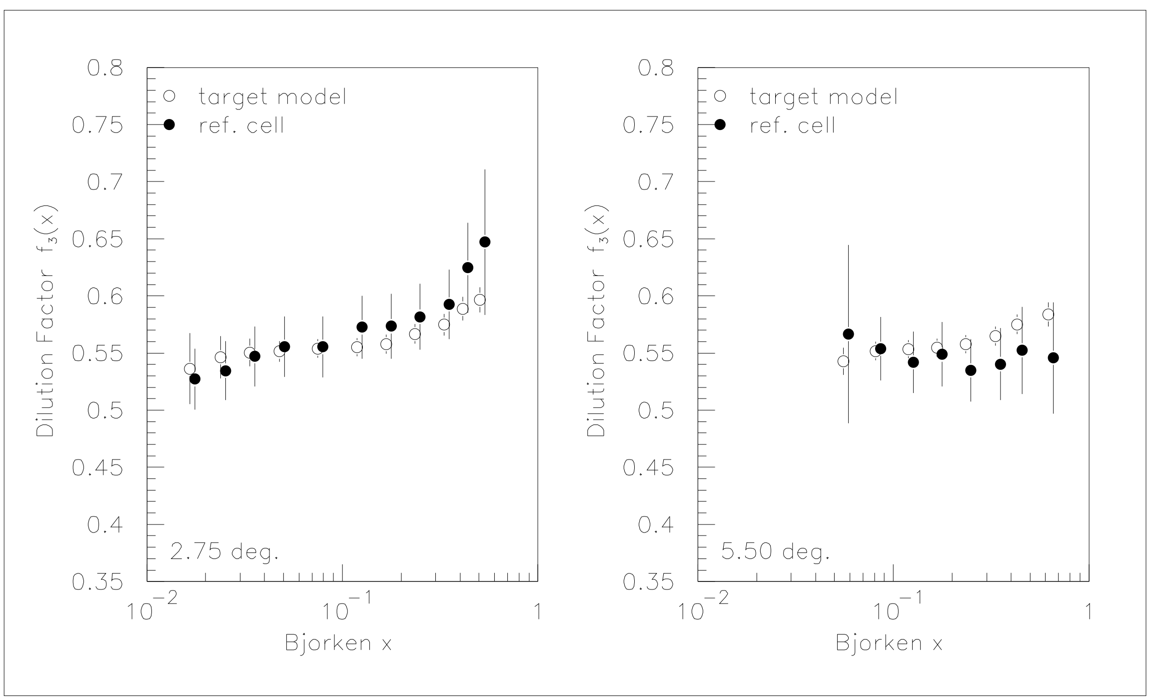

Figure 5.12: Dilution factor for the average target cell.

CHAPTER VI

Physics Analysis and Results

6.1 Asymmetry Analysis

The data runs were analyzed to determine the number of counts per incident electron per x-bin as described in Chapter 5. The number of counts per incident electron per x-bin was then used to determine the raw asymmetry, from which the structure functions can be calculated. The raw asymmetries are

$$A_{\parallel}^{raw}(x, Q^2) = \frac{(N(x)/Q_{beam})^{\downarrow\Uparrow} - (N(x)/Q_{beam})^{\uparrow\Uparrow}}{(N(x)/Q_{beam})^{\downarrow\Uparrow} + (N(x)/Q_{beam})^{\uparrow\Uparrow}} \tag{6.1}$$

and

$$A_{\perp}^{raw}(x, Q^2) = \frac{(N(x)/Q_{beam})^{\downarrow\Leftarrow} - (N(x)/Q_{beam})^{\uparrow\Leftarrow}}{(N(x)/Q_{beam})^{\downarrow\Leftarrow} + (N(x)/Q_{beam})^{\uparrow\Leftarrow}}, \tag{6.2}$$

where $\uparrow$,$\downarrow$ indicates the longitudinal electron polarization, $\Uparrow$,$\Downarrow$ indicates the longitudinal target nucleon polarization, and $\Leftarrow$,$\Rightarrow$ indicates the transverse target nucleon polarization. $N(x)$ is the number of counts and Q_{beam} is the incident electron charge for a given counting time. The Bjorken x and Q^2, the four momentum transfer squared, of each event were determined from the reconstructed momentum and scattering angle of the events that passed the electron cuts in each of the two spectrometers. The average value of Q^2 for each x-bin is the first moment of Q^2 for the individual events. The value of the raw asymmetries is on the order of 10^{-3}, for which the statistical error on the raw asymmetries is approximately

$$\sigma(A_{\parallel}^{raw}(x,Q^2)) = \left((N(x)/Q_{beam})^{\downarrow\Uparrow} + (N(x)/Q_{beam})^{\uparrow\Uparrow}\right)^{-1/2} \tag{6.3}$$

and

$$\sigma(A_{\perp}^{raw}(x,Q^2)) = \left((N(x)/Q_{beam})^{\downarrow\Leftarrow} + (N(x)/Q_{beam})^{\uparrow\Leftarrow}\right)^{-1/2}. \tag{6.4}$$

In order to calculate the structure functions according to equations 2.20 and 2.21, the raw asymmetries must be corrected. Equations 2.20 and 2.21 require the parallel and perpendicular asymmetries for a polarized electron deep inelastically scattered from polarized ^{3}He through single photon exchange only. The raw asymmetries are created using a partially polarized electron beam and a partially polarized ^{3}He target. The ^{3}He target also contains unpolarized glass and nitrogen which dilutes the ^{3}He asymmetry as described in section 4.7. There are also other processes that contribute to the measured raw asymmetries, such as charge symmetric processes, inelastic, quasi-elastic, and elastic scattering, multi-photon deep inelastic scattering, and the electro-weak process of Z^0 exchange. Also contained within the measured raw asymmetries is a small number of misidentified pions, and a small correction necessitated by the rate dependence of the spectrometer efficiency. Combining all of these corrections to the measured raw asymmetries gives the following form to the parallel experimental asymmetry (and a similar expression for the perpendicular experimental asymmetry) which is necessary for equations 2.20 and 2.21,

$$A_{\parallel} = \frac{A_{e^-}^{raw} + \Delta A^{rate} - P_B A^{EW}}{P_{3t} P_B f_3} + \Delta A^{RC}, \tag{6.5}$$

where $A_{e^-}^{raw}$ is the raw asymmetry after the background from charge symmetric electrons and misidentified pions has been subtracted, ΔA^{rate} is the rate dependent correction, A^{EW} is the electro-weak parity-violating asymmetry, ΔA^{RC} is the radiative correction, P_{3t} is the target cell polarization, P_B is the electron beam polarization, and f_3 is the ^{3}He dilution factor for the polarized ^{3}He target. All of the quantities except P_{3t} and P_B are x dependent. Each of the asymmetries and corrections will be discussed in the following sections.

6.1.1 Backgrounds

The measured raw asymmetry is formed from the collection of events that pass the electron cuts. This collection of events is composed primarily of deep inelastically scattered electrons, but also contains a contamination from various backgrounds, including charge symmetric processes such as $\pi^0 \to 2\gamma \to e^+e^-e^+e^-$. There is also a small contamination of charged pions that have passed the electron cuts and been misidentified as electrons. Denoting the total measured raw asymmetry as A^{raw}, the asymmetry of the deep inelastically scattered electrons as $A^{raw}_{e^-}$, the asymmetry of the electrons from charge symmetric processes as $A^{raw}_{e^+}$, and the asymmetry of the misidentified pions as $A^{raw}_{\pi^-}$, the measured raw asymmetry is

$$A^{raw} = A^{raw}_{e^-}\left(\frac{N_{e^-}}{N_{total}}\right) + A^{raw}_{e^+}\left(\frac{N_{e^+}}{N_{total}}\right) + A^{raw}_{\pi^-}\left(\frac{N_{\pi^-}}{N_{total}}\right), \tag{6.6}$$

where all quantities are functions of x and the fraction of events from the i^{th} source is given by $N_{i^{th}}/N_{total}$. The number of deep inelastically scattered electrons is $N_{e^-} = N_{total} - N_{e^+} - N_{\pi^-}$. To extract $A^{raw}_{e^-}$ from the measured raw asymmetry, the fraction of events from charge symmetric processes and misidentified pions must be known, as well as their asymmetry. However, since the magnitude of the asymmetry is bounded by one, the precision with which the asymmetry must be known is determined by the fraction of events.

The number of misidentified pions contained in the electron sample was determined by comparing the E/p distribution of a well-identified sample of pions with the E/p distribution of the events that pass the electron cut. By fitting the E/p distribution of a clean sample of pions from $E/p = 0.2$ to $E/p = 2.0$ and then normalizing this distribution to the E/p distribution for the electron cut in the region $0.3 < x < 0.7$ where the E/p sample is dominated by misidentified pions, the size of the pion tail leaking into the E/p peak for the electrons centered at $E/p = 1.0$ can be estimated. The E/p spectrum for the $x = 0.017$ x-bin is shown in figure 6.1. The neural net cut from the shower counter reduces the number of misidentified pions significantly.

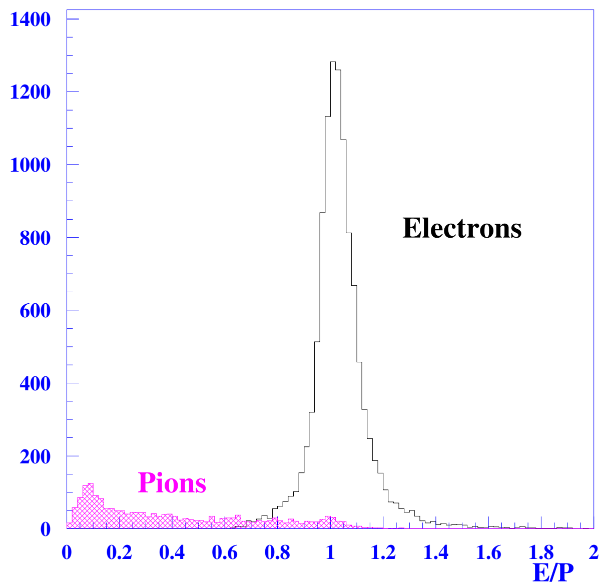

Figure 6.1: E/p spectrum for the $x = 0.017$ x-bin

Because of the small π^- fraction under the electron E/p peak, a second method for estimating the pion fraction was also used [84, 85]. In this method, the π^+ fraction was determined under the positron E/p peak and the ratio of the production rates for π^- to π^+ was used to estimate the π^- fraction under the electron E/p peak. The π^+ fraction in the positron events is much larger and it is therefore easier to determine the number of π^+ under the positron E/p peak. The results for this method are in excellent agreement with the first method and have smaller errors. Consequently, this second method was used to determine the fraction of events that are misidentified pions, and the results are shown in figure 6.2.

The pion asymmetry was calculated using pions that passed a very tight pion cut that consisted of a track with no Cherenkov in coincidence, a value of $E/p < 0.2$, and a neural net cut in the shower counter such that the event is not identified as an electron. The pion asymmetry (normalized by $P_{3t} P_B f_3$) is shown in figure 6.3 and is approximately three times smaller than the electron asymmetry and is not consistent with zero. Since the pion fraction is so small, and the pion asymmetry is flat and smaller than the electron asymmetry, a constant value for the pion asymmetry has been used in the electron analysis.

The fraction of electrons originating from charge symmetric processes was measured in the spectrometers by reversing the magnetic field of the spectrometer magnets. In this manner, the number of positrons created in the target could be measured in the spectrometers and was assumed to be equal to the number of electrons created by charge symmetric processes. A total of 81 positron runs were made using the SLAC experiment E154 polarized ^{3}He target Picard to determine the fraction of events N_{e^+}/N_{total} and the asymmetry $A_{e^+}^{raw}$. The ratio N_{e^+}/N_{total} is shown in figure 6.4 along with its statistical error bars. Calculation of the number of positrons required the subtraction of misidentified π^+s as described in the previous paragraphs. The systematic error on the experimental asymmetries is dominated in the two lowest x-bins by the uncertainty in the positron fraction. The positron asymmetry (normalized by $P_{3t}P_B f_3$) is shown in figure 6.5. The positron asymmetry is consistent with zero, and a constant value of $A_{e^+}^{raw} = 0$ was used for the electron asymmetry analysis. To be conservative, the statistical errors on the measurement of $A_{e^+}^{raw}$ were used to estimate the systematic error on g_1^n due to the asymmetry from charge symmetric processes.

6.1.2 Rate Dependence

As was discussed in chapter 5, the rate dependence of the spectrometer efficiency was determined using the method of 'pulse fiction', and the results for the α coefficients can be found in table 5.2. Assuming a spectrometer efficiency that is linear with rate and a true number of events given by $N = N^{raw}(1-\alpha)$, the effect on the asymmetry is

$$A = \frac{N^{\downarrow\Uparrow} - N^{\uparrow\Uparrow}}{N^{\downarrow\Uparrow} + N^{\uparrow\Uparrow}} \approx A^{raw}(1-\alpha)\,. \tag{6.7}$$

The systematic error from the rate dependent correction is taken to be the full size of the correction.

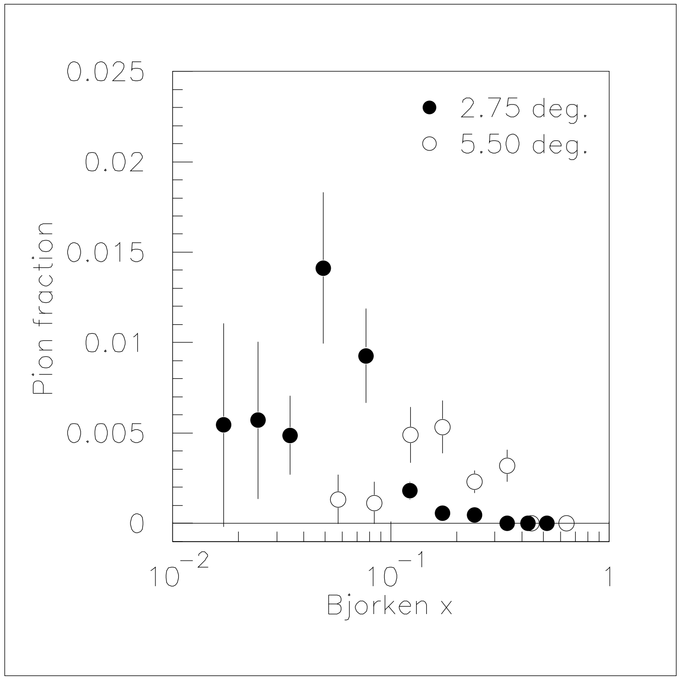

Figure 6.2: Pion fraction

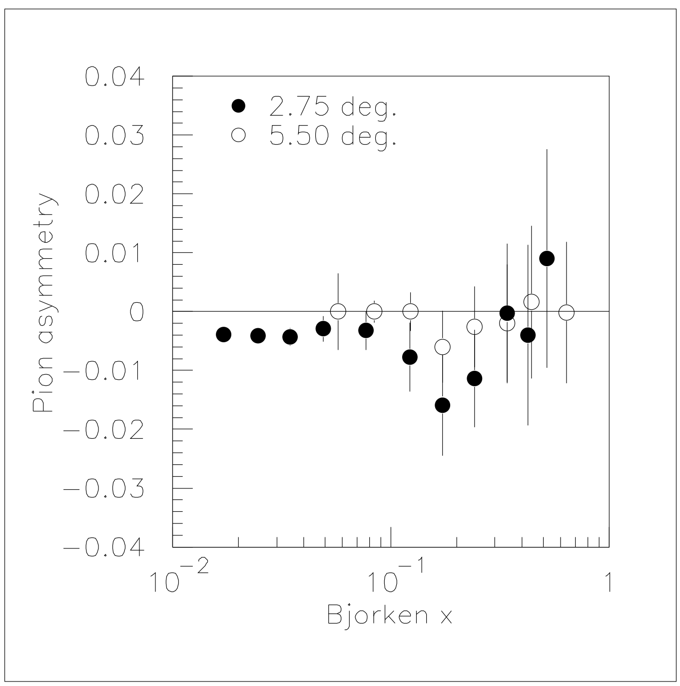

Figure 6.3: Pion asymmetry

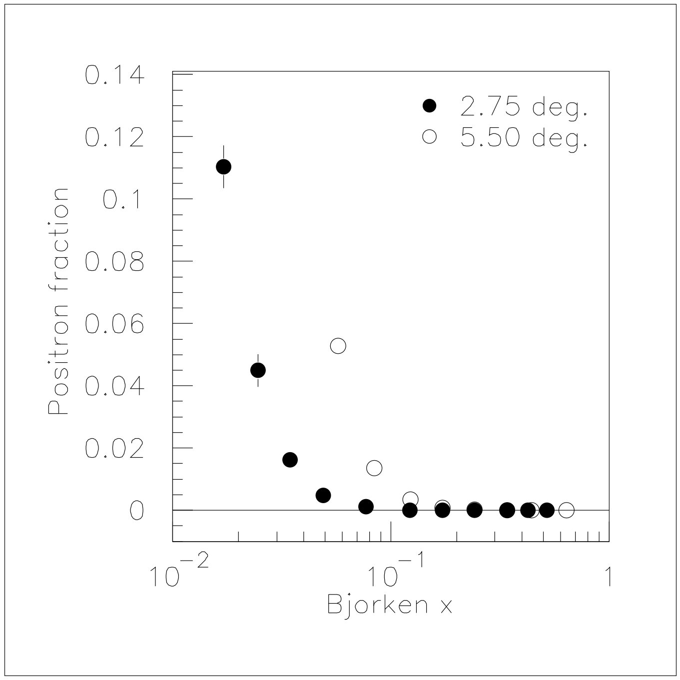

Figure 6.4: Positron fraction

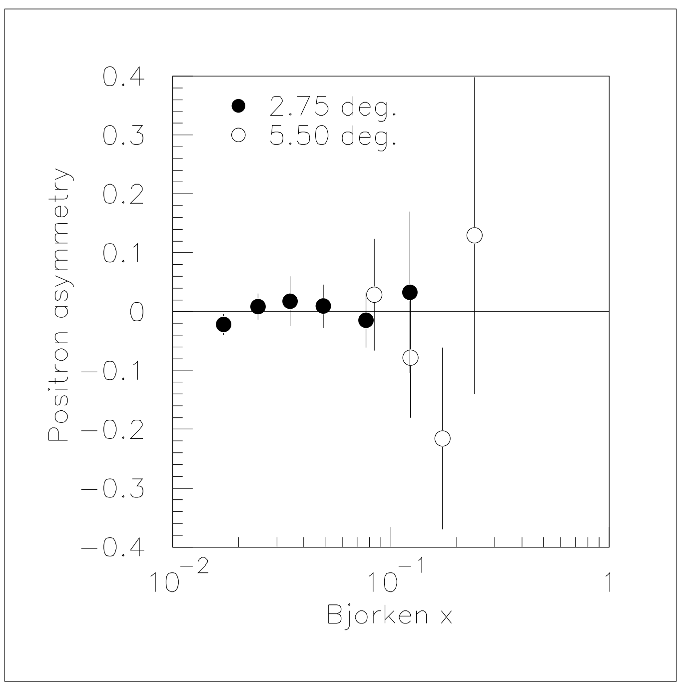

Figure 6.5: Positron asymmetry

6.1.3 Electroweak Correction

The electroweak parity-violating asymmetry arises from the interference of the γ and Z^0 exchange amplitudes. It is given by [86, 87]

$$A^{EW} = \frac{\sigma^{\downarrow\Uparrow} - \sigma^{\uparrow\Uparrow}}{\sigma^{\downarrow\Uparrow} + \sigma^{\uparrow\Uparrow}} = Q^2 \left[a_1 + a_2 \left(\frac{1-(1-y)^2}{1+(1-y)^2} \right) \right], \tag{6.8}$$

where y is the fractional energy transfer from the electrons to the hadrons. For an isoscalar target, the constants a_1 and a_2 are approximately

$$\begin{aligned} a_1 &\approx \frac{3G_F}{5\sqrt{2}\pi\alpha} \left(-\frac{3}{4} + \frac{5}{3} \sin^2 \theta_W \right) \\ a_2 &\approx \frac{9G_F}{5\sqrt{2}\pi\alpha} \left(\sin^2 \theta_W - \frac{1}{4} \right), \end{aligned} \tag{6.9}$$

where G_F is the Fermi constant, α is the fine structure constant and θ_W is the Weinberg angle.

The electroweak asymmetry is not sensitive to the direction of the target polarization and therefore its effect on the electron asymmetry is reduced by reversals of the ^{3}He target polarization. The correction is largest at high Q^2, which is in the high x-bins. It reaches 10% of $A_{||}$ in the highest x-bins, which is still much smaller than the statistical error in those x-bins. The systematic uncertainty associated with the electroweak asymmetry is estimated to be 20% of the correction, based on our knowledge of the constants a_1 and a_2.

6.1.4 Radiative Corrections

The measured raw asymmetries are the result of many processes that occur in the target. To extract the experimental asymmetries it is necessary to make a correction that takes into account these other processes. In general, the radiative corrections are broken up into two categories: those effects that occur within the nuclear field of the target (Internal) and those effects that arise from the presence of other nuclei (External). Unlike the unpolarized radiative corrections to the dilution factor from section 4.7.2, the radiative corrections to the asymmetries depend on the experimental asymmetries which are unknown. For SLAC experiment E154, the high beam energy causes the external radiative corrections to be dominated by bremsstrahlung radiation energy losses as the outgoing electrons traverse additional target material. The internal radiative corrections include contributions from higher-order photon exchange processes including electron vertex and lepton and hadron vacuum polarization processes. In addition, cross sections from other processes such as elastic, quasi-elastic and inelastic scattering contribute because of bremsstrahlung radiation energy losses before and after scattering.

A code called RCSLACPOL has been developed at SLAC for the purpose of calculating the polarized radiative corrections. It was developed by Dr. Linda Stuart of SLAC based on the paper by Kukhto and Shumeiko [88]. There exists a similar code that is used at CERN called POLRAD [89]. The results from the two codes have been compared and are in good agreement, and the code RCSLACPOL was used to calculate the polarized radiative corrections. Calculating the polarized radiative corrections requires the best possible input models for everything from nuclear electric and magnetic form factors to deep inelastic structure functions. The deep inelastic experimental asymmetries are therefore both input for the code and output of the code. The best input model for the sum of the experimental asymmetry and the radiative correction is the measured asymmetry. Consequently, if the calculated experimental asymmetry does not produce a radiative correction that is the difference between the experimental asymmetry and the measured asymmetry, the code is reiterated. The ultimate error for this iterative technique is therefore determined by the error on the measured asymmetry, which for SLAC experiment E154 is small.

Sufficient statistics were used in the calculation of the radiative corrections to make the statistical error 2–3 times smaller than the systematic error. The systematic error itself is dominated by the input models for the experimental asymmetries and the input model for unpolarized deep inelastic scattering. The results for the radiative corrections can be seen in figures 6.6–6.9. The error bars on the radiative corrections are the sum of the statistical and systematic errors added in quadrature. Also plotted in figures 6.6–6.9 are the parallel and perpendicular experimental asymmetries for ^{3}He with statistical errors only for comparison. In the lowest x-bins of the 2.75° spectrometer, the size of the radiative corrections to the parallel experimental asymmetry is as large as one third of the asymmetry, with a systematic error three times smaller than the statistical error on the parallel experimental asymmetry.

6.1.5 Results

The results for the parallel and perpendicular experimental asymmetries are given in tables 6.1–6.4. Plots of the parallel and perpendicular experimental asymmetries can be seen in figures 6.6–6.9. The data are plotted at the average x and Q^2 of each bin. The error bars on the parallel and perpendicular experimental asymmetries are statistical only; the systematic errors can be found in the tables.

6.2 The Spin Structure Function g_1^n

Using equations 2.18–2.24 and the results for the perpendicular and parallel experimental asymmetries, the spin structure function $g_1^n(x, Q^2)$ and the photon-nucleon asymmetry $A_1^n(x, Q^2)$ can be calculated. The results are given in tables 6.5 and 6.6, and a plot of $xg_1^n(x, Q^2)$ for both spectrometers is shown in figure 6.10. Each data point for $g_1^n(x, Q^2)$ is at a unique value of x and Q^2. The Q^2 dependence has been suppressed in figure 6.10 by plotting the spin structure function versus x only.

The QCD sum rules for the spin structure functions are defined at a fixed value of Q^2, the four-momentum transfer squared. In order to evaluate the QCD sum rules and to combine the data from the two spectrometers, the data must be evolved to a constant value of Q^2. The average Q^2 for SLAC experiment E154 (as weighted by statistics on $A_{||}$) is approximately 5 (GeV/c)^2, and the SLAC E154 data has been

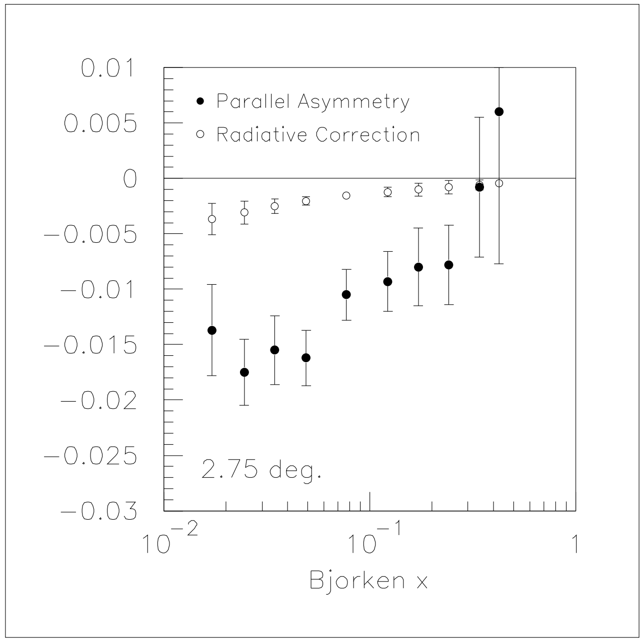

Figure 6.6: Parallel experimental asymmetry for ^{3}He and polarized radiative corrections in the 2.75° spectrometer. Error bars are explained in the text.

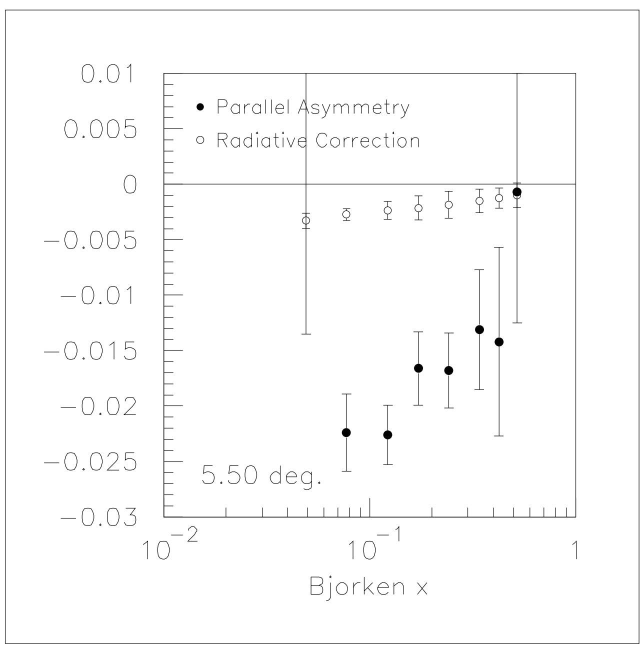

Figure 6.7: Parallel experimental asymmetry for ^{3}He and polarized radiative corrections in the 5.50° spectrometer. Error bars are explained in the text.

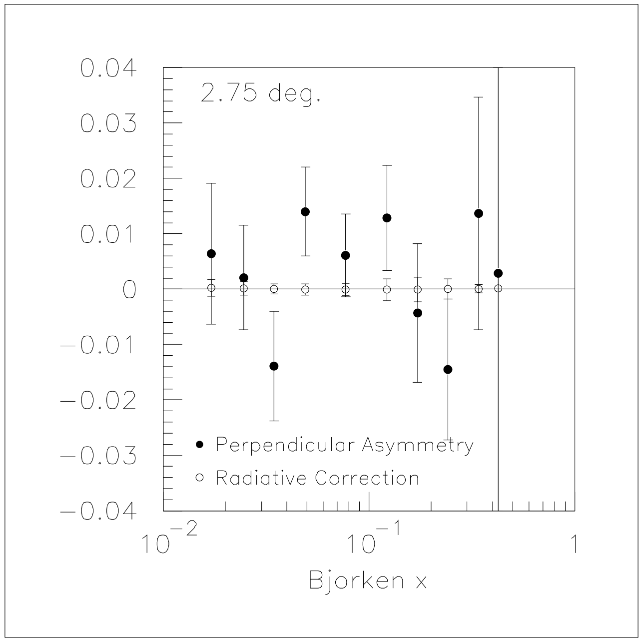

Figure 6.8: Perpendicular experimental asymmetry for ^{3}He and polarized radiative corrections in the 2.75° spectrometer. Error bars are explained in the text.

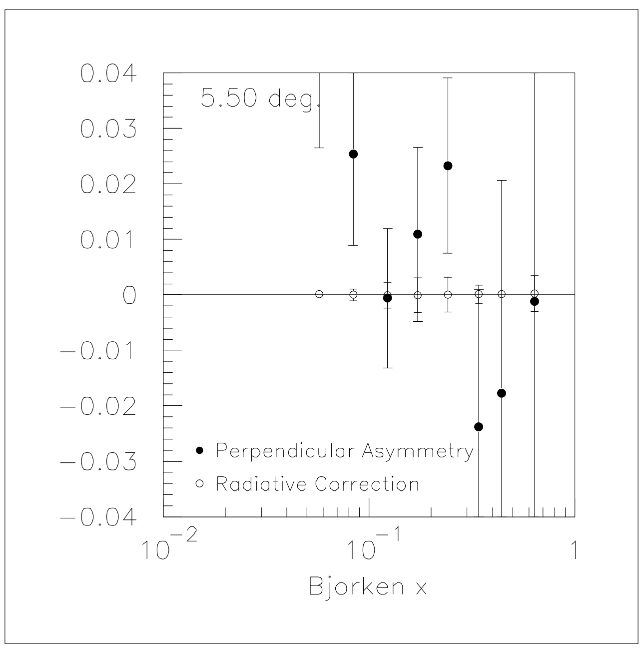

Figure 6.9: Perpendicular experimental asymmetry for ^{3}He and polarized radiative corrections in the 5.50° spectrometer. Error bars are explained in the text.

2.75° spectrometer			
x-bin	$\langle x \rangle$	$\langle Q^2 \rangle$	$A_{\parallel} \pm$ stat. $\pm$ syst.
0.014–0.02	0.017	1.2 $(\mathrm{GeV/c})^2$	-0.0137 $\pm$ 0.0041 $\pm$ 0.0036
0.02–0.03	0.025	1.6 $(\mathrm{GeV/c})^2$	-0.0175 $\pm$ 0.0030 $\pm$ 0.0025
0.03–0.04	0.035	2.1 $(\mathrm{GeV/c})^2$	-0.0155 $\pm$ 0.0031 $\pm$ 0.0018
0.04–0.06	0.049	2.6 $(\mathrm{GeV/c})^2$	-0.0162 $\pm$ 0.0025 $\pm$ 0.0011
0.06–0.10	0.077	3.3 $(\mathrm{GeV/c})^2$	-0.0105 $\pm$ 0.0023 $\pm$ 0.0009
0.10–0.15	0.122	4.1 $(\mathrm{GeV/c})^2$	-0.0093 $\pm$ 0.0027 $\pm$ 0.0007
0.15–0.20	0.172	4.7 $(\mathrm{GeV/c})^2$	-0.0080 $\pm$ 0.0035 $\pm$ 0.0008
0.20–0.30	0.242	5.1 $(\mathrm{GeV/c})^2$	-0.0078 $\pm$ 0.0036 $\pm$ 0.0007
0.30–0.40	0.341	5.5 $(\mathrm{GeV/c})^2$	-0.0008 $\pm$ 0.0063 $\pm$ 0.0005
0.40–0.50	0.425	5.9 $(\mathrm{GeV/c})^2$	0.0060 $\pm$ 0.0137 $\pm$ 0.0007

Table 6.1: Parallel experimental asymmetry for ^{3}He in the 2.75° spectrometer

5.50° spectrometer			
x-bin	$\langle x \rangle$	$\langle Q^2 \rangle$	$A_{\parallel} \pm$ stat. $\pm$ syst.
0.04–0.06	0.057	4.0 $(\mathrm{GeV/c})^2$	0.0126 $\pm$ 0.0261 $\pm$ 0.0027
0.06–0.10	0.084	5.5 $(\mathrm{GeV/c})^2$	-0.0224 $\pm$ 0.0035 $\pm$ 0.0022
0.10–0.15	0.123	7.2 $(\mathrm{GeV/c})^2$	-0.0226 $\pm$ 0.0027 $\pm$ 0.0017
0.15–0.20	0.173	8.9 $(\mathrm{GeV/c})^2$	-0.0166 $\pm$ 0.0033 $\pm$ 0.0012
0.20–0.30	0.242	10.7 $(\mathrm{GeV/c})^2$	-0.0168 $\pm$ 0.0034 $\pm$ 0.0013
0.30–0.40	0.342	12.5 $(\mathrm{GeV/c})^2$	-0.0131 $\pm$ 0.0054 $\pm$ 0.0018
0.40–0.50	0.442	13.8 $(\mathrm{GeV/c})^2$	-0.0142 $\pm$ 0.0085 $\pm$ 0.0013
0.50–0.70	0.638	15.6 $(\mathrm{GeV/c})^2$	-0.0007 $\pm$ 0.0118 $\pm$ 0.0008

Table 6.2: Parallel experimental asymmetry for ^{3}He in the 5.50° spectrometer

2.75° spectrometer			
x-bin	$\langle x \rangle$	$\langle Q^2 \rangle$	$A_\perp$ ± stat. ± syst.
0.014–0.02	0.017	1.2 (GeV/c)^2	0.0064 ± 0.0127 ± 0.0017
0.02–0.03	0.025	1.6 (GeV/c)^2	0.0021 ± 0.0094 ± 0.0013
0.03–0.04	0.035	2.1 (GeV/c)^2	-0.0139 ± 0.0099 ± 0.0019
0.04–0.06	0.049	2.6 (GeV/c)^2	0.0140 ± 0.0080 ± 0.0015
0.06–0.10	0.077	3.3 (GeV/c)^2	0.0061 ± 0.0075 ± 0.0013
0.10–0.15	0.122	4.1 (GeV/c)^2	0.0129 ± 0.0095 ± 0.0022
0.15–0.20	0.172	4.7 (GeV/c)^2	-0.0043 ± 0.0125 ± 0.0022
0.20–0.30	0.242	5.1 (GeV/c)^2	-0.0145 ± 0.0127 ± 0.0020
0.30–0.40	0.341	5.5 (GeV/c)^2	0.0137 ± 0.0210 ± 0.0038
0.40–0.50	0.425	5.9 (GeV/c)^2	0.0029 ± 0.0443 ± 0.0008

Table 6.3: Perpendicular experimental asymmetry for ^{3}He in the 2.75° spectrometer

5.50° spectrometer			
x-bin	$\langle x \rangle$	$\langle Q^2 \rangle$	$A_\perp$ ± stat. ± syst.
0.04–0.06	0.057	4.0 (GeV/c)^2	0.1490 ± 0.1225 ± 0.0151
0.06–0.10	0.084	5.5 (GeV/c)^2	0.0254 ± 0.0165 ± 0.0026
0.10–0.15	0.123	7.2 (GeV/c)^2	-0.0006 ± 0.0126 ± 0.0025
0.15–0.20	0.173	8.9 (GeV/c)^2	0.0109 ± 0.0157 ± 0.0033
0.20–0.30	0.242	10.7 (GeV/c)^2	0.0233 ± 0.0158 ± 0.0034
0.30–0.40	0.342	12.5 (GeV/c)^2	-0.0238 ± 0.0247 ± 0.0022
0.40–0.50	0.442	13.8 (GeV/c)^2	-0.0177 ± 0.0383 ± 0.0015
0.50–0.70	0.638	15.6 (GeV/c)^2	-0.0012 ± 0.0547 ± 0.0035

Table 6.4: Perpendicular experimental asymmetry for ^{3}He in the 5.50° spectrometer

2.75° spectrometer			
$\langle x \rangle$	$\langle Q^2 \rangle$	g_1^n ± stat. ± syst.	A_1^n ± stat. ± syst.
0.017	1.2 $(\mathrm{GeV/c})^2$	-0.362 ± 0.118 ± 0.107	-0.060 ± 0.020 ± 0.018
0.025	1.6 $(\mathrm{GeV/c})^2$	-0.387 ± 0.074 ± 0.064	-0.083 ± 0.016 ± 0.015
0.035	2.1 $(\mathrm{GeV/c})^2$	-0.292 ± 0.061 ± 0.037	-0.078 ± 0.018 ± 0.011
0.049	2.6 $(\mathrm{GeV/c})^2$	-0.240 ± 0.046 ± 0.024	-0.101 ± 0.018 ± 0.011
0.077	3.3 $(\mathrm{GeV/c})^2$	-0.121 ± 0.033 ± 0.013	-0.079 ± 0.019 ± 0.009
0.122	4.1 $(\mathrm{GeV/c})^2$	-0.082 ± 0.033 ± 0.010	-0.097 ± 0.034 ± 0.012
0.172	4.7 $(\mathrm{GeV/c})^2$	-0.063 ± 0.030 ± 0.008	-0.090 ± 0.048 ± 0.013
0.242	5.1 $(\mathrm{GeV/c})^2$	-0.052 ± 0.027 ± 0.007	-0.076 ± 0.075 ± 0.018
0.341	5.5 $(\mathrm{GeV/c})^2$	-0.001 ± 0.036 ± 0.004	-0.166 ± 0.206 ± 0.051
0.425	5.9 $(\mathrm{GeV/c})^2$	0.037 ± 0.077 ± 0.009	0.226 ± 0.801 ± 0.045

Table 6.5: Results of this dissertation for the neutron spin structure function g_1^n and the photon-nucleon asymmetry A_1^n in the 2.75° spectrometer

5.50° spectrometer			
$\langle x \rangle$	$\langle Q^2 \rangle$	g_1^n ± stat. ± syst.	A_1^n ± stat. ± syst.
0.057	4.0 $(\mathrm{GeV/c})^2$	0.235 ± 0.299 ± 0.037	0.047 ± 0.126 ± 0.013
0.084	5.5 $(\mathrm{GeV/c})^2$	-0.152 ± 0.029 ± 0.019	-0.104 ± 0.018 ± 0.013
0.123	7.2 $(\mathrm{GeV/c})^2$	-0.117 ± 0.017 ± 0.012	-0.110 ± 0.015 ± 0.012
0.173	8.9 $(\mathrm{GeV/c})^2$	-0.058 ± 0.016 ± 0.007	-0.089 ± 0.023 ± 0.011
0.242	10.7 $(\mathrm{GeV/c})^2$	-0.040 ± 0.012 ± 0.005	-0.118 ± 0.030 ± 0.016
0.342	12.5 $(\mathrm{GeV/c})^2$	-0.020 ± 0.013 ± 0.005	-0.061 ± 0.072 ± 0.023
0.442	13.8 $(\mathrm{GeV/c})^2$	-0.013 ± 0.016 ± 0.003	-0.018 ± 0.147 ± 0.018
0.638	15.6 $(\mathrm{GeV/c})^2$	0.003 ± 0.008 ± 0.001	0.100 ± 0.297 ± 0.032

Table 6.6: Results of this dissertation for the neutron spin structure function g_1^n and the photon-nucleon asymmetry A_1^n in the 5.50° spectrometer

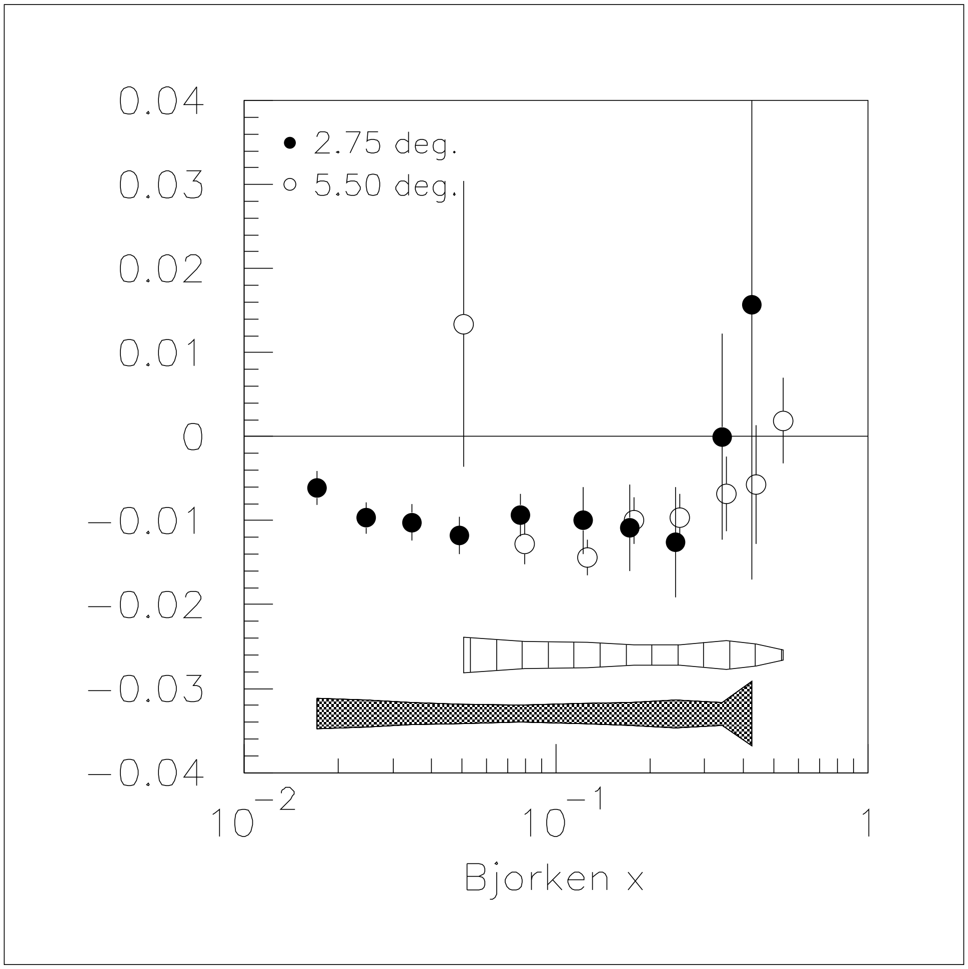

Figure 6.10: The spin dependent structure function g_1^n plotted as xg_1^n. The error bars are statistical only and the shaded area has a height equal to 2 standard deviation systematic errors. The data for the 5.50° spectrometer has been offset slightly for clarity. (Note that the two spectrometers are at different Q^2s.) These are the results of this dissertation and not the 'official' SLAC experiment E154 results [90,91].

evolved to 5 $(\mathrm{GeV/c})^2$. The method used to evolve the data was the traditional method which assumes that for $Q^2 > 1$ $(\mathrm{GeV/c})^2$ the ratio of the polarized to unpolarized structure functions, g_1/F_1, is independent of Q^2 for any given value of x. This Q^2 independent evolution has been motivated by the data from previous experiments that have shown no significant Q^2 dependence within the limited precision of the data [92]. The data for the two spectrometers at 5 $(\mathrm{GeV/c})^2$ was then combined in the common x-bins using the statistical error on g_1^n as the weight. The average value of x and Q^2 for each bin were determined using the same weighting. The average value of the spin structure function $g_1^n(x)$ at a Q^2 of 5 $(\mathrm{GeV/c})^2$ is given in table 6.7 and shown in figure 6.11. Also shown in figure 6.11 is $g_1^n(x)$ plotted as $xg_1^n(x)$.

Although the assumption of g_1/F_1 scaling (Q^2 independence) contradicts the predictions of perturbative QCD, it is a reasonable assumption if the range of Q^2 is not large and the error due to the assumption is significantly smaller than the uncertainty in the data. For SLAC experiment E154, the data is precise enough that the error due to the scaling assumption is a reasonable fraction of the uncertainty in the data and a next-to-leading order perturbative QCD analysis of the world's polarized deep inelastic scattering data is a meaningful exercise [93].

6.3 Integrals and Sum Rules

The integral of the spin structure function $g_1^n(x)$ in the data range was obtained by summing the values of the structure function in every bin multiplied by the bin width. The statistical errors are uncorrelated from bin to bin and are added in quadrature. Most of the systematic errors are largely correlated bin to bin and therefore add linearly. The systematic errors that are not correlated bin to bin (positron asymmetry, pion asymmetry, and g_1^p) have been added in quadrature. The result for the integral in the data range is

$$\int_{0.0135}^{0.7} g_1^n(x)dx = -0.0373 \pm 0.0040 \pm 0.0044, \tag{6.10}$$

Both spectrometers evolved to 5 (GeV/c)^2	
$\langle x \rangle$	g_1^n ± stat. ± syst.
0.017	-0.512 ± 0.168 ± 0.152
0.025	-0.497 ± 0.095 ± 0.084
0.035	-0.347 ± 0.073 ± 0.046
0.049	-0.258 ± 0.051 ± 0.027
0.081	-0.140 ± 0.022 ± 0.016
0.123	-0.107 ± 0.014 ± 0.011
0.173	-0.059 ± 0.014 ± 0.007
0.242	-0.043 ± 0.011 ± 0.005
0.342	-0.019 ± 0.013 ± 0.005
0.442	-0.013 ± 0.015 ± 0.002
0.638	0.005 ± 0.012 ± 0.001

Table 6.7: Results for the neutron spin structure function g_1^n at a Q^2 of 5 (GeV/c)^2. These are the results of this dissertation and not the 'official' SLAC experiment E154 results [90,91].

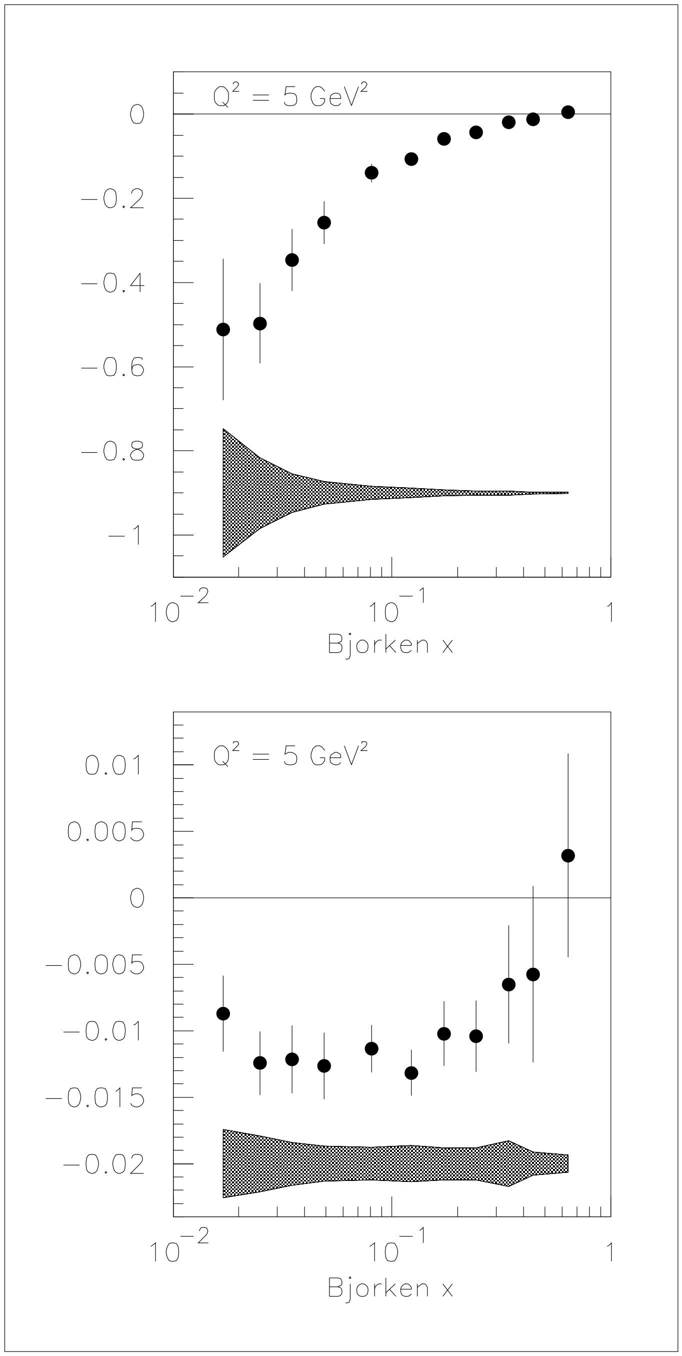

Figure 6.11: The spin dependent structure function g_1^n at 5 $(\mathrm{GeV/c})^2$ plotted as g_1^n in the top graph and as xg_1^n in the bottom graph. The error bars are statistical only and the shaded area has a height equal to 2 standard deviation systematic errors. These are the results of this dissertation and not the 'official' SLAC experiment E154 results [90,91]

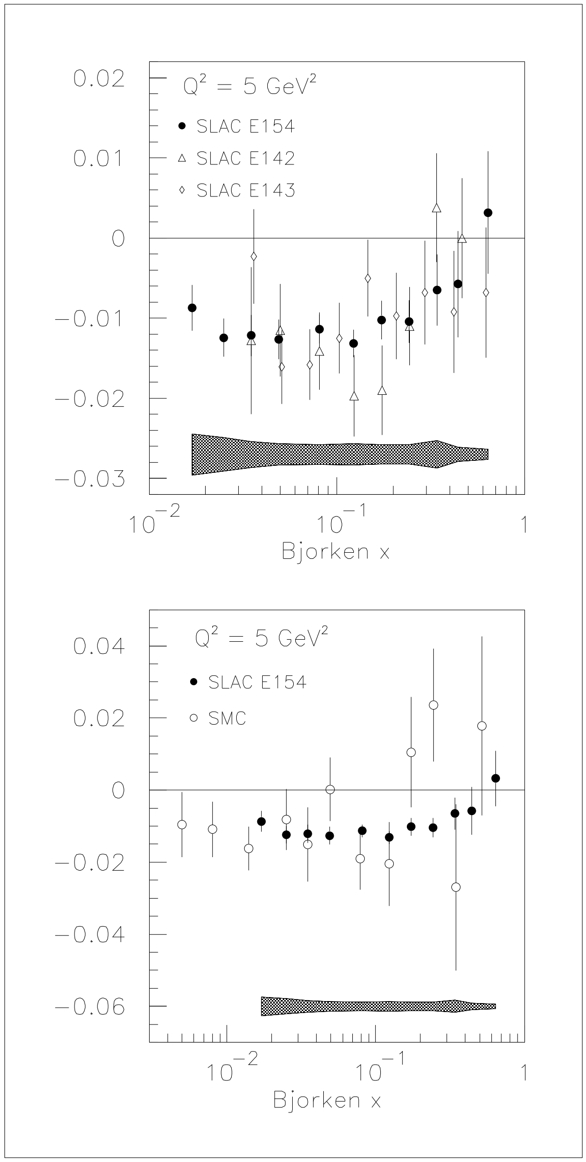

Figure 6.12: The spin dependent structure function g_1^n at 5 $(\mathrm{GeV/c})^2$ plotted as xg_1^n. The top graph is a comparison of SLAC experiment E154 with previous SLAC experiments and the bottom graph is a comparison with the results of the SMC collaboration at CERN. The error bars for SLAC experiment E154 are statistical only and the shaded area has a height equal to 2 standard deviation systematic errors. For the other experiments, the statistical and systematic errors have been added in quadrature.

where the first error is statistical and the second is systematic. The largest contribution to the systematic error on the integral is from those parameters that adjust the overall scale: the target polarization (0.0022) and the dilution factor (0.0022).

Experiments cannot measure $g_1^n(x)$ over the entire kinematic range of $x = 0 \rightarrow 1$. To evaluate the sum rules it is necessary to extrapolate the integrals beyond the measured x range both to $x = 0$ and to $x = 1$. The extrapolation to $x = 1$ is straightforward. As $x \rightarrow 1$, it is expected that the struck quark carries all of the momentum and spin of the nucleon. Using quark counting rules, it is predicted that the structure functions fall off as $(1 - x)^3$ as x $\rightarrow$ 1 [94]. Using the data point in the highest x-bin to set the scale and assuming a $(1 - x)^3$ dependence for $g_1^n(x)$ as $x \rightarrow 1$, the contribution to the integral from the unmeasured high x region is

$$\int_{0.7}^{1} g_1^n(x)dx = 0.00015 \pm 0.00042, \tag{6.11}$$

where the error on the extrapolation is due to the uncertainty in the value of $g_1^n(x)$ in the last measured x-bin.

Before proceeding to the discussion of the low x extrapolation, which is not straightforward, the sum rules will be evaluated from the lowest measured x value for SLAC experiment E154 to $x = 1$. Figure 6.13 shows the integral of the neutron spin structure function from a given x_{min} to 1, $\int_{x_{min}}^{1} g_1^n(x)dx$. By $x = 0.0135$, the integral exceeds the prediction of the Ellis-Jaffe sum rule ($\Gamma^n = -0.028 \pm 0.010$ at a Q^2 of 5 (GeV/c)^2) by 2σ and appears to continue to diverge. SLAC experiment E154 then confirms the violation of the Ellis-Jaffe sum rule.

One of the primary goals of SLAC experiment E154 was to evaluate the Bjorken sum rule. Figure 6.14 shows the integral of the difference between the proton and the neutron spin structure functions from a given x_{min} to 1, $\int_{x_{min}}^{1} \left[g_1^p(x) - g_1^n(x)\right] dx$. A fit to the proton data of SLAC E143 and CERN SMC have been used for $g_1^p(x)$. The Bjorken sum rule evaluated at a $Q^2 = 5$ (GeV/c)^2 to $O(\alpha_S^3)$,

$$\Gamma^{p-n} = 0.181 \pm 0.003 \tag{6.12}$$

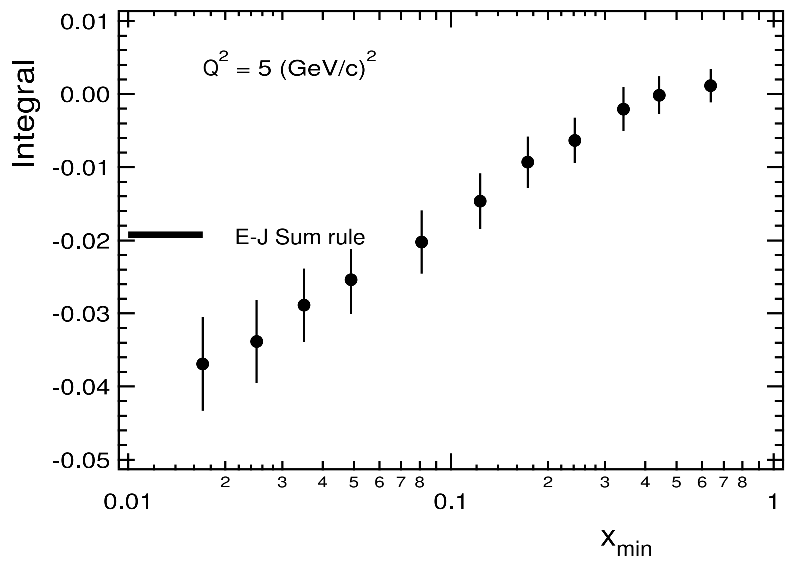

Figure 6.13: The spin dependent structure function g_1^n of the neutron integrated from x_{min} to 1 and plotted versus x_{min}. The statistical and systematic error have been added in quadrature. The errors on the plot are strongly correlated from point to point.

is almost saturated by the integral over the measured region.

6.3.1 Low x

"Aye, there's the rub, ..." –Shakespeare

The value of $g_1^n(x)$ is large in the lowest few x-bins and the behavior of the neutron spin structure function in the lowest few x-bins suggests the possibility of highly divergent behavior. As a result, the extrapolation to $x = 0$ makes a large contribution to the integral of $g_1^n(x)$. While the contribution to the integral from the high x extrapolation is negligible and well justified theoretically, the theoretical models for the low x extrapolation vary widely. Traditionally, a Regge behavior of $g_1 \sim Cx^{-\alpha}$, where α is bound between 0 and 0.5, has been used for the low x extrapolation [95, 96]. However, the Regge theory does not explicitly specify the kinematic domain in which the prediction of asymptotic behavior is applicable. Consequently, the

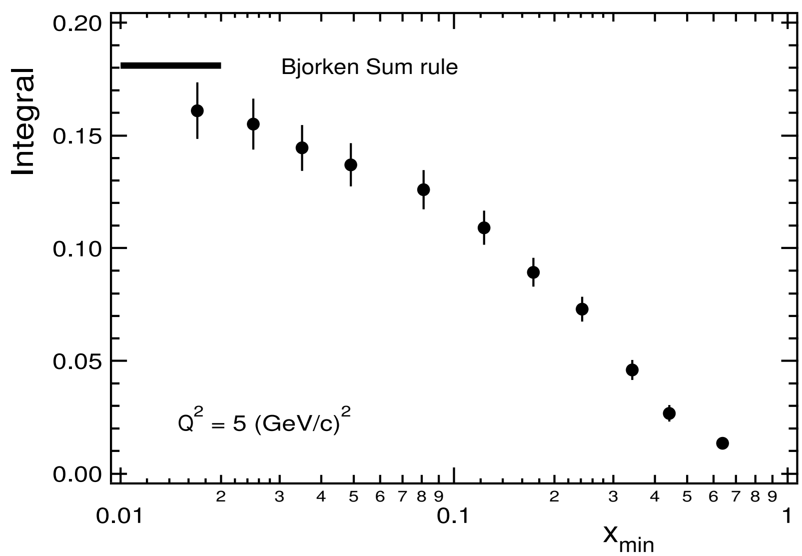

Figure 6.14: The difference between the spin dependent structure functions g_1^p of the proton and g_1^n of the neutron integrated from x_{min} to 1 and plotted versus x_{min}. SLAC E154 data was used to evaluate g_1^n and a fit to the SLAC E143 and CERN SMC data was used for g_1^p. The statistical and systematic error have been added in quadrature. The errors on the plot are strongly correlated from point to point.

approach adopted by the experimental collaborations was to fit the data to a Regge-type power function, $g_1 \sim Cx^{-\alpha}$ in the lowest x-bins [25, 27, 28, 29].

Fitting the data to $g_1 = C$ ($\alpha = 0$), the upper bound for the extrapolation of the integral to $x = 0$ using Regge theory might be obtained. However, the result for the extrapolation depends upon what data range is used for the extrapolation. Using the last two x-bins of the SLAC E154 data gives $C = -0.50$, while using the last three x-bins of the SLAC E154 data gives $C = -0.40$. Using the last two x-bins of the SLAC E154 data ($x < 0.03$) and the CERN SMC data below $x = 0.03$ gives $C = -0.55$. These produce integrals in the unmeasured low x region from $x = 0$ to $x = 0.0135$ of -0.0054 to -0.0074. The fit to the world's data (SLAC E154 and CERN SMC) for $x < 0.03$ is shown in figure 6.15 along with the low x data for SLAC experiment E154 and CERN experiment SMC.

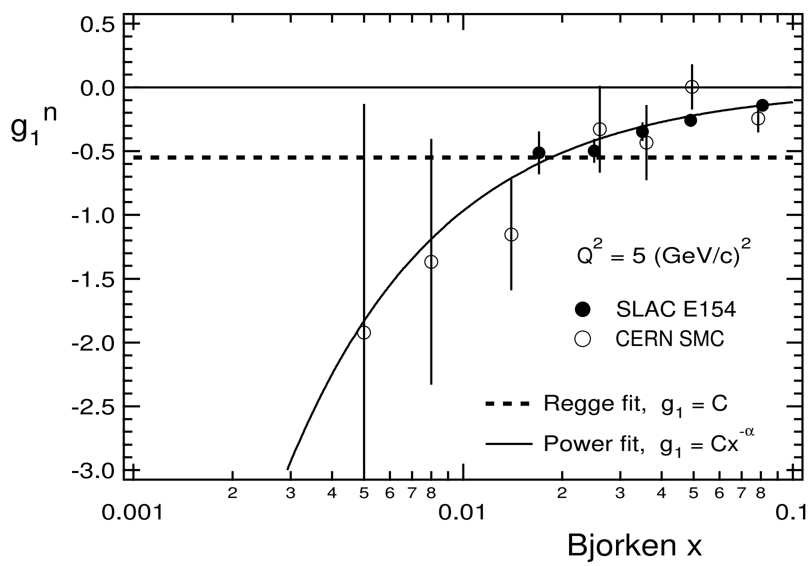

Figure 6.15: Low x fits to the neutron spin structure function $g_1^n(x)$. The filled circles are the SLAC E154 data and the open circles are the CERN SMC data. The dotted line is a fit to $g_1^n(x) = C$ for the SLAC E154 and the CERN SMC data below $x = 0.03$. The solid line is a fit to $g_1^n(x) = Cx^{-\alpha}$ for the last five SLAC E154 data points.

Assuming constant Regge behavior ($g_1 = C$) for $x < 0.03$ and using a fit to the world's data (SLAC E154 and CERN SMC) gives $C = -0.55$ and a value for the integral in the unmeasured low x region of

$$\int_0^{0.0135} g_1^n(x)dx = -0.0074 \pm 0.0010 \pm 0.0011, \tag{6.13}$$

where the first error is statistical and the second error is systematic. This assumption gives a value for the first moment of the neutron spin structure function at a Q^2 of 5 $(\mathrm{GeV/c})^2$ of

$$\int_0^1 g_1^n(x)dx = -0.0446 \pm 0.0042 \pm 0.0055, \tag{6.14}$$

where the first error is statistical and the second error is systematic. This result is almost a factor of two greater than the prediction of the Ellis-Jaffe sum rule at a Q^2 of 5 $(\mathrm{GeV/c})^2$ ($\Gamma^n = -0.028 \pm 0.010$). However, there is no indication that the data are converging to a constant and a fit to $g_1 = C$ is justified.

Fitting the last five SLAC experiment E154 data points to the function $g_1 = Cx^{-\alpha}$ gives $C = -0.014 \pm 0.008$ and $\alpha = 0.92 \pm 0.18$. This power fit is shown in figure 6.15. The value of α obtained from the fit is outside of the allowed Regge region ($0 < \alpha < 0.5$), but is small enough to allow the extrapolation of the integral to $x = 0$ to be finite ($\alpha < 1$).

If a Regge-type power function is used ($g_1 = Cx^{-\alpha}$), then the value of the integral in the unmeasured low x region is

$$\int_0^{0.0135} g_1^n(x)dx = -0.124, \tag{6.15}$$

where no error is given since it is not meaningful. The integral is only convergent for $\alpha < 1$, so the integral is less than one standard deviation from infinity. This result is unsatisfactory and clearly more data at lower values of Bjorken x are necessary so that the true asymptotic behavior of the neutron spin structure function $g_1^n(x)$ can be found. A possible interpretation of the SLAC experiment E154 data is that it is dominated by sea quark and gluon contributions, which could produce very divergent behavior at low x [97]. Consequently, no value of the quark helicity contribution $\Delta\Sigma$ will be given.

To evaluate the Bjorken sum rule, the results from assuming a constant Regge behavior ($g_1 = C$) for the spin structure function g_1^n at $x < 0.03$ can be used along with the results for a global fit to the spin structure function of the proton evolved to 5 (GeV/c)^2 and an assumption of constant Regge behavior ($g_1 = C$) for $x < 0.03$, with

$$\int_0^1 g_1^p(x)dx = 0.132 \pm 0.005 \pm 0.009, \tag{6.16}$$

which gives for the difference

$$\int_0^1 \left[g_1^p(x) - g_1^n(x)\right] dx = 0.177 \pm 0.006 \pm 0.011. \tag{6.17}$$

This is in good agreement with the prediction of the Bjorken sum rule evaluated at $Q^2 = 5$ (GeV/c)^2 to $O(\alpha_S^3)$ (equation 6.12). However, there is no clear evidence that the measured data has entered a constant Regge regime and while the result is in good agreement with the Bjorken sum rule, the low x extrapolation stands on shaky ground.

Rather than extrapolate the spin structure functions for the neutron and the proton separately, a test of the Bjorken sum rule could be made using the present data and an extrapolation to low x of the difference between the proton and neutron spin structure functions, $(g_1^p - g_1^n)(x)$. The difference is a purely non-singlet, valence quark distribution and is expected to have a much softer behavior at low x [97]. Using the data from SLAC E143 and CERN SMC to evaluate the contribution from the spin structure function of the proton at $Q^2 = 5$ (GeV/c)^2, the value of the difference integrated over the SLAC E154 data range and extrapolated to $x = 1$ is

$$\int_{0.0135}^1 \left[g_1^p(x) - g_1^n(x)\right] dx = 0.157 \pm 0.006 \pm 0.009. \tag{6.18}$$

The difference $(g_1^p - g_1^n)(x)$ is plotted in figure 6.16 for the five lowest x-bins ($x < 0.1$) along with a fit to an unconstrained power law function $(g_1^p - g_1^n)(x) = Cx^{-\alpha}$. The difference of the two structure functions indeed displays a more convergent behavior and fits the power law function with the values $C = 0.12$ and $\alpha = 0.53$ and a

$\chi^2 << 1$. The contribution to the integral from the unmeasured low x region is

$$\int_0^{0.0135} [g_1^p(x) - g_1^n(x)]\, dx = 0.034 \pm 0.007, \tag{6.19}$$

which gives for the difference

$$\int_0^1 [g_1^p(x) - g_1^n(x)]\, dx = 0.191 \pm 0.006 \pm 0.012. \tag{6.20}$$

This is in good agreement with the prediction of the Bjorken sum rule at a Q^2 of 5 $(\mathrm{GeV/c})^2$ (equation 6.12) and the results of using a Regge extrapolation to low x (equation 6.17)

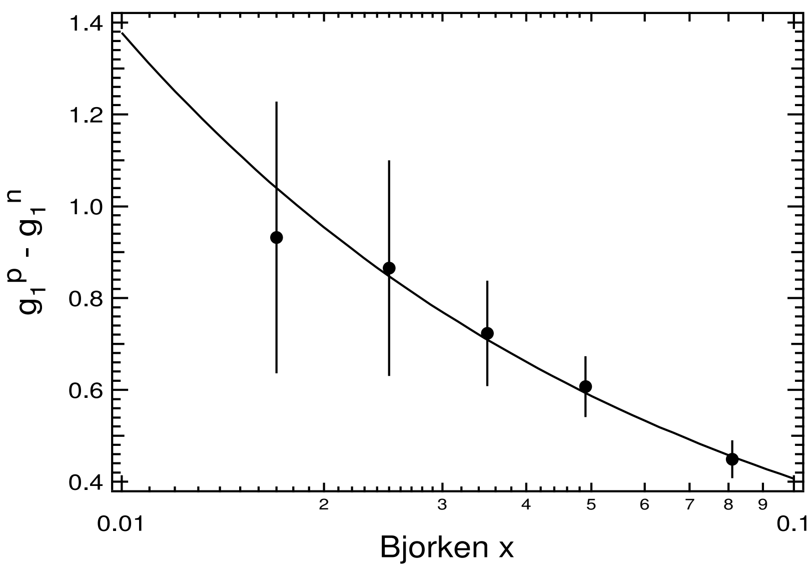

Figure 6.16: Power law fit to the difference in the the spin structure function for the proton, $g_1^p(x)$, and the neutron, $g_1^n(x)$.

6.4 Conclusion

The results of SLAC experiment E154, as described in this dissertation, are the most precise measurement of the spin structure function of the neutron, g_1^n, over the Bjorken x range $0.0135 < x < 0.7$ to date. The goal was to provide precise data on the spin structure function of the neutron at lower values of Bjorken x than had been previously been achieved. Compared to previous spin structure function experiments at SLAC, the increased beam energy allowed a broader kinematic range of $0.0135 < x < 0.7$ to be explored. The hope was that a precision measurement that reached these low values of Bjorken x would provide sufficient insight into the behavior of the spin structure function of the neutron as $x \to 0$ that a definitive statement about the validity of the Bjorken sum rule could be made. What was discovered was that the behavior of the spin structure function of the neutron was highly divergent at the low x values of SLAC experiment E154. Future experiments will surely be needed to provide precision data on the spin structure function of the neutron at even lower x.

The low x data provided by this experiment calls into question the predictions of the conventional Regge theory and the methods used to extrapolate spin structure functions to $x = 0$. However, the data are precise enough that, when combined with the existing data on the spin structure function of the proton, they allow a next-to-leading order perturbative QCD analysis to make more reliable predictions for the low x behavior. These evolution equations in next-to-leading order not only constrain the first moments of the polarized valence quark distributions, but also provide insight into the polarized sea quark distributions and polarized gluon distributions. Using the same two spectrometers as SLAC experiment E154 and adding a third at 10.5°, SLAC experiment E155 will use a polarized proton and a polarized deuteron target to provide more precision data over a larger range of Q^2 for the next-to-leading order perturbative QCD analysis. Also scheduled in the winter of 1998–1999 for the SLAC experiment E155 collaboration is a dedicated data taking run with a transversely polarized target that will provide precision data on the spin structure functions g_2^p and g_2^d.

These experiments at SLAC are a few of the many which followed the EMC discovery of the violation of the Ellis-Jaffe sum for the proton [20] and the beginning of the 'spin crisis'. The results of SLAC experiment E154 are consistent with the

EMC results and also show a violation of the Ellis-Jaffe sum rule for the neutron at the 2σ level. Attempts to evaluate the Bjorken sum rule and to solve for $\Delta\Sigma$ are best handled using the methods of next-to-leading order perturbative QCD (NLO) now that precision data from SLAC experiment E154 on the neutron spin structure function are available [90,91]. The result for the Bjorken sum rule from the NLO analysis by the SLAC experiment E154 collaboration confirms the Bjorken sum rule at the level of 8% at a Q^2 of 5 (GeV/c)^2 [93]. The NLO analysis also provides a result of $\Delta\Sigma = 0.24 \pm 0.09$ for the quark helicity contribution [93].

The precision of SLAC experiment E154 would not have been possible without the substantial improvements that were made to the polarized ^{3}He target. The improvement in the dilution factor through inverted thin windows, the use of diode lasers arrays for optical pumping, and the improved pickup coil design provided a target that performed well and had small systematic errors. While the systematic errors associated with the target are the largest contributors to the systematic error on the integral of g_1^n, they represent a factor of 2–3 improvement over SLAC experiment E142. However, some improvements are still possible, particularly with optimizing the target operating parameters to provide a higher ^{3}He polarization.

Another experiment, HERMES at DESY, is still collecting data on spin structure functions and has plans to study the semi-inclusive reactions that occur during deep inelastic scattering. By tagging the flavor of the leading hadron, HERMES is able to directly probe the valence and sea quark distributions inside the nucleon. The data could be promising. A new facility capable of accelerating electrons to higher energy, such as the proposed *Next Linear Collider* could allow direct measurements of the low x regime, as could polarizing the protons at the collider facility at DESY. Spin-dependent gluon structure functions could be directly measured by colliding polarized protons with polarized protons at the *Relativistic Heavy Ion Collider* (RHIC) at Brookhaven National Laboratory. There is still a lot to learn about the spin structure functions of the nucleon. SLAC experiment E154 has created new questions while attempting to answer old ones, but such is often the nature of science. Future experimental programs promise to be exciting.

APPENDIX

APPENDIX

Spin Exchange in a Double Chambered Cell

In this appendix, the solution for the temporal evolution of a double chamber spin exchange cell will be presented. The model consists of a pumping chamber with a volume of V_P at a constant temperature of T_P and a target chamber with a volume of V_T at a constant temperature of T_T. It is a sealed cell with total of N ^{3}He atoms inside. The number of ^{3}He atoms in the pumping chamber is N_P and the number of ^{3}He atoms in the target chamber is N_T, such that $N = N_P + N_T$. The two chambers are connected by a transfer tube with negligible volume. The connection between the two chambers allows ^{3}He atoms to be exchanged between the pumping cell and the target cell. When the temperature of the two cells is different, ^{3}He atoms will flow from the hot cell to the cold cell until the density in the two cells is such that the pressure in the two cells is the same. Using the ideal gas law to gives the following relationship between the number of ^{3}He atoms in the pumping and target cells.

$$\frac{N_P}{N_T} = \frac{T_T}{T_P}\frac{V_P}{V_T} \tag{A.1}$$

The ^{3}He atoms in each cell can be either spin up, n_+ or spin down, n_-.

$$N_P = n_{+P} + n_{-P} \tag{A.2}$$

$$N_T = n_{+T} + n_{-T} \tag{A.3}$$

The processes that exchange atoms from one spin state to the other are spin relaxation and spin exhange. Spin relaxation works in both directions and occurs in both cells while spin exchange takes place in only one direction and only in the pumping cell. There is also an exchange of atoms from one cell to the other which is assumed to be spin preserving. A reasonable assumption since the transfer time from one cell to the other is much shorter than the characteristic spin relaxation time of the cell. Figure A.1 shows a schematic of the optical pumping process in a double chambered cell.

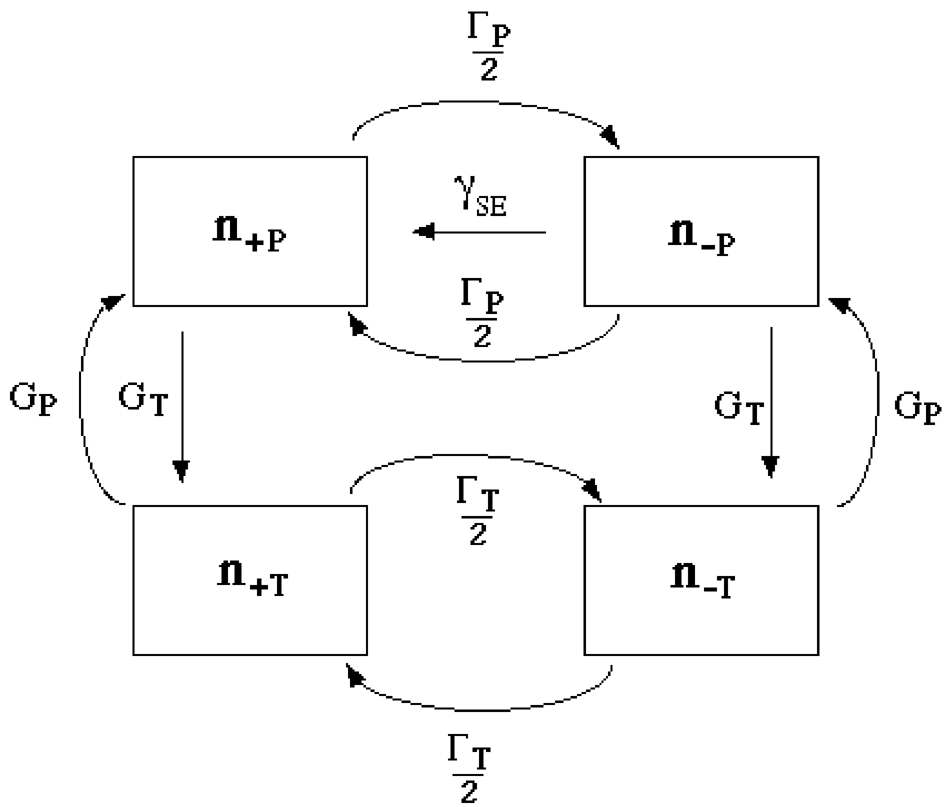

Figure A.1: Schematic of optical pumping in a double cell.

The spin relaxation rate in the pumping cell is Γ_P, the spin relaxation rate in the target cell is Γ_T, the spin exchange rate is γ_{SE}, the rate at which ^{3}He atoms leave the pumping cell and enter the target cell is G_T, and the rate at which ^{3}He atoms leave the target cell and enter the pumping cell is G_P. Because the number of ^{3}He atoms in the cell is fixed and the cell must remain in pressure equilibrium, the rate at which ^{3}He atoms leave and enter a particular cell must be the same. This gives the following relationship for the rate of ^{3}He atom exchange between the two cells

$$N_T G_P = N_P G_T \tag{A.4}$$

Assuming a rubidium polarization of 1, the time evolution of the spin states in the two cells is

$$\begin{aligned}
\frac{\mathrm{dn_{+P}}}{\mathrm{dt}} &= -\frac{\Gamma_P}{2} n_{+P} + \frac{\Gamma_P}{2} n_{-P} - G_T n_{+P} + G_P n_{+T} + \gamma_{SE} n_{-P} && \text{(A.5)} \\
\frac{\mathrm{dn_{-P}}}{\mathrm{dt}} &= -\frac{\Gamma_P}{2} n_{-P} + \frac{\Gamma_P}{2} n_{+P} - G_T n_{-P} + G_P n_{-T} - \gamma_{SE} n_{-P} && \text{(A.6)} \\
\frac{\mathrm{dn_{+T}}}{\mathrm{dt}} &= -\frac{\Gamma_T}{2} n_{+T} + \frac{\Gamma_T}{2} n_{-T} - G_P n_{+T} + G_T n_{+P} && \text{(A.7)} \\
\frac{\mathrm{dn_{-T}}}{\mathrm{dt}} &= -\frac{\Gamma_T}{2} n_{-T} + \frac{\Gamma_T}{2} n_{+T} - G_P n_{-T} + G_T n_{-P} && \text{(A.8)}
\end{aligned}$$

Defining $\Delta_P = n_{+P} - n_{-P}$ to be the difference between the spin states in the pumping cell and $\Delta_T = n_{+T} - n_{-T}$ to be the difference in the target cell, the time evolution of the spin state differences is

$$\begin{aligned}
\frac{\mathrm{d\Delta_P}}{\mathrm{dt}} &= -\left(\Gamma_P + \gamma_{SE} + G_T\right) \Delta_P + G_P \Delta_T + \gamma_{SE} N_P && \text{(A.9)} \\
\frac{\mathrm{d\Delta_T}}{\mathrm{dt}} &= -\left(\Gamma_T + G_P\right) \Delta_T + G_T \Delta_P && \text{(A.10)}
\end{aligned}$$

The solutions to these coupled differential equations are double exponentials. Defining the following constants:

$$\begin{aligned}
A &= \Gamma_P + \Gamma_T + G_P + G_T + \gamma_{SE} && \text{(A.11)} \\
B &= \Gamma_P \Gamma_T + \Gamma_P G_P + \Gamma_T G_T + \gamma_{SE} \left(\Gamma_T + G_P\right) && \text{(A.12)} \\
C &= G_P \gamma_{SE} N_T && \text{(A.13)}
\end{aligned}$$

The solution for the difference in the target cell is

$$\Delta_T = k_1 \exp\left(-m_1 t\right) + k_2 \exp\left(-m_2 t\right) + \frac{C}{B} \tag{A.14}$$

where k_1 and k_2 are constants determined by the difference in the target and pumping cells at $t = 0$ and m_1 and m_2 are the two characteristic rate constants for the spin exchange process in a double chambered cell.

$$m_1 = \frac{1}{2}\left(A + \sqrt{A^2 - 4B}\right) \quad (A.15)$$
$$m_2 = \frac{1}{2}\left(A - \sqrt{A^2 - 4B}\right) \quad (A.16)$$

The rate constant m_1 is large and represents the fast process of ^{3}He atom exchange between the cells. The rate constant m_2 is small and represents the slow process of spin exchange.

The solution for the difference in the pumping cell can be found from equations A.9 and A.14.

$$\Delta_P = G_T{}^{-1}\Big[(\Gamma_T + G_P)\left(k_1 \exp(-m_1 t) + k_2 \exp(-m_2 t) + \frac{C}{B}\right) - k_1 m_1 \exp(-m_1 t) + k_2 m_2 \exp(-m_2 t)\Big] \quad (A.17)$$

The constants k_2 and k_1 can be expressed in terms of the initial spin state differences in the pumping and target cells.

$$k_2 = (m_2 - m_1)^{-1}\left[\Delta_T(0)(\Gamma_T + G_P - m_1) - \Delta_P(0) G_T + \frac{C}{B} m_1\right] \quad (A.18)$$
$$k_1 = \Delta_T(0) - k_2 - \frac{C}{B} \quad (A.19)$$

It is clear from equation A.14 that the equilibium spin state difference in the target cell is

$$\Delta_T(\infty) = \frac{C}{B} = G_P \gamma_{SE} N_T \Big(\Gamma_P \Gamma_T + \Gamma_P G_P + \Gamma_T G_T + \gamma_{SE}(\Gamma_T + G_P)\Big)^{-1} \quad (A.20)$$

from which the equilibrium polarization of the target cell, $\Delta_T(\infty)/N_T$ can be calculated. Assuming that the average rubidium polarization is $\langle P_{Rb}\rangle$ instead of 1, as has been assumed thus far, the equilibrium polarization of the target cell is

$$P_T(\infty) = \langle P_{Rb}\rangle \gamma_{SE}\left(\gamma_{SE} + \Gamma_P + \Gamma_T\left(\frac{N_T}{N_P}\right)\left(1 + \frac{\gamma_{SE}}{G_T} + \frac{\Gamma_P}{G_T}\right)\right)^{-1} \quad (A.21)$$

This equation should be compared with equation 4.9 for which the equilibrium polarization is $\langle P_{Rb}\rangle \gamma_{SE}/(\gamma_{SE} + \Gamma)$ where Γ was the total spin relaxation rate which is approximately $\Gamma_P + \Gamma_T$.

The behavior of the model can be seen in figures A.2 and A.3. In figure A.2, the short time behavior of the target cell polarization can be seen for the SLAC experiment E154 target cell SMC. The polarization data were fitted to the model to find the fast rate m_1, and the transfer time was found to be 50 ± 5 minutes. The target cell SMC is the only cell for which a collection of data was taken within the first hour of a spin up. However, since the SLAC experiment E154 target cells were all identical in design and similar in dimensions, and were operated at approximately the same temperature, it is expected that the transfer time in all of the cells would be about the same.

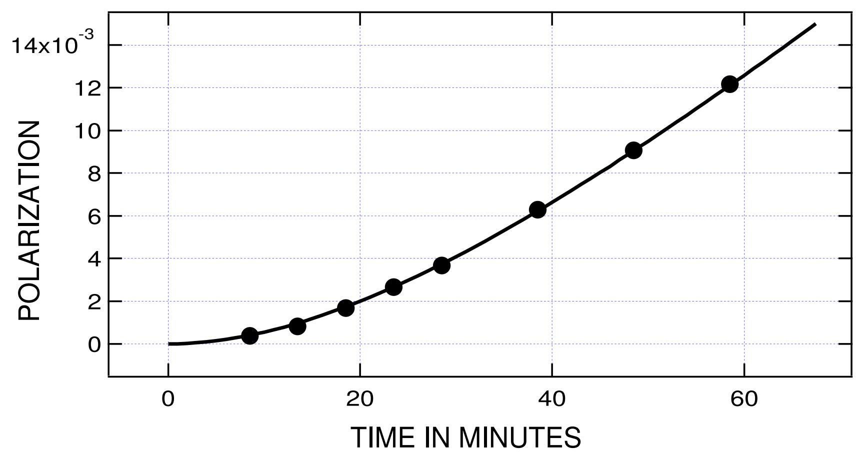

Figure A.2: Spin up of the SLAC experiment E154 target cell SMC and fit to the model of equation A.14.

Using the value of the transfer time measured for the SLAC experiment E154 target cell SMC, the values of the lifetime of the target cell Picard with both the beam on (55 hours) and off (84 hours), and the dimensions and operating temperatures of the target cell Picard under normal running conditions, the spin up data for the target cell Picard can be fit to determine the spin exchange rate γ_{SE} and the average rubidium polarization. The results are ${\gamma_{SE}}^{-1} = 10 \pm 1$ hours and $\langle P_{Rb} \rangle = 0.80 \pm 0.07$. Using these values for the model, the prediction of the model is shown in figure A.3. The equilibrium polarization predicted for the pumping cell is 0.50,

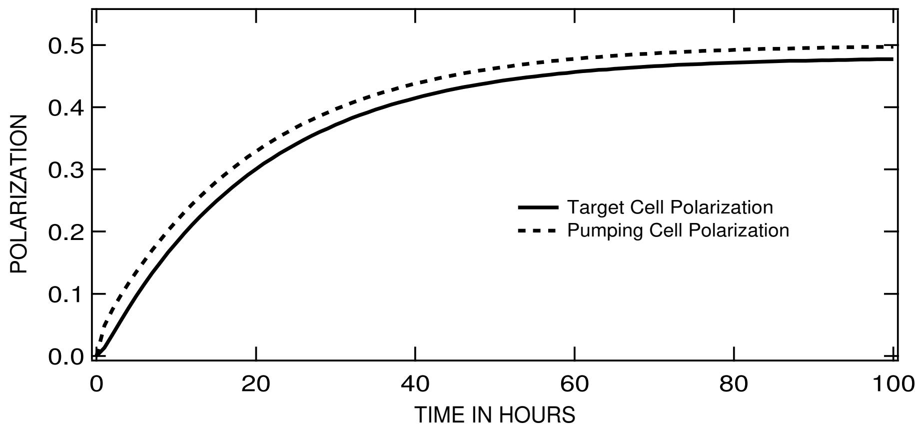

Figure A.3: Model prediction for the time evolution of the polarization of the SLAC experiment E154 target cell Picard.

and the equilibrium polarization predicted for the target cell is 0.485, giving a value of 0.97 ± 0.015 for D_{tt}, the ratio of the target cell to pumping cell polarization. The value of D_{tt} is primarily determined by the transfer time and is in good agreement with similar calculations based on the transfer time by Chupp *et al.* [63].

BIBLIOGRAPHY

BIBLIOGRAPHY

[1] E. Rutherford, *The Scattering of α and β Particles by Matter and the Structure of the Atom*, Phil. Mag. **21**, (series VI), 669 (1911)

[2] H. Geiger and E. Marsden, *The Laws of Deflexion of α Particles through Large Angles*, Phil. Mag. **25**, (series VI), 604 (1913)

[3] Dupen, Douglas Wm., *The Story of Stanford's Two-Mile-Long Accelerator*, SLAC-0062, (May 1966)

[4] Bloom, E. D. et al., *High Energy Inelastic e-p Scattering at* $6°$ *and* $10°$, Phys. Rev. Lett. **23**, 930 (1969)

[5] Breidenbach, M. et al., *Observed Behavior of Highly Inelastic Electron-Proton Scattering*, Phys. Rev. Lett. **23**, 935 (1969)

[6] Bjorken, J. D., *Asymptotic Sum Rules at Infinite Momentum*, Phys. Rev. **179**, 1547 (1969)

[7] Callan, C. G., Jr., and Gross, David J., *High-Energy Electroproduction and the Constitution of the Electric Current*, Phys. Rev. Lett. **22**, 156 (1969)

[8] Feynman, R. P., *Very High-Energy Collisions of Hadrons*, Phys. Rev. Lett. **23**, 1415 (1969)

[9] Feynman, R. P., *Photon-Hadron Interactions*, W. A. Benjamin, INC., Reading, Massachusetts (1972)

[10] Roberts, R. G., *The structure of the proton*, Cambridge University Press, Cambridge, England (1990)

[11] The EMC Collaboration, Aubert, J. J. et al., *The Ratio of the Nucleon Structure Functions $F_2{}^n$ for Iron and Deuterium*, Phys. Lett. **B123**, 275 (1983)

[12] The EMC Collaboration, Ashman, J. et al., *Measurement of the Ratios of Deep Inelastic Muon-Nucleus Cross-Sections on Various Nuclei Compared to Deuterium*, Phys. Lett. **B202**, 603 (1988)

[13] Bjorken, J. D., *Applications of the Chiral U(6) $\otimes$ U(6) Algebra of Current Densities*, Phys. Rev. **148**, 1467 (1966)

[14] Ellis, J., and Jaffe, R. L., *Sum Rule for Deep-Inelastic Electroproduction from Polarized Protons*, Phys. Rev. **D9**, 1444 (1974)

[15] The E80 Collaboration, Alguard, M. J. et al., *Deep Inelastic Scattering of Polarized Electrons by Polarized Protons*, Phys. Rev. Lett. **37**, 1261 (1976)

[16] The E80 Collaboration, Alguard, M. J. et al., *Deep Inelastic e-p Asymmetry Measurements and Comparison with the Bjorken Sum Rule and Models of the Proton Spin Structure*, Phys. Rev. Lett. **41**, 70 (1978)

[17] The E130 Collaboration, Baum, G. et al., *A New Measurement of Deep Inelastic e-p Asymmetries*, Phys. Rev. Lett. **51**, 1135 (1983)

[18] The EMC Collaboration, Ashman, J. et al., *A Measurement of the Spin Asymmetry and Determination of the Structure Function g_1 in Deep Inelastic Muon-Proton Scattering*, Phys. Lett. **B206**, 364 (1988)

[19] The EMC Collaboration, Hughes, V. et al., *The Integral of the Spin Dependent Structure Function $g_1{}^p$ and the Ellis-Jaffe Sum Rule*, Phys. Lett. **B212**, 511 (1988)

[20] The EMC Collaboration, Ashman, J. et al., *An Investigation of the Spin Structure of the Proton in Deep Inelastic Scattering of Polarized Muons on Polarized Protons*, Nucl. Phys. **B328**, 1 (1989)

[21] Gross, D. J., and Wilczek, F., *Asymptotically free gauge theories*, Phys. Rev. **D9**, 980 (1974)

[22] Ellis, J. and Karliner, M., *The strange Spin of the Nucleon*, preprint, CERN-TH/95-334, (1995)

[23] Friar, J. L., et al., *Neutron polarization in polarized ^3He targets*, Phys. Rev. **C42**, 2310 (1990)

[24] The SMC Collaboration, Adeva, B. et al., *Measurement of the Spin-Dependent Structure Function $g_1(x)$ of the Deuteron*, Phys. Lett. **B302**, 533 (1993)

[25] The SMC Collaboration, Adams, D. et al., *Measurement of the Spin-Dependent Structure Function $g_1(x)$ of the Proton*, Phys. Lett. **B329**, 399 (1994)

[26] The SMC Collaboration, Adams, D. et al., *A New Measurement of the Spin-Dependent Structure Function $g_1(x)$ of the Deuteron*, Phys. Lett. **B357**, 248 (1995)

[27] The E142 Collaboration, Anthony, P. L. et al., *Determination of the Neutron Spin Structure Function*, Phys. Rev. Lett. **71**, 959 (1993)

[28] The E142 Collaboration, Anthony, P. L. et al., *Deep Inelastic Scattering of Polarized Electrons by Polarized ^3He and the Study of the Neutron Spin Structure*, Phys. Rev. **D54**, 6620 (1996)

[29] The E143 Collaboration, Abe, K. et al., *Precision Measurement of the Proton Spin Structure Function $g_1{}^p$*, Phys. Rev. Lett. **74**, 346 (1995)

[30] The E143 Collaboration, Abe, K. et al., *Precision Measurement of the Deuteron Spin Structure Function* ${g_1}^d$, Phys. Rev. Lett. **75**, 25 (1995)

[31] Zakharov, V. I., *Lecture notes on Quantum Chromodynamics*, unpublished (1996)

[32] Close, F. E., *An Introduction to Quarks and Partons*, Academic Press, INC., San Diego, California (1979)

[33] The NMC Collaboration, Arneodo, M., et al., *Measurement of the proton and the deuteron structure functions,* ${F_2}^p$ *and* ${F_2}^d$, Phys. Lett. **B364**, 107 (1995)

[34] Whitlow, L. W., et al., *A precise extraction of* $R = \sigma_L/\sigma_T$ *from a global analysis of SLAC deep inelastic e–p and e–d scattering cross sections*, Phys. Lett. **B250**, 193 (1990)

[35] Ciofi degli Atti, C., Scopetta, S., Pace, E., and Salmè, G., *Nuclear effects in deep inelastic scattering of polarized electrons off polarized* ^{3}*He and the neutron spin structure functions*, Phys. Rev. **C48**, R968 (1993)

[36] Particle Data Group, (Barnett, R. M., et al.), *Review of Particle Properties*, Phys. Rev. **D54**, 48 (1996)

[37] Larin, S. A., and Vermaseren, J. A. M., *The* α_s^3 *corrections to the Bjorken sum rule for polarized electroproduction and to the Gross-Llewellyn Smith sum rule*, Phys. Lett. **B259**, 345 (1991)

[38] Alley, R., et al., *The Stanford Linear Accelerator Polarized Electron Source*, Nucl. Inst. Meth. Phys. Res. **A365**, 1 (1995)

[39] Band, H. R., et al., *The E154 Møller Polarimeter*, E-154 Technical Note # 40 (1996), unpublished

[40] Arrington, J., et al., *A variable energy Møller Polarimeter at the MIT-Bates Linear Accelerator Center*, Nucl. Inst. Meth. Phys. Res. **A311**, 39 (1992)

[41] Møller, C., *High Energy electron-electron scattering*, Ann. Phys. **14**, 532 (1932)

[42] Scott, G. G., and Sturner, H. W., *Magnetomechanical ratios for Fe-Co alloys* Phys. Rev. **184** 490 (1969)

[43] Levchuk, L. G., *The intra-atomic motion of bound electrons as a possible source of the systematic error in electron beam polarization measurements by means of a Møller polarimeter*, Nucl. Inst. Meth. Phys. Res. **A345**, 496 (1994)

[44] Stuart, L., *E154 Beam Energies and Spin Precession*, E-154 Technical Note # 6 (1995), unpublished

[45] Johnson, J. R., et al., *The SLAC high-density gaseous polarized ^{3}He target*, Nucl. Inst. Meth. Phys. Res. **A356** 148 (1995)

[46] Wang, J., *private communication*, (1996)

[47] Happer, W., *Optical Pumping*, Rev. Mod. Phys. **44**, 169 (1972)

[48] Bouchiat, M. A., Carver, T. R., and Varnum, C. M., *Nuclear Polarization in ^{3}He Gas Induced by Optical Pumping and Dipolar Exchange*, Phys. Rev. Lett. **5**, 373 (1960)

[49] Colegrove, F. D., Schearer, L. D., and Walters, G. K., *Polarization of ^{3}He Gas by Optical Pumping*, Phys. Rev. **132**, 2561 (1963)

[50] Fitzsimmons, W. A., and Walters, G. K., *Very Long Nuclear Spin Relaxation Times in Gaseous ^{3}He by Suppression of ^{3}He–Surface Interactions*, Phys. Rev. Lett. **19**, 943 (1967)

[51] Timsit, R. S., Daniels, J. M., and May, A. D., *Nuclear Relaxation of ^{3}He Gas on Various Solid Surfaces*, Can. Jour. Phys. **49**, 560 (1971)

[52] Chupp, T. E., and Coulter, K. P., *Polarization of* ^{21}Ne *by Spin Exchange with Optically Pumped Rb Vapor*, Phys. Rev. Lett. **55**, 1074 (1985)

[53] Coulter, K. P., *Measurements of Parity Violation in a Search for Candidate Resonances for a Test of Time Reversal Invariance in Neutron Absorption*, Ph.D. dissertation, (unpublished, Princeton University, 1989)

[54] Newbury, N. R., et al., *Polarization-dependent frequency shifts from Rb-*^3He *collisions*, Phys. Rev. **A48**, 558 (1993)

[55] Kastler, A., *Un Systeme de Franges de Diffraction de Grand Contraste*, Jour. Phys. Radium **11**, 255 (1950)

[56] Wagshul, M. E., and Chupp, T. E., *Laser Optical Pumping of High Density Rb in Polarized* ^3He *Targets*, Phys. Rev. **A49**, 3854 (1994)

[57] Anderson, L. W., and Walker, T., *The effect of radiation trapping on a high field spin exchange optically pumped target*, Nucl. Inst. Meth. Phys. Res. **A316** 123 (1992)

[58] Hrycyshyn, E. S., and Kraus, L., *Inelastic collisions between excited alkali atoms and molecules. VII. Sensitized flouresence and quenching in mixtures of rubidium with* H_2, *HD*, D_2, N_2, CH_4, CD_4, C_2H_4, *and* C_2H_6, Can. Jour. Phys. **48**, 2761 (1970)

[59] Happer, W., et al., *Polarization of the Nuclear Spins of Noble Gas Atoms by Spin Exchange with Optically Pumped Alkali Metal Atoms*, Phys. Rev. **A29**, 3092 (1984)

[60] Walker, T. G., and Happer, W., *Spin Exchange Optical Pumping of Noble Gas Nuclei*, Rev. Mod. Phys. **69**, 629 (1997)

[61] Gamblin, R. L., and Carver, T. R., *Polarization and Relaxation Processes in* He^3 *Gas*, Phys. Rev. **A138**, 946 (1965)

[62] Newbury, N. R., et al., *Gaseous* ^3He*–*^3He *magnetic dipolar spin relaxation*, Phys. Rev. **A48**, 4411 (1993)

[63] Chupp, T. E., et al., *Tests of a high density* ^3He *target for electron scattering*, Phys. Rev. **C45**, 915 (1992)

[64] Bonin, K., Walker, T., and Happer, W., *Relaxation of gaseous spin-polarized* ^3He *targets due to ionizing radiation*, Phys. Rev. **A37**, 3270 (1988)

[65] Chupp, T. E., Coulter, K. P., Hwang, S. R., Smith, T. B., and Welsh R. C., *Progress Toward a Spin Exchange Pumped* ^3He *Neutron Spin Filter*, J. Neutron Research, Vol. **5**, 11 (1996)

[66] Romalis, M. V., Miron, E., and Cates, G. D., *Pressure Broadening of Rb* D_1 *and* D_2 *lines by* ^3He*,* ^4He*,* N_2*, and Xe: line cores and near wings*, to be published in Phys. Rev. **A**

[67] Abragam, A., *Principles of Nuclear Magnetism*, Oxford University Press, Oxford, England (1961)

[68] Bloch, F., and Siegert, A., *Magnetic Resonance for Nonrotating Fields*, Phys. Rev. **57**, 522 (1940)

[69] Romalis, M. V., and Smith, T. B., *E154 Target Polarization Technical Note*, E-154 Technical Note # 47 (1996), unpublished

[70] Simpson, J. H., and Carr, H. Y., *Diffusion and Nuclear Spin Relaxation in Water*, Phys. Rev. **111**, 1201 (1956)

[71] Meiboom, S., Luz, Z., and Gill, D., *Proton Relaxation in Water*, Jour. Chem. Phys. **27**, 1411 (1957)

[72] Meiboom, S., *Nuclear Magnetic Resonance Study of the Proton Transfer in Water*, Jour. Chem. Phys. **34**, 375 (1960)

[73] Glick, R. E., and Tewari, K. C., *Proton Nuclear Magnetic Relaxation Studies on Water: The Rates of Acid and Base Catalyzed Proton Exchange*, Jour. Chem. Phys. **44**, 546 (1966)

[74] Grover, B. C., *Noble-Gas NMR Detection through Noble-Gas-Rubidium Hyperfine Contact Interaction*, Phys. Rev. Lett. **40**, 391 (1978)

[75] Schaefer, S. R., et al., *Frequency shifts of the magnetic-resonance spectrum of mixtures of nuclear spin-polarized noble gases and vapors of spin-polarized alkali-metal atoms*, Phys. Rev. **A39**, 5613 (1989)

[76] Happer, W., and Tam, C. A., *Effect of rapid spin exchange on the magnetic-resonance spectrum of alkali vapors*, Phys. Rev. **A16**, 1877 (1977)

[77] Barton, A. S., et al., *Self-calibrating measurement of polarization-dependent frequency shifts from Rb–^{3}He collisions*, Phys. Rev. **A49**, 2766 (1994)

[78] *Material Information Sheet, glass code 1720* Corning Glass Works, Corning, NY.

[79] Smirnov, G. I., *On the universality of the x and A dependence of the EMC effect and its relation to parton distributions in nuclei*, Phys. Lett. **B364**, 87 (1995)

[80] Gomez, J., et al., *Measurement of the A-dependence of deep inelastic electron scattering*, Phys. Rev. **D49**, 4348 (1994)

[81] *GEANT Detector Description and Simulation Tool*, CERN Program Library, **W5013** (1994)

[82] Breton, V., et al., *Application of neural networks and cellular automata to interpretation of calorimeter data*, Nucl. Inst. Meth. Phys. Res. **A362** 478 (1995)

[83] Zyla, Piotr, *E154 Rate Dependence Studies*, E-154 Technical Note (1996), unpublished

[84] Incerti, S., and Breton, V., *A method to estimate the pion contamination*, E-154 Technical Note # 36 (1996), unpublished

[85] Sabatie, F., *Background subtraction*, E-154 Technical Note # 45 (1996), unpublished

[86] Cahn, R., and Gilman, F., *Polarized electron-nucleon scattering in gauge theories of weak and electromagnetic interactions*, Phys. Rev. **D17**, 1313 (1978)

[87] Beck, D., *Flavor structure of the nucleon from future parity violating electron scattering experiments*, Nucl. Phys. **A532**, 507 (1990)

[88] Kukhto, T. V., and Shumeiko, N. M., *Radiative effects in deep inelastic scattering of polarized leptons by polarized nucleons*, Nucl. Phys. **B129**, 412 (1983)

[89] Akushevich, I. V., and Shumeiko, N. M., *Radiative effects in deep inelastic scattering of polarized leptons by polarized light nuclei*, J. Phys. **G20**, 513 (1994)

[90] The E154 Collaboration, Abe, K. et al., *A precision determination of the neutron spin structure function g_1^n*, SLAC PUB 7459, 1 (1997)

[91] The E154 Collaboration, Abe, K. et al., *A precision determination of the neutron spin structure function g_1^n*, Phys. Rev. Lett. **79**, 26 (1997)

[92] The E143 Collaboration, Abe, K. et al., *Measurements of the Q^2 dependence of the proton and deuteron spin structure functions ${g_1}^p$ and ${g_1}^d$*, Phys. Lett. **B364**, 61 (1995)

[93] The E154 Collaboration, Abe, K. et al., *Next-to-leading order QCD analysis of polarized deep inelastic scattering data*, Phys. Lett. **B405**, 180 (1997)

[94] Brodsky, S. J., Burkardt, M., and Schmidt, I., *Perturbative QCD constraints on the shape of polarized quark and gluon distributions*, Nucl. Phys. **B441** 197 (1995)

[95] Heimann, R. L., *Scaling of the longitudinal photon cross section and its relation to massless quarks* , Nucl. Phys. **B78**, 525 (1974)

[96] Anselmino, M., Efremov, A., and Leader, E., *The theory and phenomenology of polarized deep inelastic scattering*, Phys. Rept. **261**, 1 (1995), Erratum-ibid **281** 399 (1997)

[97] Bartels, J., Ermolaev, B. I., and Ryskin, M. G., *Flavor singlet contribution to the structure function g_1 at small x*, Z. Phys. **C70** 273 (1996)

ABSTRACT

A PRECISION MEASUREMENT OF THE NEUTRON SPIN STRUCTURE FUNCTIONS USING A POLARIZED ^{3}He TARGET

by

Todd B. Smith

Chairperson: Professor Timothy Chupp

This thesis describes a precision measurement of the neutron spin dependent structure function, $g_1^n(x)$. The measurement was made by the E154 collaboration at SLAC using a longitudinally polarized, 48.3 GeV electron beam, and a ^{3}He target polarized by spin exchange with optically pumped rubidium. A target polarization as high as 50% was achieved. The elements of the experiment which pertain to the polarized ^{3}He target will be described in detail in this thesis. To achieve a precision measurement, it has been necessary to minimize the systematic error from the uncertainty in the target parameters. All of the parameters of the target have been carefully measured, and the most important parameters of the target have been measured using multiple techniques. The polarization of the target was measured using nuclear magnetic resonance techniques, and has been calibrated using both proton NMR and by measuring the shift of the Rb Zeeman resonance frequency due to the ^{3}He polarization. The fraction of events which originated in the ^{3}He, as measured by the spectrometers, has been determined using a physical model of the target and the spectrometers. It was also measured during the experiment using a variable pressure ^{3}He reference cell in place of the polarized ^{3}He target.

The spin dependent structure function $g_1^n(x)$ was measured in the Bjorken x range of $0.014 < x < 0.7$ with an average Q^2 of 5 (GeV/c)^2. One of the primary motivations for this experiment was to test the Bjorken sum rule. Because the experiment had smaller statistical errors and a broader kinematic coverage than previous experiments, the behavior of the spin structure function $g_1^n(x)$ could be studied in detail at low values of the Bjorken scaling variable x. It was found that $g_1^n(x)$ has a strongly divergent behavior at low values of x, calling into question the methods commonly used to extrapolate the value of $g_1^n(x)$ to low x. The precision of the measurement made by the E154 collaboration at SLAC puts a tighter constraint on the extrapolation of $g_1^n(x)$ to low x, which is necessary to evaluate the Bjorken sum rule.